# Deposit & Copying of Dissertation Declaration

UNIVERSITY OF CAMBRIDGE

**Board of Graduate Studies**

Please note that you will also need to bind a copy of this Declaration into your final, hardbound copy of thesis - this has to be the very first page of the hardbound thesis.

| 1 Surname (Family Name) | Forenames(s) | Title |
|---|---|---|
| Halat | David Michael | Mr |

| 2 Title of Dissertation as approved by the Degree Committee |
|---|
| $^{17}$O Solid-State NMR Spectroscopy of Functional Oxides for Energy Conversion |

In accordance with the University Regulations in *Statutes and Ordinances* for the PhD, MSc and MLitt Degrees, I agree to deposit one print copy of my dissertation entitled above and one print copy of the summary with the Secretary of the Board of Graduate Studies who shall deposit the dissertation and summary in the University Library under the following terms and conditions:

**1. Dissertation Author Declaration**

I am the author of this dissertation and hereby give the University the right to make my dissertation available in print form as described in 2. below.

My dissertation is my original work and a product of my own research endeavours and includes nothing which is the outcome of work done in collaboration with others except as declared in the Preface and specified in the text. I hereby assert my moral right to be identified as the author of the dissertation.

The deposit and dissemination of my dissertation by the University does not constitute a breach of any other agreement, publishing or otherwise, including any confidentiality or publication restriction provisions in sponsorship or collaboration agreements governing my research or work at the University or elsewhere.

**2. Access to Dissertation**

I understand that one print copy of my dissertation will be deposited in the University Library for archival and preservation purposes, and that, unless upon my application restricted access to my dissertation for a specified period of time has been granted by the Board of Graduate Studies prior to this deposit, the dissertation will be made available by the University Library for consultation by readers in accordance with University Library Regulations and copies of my dissertation may be provided to readers in accordance with applicable legislation.

| 3 Signature | Date |
|---|---|
| David M. Halat | 11 JANUARY 2018 |

**Corresponding Regulation**

Before being admitted to a degree, a student shall deposit with the Secretary of the Board one copy of his or her hard-bound dissertation and one copy of the summary (bearing student's name and thesis title), both the dissertation and the summary in a form approved by the Board. The Secretary shall deposit the copy of the dissertation together with the copy of the summary in the University Library where, subject to restricted access to the dissertation for a specified period of time having been granted by the Board of Graduate Studies, they shall be made available for consultation by readers in accordance with University Library Regulations and copies of the dissertation provided to readers in accordance with applicable legislation.

# $^{17}$O Solid-State NMR Spectroscopy of Functional Oxides for Energy Conversion

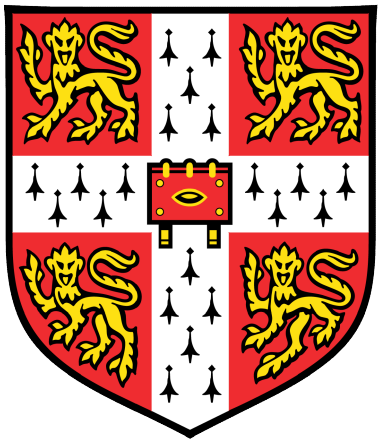

**David Michael Halat**

Department of Chemistry

University of Cambridge

This dissertation is submitted for the degree of

*Doctor of Philosophy*

Churchill College

September 2017

# Abstract


## $^{17}$O Solid-State NMR Spectroscopy of Functional Oxides for Energy Conversion

**David Michael Halat**

The main aim of this thesis is the development of $^{17}$O solid-state nuclear magnetic resonance (NMR) spectroscopic techniques to study the local structure and ion dynamics of functional oxide materials for applications in energy conversion, in particular as electrodes and electrolytes in solid oxide fuel cells (SOFCs). Broadly, the work comprises two related areas: (1) application of a combined experimental and computational methodology to enable the first $^{17}$O solid-state NMR studies of *paramagnetic* oxides, in particular a class of perovskite-derived structures used as mixed ionic-electronic conductors (MIECs) for SOFC cathodes, and (2) further uses of multinuclear variable-temperature NMR spectroscopy, with emphasis on $^{17}$O NMR results, to elucidate mechanistic details of oxide-ion motion and sublattice exchange in a novel family of promising SOFC electrolyte materials based on $\delta$-$Bi_2O_3$.

In the first section, $^{17}$O magic-angle spinning (MAS) NMR spectra of the paramagnetic MIEC, $La_2NiO_{4+\delta}$, are presented and rationalized with the aid of periodic DFT calculations. Advanced NMR pulse programming and quadrupolar filtering techniques are coupled to extract high-resolution spectra. In particular, these data reveal local structural distortions in $La_2NiO_{4+\delta}$ that arise from incorporation of interstitial oxide defects. Moreover, variable-temperature spectra indicate the onset of oxide-ion motion involving the interstitials at 130 °C, which is linked to an orthorhombic–tetragonal phase transition. By analyzing the ion dynamics on the spectral timescale, specific motional mechanisms are elucidated that prove relevant to understanding the functionality and conductivity of this phase.

Next, a similar methodology is applied to the Sr-doped analogues, $La_{2-x}Sr_xNiO_{4+\delta}$, in an exploration of the defect chemistry and electronic structure of these phases ($0 \leq x \leq 1$). By

following the doping-induced evolution of spectral features assigned to interstitial and equatorial oxygen environments, changes in the ionic and electronic conductivity, respectively, are rationalized. This approach has been extended to the acquisition and assignment of $^{17}O$ NMR spectra of isostructural $Sm_{2-x}Sr_xNiO_{4+\delta}$ and $Pr_{2-x}Sr_xNiO_{4+\delta}$ phases, promising SOFC cathode materials that exhibit paramagnetism on the A site (A = Sm, Pr).

The final section details the characterization of oxide-ion motion in the fluorite-type phases $Bi_{1-x}V_xO_{1.5+x}$ and $Bi_{1-x}P_xO_{1.5+x}$ ($x$ = 0.087 and 0.148) developed as SOFC electrolytes. Variable-temperature NMR experiments between room temperature and 923 K reveal two distinct mechanisms. For the V-doped phases, an oxide-ion conduction mechanism is observed that involves oxygen exchange between the Bi-O sublattice and rapidly rotating $VO_4$ tetrahedral units. The more poorly conducting P-doped phase exhibits only vacancy conduction with no evidence of sublattice exchange, a result ascribed to the differing propensities of the dopants to undergo variable oxygen coordination. These initial insights suggest chemical design rules to improve the next generation of oxide-ion conducting materials.

*To my mother and father*

# Declaration

I hereby declare that except where specific reference is made to the work of others, the contents of this dissertation are original and have not been submitted in whole or in part for consideration for any other degree or qualification in this, or any other University. This dissertation is the result of my own work and includes nothing that is the outcome of work done in collaboration, except where specifically indicated in the text. This dissertation contains less than 60,000 words excluding the table of contents, figure captions, bibliography, acknowledgments and appendices.

David Michael Halat

September 2017

# Acknowledgments

First and foremost, I would like to thank my fantastic supervisor Professor Clare P. Grey for her support throughout my time here, for sharing of her time and her deep experience, and for the opportunities that have sprung from working in her lab. I feel truly privileged to have spent time learning from such a brilliant scientist, and can only hope to emulate her.

Many thanks are due to those who have guided me through my PhD, in particular Dr Gunwoo Kim for training me in experimental NMR spectroscopy from scratch; Dr Michal Leskes and Dr Andrew Pell for challenging me to go further into the complexities of NMR; and Dr Raphaële Clément and Dr Ieuan Seymour for their assistance and advice with first-principles calculations.

I would like to thank all past and present members of the Grey group for their support, enthusiasm and camaraderie, which have made the past four years truly transformative for me. I am particularly grateful for my long friendships with my B110 officemates: Dr Matthew Dunstan, for constant encouragement, mentorship, helpful advice, and his excellent sense of humor; Dr Alex Forse, for his useful suggestions and good-natured approach to life, as well as for our shared passion for Glenn T. Seaborg; and Dr Sylvia Britto, for our many scientific discussions, and for her contagious happiness and inspiring strength. All of my friends in Churchill College are also gratefully acknowledged, especially Mr Kent Griffith, with whom I have shared more experiences, in many different places, than either of us probably expected, all of them arguably worthwhile. Mr Michael Hope, also of the Grey group, is gratefully acknowledged for proofreading what is probably more than his fair share of this thesis!

I acknowledge all those who have collaborated on aspects of these projects, especially Dr Matthew Dunstan (Department of Chemistry, University of Cambridge) for his assistance in the work presented in Chapter 5, as well as Mr Matthew Tate and Dr Ivana Radosavljević

Evans (Department of Chemistry, Durham University) for synthesizing and providing the bismuth oxide samples studied in that work. Dr Yingjun Liu (Department of Materials Science and Metallurgy, University of Cambridge) is also gratefully acknowledged for providing me with the $Sm_{2-x}Sr_xNiO_{4+\delta}$ samples (see Chapter 4) that were prepared and characterized by Dr A. P. Khandale (present address, School of Chemistry, University of St Andrews).

I am very grateful to the Cambridge Commonwealth, European and International Trusts for awarding me a Schlumberger Cambridge International Scholarship that has allowed me to undertake my doctoral studies, and to the NorthEast Center for Chemical Energy Storage (NECCES), which is an Energy Frontier Research Center (EFRC) sponsored by the U.S. Department of Energy, Office of Science, Basic Energy Sciences (#DE-SC0012583) for additional funding.

Finally, I express boundless gratitude to my mother and father for their unceasing generosity and love; without them, none of this would have been possible.

# List of Publications

Chapter 3 contains material from the publication:

**Halat, D. M.**; Dervişoğlu, R.; Kim, G.; Dunstan, M. T.; Blanc, F.; Middlemiss, D. S.; Grey, C. P. Probing Oxide-Ion Mobility in the Mixed Ionic–Electronic Conductor $La_2NiO_{4+\delta}$ by Solid-State $^{17}O$ MAS NMR Spectroscopy. *J. Am. Chem. Soc.* **138,** 11958–11969 (2016).

Publications not included in this thesis:

Seymour, I. D.; Middlemiss, D. S.; **Halat, D. M.**; Trease, N. M.; Pell, A. J.; Grey, C. P. Characterizing Oxygen Local Environments in Paramagnetic Battery Materials via $^{17}O$ NMR and DFT Calculations. *J. Am. Chem. Soc.* **138,** 9405–9408 (2016).

Pecher, O.*; **Halat, D. M.***; Lee, J.; Liu, Z.; Griffith, K. J.; Braun, M.; Grey, C. P. Enhanced efficiency of solid-state NMR investigations of energy materials using an external automatic tuning/matching (eATM) robot. *J. Magn. Reson.* **275**, 127–136 (2017). (* = equal contribution)

Hope, M. A.; **Halat, D. M.**; Magusin, P. C. M. M.; Paul, S.; Peng, L.; Grey, C. P. Surface-selective direct $^{17}O$ DNP NMR of $CeO_2$ nanoparticles. *Chem. Commun.* **53**, 2142–2145 (2017).

Kim, G.; Griffin, J. M.; Blanc, F.; **Halat, D. M.**; Haile, S. M.; Grey, C. P. Revealing Local Dynamics of the Protonic Conductor $CsH(PO_3H)$ by Solid-State NMR Spectroscopy and First-Principles Calculations. *J. Phys. Chem. C* **121**, *27830* (2017).

# Contents

# List of Figures

# List of Tables

# List of Abbreviations

| | |
|---|---|
| BS-I | Basis set one (contracted) |
| BS-II | Basis set two (extended) |
| CSA | Chemical shift anisotropy |
| DFT | Density functional theory |
| EFG | Electric field gradient |
| FC | Fermi contact |
| HF | Hartree–Fock |
| LCAO | Linear combination of atomic orbitals |
| LOESS | Local regression |
| MAS | Magic-angle spinning |
| MATPASS | Magic-angle turning and phase-adjusted sideband separation |
| MIEC | Mixed ionic–electronic conductor |
| NMR | Nuclear magnetic resonance |
| rf | Radio frequency |
| SCF | Self-consistent field |
| SOFC | Solid oxide fuel cell |

| | |
|---|---|
| TGA | Thermogravimetric analysis |
| VOCS | Variable offset cumulative spectrum |
| VT-NMR | Variable-temperature nuclear magnetic resonance |
| XANES | X-ray absorption near-edge structure |
| XRD | X-ray diffraction |
| YSZ | Yttria-stabilized zirconia |
| $B_0$ | External magnetic field |
| $C_Q$ | Quadrupolar coupling constant |
| $\eta_Q$ | Quadrupolar asymmetry parameter |
| $T_1$ | Spin-lattice (longitudinal) relaxation time constant |
| $T_2$ | Spin-spin (transverse) relaxation time constant |
| $\tau_c$ | Correlation time |
| $\omega_0$ | Larmor frequency |

# Chapter 1 Introduction

*Solid oxide fuel cells (SOFCs) are promising, highly fuel-efficient electrochemical conversion devices which are limited in practical implementation by the need for high-temperature operation (>800 °C). To lower operating temperatures, novel oxide-ion conducting materials must be synthesized and thoroughly studied as prospective electrolytes and electrodes. SOFC cathodes based on mixed ionic-electronic conductors (MIECs) show improved electrocatalytic performance, but the rich interplay of electronic properties, ionic conduction mechanisms and dopant ordering in these materials remains incompletely understood. Similarly, the development of new and improved SOFC electrolyte materials requires knowledge of the connections between structure and oxide-ion conductivity*.

## 1.1 Introduction to solid oxide fuel cells (SOFCs)

Global energy demands have dramatically increased in the last few decades, especially in emerging markets: since 1990, energy consumption in the Middle East has grown by 170%, in China by 146%, in India by 91%, and in Africa and Latin America by 70%.[1] The vast majority of this energy continues to be derived from conventional, non-renewable, carbon-based fuels. Despite the promise of renewables such as wind power, hydropower, and solar energy, incompatibilities between these technologies and existing infrastructure have hampered widespread implementation.[2,3] Moreover, current fuel-based systems, because they primarily rely on internal combustion engines (ICEs), cannot exceed rather poor theoretical fuel efficiencies of 30–40%. Burning fuels also produces environmental pollutants and greenhouse gases that drive global warming, such as CO, $CO_2$, $SO_x$, and $NO_x$ species.[4,5] Finally, the centralized nature of modern power distribution networks, with a backbone of

combustion-driven power stations, hinders access to electricity for those in rural and remote areas of the planet.[6]

Recent developments in fuel cell technology are of great interest in addressing these problems. The past few decades have witnessed significant improvements in polymer electrolyte membrane fuel cells (PEMFCs),[7,8] molten carbonate fuel cells (MCFCs),[9–12] and solid oxide fuel cells (SOFCs).[13–15] SOFCs stand out for their excellent fuel versatility and energy efficiency, but unfortunately require operation at high temperatures (800–1000 °C).[16] Like all fuel cells, SOFCs produce electrical energy directly from chemical energy, *i.e.*, without intermediate conversion to thermal energy *via* combustion, and are therefore not limited by theoretical Carnot cycle efficiencies. Proven fuel sources for SOFCs include pure $H_2$, hydrocarbons, renewable biofuels, and syn-gas (mixtures of $H_2$ and CO).[17,18] In the mid-range (100 kW to 10 MW) power class, SOFCs are among the most efficient fuel-powered devices known, and demonstrate up to 70% fuel efficiency in combined heating and power applications (Figure 1.1). Stationary SOFC stacks developed by Siemens Westinghouse have undergone continuous operation for specialized on-site power generation with lifetimes of over 35,000 hours (~4 years).[19]

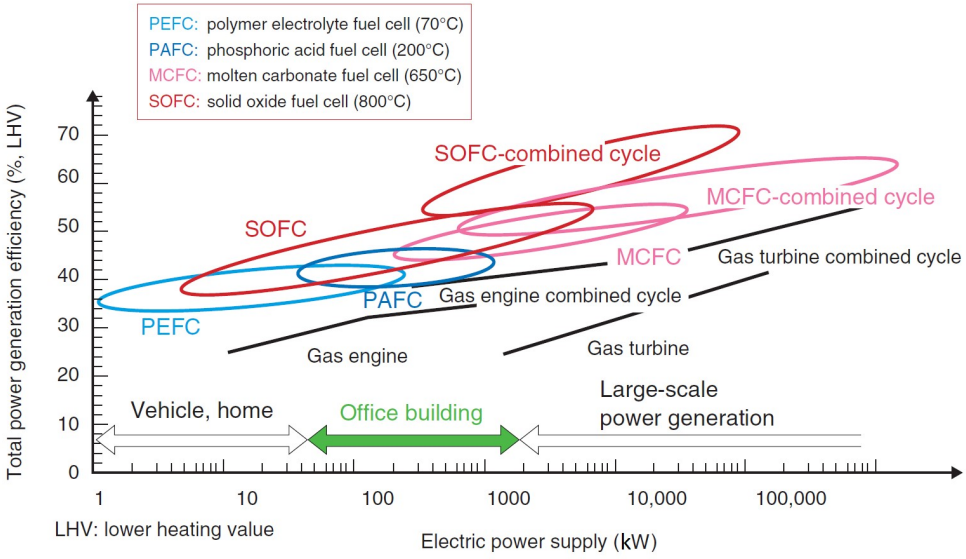


Figure 1.1: Comparison of conversion efficiencies for various fuel cell technologies and combustion engines, as a function of typical generated power; figure reproduced from Hayashi *et al.*[20]

A typical SOFC comprises two electrodes (the anode and cathode) on either side of the electrolyte (Figure 1.2). Interconnects (typically either metallic or based on rare earth chromites) are used between cells to build larger SOFC stacks. Various geometries are possible, *e.g.*, anode- *vs.* electrolyte-supported, or planar *vs.* tubular, with the depicted electrolyte and electrode layers commonly between 10 and 500 $\mu$m in thickness, so that each cell is usually no more than 1 to 2 mm thick.[21] The constituent materials are ceramics or mixed ceramic–metallic composites (cermets) which allow ionic and/or electronic conductivity at elevated temperatures, and possess mutually compatible thermal expansion coefficients.

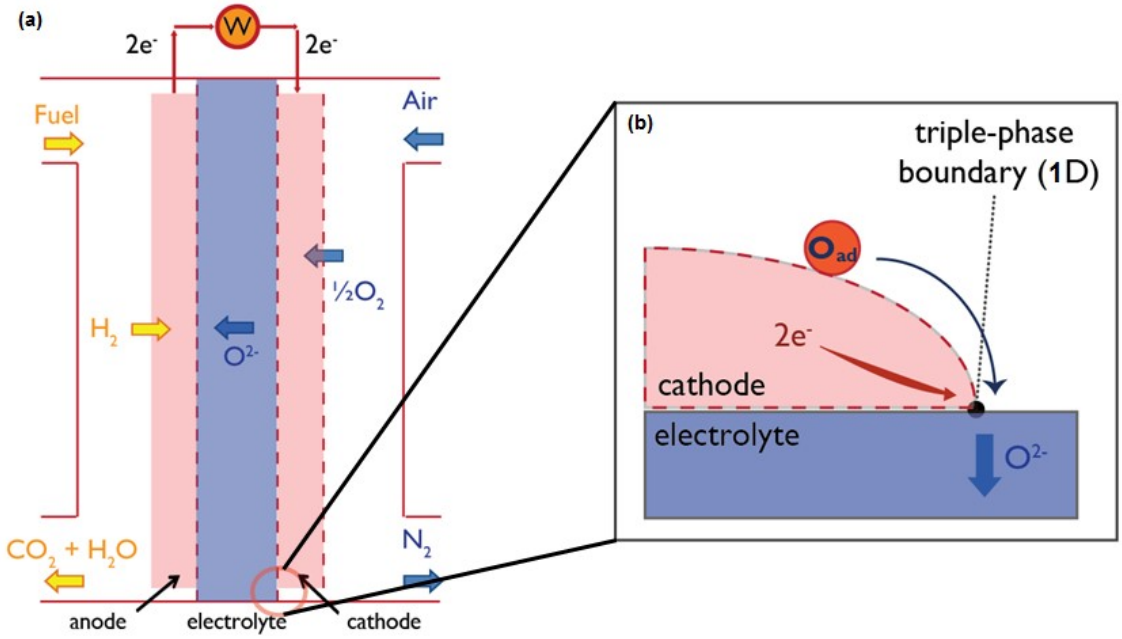


Figure 1.2: (a) Simplified cross-sectional schematic of an operational SOFC, highlighting (b) the performance-limiting oxygen reduction reaction at the triple phase boundary (TPB). While the TPB is shown schematically at the edge, for a porous electrode the actual TPB will comprise all regions of the cathode–electrolyte interface with access to air.

During operation at elevated temperatures, $O_2$ from the ambient air is catalytically reduced to oxide ($O^{2-}$) anions at the porous cathode; this is typically considered to occur at the triple-phase boundary (TPB) regions where cathode, electrolyte, and gas meet. These then propagate through the dense oxide-ion conducting electrolyte to the interface with the porous anode, reacting with incoming fuel (*e.g.,* $H_2$ or hydrocarbons) to produce gaseous waste

($H_2O$, $CO_2$) and electrons to drive the external electric circuit. The interconnect material connects single cells in series or in parallel to form high-voltage, high-power SOFC stacks, and plays no role in electrochemical conversion. The electrolyte material is required to be an excellent oxide-ion conductor but also an electrical insulator, as transport of electrons exclusively *via* the external circuit is required to minimize polarization losses. Similarly, the electrodes must be optimized for high electrical conductivity and catalytic activity. Finally, all the materials must be stable at high operational temperatures in either highly oxidizing or reducing atmospheres at the cathode and anode, respectively, and exhibit mechanical and chemical compatibility.[22]

These extreme operating conditions constrain the choices of materials for the anode, cathode, and electrolyte. Operation at 800–1000 °C is particularly problematic but is necessitated by (1) poor oxide-ion conductivity in prospective electrolytes and (2) significantly reduced oxygen reduction reaction (ORR) activity at the cathode at lower temperatures. Typical selections for the electrolyte, anode, and cathode are 8 mol% yttria-stabilized zirconia (YSZ, *i.e.*, $(Y_2O_3)_{0.08}(ZrO_2)_{0.92}$), a Ni-YSZ cermet, and an electrocatalytic perovskite such as $La_{1-x}Sr_xMnO_3$ (lanthanum strontium manganite, LSM), respectively.[23] While high-temperature operation does have benefits, such as facile reforming of diverse fuels and recovery of waste heat *via* combined heat and power (CHP) systems,[19] these are more than negated by long start-up times, accelerated degradation, and delamination of the electrodes on repeated thermal cycling. The majority of recent research has therefore focused on improving performance at lower temperatures (500–800 °C),[22,24,25] with devices operating in this range referred to as intermediate-temperature SOFCs (IT-SOFCs). Notably, at intermediate temperatures, less expensive ferritic steel interconnects can also be used, lowering overall manufacturing costs.[26]

Approaches to reduce the operational temperature of SOFCs have been advanced from both the fields of materials chemistry and engineering, but here only the former is considered. Novel electrolyte materials with impressive oxide-ion conductivity at lower temperatures have been discovered and optimized. Ceria-based electrolytes, just like YSZ, adopt the fluorite-type structure, and doped ceria and YSZ have similar maximum ionic conductivities (~0.1 S $cm^{-1}$) but at different temperatures: Gd-doped ceria or Sm-doped ceria at ~800 °C,

and YSZ at ~1000 °C.[27] A related class of purely oxide-ion conducting materials is the doped δ-$Bi_2O_3$ phases which adopt a pseudo-cubic, long-range ordered fluorite-type structure, and are described in further detail in Section 1.3. The discovery of oxide-ion conductors of other structure types, with aliovalent doping commonly employed to enhance conductivity, has also led to significant progress in the field. Ishihara *et al.*, concurrently with Goodenough, made the critical discovery of electrolytes based on $LaGaO_3$ with a perovskite rather than fluorite structure.[28,29] As perovskites ($ABO_3$) tolerate a wide variety of dopants on both the A and B sites, a broad compositional space is available for optimization of these materials.

Even with the use of optimized electrolyte materials, as the SOFC operating temperature is reduced, the cathode performance will suffer due to poor reaction kinetics and reduced gas transport, severely limiting the overall performance. The ORR at the cathode (Figure 1.2b) depends on gas transport and electronic and ionic conductivities, and is therefore confined to the gas–cathode–electrolyte TPB. Cathode and thus overall SOFC performance has been shown to directly correlate with the TPB length.[30–33] However, by using a compatible mixed ionic–electronic conductor (MIEC) as the cathode, the reaction kinetics are enhanced by increasing the dimensionality of the reaction boundary. In addition to providing electronic conductivity, MIEC cathodes allow transport of oxide ions so that oxygen reduction can occur along the entire cathode surface, and the larger area of the MIEC–gas two-phase boundary determines SOFC performance. Moreover, conventional cathode materials such as LSM, which are very poor oxide-ion conductors, must remain porous at elevated temperature to ensure an active TPB.[26] A highly stable porous cathode morphology is less critical for MIEC cathodes, simplifying processing constraints.

Huang and Goodenough showed that the use of MIEC cathodes in SOFCs operating at 800 °C yields impressive current densities at modest overpotentials, especially compared to the non-MIEC material LSM.[26] In that study, the MIECs chosen were transition metal perovskite oxides (*e.g.*, $La_{0.6}Sr_{0.4}CoO_{3-\delta}$ and $SrCo_{0.8}Fe_{0.2}O_{3-\delta}$) with high concentrations of oxide vacancies to promote high oxide-ion conductivity. Aspects of the oxygen reduction reaction kinetics and the oxide-ion conductivity in perovskite-based MIECs remain controversial, in particular the effect of cation segregation at the MIEC surface, and the mechanisms of oxygen vacancy formation, trapping, and movement.[34–38] As detailed in the next section, a

thorough understanding of the fundamental electronic and ionic conduction mechanisms in MIECs is important to design the next generation of SOFC cathode materials.

## 1.2 $La_2NiO_{4+\delta}$ and related SOFC cathode materials

Unlike the previously discussed MIECs which possess a purely perovskite structure, $La_2NiO_{4+\delta}$ has a distinctive $K_2NiF_4$-type structure and was the first oxide discovered with this crystal structure by Rabenau and Eckerlin in 1958.[39] Early workers were unaware of the significant oxygen nonstoichiometry ($\delta$) in their samples, yielding an unfortunate litany of divergent experimental results and interpretations.[40,41] Buttrey *et al.* thereafter performed careful studies of single crystals of $La_2NiO_{4+\delta}$ with compositions characterized by iodometric titration,[42–46] and in 1988 Jorgensen *et al.* determined the structure of the interstitial oxygen defects[47] which give rise to the observed hyperstoichiometry. Despite renewed interest in $La_2NiO_{4+\delta}$ and related materials due to the discovery of high-temperature superconductivity in the isostructural cuprates (*e.g.* Sr-doped $La_2CuO_4$), and subsequent debates over interstitial oxygen order and rearrangement in these phases, their relevance as oxide-ion conductors escaped notice until the turn of the century with the ionic transport studies of Kharton *et al.*,[48–50] followed by Skinner *et al.*[51,52] and Bassat *et al.*[53] These researchers were also among the first to exploit the mixed ionic-electronic conductivity of $La_2NiO_{4+\delta}$ in operational SOFC cathodes.

Structurally, the tetragonal $K_2NiF_4$ structure of $La_2NiO_{4+\delta}$ consists of perovskite ($LaNiO_3$) and rock salt ("LaO") layers that alternate along the *c* crystallographic axis (Figure 1.3). The rock salt interlayers are accommodated structurally by the displacement of each perovskite layer in the [110] direction (for the axis choice shown in Figure 1.3), relative to the adjacent layers above and below. The alternating structural motif thus repeats after two pairs of perovskite (*P*) and rock salt (*R*) layers (*i.e.*, *PRP′R′*) resulting in a unit cell with a high degree of tetragonality. Higher-order layered phases $La_{n+1}Ni_nO_{3n+1}$ are also known, the so-called Ruddlesden-Popper structures, which consist of *n* perovskite layers between each rock salt interlayer. $La_2NiO_{4+\delta}$ is the Ruddlesden-Popper phase with $n = 1$, and the perovskite $LaNiO_3$ can be considered as the limiting case of $n = \infty$.

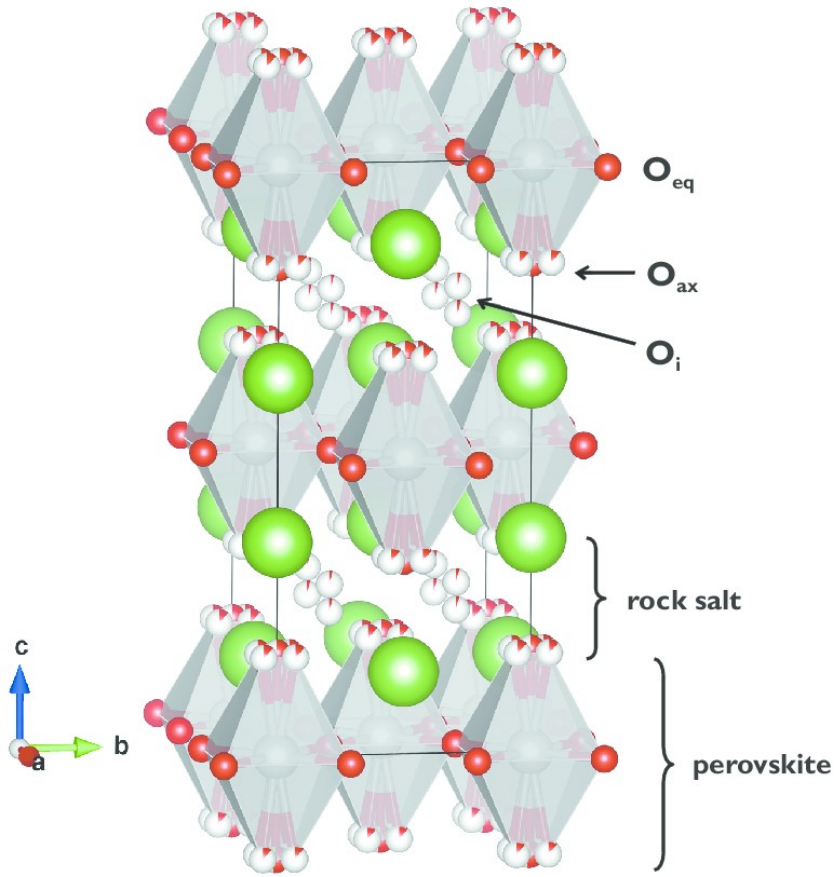


Figure 1.3: Low-temperature orthorhombic (*Fmmm*) structure adopted by $La_2NiO_{4+\delta}$ below ~150 °C, with $\delta = 0.17$.[54] La sites are depicted in green, Ni in grey (at the center of each $NiO_6$ octahedron), and O in red. Partially occupied oxygen sites ($O_{ax}$ and $O_i$) are depicted with correspondingly partially filled red spheres, with $O_{ax}$ split into multiple sites as a consequence of octahedral tilting.

As characterized by the ratio of the ionic radii of the $La^{3+}$ and $Ni^{2+}$ cations (1.22 Å and 0.70 Å, respectively) *via* the Goldschmidt tolerance factor, stoichiometric $La_2NiO_4$ is near the structural stability limit for the $K_2NiF_4$ geometry. The short average La–O distance stretches the rock salt layers and compresses the perovskite layers.[55,56] This structural strain is relieved by (1) cooperative tilting of the $NiO_6$ octahedra and/or (2) intercalation of interstitial oxygen within the rock salt layers. The former mechanism gives rise to an asymmetric distortion propagating through the basal planes, which can induce the normally tetragonal $K_2NiF_4$ structure to adopt an orthorhombic symmetry. Significant $NiO_6$ tilting may also split the axial oxygen sites into crystallographically distinct environments (as shown in Figure 1.3).

In this thesis, the three types of oxygen environments present in $La_2NiO_{4+\delta}$ and related phases are denoted $O_{eq}$ (equatorial), $O_{ax}$ (axial) and $O_i$ (interstitial). $O_{eq}$ and $O_{ax}$ correspond to the O(1) and O(2) sites, respectively, in the work of James and Attfield,[57] Takeda *et al.*,[58] and Jorgensen *et al.*,[47] but this convention is reversed in the studies of Skinner[54] and Millburn *et al.*[59] $O_{eq}$ lies in the perovskite basal (*ab*) planes and is coordinated by two Ni cations; $O_{ax}$ straddles the perovskite and rock salt layers and is adjacent to one Ni cation; and $O_i$ adopts a pseudo-tetrahedral configuration with respect to the four nearby La sites, with no Ni in its immediate coordination environment.

The concentration of interstitial oxygen defects in $La_2NiO_{4+\delta}$, and thus the value of $\delta$, is highly dependent on the thermal and oxidative history of the synthesized samples. Typically, $La_2NiO_{4+\delta}$ prepared under ambient conditions possesses an oxygen excess of $\delta = 0.1–0.2$,[54,60] but oxygen-rich phases with $\delta = 0.25$ and 0.3 have been prepared by electrochemical oxidation[61,62] and high-pressure oxygen annealing,[63] respectively. Because of the interplay between interstitial incorporation and tilting of $NiO_6$ octahedra that gives rise to orthorhombic distortions, the phase diagram of $La_2NiO_{4+\delta}$ is complex,[64] with sensitive dependence on $\delta$ and the presence of biphasic regions (Figure 1.4). In the present discussion, phases with $\delta > 0.16$ are predominantly considered, as prior SOFC research has focused on more oxide-ionic conducting samples with high interstitial content. For these stoichiometries, the low-temperature orthorhombic *Fmmm* phase undergoes a phase transition on heating to a higher symmetry tetragonal *F*4/*mmm* (or alternatively *I*4/*mmm*) phase at or above room temperature, in agreement with the results of Skinner[54] and Aguadero *et al.*,[65] who both identified a phase transition at around 150 °C for $\delta = 0.17$ and $\delta = 0.30$, respectively. An outstanding question is whether these phase transitions are connected to motion of the interstitial defects, which could indicate the onset of oxide-ion conductivity at relatively modest temperatures. In support of this hypothesis, Tranquada *et al.* performed neutron diffraction studies revealing complex interstitial staging structures at smaller values of $\delta$ ($\leq$ 0.1),[66] but only at temperatures below 290 K; the sluggishness of the transition, which also involves an orthorhombic-to-tetragonal phase conversion, suggested kinetics limited by oxide-ion diffusion.

Following the recognition of excellent oxide-ion conductivity in $La_2NiO_{4+\delta}$ at intermediate temperatures (*e.g.*, tracer diffusion coefficient $D^* \approx 3 \cdot 10^{-8}$ cm$^2$ s$^{-1}$ at 700 °C),[51] subsequent studies have focused on the mechanistic details of the oxygen motion and how this is related to the local structure. Oxygen permeation through dense ceramics of doped $La_2NiO_{4+\delta}$ (and isostructural materials) indirectly distinguishes between vacancy diffusion and interstitial diffusion; the latter, which presumably occurs *via* an "interstitialcy" mechanism (see below), is limited to the *ab* plane parallel to the rock salt layers but dominates under conditions of high $pO_2$.[48,49] Isotopic $^{16}O/^{18}O$ exchange results of Bassat *et al.* corroborate highly anisotropic oxide ion diffusion in single crystals of $La_2NiO_{4+\delta}$, with diffusion parallel to the *ab* planes (rock salt layers) over an order of magnitude higher than that along the *c*-axis.[67] Discrepancies have persisted, however, over relative activation energies for these processes, with Bassat *et al.* finding a much smaller $E_a$ for diffusion along the *c*-axis than within the *ab* planes,[67] whereas results of Burriel *et al*. on thin films have shown the reverse.[68] Recently, work by Burriel *et al.* has shown these apparent discrepancies relate to the sample-dependent presence of impurities as well as the occurrence of surface rearrangement processes.[69]

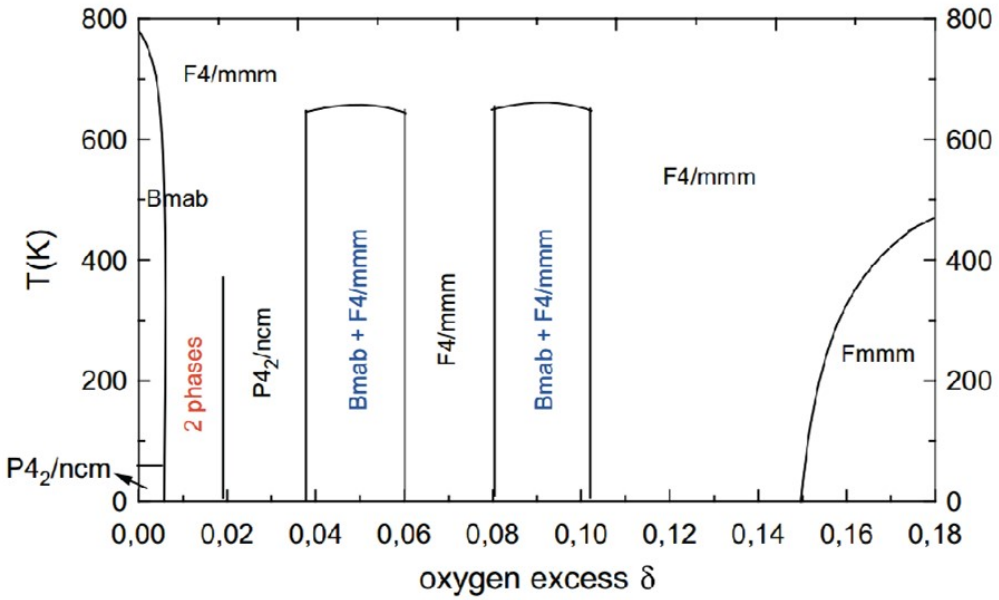


Figure 1.4: The phase diagram of $La_2NiO_{4+\delta}$ as a function of temperature and the hyperstoichiometry $\delta$, reproduced from Poirot *et al.*[64]

Speculative migration pathways for oxide-ion movement in $La_2NiO_{4+\delta}$ have been proposed by several computational studies. Frayret *et al.* have considered a direct diffusion mechanism

involving atomic jumps of the interstitial oxygen ions in the rock salt layer,[55] whereas static atomistic simulations by Minervini *et al.* instead favor a lower energy "interstitialcy" mechanism whereby interstitial defects first displace axial oxygen into unoccupied interstitial sites before taking their place.[70] Molecular dynamics (MD) simulations by Chroneos *et al.* also favor this motional process, visualizing the interstitialcy mechanism in the *ab* plane (Figure 1.5), with an associated $E_a$ value of 0.51 eV.[71] Yashima *et al.* have experimentally confirmed a similar interstitialcy pathway in the isostructural doped compound $(Pr_{0.9}La_{0.1})_2(Ni_{0.74}Cu_{0.21}Ga_{0.05})O_{4+\delta}$ by analysis of nuclear density distribution plots obtained from powder neutron diffraction.[72,73]

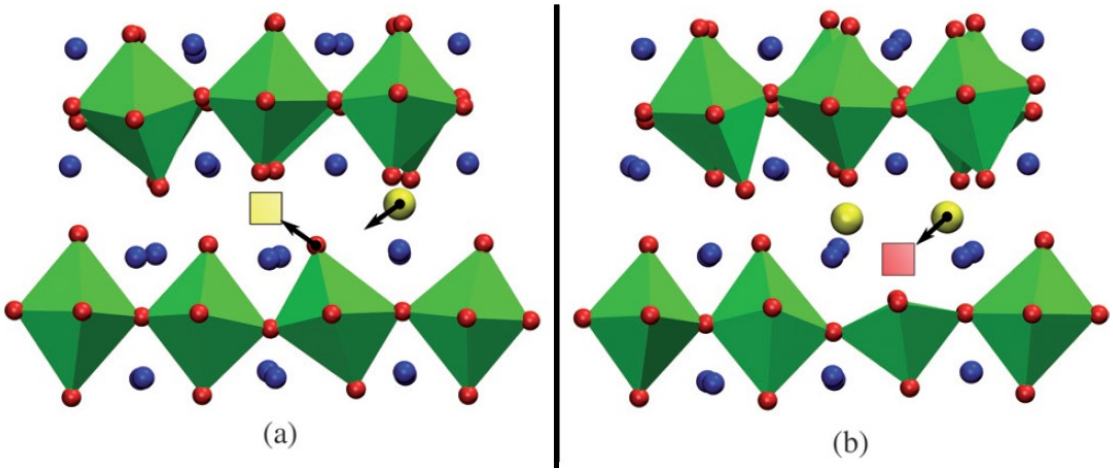


Figure 1.5: Proposed interstitialcy mechanism for oxide-ion diffusion in the rock salt layers of $La_2NiO_{4+\delta}$, consisting of (a) displacement of axial oxygen into a vacant interstitial site, producing (b) a transient axial vacancy available for occupation by a nearby interstitial oxygen. Figure reproduced from Chroneos *et al.*[71]

Interestingly, the electronic conductivity of $La_2NiO_{4+\delta}$ indirectly results from the intercalation of interstitial oxygen. Charge compensation of each incorporated $O^{2-}$ interstitial dopes a maximum of two holes into the electronic structure, and it is generally agreed that this results in partial oxidation of $Ni^{2+}$ to $Ni^{3+}$ rather than localization of holes on oxygen sites.[74–76] The observed Jahn-Teller elongation of the Ni sites implies that these holes reside in the strongly correlated $\sigma_{x^2-y^2}$ band of mixed Ni $3d_{x^2-y^2}$ and O $2p$ parentage, inducing metallic conduction at higher temperatures (above 600 K).[43,56,77,78] Experimental results confirm room temperature *p*-type semiconductivity that is several orders of magnitude larger in the basal planes containing Ni–$O_{eq}$ bonds (and $3d_{x^2-y^2}$ orbitals) than along the *c*-axis.[46,48,79]

Aguadero *et al.* have also indirectly confirmed the origin of the anisotropy in the conductivity by showing the correlation between Ni–O bond lengths and electrical resistivity.[65] The electronic conductivity can be further enhanced by aliovalent A-site doping (*e.g.*, $Sr^{2+}$ on $La^{3+}$ sites) which increases the concentration of holes,[58] as detailed later in this thesis.

Finally, $La_2NiO_{4+\delta}$ exhibits a rich variety of magnetic properties as a function of $\delta$ and temperature, which have a significant influence on the nuclear magnetic resonance (NMR) results presented later. Stoichiometric $La_2NiO_4$ is a 3D antiferromagnet with a Néel temperature $T_N \approx 330$ K;[79–82] small amounts of oxygen excess ($\delta \leq 0.1$) lower the Néel temperature,[83] but above this value of $\delta$ a transition to incommensurate magnetic order occurs with a concomitant *increase* in the Néel temperature.[84–87] For the purposes of this thesis, only compositions with $\delta \approx 0.2$ are considered, which exhibit Curie-Weiss paramagnetic behavior above $T_N \approx 200$ K with a Curie coefficient of $\mu_{\text{eff}} \approx 2.56\ \mu_B$ and a Weiss temperature of $\Theta \approx -400$ K.[78,88] Thus, the $La_2NiO_{4+\delta}$ samples studied in this work are paramagnetic at room temperature and above, and the paramagnetic NMR methodology of Kim *et al.*[89] (introduced in Section 2.2.3.1) is applicable.

In summary, outstanding questions in studying the mixed ionic–electronic conductivity of $La_2NiO_{4+\delta}$ and related phases include (1) the nature of the oxide-ion conduction mechanism(s) and how this is connected to local structural distortions (*i.e.*, $NiO_6$ octahedral tilting) as well as the orthorhombic-to-tetragonal phase transition at ~150 °C; and (2) how the fundamental defect chemistry can be controlled to optimize the functional performance of these materials, especially in systems with both A- and B-site doping.

## 1.3 Doped $\delta$-$Bi_2O_3$ and related SOFC electrolyte materials

In the 1970s, Takahashi *et al.* discovered that the high-temperature cubic fluorite-type polymorph of bismuth oxide, $\delta$-$Bi_2O_3$, possesses the highest oxide-ion conductivity of any known material, ~1 S $cm^{-1}$ at 750 °C.[90–92] The impressive conductivity of $\delta$-$Bi_2O_3$ derives from (1) its very high concentration (25%) of disordered intrinsic vacancies, *i.e.*, with respect to the fluorite $AO_2$ structure, the composition may be written as $BiO_{1.5}\square_{0.5}$ (where $\square$ denotes an oxygen vacancy); (2) the polarizability of the cation network due to the $Bi^{3+}$ $6s^2$

stereoactive lone pair electrons; and (3) the ability of the Bi cations to accommodate highly asymmetric local environments.[93,94] However, the practical application of pure $\delta$-$Bi_2O_3$ as a SOFC electrolyte material is extremely limited due to its narrow stability range (between 730 °C and 825 °C, its melting point)[95,96] as well as its chemical reactivity towards standard SOFC cathode materials[97,98] and its instability under reducing conditions.[99,100]

The high-temperature cubic phase may be stabilized at lower temperatures through doping, most commonly isovalent doping of rare earth $Ln^{3+}$ (or $Y^{3+}$) cations at the $Bi^{3+}$ site.[101] Verkerk *et al.* have hypothesized that doping with smaller rare earth cations leads to a stabilizing contraction of the cubic structure that persists over a wider temperature range,[94,102] whereas doping with cations of a similar size to $Bi^{3+}$ (such as $Gd^{3+}$) results instead in the formation of a low-temperature rhombohedral phase with poorer oxide-ion conductivity.[103,104] However, many of the nominally stabilized cubic $\delta$-$Bi_2O_3$ phases undergo an unfavorable conductivity decay of up to 80% over a period of several days at intermediate temperatures (~500 °C), attributed to slow ordering of the anion sublattice into a long-range superstructure.[104] Moreover, this effect is more pronounced for dopants with smaller radii that are less polarizable (*e.g.*, $Yb^{3+}$, $Tm^{3+}$).[105] The competition between stabilization of the cubic phase and suppression of conductivity decay, therefore, makes the choice of an optimal isovalent dopant difficult. Nonetheless, many of the most promising $Bi_2O_3$-derived electrolytes employ one or more isovalent dopants. Promising examples include the doubly-doped $Bi_{12.5}La_{1.5}ReO_{24.5}$ and $Bi_{0.85}Pr_{0.105}V_{0.045}O_{1.545}$ phases, which at low- and intermediate-temperatures are among the best $\delta$-$Bi_2O_3$-type oxide-ion conductors discovered thus far, with oxide-ion conductivity values of $10^{-3}$–$10^{-2}$ S $cm^{-1}$ at 300–400 °C.[106,107] The former phase in particular is among the best *isotropic* oxide-ion conductors at low temperature. However, issues with stability under thermal cycling (analogous to the conductivity decay previously described) have not yet been addressed.[108]

Stabilization of $\delta$-$Bi_2O_3$ through aliovalent doping is an alternative strategy, with pentavalent dopants (*i.e.*, P, V, Nb, and Ta) of particular interest due to the promising oxide-ion conductivity in the related Aurivillius layered-perovskite BIMEVOX phases ($Bi_4V_{2(1-x)}M_{2x}O_{11-3x}$ with $M$ = Cu, Ni).[109,110] The formation of stabilized defect fluorite-type structures related to $\delta$-$Bi_2O_3$ is only observed for specific doping ranges in the $Bi_{1-x}M_xO_{1.5+x}$

(*M* = P, V, Nb, Ta) phase space and depends on the identity of the dopant ion; many such phases are not nominally cubic but nonetheless exhibit fluorite-type superstructures. Takahashi *et al*. first synthesized cubic structures of 15–25 mol% $Nb_2O_5$-doped and 18–25% $Ta_2O_5$-doped $Bi_2O_3$ at room temperature, but could not obtain reliably single-phase fluorite-type V-doped materials.[93,100,111] In that work, the vacancy concentration and thus the oxide-ion conductivity decreased with increased Nb or Ta concentration within the $\delta$-$Bi_2O_3$ stabilization regime, suggesting that doping should be kept as small as possible to optimize the oxide-ion conductivity.

Zhou first reported single-phase 3×3×3 fluorite-type superstructures of $Bi_{1-x}V_xO_{1.5+x}$ which all possess similar structures generally referred to as type I (for $0.074 < x \leq 0.111$) and type II (for $0.111 < x \leq 0.222$).[112,113] Darriet *et al.* and Mauvy *et al.* described the structural principle underlying these phases as a stacking of $[Bi_{18}O_{27}]$ and $[Bi_{14}V_4O_{31}]$ layers (Figure 1.6). For example, the lowest-doped $x = 0.074$ phase corresponds to a sequence of two $[Bi_{18}O_{27}]$ layers followed by one $[Bi_{14}V_4O_{31}]$ layer; the intermediate $x = 0.148$ phase to one $[Bi_{18}O_{27}]$ layer followed by two $[Bi_{14}V_4O_{31}]$ layers; and the most highly-doped $x = 0.222$ phase to a structure comprising all $[Bi_{14}V_4O_{31}]$ layers.[114,115] (Compositions below $x = 0.074$ and above $x = 0.222$ are apparently incompatible with the 3×3×3 cubic superstructure, and instead form V-doped $\gamma$-$Bi_2O_3$-like sillenite phases and layered Aurivillius phases, respectively.) Phases of type I and type II therefore adopt very similar superstructures with fully isolated $VO_4$ tetrahedra, but exhibit subtle differences in long-range cation ordering; the lower-doped type I structure has a small rhombohedral distortion of the fluorite-type superstructure,[116] whereas the type II phases adopt more distorted monoclinic or triclinic crystal structures.[117,118] The composition $x \approx 0.111$ (equivalently $Bi_{16}V_2O_{29}$) that divides the two types of structures appears to correspond to a critical concentration of oxygen vacancies such that, above this doping level, V sites begin to share oxygen vacancies and/or the V cations are slightly overbonded,[119,120] which accounts for the shorter distances between adjacent $VO_4$ units and the lowering of the unit cell symmetry.[118]

Although studied less extensively, the P-doped materials appear to adopt similar structures. Wignacourt *et al.* found several $Bi_{1-x}P_xO_{1.5+x}$ phases structurally analogous to the V-doped

materials,[121,122] and Watanabe reported that $Bi_{46}V_8O_{89}$ and $Bi_{46}P_8O_{89}$ ($x$ = 0.148) were isostructural.[123]

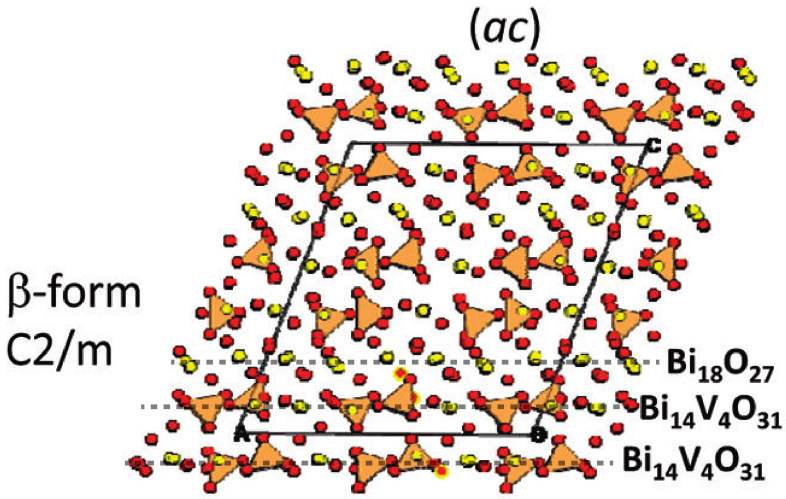


Figure 1.6: Depiction of the monoclinic ($C2/m$) $\beta$-form of $Bi_{46}V_8O_{89}$ ($Bi_{1-x}V_xO_{1.5+x}$ with $x$ = 0.148), showing the stacking of one [$Bi_{18}O_{27}$] and two [$Bi_{14}V_4O_{31}$] layers along the $c$ axis. Layers are indicated by dashed lines. The $VO_4$ tetrahedral units, which are isolated, are depicted in orange, Bi atoms are depicted in yellow and oxygen atoms are depicted in red. Figure modified from Kuang et al.[118]

Watanabe and Kitami also measured the oxide-ion conductivity of the $Bi_{46}V_{8-y}P_yO_{89}$ ($0 \leq y \leq 8$; $x$ = 0.148) solid-solution series. Conductivity values ranged from ~$10^{-3}$ S cm$^{-1}$ for $Bi_{46}P_8O_{89}$ to ~$3 \cdot 10^{-3}$ S cm$^{-1}$ for $Bi_{46}V_8O_{89}$ at 500 °C,[123,124] comparable to or slightly better than that of YSZ at the same temperature.[125] Their work also demonstrated the general principle that the V-doped materials were significantly better conductors than their P-doped analogues. Similarly, a dramatic decrease in conductivity was noted by Mauvy *et al.* for the highly P-doped $Bi_{14}P_4O_{31}$ phase ($x$ = 0.222), with $\sigma = 4 \cdot 10^{-7}$ S cm$^{-1}$ at 650 °C, whereas similar V-containing materials retained acceptable conductivities.[115]

Recently, much of the earlier work on oxide-ion conductivity of the fluorite-type bismuth vanadates was revisited by Kuang *et al.*, who performed two comprehensive studies on the type II $x$ = 0.148 phase[118] as well as the similar type I $x$ = 0.087 and $x$ = 0.095 phases.[126] Importantly, they showed that the $x$ = 0.148 material has two distinct polymorphs, with $\alpha$-$Bi_{46}V_8O_{89}$ (monoclinic $P21/c$, or possibly triclinic $P\bar{1}$) and $\beta$-$Bi_{46}V_8O_{89}$ (monoclinic $C2/m$; see Figure 1.6) adopting different cation orderings within the [$Bi_{14}V_4O_{31}$] layers. Moreover,

they clarified that the prior conductivity data of Watanabe were consistent with a sample of the $\beta$-form, whereas the original single-crystal refinement study of Darriet *et al* had determined the structure of $\alpha$-$Bi_{46}V_8O_{89}$. In support of this, Kuang *et al.* measured oxide-ion conductivity values of $\beta$-$Bi_{46}V_8O_{89}$ in good agreement with those of Watanabe, and with a similar temperature-dependent activation energy between 0.73 eV and 0.98 eV.

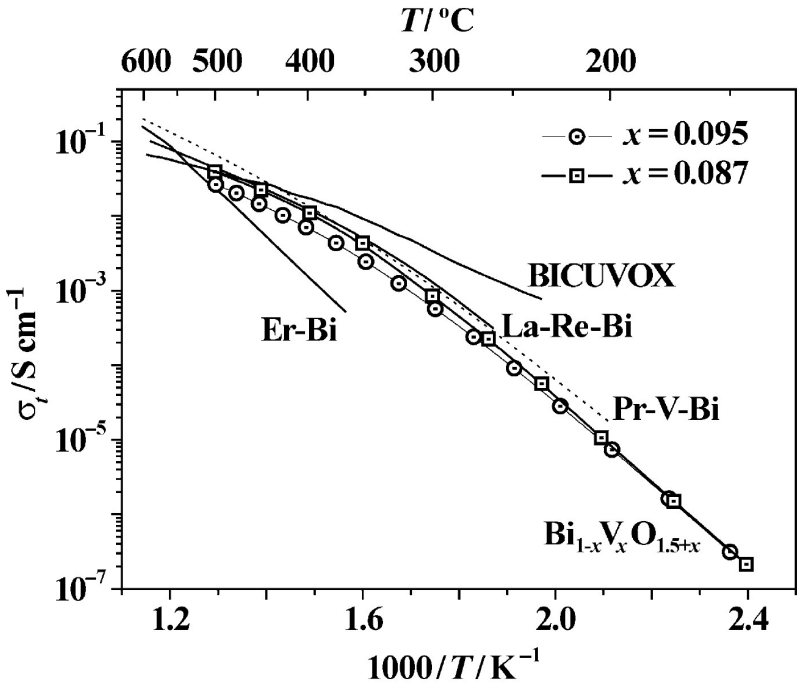


Figure 1.7: Oxide-ion conductivity data from 100–500 °C for two of the so-called type I fluorite-type bismuth vanadates, *i.e.*, $Bi_{0.905}V_{0.095}O_{1.595}$ (open circles) and $Bi_{0.913}V_{0.087}O_{1.587}$ (open squares), with data for other promising oxide-ion conductors based on $Bi_2O_3$ or related materials, that is, $Bi_2V_{0.9}Cu_{0.1}O_{5.35}$ (BICUVOX), $Bi_{0.85}Pr_{0.105}V_{0.045}O_{1.545}$ ("Pr-V-Bi"), $Bi_{12.5}La_{1.5}ReO_{24.5}$ ("La-Re-Bi"), and $Bi_{0.8}Er_{0.2}O_{1.5}$ ("Er-Bi"). Figure reproduced from Kuang *et al.*[126] The data for the type II $Bi_{0.852}V_{0.148}O_{1.648}$ phase (*i.e.*, $\beta$-$Bi_{46}V_8O_{89}$) studied separately by Kuang *et al.* lie roughly an order of magnitude below those of $Bi_{0.905}V_{0.095}O_{1.595}$ and $Bi_{0.913}V_{0.087}O_{1.587}$.

For the type I materials ($x$ = 0.087 and $x$ = 0.095, collectively referred to as "$Bi_{18}V_2O_{32}$" in their work), Kuang *et al.* reported exceptional conductivities of $2.6 \cdot 10^{-2}$ S cm$^{-1}$ and $3.9 \cdot 10^{-2}$ S cm$^{-1}$ at 500 °C, roughly an order of magnitude higher than that of $\beta$-$Bi_{46}V_8O_{89}$, and comparable to the best-performing doubly-substituted $\delta$-$Bi_2O_3$ materials such as $Bi_{0.85}Pr_{0.105}V_{0.045}O_{1.545}$ and $Bi_{12.5}La_{1.5}ReO_{24.5}$ (Figure 1.7).[126] Moreover, their study highlighted the tendency of some of these materials to undergo sluggish phase segregation at

lower temperatures, *e.g.*, the partial decomposition of $x = 0.087$ into V-doped $\gamma$-$Bi_2O_3$ and $Bi_{16}V_2O_{29}$ (*i.e.*, $x = 0.111$) occurring between 450 °C and 825 °C over a period of several days. This process could be reversed, however, by briefly refiring the samples at temperatures above 825 °C. Consequently, the results of Takahashi *et al.* showing a much poorer oxide-ion conductivity for materials of similar composition ($Bi_{0.91}V_{0.09}O_{1.595}$) were attributed to high-temperature decomposition occurring during measurements performed at temperatures within this instability regime,[111] explaining why the excellent performance of these materials had not been previously discovered. The "$Bi_{18}V_2O_{32}$" samples prepared by Kuang *et al.* also showed improved stability with repeated thermal cycling between room temperature and 500 °C, as compared to rare earth-doped $Bi_2O_3$ phases.

Finally, Kuang *et al.* performed *ab initio* molecular dynamics (MD) simulations in an effort to understand details of the oxide-ionic conductivity mechanisms of both the type I and type II bismuth vanadates.[118,126] In all simulations, including those at the lowest temperature of 473 K, the $VO_4$ tetrahedral units underwent rapid, flexible rotation with formation of transient over-coordinated $VO_5$ species, such that these groups were more accurately described as "$VO_n$" polyhedra. However, at low temperature the oxide-ion motion remained localized to the immediate environment of the $VO_n$ units, with no evidence of long-range conductivity. At a higher temperature (873 K), MD simulations on a supercell corresponding to the type I structure showed evidence of increased oxide-ion exchange between the distinct Bi–O and $VO_n$ sublattices, as well as the onset of diffusion through the $Bi_2O_3$-like slabs. For the higher-doped $x = 0.148$ phase, simulations also demonstrated long-range oxide-ion exchange occurring between $VO_n$ units, but only at a much higher temperature of 1373 K, a result consistent with the lower experimental conductivity of this material; the diffusion mechanism comprised a series of jumps through the Bi–O sublattice, involving octahedral $\square Bi_6$ sites (where $\square$ denotes an oxygen vacancy) as well as $OBi_4$ and $OBi_3$ groups, coupled to $VO_n$ polyhedral rotations (Figure 1.8). Kuang *et al.* interpreted these findings in support of their hypotheses on the competing effects of aliovalent doping in $Bi_2O_3$-derived oxide-ion conductors. That is, while doping with an element that can undergo variable coordination, such as V, leads to cooperative long-range oxide-ion conduction as well as an increase in the number of mobile vacancies on the Bi–O sublattice, doping in general interrupts the network of conduction pathways through the fluorite-type structure and ultimately decreases the

overall vacancy concentration. These conclusions provide a tentative mechanistic explanation for the improved conductivity at lower dopant levels as well as the enhanced performance of the V-doped materials over the P-doped analogues. Results from the MD simulations can also be contrasted to the earlier work of Darriet *et al.*, in which the differences in conductivity of the $Bi_{46}V_8O_{89}$ and $Bi_{46}P_8O_{89}$ phases were instead ascribed to partial occupancy of oxygen sites in the refined structures,[114] as well as to prior studies suggesting that conduction only involves the Bi–O sublattice with minimal contribution from motion within $MO_4$ ($M$ = P, V) tetrahedral units.[127]

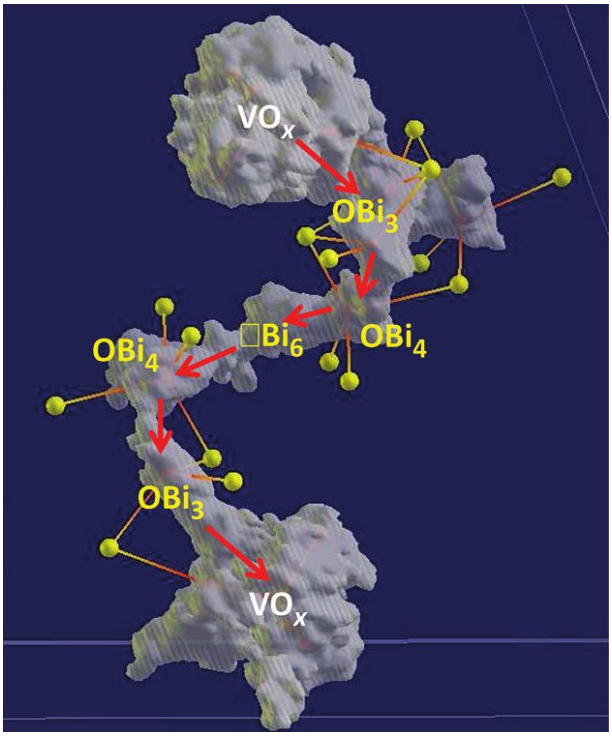


Figure 1.8: Depiction of the hypothesized long-range oxide-ion conductivity mechanism in $\beta$-$Bi_{46}V_8O_{89}$ (*i.e.*, $Bi_{1-x}V_xO_{1.5+x}$ with $x$ = 0.148), obtained from analysis of *ab initio* MD simulations at 1373 K. The grey clouds indicate the extent of motion of oxide ions throughout the 20 ps trajectory, and red arrows show the local directionality of the diffusion process. Yellow spheres represent Bi atoms. Figure reproduced from Kuang *et al.*[118]

In this thesis, three distinct materials in the system of aliovalently-doped long-range ordered fluorite-type $Bi_{1-x}M_xO_{1.5+x}$ ($M$ = P, V) phases have been studied, namely, $Bi_{0.913}V_{0.087}O_{1.587}$, $Bi_{0.852}V_{0.148}O_{1.648}$, and $Bi_{0.852}P_{0.148}O_{1.648}$. These respectively correspond to two of the phases reported by Kuang *et al.* ("$Bi_{18}V_2O_{32}$" and $\beta$-$Bi_{46}V_8O_{89}$)[118,126] as well as the $Bi_{46}P_8O_{89}$ phase

of Watanabe (and Darriet *et al.*), which is isostructural to $\beta$-$Bi_{46}V_8O_{89}$.[114,123] To recapitulate, the previously measured oxide-ion conductivity is highest (nearly best-in-class) for the type I composition with low V content ($x$ = 0.087), intermediate for the type II phase with low V content ($x$ = 0.148), and poorest for the type II P-substituted material. There remain a number of key questions about the fundamental properties of these systems, some of which are answered in this thesis. These include an understanding of the relative contributions to the oxide-ion conductivity from dynamics within (and between) the Bi–O and "$VO_n$" sublattices; experimental confirmation of speculative mechanistic details at the local atomic level; and unraveling the origin of the divergent performance of the V- and P-doped materials, as well as differences dependent upon the dopant content. Looking further ahead, one might speculate as to how these stabilizing $VO_4$/$PO_4$ tetrahedral units, structural motifs lacking in the rare earth-doped materials, lead to improvements in thermal cycling performance and minimization of the low-temperature conductivity decay.

## 1.4 Outlook

The utility of both classes of materials discussed in this chapter is due to their excellent oxide-ion conductivity, which in turn depends on the structural and motional properties of both oxygen sites and vacancies. Therefore, the primary aim of this thesis is the development of combined experimental and theoretical methodologies to investigate the local structure and dynamics of oxygen environments within these phases. The next chapter introduces the main techniques: paramagnetic and/or variable-temperature solid-state NMR spectroscopy of quadrupolar nuclei (*e.g.* $^{17}O$), with spectral assignment aided by first principles calculations; this is followed by an outline of the remainder of the work.

# Chapter 2 Methodology

## 2.1 Solid-state nuclear magnetic resonance (NMR)

Unlike diffraction-based methods, which are powerful tools to study long-range order in solid materials, solid-state nuclear magnetic resonance (NMR) provides more local, element-specific structural information. Solid-state NMR is well-suited to the study of disordered or amorphous systems, or materials where properties are significantly influenced by dopants or defects, and has been used to probe the local atomic and electronic structure of many energy storage and conversion materials including those used in secondary (rechargeable) batteries, supercapacitors, fuel cells, and chemical looping devices.[128–132] Moreover, by following spectral changes as a function of temperature one can obtain detailed, mechanistic insight into dynamics on the atomic level, which can prove highly relevant to understanding the underlying functionality of ion conductors used as electrodes and electrolytes in fuel cells.[130,133,134] A short introduction to the principles of solid-state NMR is given here, with a focus on the spin interactions and specific pulse programs relevant to the work undertaken in this thesis; many other reference works with greater detail are available elsewhere.[135–137]

### 2.1.1 Basic NMR experiments

#### 2.1.1.1 Background and "one-pulse" experiments

Many atomic nuclei possess an intrinsic spin, which is defined by the spin quantum number $I = \frac{n}{2}$ for non-negative integer values of $n$. (In fact, except for cerium and argon, all naturally occurring, non-radioactive elements have at least one stable nuclide with a non-zero value of $I$ and are, in principle, NMR-active.) Nuclear spin, which is entirely analogous to electron spin, is a quantized form of angular momentum that gives rise to a non-zero magnetic dipole moment for $I \geq ½$. There exist $2I + 1$ spin states of a spin-$I$ nucleus, which

are each described by the magnetic quantum number $m_I$ ($= -I, -I + 1, \ldots, +I$). In the presence of an applied magnetic field $B_0$ (conventionally applied along the $z$-axis of a principal axis system in the laboratory frame), the degeneracy of these $2I + 1$ energy levels is lifted due to the nuclear Zeeman interaction between the magnetic field and the nuclear magnetic dipole moment, which gives rise to a splitting $\Delta E$ between consecutive spin states given by:

$$\Delta E = \hbar|\omega_0| = -\hbar\gamma_I B_0, \tag{2.1}$$

where $\omega_0$ is the so-called Larmor frequency given by $\omega_0 = -\gamma_I B_0$ and $\gamma_I$ is the nucleus-specific gyromagnetic ratio. In NMR spectroscopy, only the spin transitions between consecutive Zeeman spin states, that is, subject to the single-quantum selection rule $\Delta m_I = \pm 1$, are directly experimentally observed at a frequency of $\omega_0$. For the magnetic fields used in solid-state NMR which typically range from 5 to 25 T, the transition frequencies correspond to the radio frequency region of the electromagnetic spectrum.

In practice, the application of a radio frequency (rf) pulse at the Larmor frequency, which is *resonant* with the spin system under the externally applied magnetic field $B_0$, induces mixing of the Zeeman states. The subsequent evolution of the excited spin system as it relaxes back to equilibrium is then directly observed as a decaying rf response from the sample, which is called the free induction decay (FID). The effect of any grouping of rf pulses (*i.e.*, a pulse sequence) on the evolution of the spin system, including the components of the spin system that are experimentally detected following the pulse sequence, can be determined analytically using the product operator formalism. This mathematical formalism considers the effect of each pulse as a Hamiltonian that is expanded as a set of spin operators, which sequentially act on the spin system during the pulse sequence. However, for the purposes of this thesis, it is sufficient to consider only the vector model of NMR, which is a more convenient pictorial formalism to visualize the operation of pulsed NMR experiments.

According to the vector model, the sample comprises a large number of individual nuclei that thermally occupy the Zeeman spin states according to a Boltzmann distribution. The slight excess of spins aligned with (as opposed to against) the external magnetic field gives rise to a small net magnetization $M_0$ along $B_0$, which by convention lies along the laboratory $z$-axis

(Figure 2.1a). The main principle of the pulsed NMR experiment is that the application of a resonant rf pulse generates a rotating magnetic field of strength $B_1$ and frequency $\omega_1$, that perturbs the magnetization vector away from its equilibrium position along $z$. Although the rf pulse is an oscillating electromagnetic field that can be decomposed into counter-rotating magnetic fields with frequencies $+\omega_1$ and $-\omega_1$, only the component rotating in the same direction as the Larmor precession induces any change in the spin system, and so the other component can be safely ignored.

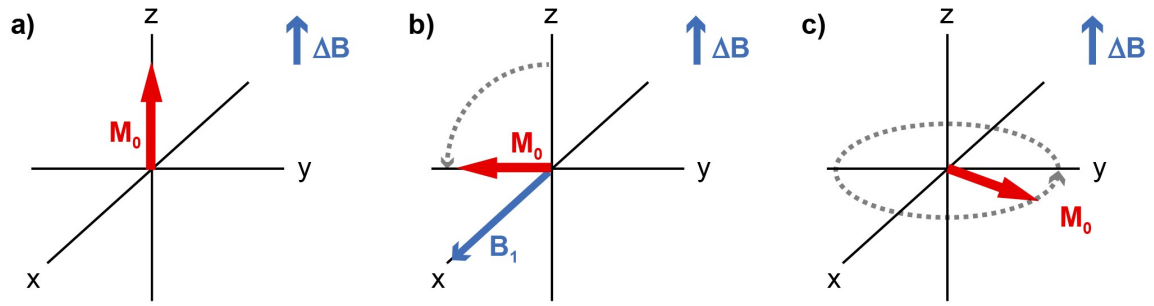


Figure 2.1: Depiction of the effect of a simple 90° pulse, viewed from the rotating frame, according to the vector model formalism. (a) Magnetization aligned along the $z$-axis during equilibrium, (b) application of a 90° pulse along the $x$-axis, and (c) free precession of the magnetization vector within the $xy$-plane.

If we then view the vector model from a rotating frame of reference at the rf frequency of $\omega_1$, then the $B_1$ field appears static, and is here taken to lie along the $x$-axis (Figure 2.1b). In this rotating frame, the applied magnetic field $B_0$ appears as a reduced field $\Delta B = (\omega_0 + \omega_1) / \gamma$. The Larmor frequency is here taken to be negative, and the positive transmitter frequency $\omega_1$ of the applied rf pulse is typically comparable to the magnitude of the Larmor frequency, so that the reduced field $\Delta B$ is small.[137] Under these conditions, the applied field $B_1$ is much larger than the reduced field $\Delta B$, and the magnetization $M_0$ will rotate ("nutate") away from $z$ in the plane perpendicular to $\Delta B$. If the pulse length is of the correct duration or "flip angle", in this case a so-called 90° (or $\pi/2$) pulse, then at the end of the rf pulse the magnetization will lie along the $-y$ direction (Figure 2.1b). Following the pulse, the magnetization precesses freely in the $xy$-plane under the influence of the reduced field $\Delta B$ (Figure 2.1c). This precession is recorded by the rf receiver coil as the FID and can be Fourier transformed to give the NMR spectrum. After some time, the magnetization returns to thermal equilibrium along the $z$-axis by spin-lattice relaxation, which is described by the time constant $T_1$.

Additionally, the relaxation of the transverse components of the magnetization (spin-spin relaxation) occurs within the *xy*-plane, a process of decoherence described by the time constant $T_2$. In almost all situations $T_1$ is longer than $T_2$ because the local transient magnetic fields that contribute to spin-lattice ($T_1$) relaxation also induce spin-spin ($T_2$) relaxation, and there are additional factors that contribute to $T_2$ relaxation yet affect $T_1$ to a lesser degree.

#### 2.1.1.2 Spin echo experiments

The experiment presented in Figure 2.1 is the simplest possible pulse sequence, which is commonly referred to as a "one-pulse" or "pulse–acquire" experiment. In practice, a dead time must be left between application of the 90° pulse and the start of the signal acquisition to switch between pulsing and acquisition modes, as well as to allow for the "ringdown" of the NMR probe hardware after the rf pulse. The hardware limitation that necessitates a short delay prior to acquisition means that during the dead time, any signal arising from the sample cannot be recorded, leading to reduced signal intensity. Moreover, residual ringdown beyond the dead time is often recorded as part of the FID, and commonly yields characteristic baseline distortions in the Fourier transformed spectrum. These issues can be avoided by use of a spin echo (also called Hahn echo) experiment. Here a 90° ($\pi/2$) pulse is applied followed by a "refocusing" 180° ($\pi$) pulse (which typically has the same rf power, but double the length, of the 90° pulse) after a delay of duration $\tau$. After another $\tau$ delay following the 180° pulse, a spin echo forms and the FID is recorded.

One can rationalize the formation of the spin echo by considering the dephasing that occurs during free precession of the magnetization components during the first $\tau$ delay. This dephasing arises from precession of components at slightly different frequencies due to different local chemical environments and/or local inhomogeneities in the applied magnetic field. Upon application of the 180° ($\pi$) pulse, the spin components are flipped in the *xy*-plane and the phase acquired by precession during the $\tau$ delay is inverted. Free precession then continues at the characteristic frequency of each spin component, which after another time $\tau$ returns the relative phases of all components back to zero, *i.e.*, refocuses the spins. At this point, the state of the spin system is exactly equivalent to that following a single 90° pulse, aside from any inherent $T_2$ relaxation that has occurred during the $2\tau$ period, and the FID can

be recorded. In the spin echo experiment, because the application of the final pulse is temporally separated from the start of acquisition, the dead time can be incorporated into the $\tau$ delay, and any residual ringdown should have finished by the end of the $\tau$ delay. Moreover, background signals from the probe are typically suppressed in a spin echo experiment because only spins within the rf coil are effectively refocused. The improved background makes the spin echo experiment an indispensable tool in the acquisition of extremely broadened spectra, such as in the paramagnetic systems studied in this work. However, the application of the longer 180° pulse decreases the range of frequencies effectively probed by this experiment. Shorter rf pulses are "harder", *i.e.*, they excite spins that precess at frequencies much further from the transmitter frequency, whereas longer pulses are more selective for a narrower range of frequencies. The excitation bandwidth of the spin echo experiment is therefore smaller than that of a standard one-pulse experiment by up to a factor of ½. For this reason, more complicated techniques such as spin-echo mapping (also called variable offset cumulative spectroscopy, VOCS) must be used to acquire useful wideline NMR spectra (see Section 2.1.2).

#### 2.1.1.3 Magic-angle spinning (MAS)

In addition to the external applied magnetic field $B_0$, which results in the Zeeman splitting of nuclear spin states by the Larmor frequency, numerous internal magnetic fields are also present at the atomic level. These additional spin interactions lead to subtle shifts in the energy of the spin states that are the source of the chemical and local structural sensitivity of NMR. The most familiar spin interactions in solution-state NMR spectroscopy of diamagnetic systems are (1) the chemical shielding (or deshielding), which arises from a reduction (or enhancement) in the apparent magnetic field due to the response of electrons to the $B_0$ field, and (2) the scalar ($J$) and dipolar coupling, which are through-bond and through-space interactions between proximate nuclear spins, respectively. Additional interactions can occur between unpaired electron spins and nuclear spins, such as the Knight shift in metals which results from the interaction with conduction electrons, and the hyperfine (*e.g.*, Fermi contact) interaction with localized unpaired electron spins in paramagnetic systems. Finally, nuclei with $I \geq 1$ possess an electric quadrupole moment and are subject to a quadrupole

coupling interaction with electric field gradients at the nuclear position that are due to local charge asymmetry (see Section 2.1.4).

The energy of most of the internal spin interactions possesses an inherent angular dependence, *i.e.*, the relative orientation between the axes in the local, molecular frame and the external field $B_0$ has an effect on the energy of the observed spin transition. These anisotropic spin interactions are typically represented mathematically through second-rank tensors. In the solution state, rapid molecular tumbling faster than the NMR timescale averages out the anisotropy of many of the spin interactions, resulting in the observation of sharp resonances at the isotropic value of the shift tensor. In the solid state, however, the molecular orientations typically remain fixed with respect to the applied magnetic field on the NMR timescale, and the anisotropic interactions can be directly observed in the resulting spectra. For a powdered crystalline sample with randomly oriented crystallites, the experimental NMR spectrum comprises a superposition of the transitions arising in each crystallite, which is referred to as a powder pattern (Figure 2.2a). The lineshape of the powder pattern can in principle be fit to a model to obtain the principal components of the relevant spin interaction tensor(s). However, these spectral powder patterns can also be subject to severe anisotropic broadening that hinders acquisition and obscures useful chemical information.

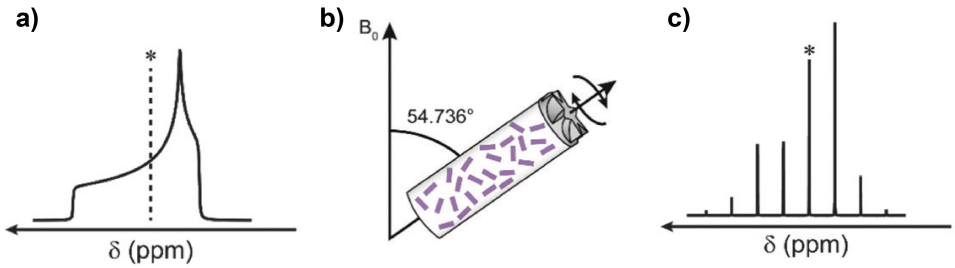


Figure 2.2: Schematic representation of a) a static powder pattern of a polycrystalline sample subject to an anisotropic nuclear spin interaction, with b) the magic-angle spinning experiment where the sample is packed into a spinning rotor and spun at an angle of 54.736° with respect to the external magnetic field, and c) the resulting NMR spectrum of the same system as depicted in a) but under MAS, where the experimental spinning frequency is comparable to the size of the interaction. Spinning sidebands are evenly spaced at the spinning speed, and the isotropic shift is denoted by an asterisk. Figure adapted from Ashbrook and McKay.[138]

Magic-angle spinning (MAS) is commonly employed to remove the effects of anisotropy by rapidly spinning the sample container ("rotor") around an angle of 54.736° (the magic angle) with respect to the applied magnetic field (Figure 2.2b). To first order, the energy of many of the nuclear spin interactions is proportional to $(3\cos^2\theta - 1)$, where $\theta$ is one of the Euler angles representing the orientation of the interaction tensor with respect to the applied magnetic field. By spinning at an angle of 54.736°, the anisotropic orientation dependence averages to zero and a sharp resonance is observed at the isotropic shift with an appearance similar to the equivalent solution-state NMR spectrum (Figure 2.2c). The magic angle is the angle between the edge and body diagonal of a cube, so one can also imagine magic-angle spinning as the rapid limit of a rotation that interconverts the axes of an anisotropic tensor, recovering the average or isotropic value of that tensor. Typical MAS speeds used in solid-state NMR are on the order of 20 kHz, with the fastest commercial systems at the present time allowing speeds up to roughly 120 kHz. Completely averaging out the powder pattern necessitates spinning frequencies roughly three to four times that of the relevant anisotropic interaction.[135] Intermediate spinning speeds give rise to spectral artifacts called spinning sidebands that are spaced at multiples of the spinning speed with respect to the isotropic resonance or "centerband", and the envelope of the intensities of the spinning sidebands approximates the static powder pattern (Figure 2.2c).

#### 2.1.1.4 Saturation recovery experiments: measuring $T_1$

Nuclear spin interactions influence not only the energy of the spin transitions, resulting in the observed NMR shifts, but also contribute to relaxation mechanisms that give rise to variations in the spin-lattice ($T_1$) relaxation times. The $T_1$ values therefore provide another important spectroscopic handle to distinguish between different local environments. The dependence of the $T_1$ relaxation times on the sample temperature is also a sensitive probe of ion dynamics in solid-state materials and will be discussed later (see Section 2.1.5.2).

Transient variations in the local magnetic fields on the order of the Larmor frequency have an effect on the spin system similar to that of rf pulses, and can induce spin-lattice relaxation towards equilibrium. The large magnetic moments of any unpaired electrons in the system, in particular, mean that rapid fluctuations in the electron–nuclear hyperfine interaction are

particularly effective at promoting $T_1$ relaxation. In many of the paramagnetic materials studied in this thesis, the $T_1$ relaxation times for the resonances arising from sites in close proximity to paramagnetic centers are on the order of several milliseconds (ms) or less; this is approaching the minimum $T_1$ values that can be readily measured with currently available NMR hardware.

The measurement of the spin-lattice relaxation time is most conveniently performed with the saturation recovery method, using the pulse sequence depicted in Figure 2.3a, which is performed as a series of one-dimensional experiments. In the first step, any coherent magnetization in the equilibrium state (aligned along the $z$-axis) is destroyed through the application of a rapid saturation train of many (up to several hundred) 90° pulses separated by short delays on the order of ~1 ms. The magnetization is then allowed to recover towards equilibrium by spin-lattice relaxation during a delay period $\tau$. A one-pulse or spin echo sequence follows the delay period to read out the recovered magnetization. The experiment is repeated for, ideally, a logarithmically spaced set of delays $\tau$. To obtain the experimental $T_1$ value, the resulting integrated signal intensity $I(\tau)$ as depicted in Figure 2.3b is fit to the saturation recovery equation:

$$I(\tau) = I_0 \left[1 - \exp\left(-\frac{\tau}{T_1}\right)\right], \tag{2.2}$$

where the equilibrium magnetization $I_0$ is observed in the limit of an infinite delay.

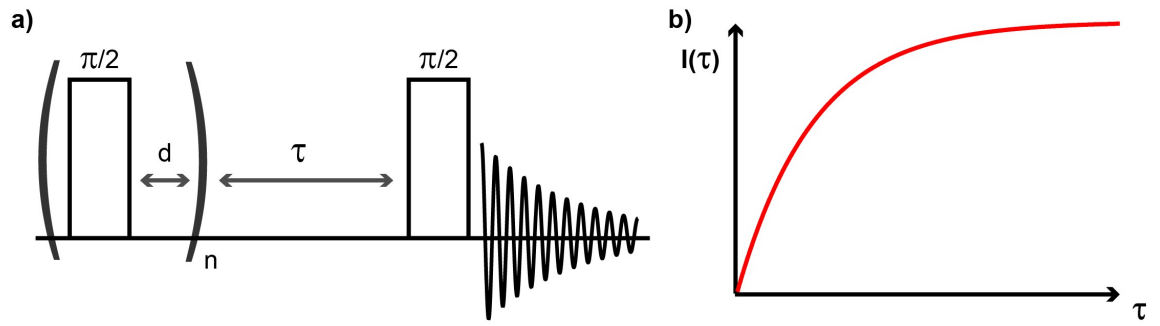


Figure 2.3: a) Schematic of a saturation recovery pulse sequence, with b) the magnetization recovery build-up curve as a function of the delay time $\tau$.

The primary advantage of the saturation recovery pulse sequence, relative to other methods such as inversion recovery for measuring $T_1$ constants, is that the spin system does not need to

fully recover to equilibrium before measuring the next point, as the equilibrium magnetization will again be destroyed anyway. Thus saturation recovery is generally a much faster approach, although this advantage is negated somewhat in the case of systems possessing short $T_1$ values. Finally, for paramagnetic systems, the short delays between the pulses in the saturation train need to be chosen carefully, so as to be significantly less than the $T_1$ value of the system; otherwise, rather than being destroyed by the saturation train, the magnetization will partially recover during this time.

### 2.1.2 Advanced pulse programs and experiments

#### 2.1.2.1 Spin-echo mapping (VOCS)

Solid-state NMR spectra broadened by very large nuclear spin interactions, in particular paramagnetic and quadrupolar coupling interactions, can span a frequency range that exceeds the spectral excitation of the pulse sequence, the inherent bandwidth of the NMR probe, or both. This problem is directly encountered in this thesis in the context of $^{17}$O NMR studies of paramagnetic functional oxides. Several specialized methods have been developed for the acquisition of NMR signals with spectral widths in excess of 250 kHz, which Schurko and others have referred to as ultra-wideline solid-state NMR spectroscopy.[139,140]

Among these ultra-wideline procedures, the simplest method is spin-echo mapping, also referred to as variable offset cumulative spectroscopy (VOCS), or "frequency-sweep" measurements.[141–143] In this approach, multiple sub-spectra are acquired with the rf transmitter centered at variable offsets, and the sub-spectra are summed together (optionally subject to an additional noise-filtering procedure) to obtain the entire broadband spectrum. The maximum rf offset spacing between consecutive sub-spectra is determined by the excitation bandwidth of the pulse sequence. Tong has shown that for spin echo experiments under static conditions, provided that the carrier frequency offset spacing is strictly less than or equal to the rf pulse strength $\omega_1$, the spin-echo mapped spectrum is equivalent to that obtained from a hypothetical broadband rf excitation profile.[144] Pell *et al.* later extended these findings to solid-state NMR experiments performed under MAS using a combined theoretical and experimental approach showing that applying VOCS to paramagnetic systems will

produce the true broadband spectrum with the correct sideband intensities.[145] In the recent work of Pecher *et al.*, the spin-echo mapping or VOCS method was performed by an automatic external tuning/matching (eATM) robot; spectra broadened by extremely large quadrupole interactions (on the order of several MHz) could be obtained without human intervention and were shown to be in reasonable agreement with those predicted from simulations.[146] In this thesis, the spin-echo mapping method is used to acquire solid-state MAS NMR spectra of the quadrupolar nucleus $^{17}O$ that are broadened by very large hyperfine interactions; in addition, hard pulses with large rf strengths have been used when possible to increase the spectral excitation bandwidth and minimize the total number of sub-spectra required.

#### 2.1.2.2 Magic-angle turning and phase-adjusted sideband separation (MATPASS) experiments

Another complication arising from extremely large nuclear spin interactions is the inability to spin sufficiently fast with MAS to obtain an isotropic spectrum entirely free of anisotropic broadening. In a realistic system containing multiple resonances, the application of slow or intermediate spinning rates relative to the size of the relevant anisotropic tensors can lead to severe overlap of spinning sidebands, greatly complicating spectral assignment and analysis. In this situation, the application of two-dimensional experimental schemes that are capable of suppressing or separating out spinning sidebands, as well as correlating the isotropic shifts with their anisotropic spinning sideband patterns, is clearly beneficial.

The magic-angle turning (MAT)[147] and phase-adjusted sideband separation (PASS)[148] techniques were historically developed independently and later shown to be manifestations of the same underlying mathematical principles.[149] In practice, both methods provide the pure, isotropic spectrum expected from an "infinite" MAS rate, which is correlated to the anisotropic components of the spectrum; that is, for each isotropic resonance, its full anisotropic sideband pattern can also be extracted. These schemes have in common the application of four or five 90° or 180° pulses in a rotor-synchronized arrangement (*i.e.*, the entire pulse sequence takes an integer number of rotor periods, where one rotor period is the reciprocal of the MAS rate), such that the sequence is split into three evolution segments. The

timing of the three evolution segments is constructed such that between consecutive segments the rotor position is spaced exactly 120° apart, which averages out the anisotropic parts of the spin interaction tensors. Multiple experiments (*i.e.*, increments in the $t_1$ dimension) are recorded, where the delays between the pulses are varied according to the PASS equations.[150,151] In PASS, these pulse timings are calculated to impart to each sideband in the spectrum a specific phase shift according to the order of that sideband. The result is that the intensity of the sidebands, *i.e.*, the anisotropic components of the spectrum, seems to "evolve" in the indirect $t_1$ dimension. A two-dimensional Fourier transform of the data then separates out the sidebands according to their order ($1^{st}$, $2^{nd}$, $3^{rd}$, etc.). For MAT, the pulse delays are instead chosen such that only the isotropic centerband(s) evolve in the indirect $t_1$ dimension. For both techniques, a shearing (affine) transformation of the 2D Fourier-transformed spectrum is required to display the purely anisotropic (for PASS) or isotropic (for MAT) components in the indirect $t_1$ dimension, and the isotropic (for PASS) or anisotropic (for MAT) components in the direct $t_2$ dimension.

Although the MAT and PASS methods have many commonalities, including alteration of the interpulse delays so as to satisfy the PASS equations, major differences in implementation frustrated recognition of their underlying equivalence for many years. For example, the delays in PASS must be varied in a complicated non-linear fashion which is recalculated for the specific experimental MAS rate, which to a degree hinders its practical implementation. On the other hand, while the delays in MAT are varied in a straightforward linear fashion, the isotropic and anisotropic components are correlated to the indirect and direct dimensions, respectively, in a "backwards" manner which leads to signal artifacts due to truncated $t_1$ acquisition and also complicates data processing.[152] MAT and PASS are both constant time experiments, meaning that each individual one-dimensional slice takes the same time; Hung *et al.* recognized it was possible to combine the two methods into a so-called MATPASS experiment, co-opting advantages from both, whilst sacrificing the constant time condition.[153]

The MATPASS sequence depicted in Figure 2.4, also referred to as projection- or pj-MATPASS when short, broad bandwidth "projection" pulses (*e.g.*, 90° pulses) are used, retains the easily-implemented, linearly varying interpulse delays of five-pulse MAT and also the more robust isotropic–anisotropic correlation properties of PASS. The loss of the constant

time condition can lead to relaxation effects that result in unsuppressed spinning sidebands, but provided that the $T_2$ relaxation time is longer than the rotor period, these effects are expected to be minimal.[153] Previously this pulse sequence has been shown to yield "infinite speed" spectra of paramagnetic samples in the case of moderately quadrupolar nuclei, *e.g.*, $^{6}$Li and $^{7}$Li, with large (>1 MHz) hyperfine shift anisotropy.[153,154] In this thesis, the pj-MATPASS sequence is also used to separate overlapping sidebands arising from significant hyperfine shift anisotropy in the $^{17}$O solid-state NMR spectra of paramagnetic materials.

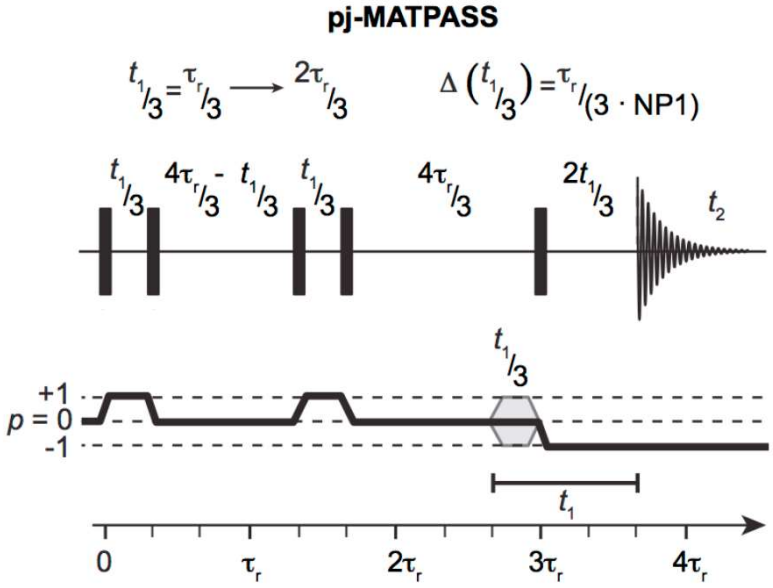


Figure 2.4: The pulse sequence for the pj-MATPASS experiment, which is derived from the conventional magic-angle turning (MAT) experiment. The black vertical bars indicate the short rf pulses, and NP1 is the number of $t_1$ increments, that is, the number of individual one-dimensional experiments performed (which is greater than or equal to the number of spinning sidebands). The experiment is synchronized with the MAS rate $\omega_r$, where the rotor period is $\tau_r = 1/\omega_r$. With each individual $t_1$ increment, the interpulse delays are changed according to the equations given at the top of the figure. The bottom part of the diagram indicates the evolution of the spin coherence throughout the pulse program; $p = 0$ indicates alignment of magnetization with the $z$-axis, whereas $p = \pm 1$ indicates magnetization within the $xy$-plane. Figure adapted from Hung *et al.*[153]

Sideband suppression pulse programs have also been extended to highly quadrupolar systems using the QPASS set of experiments which employ a sequence of nine (rather than five) pulses.[155,156] As described later in this thesis (Section 2.1.4), the second-order quadrupolar interaction has an orientational dependence with anisotropy of a higher rank that cannot be

completely averaged to zero by MAS. For similar reasons, standard pulse programs designed to remove anisotropic interactions that are present in systems of spin-½ nuclei are not guaranteed to work for systems with a large second-order quadrupolar interaction, and more advanced pulse sequences (typically with greater numbers of pulses) such as QPASS are required. For technical reasons related to the paramagnetic nature of the samples, the QPASS pulse sequence was not applied in the present work, even in the case of suppressing sidebands from resonances of quadrupolar nuclei. Because of the relatively short $T_2$ relaxation times of these systems arising from large hyperfine interactions, the longer, nine-pulse QPASS pulse program would lead to additional reductions in the observed signal intensity, which was judged to outweigh any benefit from separating components of the sideband intensity arising from second-order quadrupolar coupling effects.

### 2.1.3 Hyperfine interactions in paramagnetic NMR

Here a brief introduction is given to the electron–nuclear hyperfine interactions that are relevant to the present experimental work; many more extensive reviews are available on the subject.[157–159] The paramagnetic systems considered in this thesis contain transition metal centers with localized unpaired electrons. The unpaired electrons possess an inherent spin angular momentum, characterized by the quantum number *S*, which gives rise to a magnetic moment $\mu_e$ given by:

$$\mu_e = -\mu_B g_e S \tag{2.3}$$

where $\mu_B = e\hbar/2m_e$ is the Bohr magneton and $g_e$ = 2.0023 is the free-electron *g*-factor. Upon application of the external magnetic field $B_0$ along the *z*-axis, the electron Zeeman interaction leads to the splitting of the $2S + 1$ electron spin states (labeled by the magnetic quantum number $m_s$) with an energy splitting between consecutive spin states analogous to that given by Equation (2.1):

$$\Delta E = \mu_B g_e B_0 = -\hbar\gamma_s B_0, \tag{2.4}$$

where $\gamma_s = -\mu_B g_e/\hbar$ is the electron gyromagnetic ratio. The unpaired electrons may also possess an orbital angular momentum *L* which contributes to the magnetic moment and also

undergoes coupling with the spin angular momentum *S*. In the following discussion, we consider the "spin-only" approximation, without any contribution from the orbital angular momentum. One can show that the primary effect of the orbital angular momentum on paramagnetic solid-state NMR spectra is the appearance of an additional "pseudocontact" NMR shift which is typically more than an order of magnitude smaller than the main hyperfine interaction, that is, the Fermi contact contribution which is described below. Thus, the orbital angular momentum contribution can be safely neglected in these cases.[160]

The hyperfine interaction between electron and nuclear spins is described by the Hamiltonian

$$\widehat{\boldsymbol{H}}_{\boldsymbol{hyp}} = \hat{\boldsymbol{I}} \cdot \boldsymbol{A} \cdot \hat{\boldsymbol{S}}, \tag{2.5}$$

where $\hat{\boldsymbol{I}}$ and $\hat{\boldsymbol{S}}$ are the nuclear and electron spin vector operators, respectively, and $\boldsymbol{A}$ is the second-rank hyperfine coupling tensor. In an NMR experiment on a system containing both unpaired electron and nuclear spins, the observable spin transitions are given by the selection rules $\Delta m_I = \pm 1$ and $\Delta m_s = 0$, and thus, in principle, the hyperfine interaction should cause a given NMR resonance to split into $2S + 1$ resonances. However, in practice, the nuclei do not interact with all of the $m_s$ spin states individually; this is because the relaxation processes occurring between electron spin states are much faster than the nuclear spin dynamics as well as the timescales probed by NMR. Whereas nuclear $T_1$ relaxation times vary between $10^{-3}$ and $10^3$ s, typical electron $T_{1e}$ relaxation times are on the order of $10^{-8}$ to $10^{-12}$ s in most paramagnetic transition metal complexes.[161,162] From the point of view of the slowly relaxing nuclei, the interaction with the unpaired electrons occurs only through the average of all the electron spin states, which is represented in the Hamiltonian as the time-average of the *z*-component of the electron spin moment, $\langle S_z \rangle$. The expected hyperfine splitting of each resonance is also averaged, and as in the diamagnetic case, only one NMR transition is actually observed.

In this situation, Equation (2.5) can be expressed as the sum of two distinct interactions, namely the through-bond, isotropic Fermi contact interaction $\widehat{H}_{FC}$, and the through-space, anisotropic dipolar interaction $\widehat{\boldsymbol{H}}_{\boldsymbol{dip}}$. These hyperfine interactions are described in turn below.

### 2.1.3.1 Fermi contact interaction

The Fermi contact shift arises from the transfer of spin density from the unpaired valence electrons on the transition metal center to the NMR-active nucleus of interest. It is the unpaired electron spin density in the *s* orbitals at the nucleus of interest that contributes directly to the Fermi contact shift, as only the *s* orbital wavefunction possesses a non-zero probability at the nuclear position $\boldsymbol{R}_N$. Because the *s* orbital is spatially symmetric about the nucleus, the Fermi contact interaction is purely isotropic, with a Hamiltonian given by:

$$\widehat{H}_{FC} = -\hat{I}_z A_{\text{iso}} \langle S_z \rangle \tag{2.6}$$

where $\hat{I}_z$ is the *z*-component of the nuclear spin angular momentum, and $A_{\text{iso}}$ is the isotropic hyperfine coupling constant:

$$A_{\text{iso}} = \frac{2}{3} \hbar g_e \mu_B \mu_0 \gamma_I \rho^{\alpha-\beta}(\boldsymbol{R}_N). \tag{2.7}$$

Here $\rho^{\alpha-\beta}(\boldsymbol{R}_N)$ is the unpaired electron spin density at the nuclear position, and $\mu_0$ is the permeability of free space ($4\pi \cdot 10^{-7}$ N A$^{-2}$). Using the Hamiltonian in Equation (2.6) gives the experimental Fermi contact shift $\delta_{iso}^{\text{FC}}$ (in ppm):

$$\delta_{iso}^{\text{FC}} = \frac{10^6 A_{\text{iso}} \langle S_z \rangle}{2\hbar\omega_0 S} \tag{2.8}$$

where *S* is the formal spin of the transition metal center. The Fermi contact shifts encountered in the present work are large and positive as a consequence of spin delocalization arising from direct bonding between the transition metal center and the NMR-active nucleus ($^{17}$O); however, negative Fermi contact shifts are also possible in systems where the nucleus is further from the paramagnetic center and the spin polarization mechanism is dominant (*e.g.*, $^{6/7}$Li in paramagnetic Li-ion battery cathode materials).[128]

### 2.1.3.2 Electron–nuclear dipolar interaction

The Hamiltonian corresponding to the through-space electron–nuclear dipolar interaction is given by:

$$\widehat{\boldsymbol{H}}_{\boldsymbol{dip}} = -\hat{I}_z \boldsymbol{A}^{\mathbf{dip}} \langle S_z \rangle \tag{2.9}$$

where, if the unpaired electrons are assumed for convenience to be point dipoles, the Cartesian components of the electron–nuclear dipolar tensor $A_{ij}^{\mathrm{dip}}$ can be written as:

$$A_{ij}^{\mathrm{dip}} = \frac{\hbar g_e \mu_B \mu_0 \gamma_I}{4\pi r^3} \left[3 e_i e_j - \delta_{ij}\right] \tag{2.10}$$

with *r* defined as the electron–nuclear distance, $e_i$ and $e_j$ the Cartesian components of the unit vector between the electron spin and nuclear spin, and $\delta_{ij}$ the Kronecker delta. The electron–nuclear dipolar tensor is traceless and does not contribute to the isotropic shift, but does give rise to anisotropic broadening. The principal components of the electron–nuclear dipolar shift anisotropy tensor (in ppm) derived from Equations (2.9) and (2.10) can be written as:

$$\delta_{kk}^{\mathrm{dip}} = \frac{10^6 A_{kk}^{\mathrm{dip}} \langle S_z \rangle}{2\hbar\omega_0 S}. \tag{2.11}$$

The form of this tensor is exactly analogous to the chemical shift anisotropy (CSA) tensor commonly encountered in diamagnetic solids, and is characterized by two parameters, namely the dipolar anisotropy $\Delta_\delta$ and dipolar asymmetry $\eta$, which are defined in Section 2.2.3.1.

In the case of MAS experiments, the electron–nuclear dipolar interaction can manifest as a very broad spinning sideband manifold. The sideband intensities can, in principle, be fit to extract the values of the electron–nuclear dipolar anisotropy and asymmetry parameters. In practice, as common MAS rates are not fast enough to effectively average out this large, anisotropic interaction, advanced pulse programming methods such as MATPASS (described in Section 2.1.2.2) must be applied to obtain useful information from these paramagnetically broadened spectra.

### 2.1.3.3 Temperature dependence of paramagnetic interactions

The time-averaged value of the electron spin (so-called "Curie spin") $\langle S_z \rangle$ can be given in an explicit form[157,163] by considering the thermal Boltzmann distribution across the electron Zeeman levels that are denoted by $m_s$, according to:

$$\langle S_z \rangle = \frac{\sum_{m_s} m_s \exp\left\{-\frac{g_e \mu_B m_s B_0}{k_B T}\right\}}{\sum_{m_s} \exp\left\{-\frac{g_e \mu_B m_s B_0}{k_B T}\right\}} \tag{2.12}$$

where $k_B$ is the Boltzmann constant and $T$ is the temperature of the system. In the high-temperature approximation, $g_e \mu_B m_s B_0 \ll k_B T$, this simplifies to:

$$\langle S_z \rangle = -\frac{g_e \mu_B B_0}{3 k_B T} S(S+1). \tag{2.13}$$

The critical finding is that $\langle S_z \rangle$, and therefore both the isotropic Fermi contact shift and the magnitude of the anisotropic electron–nuclear dipolar tensor, possess an inverse dependence on the temperature of the system. The form of this temperature dependence is exactly analogous to that of the magnetic susceptibility of a paramagnetic material, which is a manifestation of the Curie law (or the Curie-Weiss law in the case of a system with residual exchange interactions between spins). In the present context, this result has two important corollaries: first, the experimentally observed Fermi contact shifts will be smaller at high temperature, so interpretation of variable-temperature NMR spectra of paramagnetic materials will need to account for this fact. Secondly, any computational methods that purport to accurately calculate the Fermi contact shift (or dipolar anisotropy) will need to properly incorporate the temperature dependence, which is most easily done by including a multiplicative scaling factor (as later described in Section 2.2.3.1).

## 2.1.4 Quadrupolar interactions

More than 70% of NMR-active nuclei, including $^{17}$O, have a nuclear spin $I > ½$ and therefore possess a non-zero nuclear electric quadrupole moment $Q$. The interaction between the inherent electric quadrupole of the nucleus and an electric field gradient (EFG) at the nuclear

position is called the quadrupolar interaction, and is described by the quadrupolar Hamiltonian:

$$\widehat{\boldsymbol{H}}_{\boldsymbol{Q}} = \frac{eQ}{2\hbar I(2I-1)} \hat{\boldsymbol{I}} \cdot \boldsymbol{V} \cdot \hat{\boldsymbol{I}} \tag{2.14}$$

where $e$ is the elementary electric charge, $\hat{\boldsymbol{I}}$ is the nuclear spin vector operator, and $\boldsymbol{V}$ is the EFG tensor.[164,165] The principal Cartesian components of the EFG are ordered such that $|V_{ZZ}| \geq |V_{XX}| \geq |V_{YY}|$, from which the magnitude and asymmetry of the quadrupolar coupling are typically expressed as the quadrupolar coupling constant (in Hz) $C_Q = eQV_{ZZ}/h$, and the quadrupolar asymmetry parameter $\eta_Q = (V_{YY} - V_{XX}) / V_{ZZ}$. The size of the $C_Q$ is a function of the local charge and bonding asymmetry at the nuclear position; for a perfectly tetrahedral or octahedral (including cubic) environment, the electric field gradient and thus the $C_Q$ are identically zero. For sites which exhibit significant deviations in bond angles and/or neighboring charges from these ideal geometries, or have a high degree of covalent bonding, the respective $C_Q$ values can become very large. Typical values for $^{17}$O ($I$ = 5/2) vary between hundreds of kHz for highly symmetric alkaline earth oxides to as much as 10 MHz for phosphates, chlorates, and organic compounds.

While the quadrupole interaction is among the largest nuclear spin interactions, it is usually at least an order of magnitude smaller than the Zeeman interaction and is therefore typically treated as a perturbation to the Zeeman interaction. First-order perturbation theory gives the following first-order quadrupolar Hamiltonian:

$$\widehat{H}_Q^{[1]} = \frac{eQ}{4\hbar I(2I-1)} \left[3\hat{I}_z^2 - I(I+1)\right] V_{zz} \,. \tag{2.15}$$

The first-order quadrupolar interaction leads to a shift of the relative energies of the $2I + 1$ spin states according to the value of $m_I$ (middle row, Figure 2.5). The energy of the (½ ↔ −½) transition (the so-called central transition) is not affected, but the other transitions (the satellite transitions) are evenly spaced on either side of the central transition by a frequency of $2\omega_Q$, where $\omega_Q$ is the quadrupolar frequency defined by $\omega_Q = \frac{3C_Q}{4I(2I-1)}$. (For the case of $I$ = 5/2 as depicted in Figure 2.5, $\omega_Q = 3C_Q / 40$.) The anisotropic part of the

first-order quadrupolar interaction contains a term that exhibits an angular dependence of $(3\cos^2\theta - 1)$, and is therefore effectively averaged by MAS; however, broad sideband manifolds are still possible if the MAS rate is small with respect to the size of the quadrupolar interaction. The first-order quadrupolar interaction also has important effects on the ability to excite the broadened spectrum comprising both central and satellite transitions. This issue arises when the quadrupolar frequency $\omega_Q$ is on the order of the rf pulse frequency $\omega_1$ and leads to so-called quadrupolar nutation effects that can also be exploited to selectively excite resonances based on the size of their $C_Q$ values (described in Section 2.1.4.1).

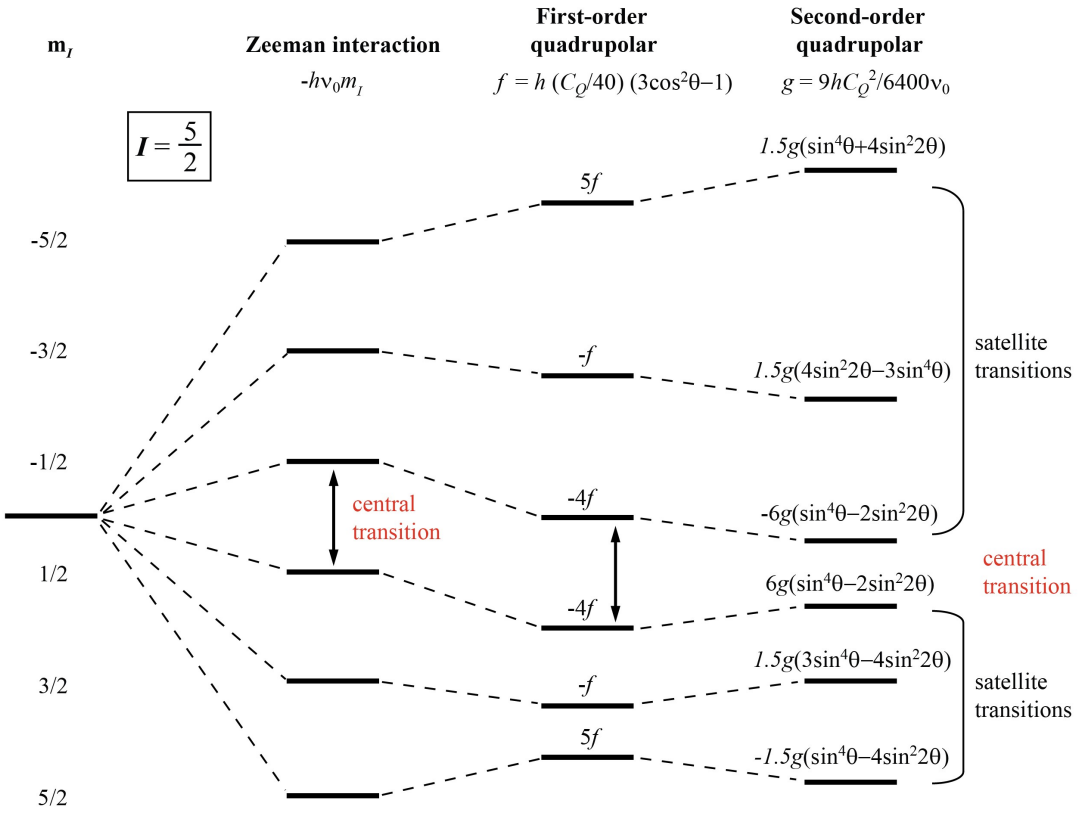


Figure 2.5: For the case of $I$ = 5/2, a depiction of the splitting of nuclear spin states by the Zeeman interaction (left), with the additional perturbations to the energy of the spin states induced by the first-order (middle) and second-order (right) quadrupolar interactions. The central transition energy is unaffected by the first-order interaction but is reduced and given an additional angular dependence by the second-order interaction. The strength of the first-order interaction scales linearly with $C_Q$ and the strength of the second-order interaction scales with $C_Q^2$ and $\omega_0^{-1}$.

For large values of $C_Q$, it is necessary to consider the next term in the quadrupolar perturbation to the Zeeman interaction. The second-order quadrupolar interaction is given by the Hamiltonian:

$$\begin{aligned}\hat{H}_Q^{[2]} = -\frac{1}{\omega_0}\left[\frac{eQ}{4\hbar I(2I-1)}\right]^2 \\ \times \left\{2V_{-1}V_1\hat{I}_z\left[4I(I+1)-8\hat{I}_z^2-1\right]\right. \\ \left. + 2V_{-2}V_2\hat{I}_z\left[2I(I+1)-2\hat{I}_z^2-1\right]\right\}\end{aligned} \tag{2.16}$$

where the components of $\boldsymbol{V}$ are given in a spherical tensor formalism, which can be expressed in terms of the Cartesian components according to:

$$\left.\begin{aligned} V_1 &= -V_{XZ} - iV_{YZ} \\ V_{-1} &= V_{XZ} - iV_{YZ} \\ V_2 &= \tfrac{1}{2}(V_{XX} - V_{YY}) + iV_{XY} \\ V_{-2} &= \tfrac{1}{2}(V_{XX} - V_{YY}) - iV_{XY} \end{aligned}\right\}. \tag{2.17}$$

The second-order quadrupolar interaction leads to a more complicated shifting of the energies of the nuclear spin states, as shown schematically in the right-hand side of Figure 2.5. One important result is that the strength of the second-order quadrupolar interaction scales inversely with the Larmor frequency, so that the second-order effects can be reduced by performing experiments at higher magnetic field. Another outcome is that the frequency of the central transition is altered, with a higher-order orientational dependence that is not fully averaged under MAS. In practice this means that (1) the experimental position of the resonance arising from the central transition shifts towards lower frequency, with a characteristic field dependence, and (2) a residual powder pattern persists in the form of distinctive second-order quadrupolar lineshapes and/or broadening, as further discussed in Section 2.1.4.2.

#### 2.1.4.1 Quadrupolar nutation effects

Because the first-order quadrupolar interaction can lead to a significant frequency separation between the satellite and central transitions, the application of a standard rf pulse may not

necessarily excite the entire spin system.[166,167] In this case, the effective flip angle of the rf pulse (*e.g.,* whether the pulse induces a 90° ($\pi$/2) rotation of the magnetization, as shown in Figure 2.1, or if the nutation behavior differs significantly) strongly depends on the relative magnitudes of the quadrupolar frequency $\omega_Q$ and the rf pulse frequency $\omega_1$. Since the experimental NMR signal is maximum for application of an effective 90° ($\pi$/2) pulse, and is exactly zero for an effective 180° ($\pi$) pulse, the quadrupolar effect on the rf flip angle is an important consideration in the acquisition of solid-state NMR spectra of quadrupolar nuclei.

Two extreme situations can be distinguished: first, suppose the rf field strength is much larger than the quadrupolar frequency, *i.e.*, $\omega_1 \gg \omega_Q$. In this case, the rf pulse is said to be non-selective, meaning that it excites both the central and satellite transition intensity, and the spin system behaves as it would in the non-quadrupolar limit. That is, the rf pulse corresponding to a nominal 90° flip angle for a non-quadrupolar reference compound is still an effective 90° pulse. The other extreme scenario is the case where the quadrupolar frequency significantly exceeds the rf field strength, *i.e.*, $\omega_Q \gg \omega_1$. The rf pulse is then said to be selective for the central transition only, and the rf pulse that would normally excite the entire spin system now excites a much smaller subset of spins, such that the effective flip angle is multiplied by a factor of $I + ½$. In the case of a quadrupolar nucleus of $I$ = 5/2 (such as $^{17}$O), this factor is equal to 3, and implies that a nominal 90° ($\pi$/2) pulse effectively becomes a 270° (3$\pi$/2) pulse for the central transition intensity. A resonance excited by such a pulse will therefore appear negative in the experimental spectrum. For this highly quadrupolar system, a nominal 30° ($\pi$/6) rf pulse will behave as an effective 90° ($\pi$/2) pulse, and this will provide the maximum signal intensity.

In the intermediate case where the rf field strength and quadrupolar frequency are of the same magnitude, the excitation properties of the rf pulse are complex and non-sinusoidal, and the factor to convert between nominal and effective flip angles must be determined from simulations; an example of the simulated nutation behavior for various values of $\omega_Q/\omega_1$ is shown in Figure 2.6.

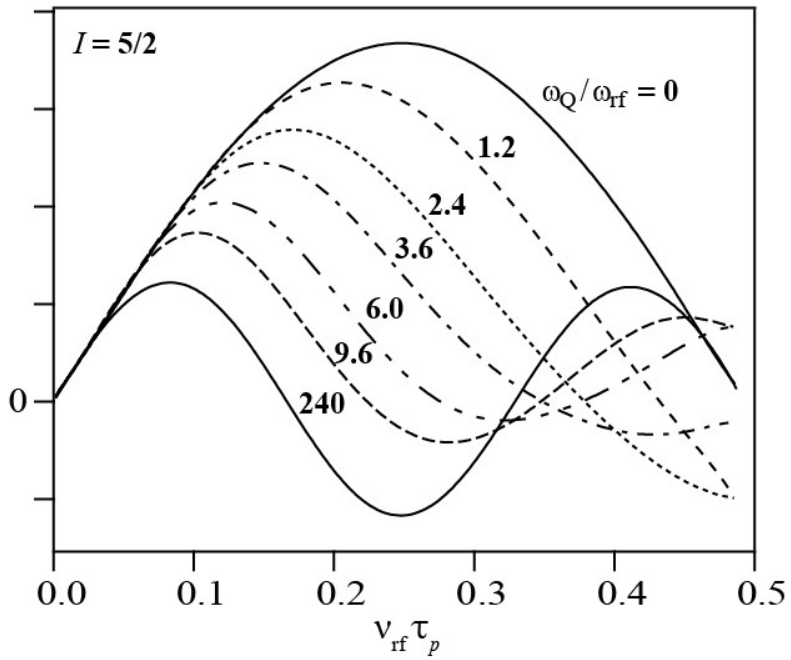


Figure 2.6: Calculated central transition signal intensities as a function of the nominal rf pulse length, for non-selective ($\omega_Q/\omega_1$ = 0), intermediate, and selective ($\omega_Q/\omega_1$ = 240) situations. The pulse length axis is normalized to a 360° or 2$\pi$ pulse, *i.e.*, a value of 0.25 corresponds to a nominal 90° pulse in the non-selective case. As seen for the intermediate case of $\omega_Q/\omega_1$ = 6.0, a nominal 90° pulse fully suppresses the signal arising from the central transition, *i.e.*, it effectively behaves as a 180° pulse would, and in the selective case the nominal 90° pulse is effectively a 270° pulse. Figure adapted from Kentgens.[166]

Importantly, quadrupolar nutation effects can be exploited to suppress resonances on the basis of the magnitude of their $C_Q$ values, which is a technique known as quadrupolar (or nutation-based) filtering. Consider the situation of a system containing two resonances arising from quadrupolar nuclei of $I$ = 5/2, with $C_Q$ values that differ by roughly a factor of 5. This example is not uncommon for crystal structures containing both locally symmetric and highly distorted crystallographic environments. One can tune the rf power to choose an optimal $\omega_1$ such that for the small-$C_Q$ resonance, the rf nutation behavior resembles the curve labelled $\omega_Q/\omega_1$ = 1.2 in Figure 2.6, and for the large-$C_Q$ resonance the curve labelled $\omega_Q/\omega_1$ = 6.0. Then the application of an rf pulse of a length corresponding to a nominal 90° ($\pi$/2) pulse (that is, a value of $\upsilon_{\mathrm{rf}}\tau_p$ = 0.25 in Figure 2.6) will produce a nearly maximal intensity of the first resonance, but fully suppress the second resonance. On the other hand, application of a much shorter pulse such as a nominal 30° ($\pi$/6) pulse, corresponding to $\upsilon_{\mathrm{rf}}\tau_p$ = 0.08 in Figure

2.6, will allow for the observation of both resonances. This approach is employed in the present work to discriminate between more and less distorted $^{17}$O environments, where the expected $C_Q$ values have been determined in advance from first-principles calculations (see Section 2.2.3.2).

### 2.1.4.2 Second-order quadrupolar shifts

The effect of the second-order quadrupolar interaction on the frequency of the central transition, which can be calculated from the second-order quadrupolar Hamiltonian in Equation (2.16), leads to the following expression for the observed experimental NMR shift (in ppm):

$$\delta_{exp} = \delta_{CS} - \frac{1}{30}\left(1 + \frac{1}{3}\eta_Q^2\right)\left[I(I+1) - \frac{3}{4}\right]\left[\frac{3C_Q}{2I(2I-1)\omega_0}\right]^2 \quad (2.18)$$

where $\delta_{exp}$ is the experimentally observed shift of the central transition, $\delta_{CS}$ is the true chemical shift in the absence of the second-order quadrupolar interaction (*e.g.*, in the limit of an infinitely large magnetic field), and $C_Q$ and $\eta_Q$ are the quadrupolar coupling constant and quadrupolar asymmetry parameter, respectively.[164] The key point is that the experimental shift has a dependence on the Larmor frequency $\omega_0$, so that by performing NMR experiments at multiple fields and plotting the values of $\delta_{exp}$ vs. $\omega_0^{-2}$, a linear fit is ideally obtained with a slope proportional to the constant $C_Q^2(1 + \frac{1}{3}\eta_Q^2)$. Because $\eta_Q$ can only take on values between 0 and 1, the experimental value of $C_Q$ can be bounded by such an approach. In this work, variable-field measurements are used in this manner to obtain approximate $C_Q$ values as well as values of the proportionality constant $C_Q^2(1 + \frac{1}{3}\eta_Q^2)$, which can then be included in fits to variable-temperature relaxometry data as a direct probe of oxide ion dynamics, as described later in Section 2.1.5.2.2.

## 2.1.5 Probing dynamics

Solid-state NMR is not only a powerful local structural technique, but also a sensitive probe of local ion dynamics, because the various timescales relevant to NMR spectroscopy span an

extremely wide temporal range (Figure 2.7). Very slow motional dynamics may interact directly with $T_1$ and $T_2$ relaxation processes, although often this is only relevant for macroscopic processes such as flow in solution-state NMR. Motional processes on the slightly faster spectral timescale ($10^{-6}$ s), which is the same rate as "slow" ionic motion in superionic conductors, can lead to characteristic disturbances in the lineshapes of NMR resonances. Finally, the Larmor timescale is roughly the inverse of the Larmor frequency and thus probes very fast dynamics ($10^{-9}$ s). While the Larmor regime (~$10^{-9}$ s) in Figure 2.7 is explicitly distinguished from the so-called relaxation timescale ($10^{-3}$ to $10^{3}$ s), in fact the motional dependence of both $T_1$ and $T_2$ relaxation times frequently becomes important when motional correlation times $\tau_c$ are on the order of the Larmor frequency $\omega_0$, because transient magnetic fields can occur that effectively promote spin relaxation. Fits to variable-temperature relaxometry data often reveal very fast ionic motion on the order of 10–100 MHz.[168]

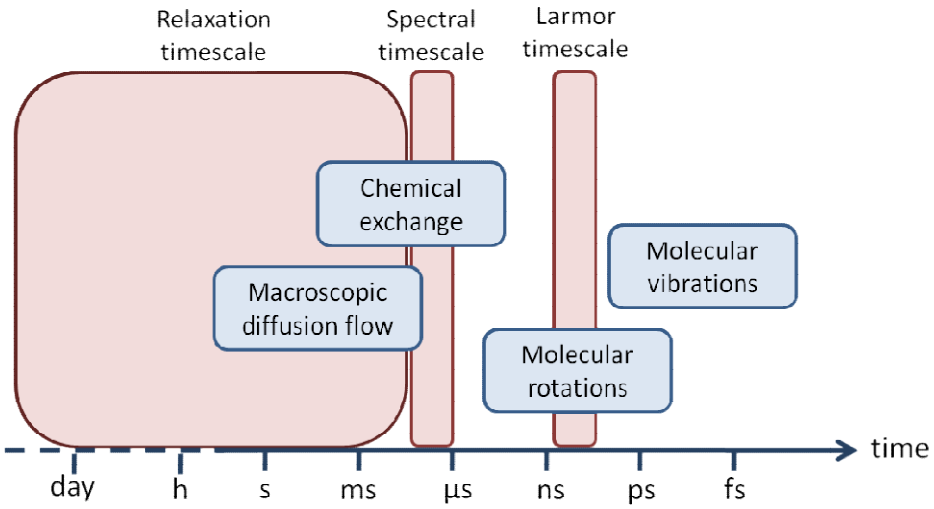


Figure 2.7: Comparison of the various timescales probed by NMR spectroscopy and how they relate to typical dynamic processes on both the macroscopic and molecular levels. Figure reproduced from Levitt.[169]

### 2.1.5.1 Lineshape changes in multi-site exchange

Chemical exchange occurring in nuclear spin systems on the order of the spectral timescale, *i.e.*, the FID acquisition time (µs to ms), can lead to characteristic changes in the observed lineshapes of the spectral resonances. Consider the simple case of two equally populated sites

A and B that undergo exchange characterized by random "hops" with an exchange rate given by $k_{\mathrm{ex}}$, and assume that the resonances arising from sites A and B have a frequency separation $\Delta\upsilon$. In the case that $k_{\mathrm{ex}} \ll \Delta\upsilon$, which is called the "slow motion" regime, the two resonances can be clearly distinguished in the NMR spectrum (Figure 2.8a, top), because the frequency components arising from the two sites persist long enough to contribute separately to the FID (Figure 2.8b and c, top).

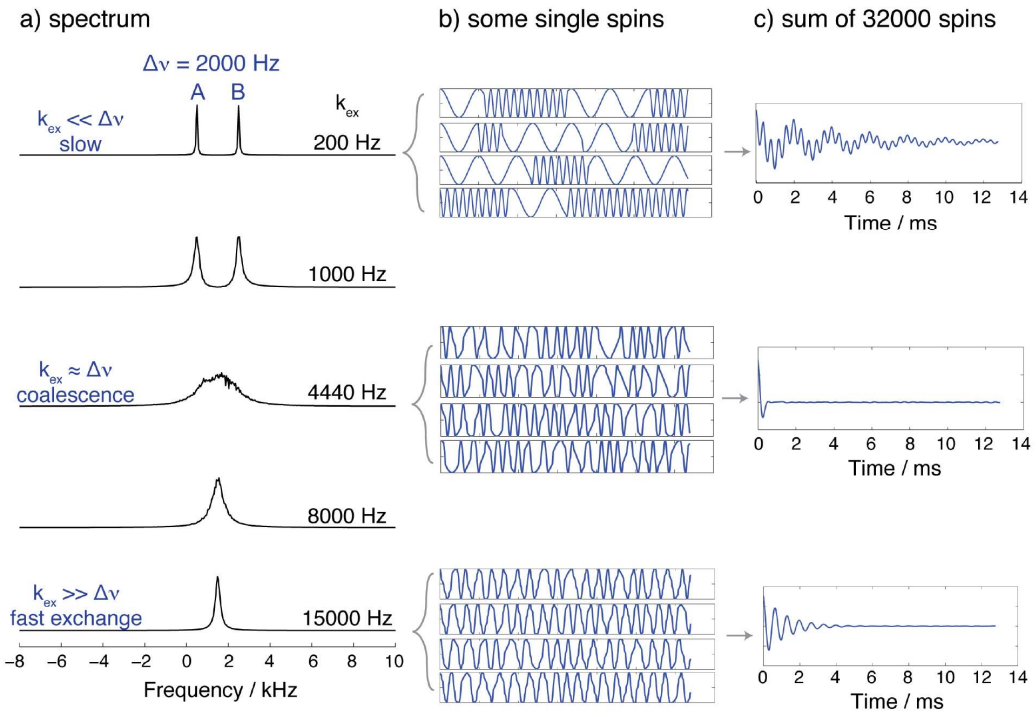


Figure 2.8: a) Simulations of spectra influenced by a two-site exchange process of rate $k_{\mathrm{ex}}$, where the frequency separation between the two sites is $\Delta\upsilon$ = 2000 Hz. b) Depiction of individual contributions of spins to the FID, for $k_{\mathrm{ex}}$ = 200, 4440, and 15000 Hz, and c) the summed FID of all the simulated spins. Figure based on Keeler[137] using the simulation code of Forse *et al.*[170,171]

As the exchange rate increases, the two resonances begin to broaden and eventually undergo coalescence into a single broad feature at $k_{\mathrm{ex}} = \frac{\pi}{\sqrt{2}}\Delta\upsilon \approx 2.22\Delta\upsilon$ (Figure 2.8a, middle). The phenomenon of coalescence can be rationalized by considering precession at the level of a single spin. While uninterrupted precession for a time period of at least $1/\Delta\upsilon$ would be required to distinguish the two frequency components, this is rendered impossible by the random hops occurring on this timescale (Figure 2.8b, middle). Moreover, the individual

spins also rapidly dephase from each other, leading to a FID with a short persistence length (Figure 2.8c, middle) corresponding to a maximally broadened resonance.

For fast exchange rates $k_{ex} \gg \Delta\upsilon$, in the limiting case of the "fast motion" regime, a single resonance is observed which further narrows with increasing exchange rate (Figure 2.8a, bottom). In this scenario, the individual spins hop many times within a single precession period and the discrete frequency components are averaged (Figure 2.8b, bottom); as the exchange rate increases, less dephasing occurs, the FID persists for a longer time (Figure 2.8c, bottom), and the resonance narrows further.

Importantly, in the case of two unequally populated sites, in the fast motion regime, the coalesced resonance appears at the population-weighted average of the shifts of the two resonances. Otherwise, the observed spectral behavior, including the characteristic exchange rate at coalescence, is analogous to the situation of equally populated sites.[172] Spectra resulting from symmetric as well as asymmetric exchange of several sites can be simulated with software such as the McMaster Exchange Code (MEXICO) developed by Bain.[173]

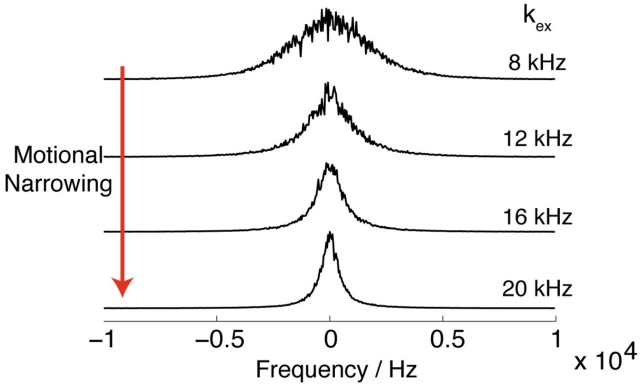


Figure 2.9: Simulations of motional narrowing with a uniform distribution of frequencies spanning a range of 6 kHz (*i.e.*, between -3 kHz and 3 kHz). Figure based on Keeler[137] using the simulation code of Forse *et al.*[170,171]

Many real spin systems comprise a broad distribution of frequency components arising from effects such as local disorder, so that in contrast to the two-site scenario previously described, the individual resonances cannot be distinguished. In this case, exchange between the resonances can also lead to motional narrowing (Figure 2.9). However, motional narrowing is only experimentally observed when the exchange rate is on the order of the inherent

frequency distribution among the exchanging sites; in the slow- and fast-exchange limits, static linewidth values are observed.

Indris *et al.* have extracted motional correlation times for dynamic processes that give rise to motional narrowing, using the implicit expression:

$$(\Delta\upsilon)^2 = (\Delta\upsilon^{\mathrm{HT}})^2 + (\Delta\upsilon^{\mathrm{LT}})^2 \cdot \frac{2}{\pi} \cdot \tan^{-1}(\alpha \cdot \Delta\upsilon \cdot \tau_c) \tag{2.19}$$

where $\Delta\upsilon$ is the experimental linewidth at a given temperature, $\Delta\upsilon^{\mathrm{HT}}$ and $\Delta\upsilon^{\mathrm{LT}}$ are the limiting values of the linewidth in the high-temperature and low-temperature plateaus, respectively, and $\alpha$ is a lineshape-dependent constant on the order of unity.[174,175] Dunstan *et al.* later reported an approximation to Equation (2.19) that was combined with the Arrhenius law to give:

$$\frac{d\ln(\Delta\upsilon)}{d(1/T)} = -\frac{E_a}{R} \tag{2.20}$$

where $T$ is the experimental temperature, $E_a$ is the activation energy, and $R$ is the molar gas constant.[132] In this analysis, only the linear region of $\ln(\Delta\upsilon)$ vs. $1/T$ is used to extract the activation energy, *i.e.*, the values of $\Delta\upsilon$ in the limiting high- and low-temperature regions are not included. Equation (2.20) is used in the present work to extract activation energies for ion dynamics causing motional narrowing; this motion can be interpreted physically as corresponding to site-specific dynamical processes (*e.g.*, rattling or polyanion rotation) that do not lead to large changes in the local chemical environment.

### 2.1.5.2 Motional effects on nuclear relaxation rates

#### 2.1.5.2.1 Low-frequency ion dynamics and $T_2$ relaxation

In the case where high-frequency processes such as electron relaxation do not contribute to $T_2$ relaxation, one can assume that low-frequency motion (*i.e.*, on the order of the spectral timescale between μs and ms) is the predominant $T_2$ relaxation mechanism.[176–178] This results in a $T_2$ which is much shorter than the $T_1$, as high-frequency processes tend to contribute to both $T_1$ and $T_2$ relaxation, but only low-frequency processes influence $T_2$. Under these

conditions, one first assumes that the motion is characterized by an exchange rate $k_{ex}$ leading to random hops between sites, where the resonances arising from these sites have a maximal frequency separation $\Delta\upsilon$. (This situation may manifest either as a two-site exchange where the $\Delta\upsilon$ is well-defined, or as a single spectral feature comprising a distribution of resonances where the $\Delta\upsilon$ is roughly on the order of the linewidth.) Then, the motion has characteristic effects on the $T_2$ relaxation time in the slow and fast motion regimes (*i.e.*, for the cases $k_{ex} \ll \Delta\upsilon$, and $k_{ex} \gg \Delta\upsilon$, respectively).

In the slow motion regime, the $T_2$ is inversely proportional to $k_{ex}$, that is, $T_2 = c/k_{ex}$. As the motional rate increases, the $T_2$ relaxation time becomes shorter. The corresponding physical picture is that the increasingly faster motion shortens the effective coherence lifetime of the magnetization, which lowers the value of $T_2$. In the fast motion regime, the $T_2$ is directly proportional to $k_{ex}$, that is, $T_2 = c' \cdot k_{ex}$. At this point, the $T_2$ relaxation time begins to increase with the motional rate; the $T_2$ relaxation becomes progressively less sensitive to this motional process, which no longer interacts with the spin system on the timescale of the frequency separation, $\Delta\upsilon$. The boundary between the two regimes is given by the coalescence condition $k_{ex} \approx 2.22\Delta\upsilon$, where the $T_2$ value is minimal.[176]

Thus by measuring $T_2$ as a function of temperature in this type of system, the values of $k_{ex}$ can be extracted, and assuming Arrhenius behavior the activation energy can be measured. In the case where the $T_2$ values cannot be measured directly because of experimental time constraints, the influence of $T_2$ relaxation on the spectral intensity can be used as a proxy for the $T_2$ value, which allows for determination of the activation energy of the relevant motional process. Further details on the derivation of this method and its specific application to the present work are given in Appendix A.

#### 2.1.5.2.2 Probing fast motion on the order of the Larmor frequency *via* $T_1$ relaxation

In diamagnetic nuclear spin systems containing quadrupolar nuclei, $T_1$ relaxation is predominantly driven by local variations in quadrupolar coupling. Because the quadrupolar interaction is typically (one of) the largest nuclear spin interaction(s), motion-induced

fluctuations in the EFG at the rate of the Larmor frequency give rise to transient fields that are very effective at promoting relaxation between spin states of quadrupolar nuclei. In this situation, the following equation holds:

$$\frac{1}{T_1} = \frac{2\pi^2}{25} \cdot C_Q^2 \left(1 + \frac{1}{3}\eta_Q^2\right) \cdot \left[\frac{\tau_c}{1 + \omega_0^2\tau_c^2} + \frac{4\tau_c}{1 + 4\omega_0^2\tau_c^2}\right] \tag{2.21}$$

where $C_Q$ and $\eta_Q$ are the quadrupolar coupling constant and quadrupolar asymmetry parameter, respectively, $\omega_0$ is the Larmor frequency, and $\tau_c$ is the motional correlation time.[174,175,179] Provided that the values of $C_Q$ and $\eta_Q$ are known, by measuring the $T_1$ of a given resonance as a function of temperature in a system with a dominant quadrupolar relaxation mechanism, values of $\tau_c$ can be extracted which are related to the local motion surrounding each site with a spectrally distinct resonance. The magnitude of the motional rate $\tau_c^{-1}$ is typically on the order of the Larmor frequency, *e.g.*, tens of MHz. Assuming an Arrhenius relationship between $\tau_c^{-1}$ and the temperature $T$, the activation energy $E_a$ can then be determined. These rapid motional processes have previously been ascribed to softening of lattice vibrations or motion of defects in systems ranging from glasses to ionic conductors.[168,180] In this thesis, the method is applied to characterize the motion of oxygen vacancies in SOFC electrolyte materials (Chapter 5).

## 2.2 First-principles electronic structure calculations

When combined with experimental approaches, computational modelling techniques can help to provide an atomic-level understanding of structure and dynamics in SOFC materials. Atomistic potential-based methods (such as classical molecular dynamics), as well as first-principles calculations based on a quantum mechanical viewpoint, have been employed in numerous studies of SOFC materials to predict oxygen bulk transport and to derive novel materials design principles.[34,70,181–184] First-principles calculations of solid-state NMR parameters, in particular the now well-established Gauge Including Projector Augmented Wave (GIPAW) approach of Pickard and Mauri,[185–187] have also found use in the interpretation of NMR spectra of energy storage and conversion materials,[138,188] including diamagnetic oxide-ion and proton conductors.[130,189,190] In this thesis first-principles electronic

structure methods are employed exclusively to calculate NMR properties, *i.e.*, quadrupolar coupling constants and hyperfine parameters, as an aid to spectral assignment.

### 2.2.1 Basic principles of electronic structure theory

The exact quantum mechanical description of a given material corresponds to solutions of the time-independent, many-body Schrödinger equation:

$$\widehat{H}\Psi = E\Psi \tag{2.22}$$

where $\widehat{H}$ is the (non-relativistic) Hamiltonian operator, $\Psi$ is the many-body wavefunction, and $E$ is the energy of the stationary state described by $\Psi$. The relevant aspects of the atomic or molecular system are described by terms in the Hamiltonian operator, including the kinetic energy of the electrons and the nuclei, and the potential (Coulombic) energy of the interactions between them. The form of the Hamiltonian is typically simplified by applying the Born–Oppenheimer approximation, which allows the electronic and nuclear components of the wavefunction to be separated under the assumption that the comparatively light electrons respond instantaneously to changes in the nuclear coordinates. The Hamiltonian operator (here expressed in atomic units) then takes the form:

$$\widehat{H} = -\frac{1}{2}\sum_{i=1}^{n}\nabla_i^2 - \sum_{i=1}^{n}\sum_{\alpha}\frac{Z_\alpha}{|\boldsymbol{r}_i - \boldsymbol{R}_\alpha|} + \sum_{i=1}^{n}\sum_{i<j}\frac{1}{|\boldsymbol{r}_i - \boldsymbol{r}_j|} \tag{2.23}$$

where $i$ and $j$ are summation indices over the $n$ electrons with positions $\boldsymbol{r}_i$ and $\boldsymbol{r}_j$, and $\alpha$ is the summation index over the nuclei with positions $\boldsymbol{R}_\alpha$ and masses $Z_\alpha$.[191] The first term in the Hamiltonian corresponds to the electron kinetic energy, the second term to the electron–nuclear potential energy, and the third term to the electron–electron potential energy. (The total energy of the system also includes the nuclear–nuclear potential energy, which does not change the electronic wavefunction obtained by solving Equations (2.22) and (2.23).)

Because the behavior of each electron is dependent on that of the other electrons *via* the electron–electron repulsion term, the many-body Schrödinger equation quickly becomes computationally intractable for relevantly sized systems. To handle this issue, one can apply the so-called Hartree–Fock method, which leads to approximate solutions to Equations (2.22)

and (2.23). In this approach, one assumes that the true many-body electronic wavefunction can be represented by an antisymmetrized product of $n$ one-electron states $\phi_i(\boldsymbol{r})$. A variational argument then produces the single-particle Hartree–Fock equations:

$$\left[-\frac{1}{2}\nabla_{\mathbf{r}}{}^2 + V(\boldsymbol{r}) + V_i^H(\boldsymbol{r}) + V_i^X(\boldsymbol{r})\right]\phi_i(\boldsymbol{r}) = \varepsilon_i\phi_i(\boldsymbol{r}) \tag{2.24}$$

where the four terms in the single-particle Hamiltonian operator correspond to the kinetic energy $-\frac{1}{2}\nabla_{\mathbf{r}}{}^2$, the external ionic potential $V(\boldsymbol{r})$, the Hartree (average Coulombic repulsion) potential $V_i^H(\boldsymbol{r})$ for electron $i$, and the exchange potential $V_i^X(\boldsymbol{r})$ for electron $i$, respectively. The latter two terms together represent an approximation to the average potential induced by the other electrons. Here the $\varepsilon_i$ values are the Hartree–Fock eigenvalues. The one-electron wavefunctions $\phi_i$ are found *via* an iterative self-consistent procedure wherein an initial set of guesses, *e.g.*, linear combinations of Gaussian basis set functions, are used to construct the single-particle Hamiltonian and solve Equation (2.24) for a new set of wavefunctions. The procedure is repeated until the newly calculated wavefunctions are equivalent within a specified tolerance to the previous ones. However, this method ignores electronic correlations by the very nature of its ansatz, and also remains computationally demanding for large systems.

Density functional theory (DFT) is an alternative and computationally inexpensive approach to solving the many-body Schrödinger equation. It reformulates the problem in terms of finding the total electron density $n(\boldsymbol{r})$, which is a function of just three spatial variables, rather than the full, 3$n$-dimensional many-body wavefunction Ψ. Hohenberg and Kohn proved that the external ionic potential $V(\boldsymbol{r})$ uniquely determines the total electron density $n(\boldsymbol{r})$, and moreover that the *exact* total energy of the system is a universal functional of the density,[192] that is:

$$E[n(\boldsymbol{r})] = F[n(\boldsymbol{r})] + \int V(\boldsymbol{r})\, n(\boldsymbol{r})\, d\boldsymbol{r} \tag{2.25}$$

where $F[n(\boldsymbol{r})]$ is a functional that does not depend on the external potential $V(\boldsymbol{r})$, and incorporates the effects of electron kinetic energy and electron–electron interactions. The true ground state electron density of the system minimizes this energy functional, and thus by

applying a similar variational argument as in the case of the Hartree–Fock method, the set of single-particle Kohn–Sham equations[193] is obtained:

$$\left[-\frac{1}{2}\nabla_{\mathbf{r}}{}^{2} + \int \frac{n(\boldsymbol{r}')}{|\boldsymbol{r} - \boldsymbol{r}'|}\, d\boldsymbol{r}' + \frac{\delta E^{XC}[n(\mathbf{r})]}{\delta n(\boldsymbol{r})} + V(\boldsymbol{r})\right]\varphi_i(\boldsymbol{r}) = \varepsilon_i \varphi_i(\boldsymbol{r}) \qquad (2.26)$$

where $F[n(\boldsymbol{r})]$ has been expanded to include terms related to the electron kinetic energy, Coulombic repulsion, and the exchange-correlation interaction described by $E^{XC}[n(\mathbf{r})]$; the $\varepsilon_i$ values are the Kohn–Sham eigenvalues. The $\varphi_i(\boldsymbol{r})$ functions are the (non-interacting) one-electron Kohn–Sham orbitals, which can be found in a self-consistent manner analogous to the Hartree–Fock method.

The exchange-correlation functional $E^{XC}[n(\mathbf{r})]$ includes the non-classical components of the electron–electron interactions, such as the effect of Pauli repulsion between electrons of the same spin. It is interesting to note that the Kohn–Sham equations set up a fictitious system of non-interacting electrons with the same density as the many-body interacting system, and thus the exchange-correlation energy must capture the differences in the kinetic and Coulombic energies between the non-interacting and interacting systems. While the exact exchange-correlation functional would give an exact description of the system, its form is unknown and must be approximated in practice. In the local density approximation (LDA), $E^{XC}[n(\mathbf{r})]$ is a functional of the electron density only, and the exchange-correlation energy is taken to be that of a homogeneous electron gas ("jellium") with the same electron density, which is a good approximation for systems with slowly varying electron density, such as metals. An improvement to this approach is given by the generalized gradient approximation (GGA), which employs a functional that depends both on the electron density $n(\boldsymbol{r})$ and its gradient $\nabla n(\boldsymbol{r})$. However, both the LDA and GGA functionals fail to properly describe the band structures of systems with strongly correlated electrons, such as insulating transition-metal oxides,[194] which is primarily a consequence of the electron self-interaction error common to pure DFT calculations. This error arises from the Coulombic repulsion term $\int \frac{n(\boldsymbol{r}')}{|\boldsymbol{r} - \boldsymbol{r}'|}\, d\boldsymbol{r}'$ in Equation (2.26), which represents an unphysical scenario wherein each electron is repelled by an electron density that includes a contribution from the electron itself. The form of the exchange-correlation potential used in the LDA and GGA functionals does

not entirely cancel out the spurious self-interaction effect, leading to delocalization of electron density and significantly underestimated or non-existent band gaps in many systems which should be insulating.

To address this problem, Anisimov *et al*. and later Dudarev *et al.* developed the DFT+U approach, which attempts to correct for the self-interaction error by incorporating an orbital-dependent energy penalty $U_{\mathrm{eff}}$ to the energy functional of the highly-correlated *d* or *f* electrons on *e.g.* transition metal sites, while the other electrons are modelled using the standard DFT framework.[195,196] However, $U_{\mathrm{eff}}$ is system-specific and must be obtained either by semi-empirical fitting to experimental data or through more extensive self-consistent calculations.[197] Alternatively, Becke proposed a hybrid functional that mixes the local or semi-local exchange-correlation functionals of LDA and GGA with a certain percentage of the exact exchange term from the Hartree–Fock approximation.[198] While the orbital-independent self-interaction of pure DFT tends to delocalize electron density, the Hartree–Fock approximation often results in overly ionic (localized) electronic states, and so mixing the two formalisms represents a pragmatic solution to correct for both of these inaccuracies. The most commonly-used hybrid functional, B3LYP, comprises 20% Hartree–Fock exchange, and is the major functional employed in the present work. One appealing aspect of hybrid functionals is that they usually employ only one adjustable parameter, *i.e.*, the extent of incorporation of Hartree–Fock exchange, whereas DFT+U may require several adjustable values of $U_{\mathrm{eff}}$ for systems containing differing transition metals with variable oxidation states and coordination geometries. A major disadvantage, however, is the greater computational cost relative to DFT+U, which limits the feasible system sizes that can be studied using hybrid functionals.

### 2.2.2 Basis functions and implementation in CRYSTAL

**CRYSTAL** is an *ab initio* linear combination of atomic orbitals (LCAO) code that solves the Hartree–Fock and Kohn–Sham single-particle equations for infinite periodic systems.[199] While most periodic electronic structure theory codes represent the periodic component of the relevant wavefunction(s) using a discrete plane wave basis set, **CRYSTAL** instead employs

basis sets comprising localized atomic orbitals; this allows for a more accurate description of *e.g.* the core electrons, which affect the Fermi contact interaction at the nuclear position.

In **CRYSTAL,** the single-particle wavefunctions in Equations (2.24) and (2.26) are represented as a linear combination of Bloch functions $\phi_\mu(\mathbf{r};\ \boldsymbol{k})$, where

$$\phi_\mu(\mathbf{r};\ \boldsymbol{k}) \ = \ \sum_{\boldsymbol{g}} \varphi_\mu\left(\boldsymbol{r} - \boldsymbol{A}_\mu - \boldsymbol{g}\right) e^{i\boldsymbol{k}\cdot\boldsymbol{g}}. \tag{2.27}$$

Here, the $\varphi_\mu(\mathbf{r})$ are local functions, *i.e.*, atomic orbitals, centered at the coordinates of the applicable nucleus $\mathbf{A}_\mu$. The sum is extended to all lattice vectors **g**, which replicates the local atomic orbitals throughout space. The factor $e^{i\boldsymbol{k}\cdot\boldsymbol{g}}$ generates for each atomic orbital $\varphi_\mu(\mathbf{r})$ a set of $\boldsymbol{k}$-parametrized Bloch functions, which can be thought of as the possible symmetry-adapted molecular orbitals formed from $\varphi_\mu(\mathbf{r})$. For example, in the simple case of a one-dimensional crystal where *a* is the lattice parameter, and assuming $\varphi_\mu$ represents an *s* orbital, $\boldsymbol{k}$ = 0 would describe a purely bonding Bloch function where all *s* orbitals have the same phase, and $\boldsymbol{k} = \frac{\boldsymbol{\pi}}{\boldsymbol{a}}$, which is at the boundary of the first Brillouin zone, would describe a purely antibonding Bloch function where the phase alternates with every other *s* orbital. The wavevector $\boldsymbol{k}$ thus describes the momentum (magnitude and direction) of the electron waves in the lattice. In practice, each calculation is performed for a discrete set of $\boldsymbol{k}$-points comprising a sufficiently dense mesh in the first Brillouin zone of reciprocal space.

The local atomic orbitals (*e.g.*, 1*s*, 2*p*, etc.) are themselves represented as linear combinations of $n_G$ normalized Gaussian-type functions (GTFs):

$$\varphi_\mu\left(\boldsymbol{r} - \boldsymbol{A}_\mu - \boldsymbol{g}\right) = \sum_j^{n_G} d_j G\left(\alpha_j;\ \boldsymbol{r} - \boldsymbol{A}_\mu - \boldsymbol{g}\right) \tag{2.28}$$

where the $d_j$ and $\alpha_j$ are the contraction coefficients and Gaussian exponents, respectively, of the GTFs. The set of values of $d_j$ and $\alpha_j$ are atom-specific, and when taken together for all the atoms in the system of interest, forms the basis set defined in the input of a **CRYSTAL** calculation. GTFs with small values of $\alpha_j$ are diffuse and generally describe valence electrons, whereas large $\alpha_j$ values lead to contracted GTFs that model electrons in

the core region. Selection of a suitable atomic basis set with optimized values of $d_j$ and $\alpha_j$ is crucial to the quality of periodic LCAO-type calculations. In this work, two kinds of basis sets, denoted BS-I and BS-II, are used for each atom type, in sequential steps in the calculations. The former is a smaller basis set used during the geometry optimization stage, whereas the latter is an extended basis set with a larger number of primitive GTFs as well as Gaussian-type atomic orbitals, allowing more degrees of freedom in the electronic relaxation. The larger BS-II basis set more accurately represents the electronic structure of the core electrons, but is more computationally expensive.

In the electronic structure calculations implemented in **CRYSTAL**, the one-electron Hartree–Fock or Kohn–Sham equations (Equations (2.24) and (2.26)) are represented in matrix form with a non-orthogonal basis set using the Roothaan–Hall equations:[199,200]

$$\boldsymbol{F}(\boldsymbol{k})\boldsymbol{C}(\boldsymbol{k}) = \boldsymbol{S}(\boldsymbol{k})\boldsymbol{C}(\boldsymbol{k})\boldsymbol{\epsilon}(\boldsymbol{k}) \tag{2.29}$$

where $\boldsymbol{F}$ is the one-electron Fock (or Kohn–Sham) matrix in reciprocal space, $\boldsymbol{C}$ is the coefficient matrix, $\mathbf{S}$ is the basis set orbital overlap matrix, and $\boldsymbol{\epsilon}$ is the diagonal energy matrix. At each step of the self-consistent field (SCF) cycle, the matrix equations are solved independently at each $\boldsymbol{k}$-point, and, in the case of unrestricted Hartree–Fock calculations, solved separately for $\alpha$ and $\beta$ spin states. The reciprocal space Fock matrix $\boldsymbol{F}(\boldsymbol{k})$ derives from a set of Fock matrices in direct space which are parameterized by the truncated set of lattice vectors $\boldsymbol{g}$. This truncation is determined by user-specified tolerances on the bielectronic Coulomb and exchange summations which contribute to the direct space Fock matrices. These Coulomb and exchange summations are recomputed with the new coefficient set $\boldsymbol{C}$ and then used to update $\boldsymbol{F}$, which completes one step of the cycle. The SCF cycle terminates when the energy difference $\|\Delta\boldsymbol{\epsilon}\|$ between two consecutive steps drops below a user-specified convergence criterion.

### 2.2.3 Calculation of NMR parameters

#### 2.2.3.1 Paramagnetic (hyperfine) parameters

While the components of NMR shielding tensors of most diamagnetic solids can be calculated with DFT (using a plane wave basis set) in a straightforward manner using well-established methods such as the aforementioned GIPAW approach, there is as yet no comparable computational methodology that can describe all of the spin interactions in a paramagnetic solid at a consistent level of theory.[187] While first-principles calculations have aided in the assignment of spectra with large Fermi contact shifts by determining the sign and magnitude of the electron spin density transfer to the observed nuclei, only comparatively few systems have been analyzed in this way.[201–203]

This thesis employs the "scaling factor" methodology of Middlemiss *et al.*[204] and Kim *et al.*[89] to calculate Fermi contact shifts and electron–nuclear dipolar tensors. In this approach, hybrid DFT calculations are first performed on the system with the unpaired electrons taken to be in a fictitious ferromagnetic state (at 0 K), to obtain the isotropic hyperfine coupling constants $A_{\mathrm{iso}}$ and principal components of the electron–nuclear dipolar tensors $A_{kk}^{\mathrm{dip}}$ at the nuclear sites of interest. The calculated hyperfine parameters are then related to the Fermi contact shifts and the principal components of the electron–nuclear dipolar coupling tensor in the experimental paramagnetic regime (*e.g.*, at room temperature) by using a multiplicative scaling factor Φ, which is the ratio of the paramagnetic magnetization to the ferromagnetically saturated magnetization.

More intuitively, it is assumed that the magnetic structure of the experimental paramagnetic state exactly resembles that of a fictitious ferromagnetic state, in which the unpaired electron spins are perfectly aligned with the external magnetic field. Only the magnitude of the magnetization differs between these two states (it is considerably smaller for the paramagnetic state), with this difference being captured by the scaling factor $\Phi < 1$. This approximation is reasonable given that, in the paramagnetic state, rapid spin fluctuations away from the external field are much faster than the NMR timescale, as described in Section 2.1.3. It is not necessarily the case, however, that the fictitious ferromagnetic state calculated

by DFT is the true ground state of the system at 0 K, which may limit the accuracy of using this fictitious state to approximate the true paramagnetic state at higher temperatures. This and further limitations of the methodology are briefly discussed later.

The scaling factor Φ may be taken from empirical results, *e.g.*, by using the Curie–Weiss law if the Curie constant and Weiss temperature of the material are known from experiment, as is done in this thesis.[205,206] Alternatively, Φ may be calculated entirely from first-principles by first evaluating the magnetic exchange (*J*) couplings between transition-metal sites and then performing a mean field or a Monte Carlo calculation to obtain the theoretical temperature dependence of the magnetization.[207]

The Fermi contact shift in the paramagnetic regime (and in the absence of spin-orbit coupling), $\delta_{\mathrm{iso}}^{\mathrm{FC}}$, is calculated (in ppm) according to:

$$\delta_{\mathrm{iso}}^{\mathrm{FC}} = \frac{10^6 A_{\mathrm{iso}}}{2\omega_0 \hbar} \Phi \tag{2.30}$$

where $\omega_0$ is the experimental Larmor frequency, $A_{\mathrm{iso}}$ is the isotropic hyperfine coupling constant obtained from first-principles calculations assuming ferromagnetic alignment, and the scaling factor Φ is given by:

$$\Phi = \frac{M_{\mathrm{para}}}{M_{\mathrm{sat}}} = \frac{B_0 \mu_{\mathrm{eff}}^2}{3 k_B \mu_B S (T - \theta)} \tag{2.31}$$

where $M_{\mathrm{para}}$ and $M_{\mathrm{sat}}$ are the paramagnetic magnetization and ferromagnetically saturated magnetization, respectively. In the case of a Curie-Weiss paramagnet, this reduces to give the expression on the right, where $\mu_{\mathrm{eff}}$ is the effective magnetic moment, which is, in the spin-only case, nominally equal to $g\sqrt{S(S+1)}\mu_B$ for a paramagnetic center of formal spin *S*; $\theta$ is the Weiss constant; $B_0$ is the external magnetic field; $\mu_B$ is the Bohr magneton; and *T* is the experimental temperature. Alternatively, if the paramagnetic material of interest does not exhibit Curie-Weiss behavior, the scaling factor can nonetheless be related directly to the experimental molar susceptibility $\chi_M$ using:

$$\Phi = \frac{B_0 \chi_M}{g \mu_B \mu_0 S}. \tag{2.32}$$

Analogously, the principal components of the electron–nuclear dipolar tensor, $\delta_{kk}^{\mathrm{dip}}$, are calculated (in ppm) according to the formula:

$$\delta_{kk}^{\mathrm{dip}} = \frac{10^6 A_{kk}^{\mathrm{dip}}}{2\omega_0 \hbar} \Phi \tag{2.33}$$

which, after ordering the principal components $\delta_{kk}^{\mathrm{dip}}$ by absolute magnitude according to the Haeberlen convention[208] so that $|\delta_{ZZ}| \geq |\delta_{XX}| \geq |\delta_{YY}|$, allows for calculating values of the dipolar anisotropy $\Delta_\delta$ (in ppm) and dipolar asymmetry $\eta$ (where $0 \leq \eta \leq 1$) according to:

$$\Delta_\delta = \delta_{ZZ} - \frac{\delta_{XX} + \delta_{YY}}{2} \tag{2.34}$$

and

$$\eta = \frac{\delta_{YY} - \delta_{XX}}{\delta_{ZZ}}. \tag{2.35}$$

In **CRYSTAL**, the calculated value of $A_{\mathrm{iso}}$ is directly proportional to the unpaired spin density at the nuclear position (*i.e.*, arising exclusively from unpaired spin in the *s* orbitals), and the electron–nuclear dipolar tensor is evaluated by integrating the magnetic dipole–dipole interaction across all relevant atomic orbitals. Because of the use of local atomic orbitals as a basis set in **CRYSTAL**, these hyperfine parameters are readily computed without projecting the calculated electron density into an atomic basis, as is required for plane wave codes.

As discussed earlier, one possible limitation of this methodology is the assumption of a fictitious ferromagnetic state which may not be the true ground state at 0 K (the temperature of the DFT calculations). The geometry optimization step is performed in this state, and so the optimized atomic positions may be representative of a slightly higher-energy configuration. However, the calculated energy differences between differing magnetic structures of transition metal oxides are typically on the order of 10 meV per formula unit, and consequently one would expect a minimal effect from the choice of spin configuration on the optimized structure.[209] Another issue not directly addressed is the presence of residual

magnetic correlations (*e.g.* antiferromagnetic couplings) between adjacent transition metal sites in the experimental, high-temperature paramagnetic state, which moreover may occur along preferential directions in the crystal structure (e.g. along 1D chains or within 2D planes). It is apparent that the isotropic scaling factor used in this thesis cannot capture these effects, although the issue could be bypassed through further calculations; for example, the methodology has been extended to obtain an anisotropic scaling factor by performing Metropolis Monte Carlo simulations on a lattice of Ising-like spins.[210] Despite these limitations, the scaling factor methodology shows good agreement with experiment (typically within 10%) and allows for the straightforward assignment of spectra affected by otherwise difficult-to-interpret Fermi contact shifts, at least for NMR-active centers that are somewhat removed (two or more bonds away) from the transition metal centers, as recently shown by Pigliapochi *et al.*[211]

Because a single solid-state DFT code (**CRYSTAL**) is employed herein in the calculation of the Fermi contact shifts and electron–nuclear dipolar tensors, this work is open to questions regarding the implementation-dependence of the method and the necessity of benchmarking the calculated results against other DFT codes. Such a project would be in line with the recent work of Lejaeghere *et al.* as part of the "Delta codes" project, wherein the impact of various DFT implementations on calculated energy values was evaluated through the so-called Δ-value.[212] (The **CRYSTAL** code was not included in that study.) However, a comparable approach would be difficult in this case, as Fermi contact shift calculations have not generally been attempted in other solid-state periodic DFT codes (excepting a study of Carlier *et al.* in which VASP was used, which predates the scaling factor methodology[201]). An alternative method of evaluating the robustness of the **CRYSTAL** code against other solid-state codes would be through the evaluation of quadrupolar coupling constants (introduced in Section 2.2.3.2). For the systems considered in this thesis and in other $^{17}$O NMR studies,[213] these NMR parameters could be easily calculated in a variety of codes (*e.g.*, CASTEP, VASP) and then compared to the **CRYSTAL** results using a similar Δ-value methodology. Such a project would constitute a promising avenue for future work.

#### 2.2.3.2 Quadrupolar coupling parameters

The determination of quadrupolar coupling parameters is significantly more straightforward than the calculation of either hyperfine parameters or NMR shielding tensors at a similar level of accuracy, as only knowledge of the ground-state charge density surrounding the relevant quadrupolar nuclei is required.[187,214] In this work, the quadrupolar parameters are evaluated from the ground state EFG tensor $\boldsymbol{V}$ at each of the nuclear positions, which is directly calculated by **CRYSTAL**. The principal components of the calculated EFG tensor are ordered by absolute magnitude such that $|V_{ZZ}| \geq |V_{XX}| \geq |V_{YY}|$. The quadrupolar coupling constant $C_Q$ (in MHz) is then evaluated according to:

$$C_Q = \frac{eQ}{\hbar} V_{ZZ} \tag{2.36}$$

where $e$ is the elementary electric charge and $Q$ is the nucleus-specific nuclear quadrupole moment. The quadrupolar asymmetry parameter $\eta_Q$ (where $0 \leq \eta_Q \leq 1$) is given by:

$$\eta_Q = \frac{V_{YY} - V_{XX}}{V_{ZZ}}. \tag{2.37}$$

In the present work the calculated quadrupolar parameters are primarily used to predict quadrupolar nutation behavior to aid in assignment, though in general they are helpful in interpreting lineshapes that are broadened by second-order quadrupolar coupling effects.

## 2.3 X-ray diffraction (XRD)

Diffraction techniques are commonly used to probe the long-range order and phase purity of crystalline materials. In a typical diffraction experiment, incident radiation (X-rays, neutrons or electrons) undergoes constructive or destructive interference after scattering off the regularly spaced regions of electron or nuclear density (*i.e.*, atoms) of a crystalline sample. In what is the most common formalism, this scattering process is treated as partial reflection off periodic planes. By varying the incident angle of irradiation and measuring the intensity of the diffracted waves, a diffraction pattern is generated in which the observed constructive interference obeys Bragg's Law:

$$n\lambda = 2d \sin\theta \tag{2.38}$$

where $n$ is an integer, $\lambda$ is the wavelength of the incident radiation, $d$ is the inter-lattice spacing and $\theta$ is the angle between the incident beam and the scattering lattice plane. Normally, diffraction patterns are presented against the experimentally measured angle of $2\theta$, where the diffractometer operates in a Bragg–Brentano geometry.[215,216]

Laboratory powder X-ray diffraction (XRD) employs monochromatic X-ray radiation of a wavelength similar to the inter-lattice spacing (typically ~1–2 Å), which arises from irradiation of a metallic target anode (commonly Cu) by thermionically emitted electrons. Diffraction experiments on a powder consisting of sufficiently small crystallites (smaller than ~10 μm) will lead to the observation of all allowed Bragg reflections and thus permit structural refinement of the unit cell parameters and atomic coordinates. However, because the X-ray scattering factor is approximately proportional to the atomic number of the scattering atom, it is typically possible to accurately refine only the positions and occupancies of the heavier atoms (*e.g.*, transition metal sites). More powerful techniques, such as powder neutron diffraction, are usually required to obtain structural information about lighter atoms such as oxygen. Nonetheless, laboratory XRD offers convenient non-destructive analysis of small quantities of powdered samples within a reasonably short timescale of minutes to hours, and is employed in this work primarily to check sample purity and follow substitution-induced changes in unit cell parameters and bond lengths.

## 2.4 Thermogravimetric analysis (TGA)

In thermogravimetric analysis (TGA), highly accurate mass measurements of a sample are recorded as a function of increasing temperature, using a thermobalance comprising a sensitive cantilever beam balance in an enclosed furnace. A small amount of sample (on the order of 10–50 mg) is placed in a refractory crucible and typically heated to a maximum temperature of 1000 °C under optional atmosphere control. Chemical phenomena that can be studied by TGA experiments include decomposition, oxidative combustion, and both solid-state and solid–gas reactions (*e.g.*, chemical looping).[217–220] The data commonly take the form of plateaus of constant mass punctuated by reaction processes at characteristic temperatures

that induce mass increases or decreases. Additionally, if the mass changes are well-separated and correspond to discrete reactions within the sample, kinetic parameters can be extracted using the formalism first derived by Coats and Redfern.[221,222] In this work, TGA is used under reducing conditions (5% $H_2$ in $N_2$) to promote the decomposition of oxygen hyperstoichiometric materials. Assuming that removal of oxygen from these phases occurs in discrete, well-resolved steps, the degree of hyperstoichiometry can then be calculated.[223]

## 2.5 X-ray absorption near edge structure (XANES) spectroscopy

X-ray absorption near-edge structure (XANES) spectroscopy is a local structure technique considered complementary to solid-state NMR spectroscopy, as the former can provide structural details of sites, *e.g.* paramagnetic transition metals, which remain insensitive or inaccessible by the latter technique. As with solid-state NMR, XANES is sensitive to local coordination environments, but unlike NMR, XANES can also determine the oxidation state(s) of the element of interest within the sample.[224,225] In a typical XANES experiment, resonant electronic transitions are excited with synchrotron X-ray radiation, according to the angular momentum selection rule $\Delta l = \pm 1$. In the Ni K-edge spectra presented in this thesis, this corresponds to a primary transition from a core Ni 1*s* orbital to an empty Ni 4*p* orbital. A large increase in the absorption coefficient occurs as the incoming photon energy exceeds the electronic binding energy. The energy of this absorption edge is sensitive to the electronic density of the ground state, and thus the position of this edge is diagnostic for the oxidation state. That is, as the oxidation state of the element increases, electrons around the nucleus are stabilized to a greater extent, which increases the energy required to promote core electrons.[226]

Pre-edge features at slightly lower energy with respect to the absorption edge are sometimes observed, particularly for transition metals. These correspond to formally forbidden *s* to *d* orbital transitions ($\Delta l = \pm 2$) that nonetheless arise due to mixing (hybridization) of unoccupied $p$ states in locally distorted, non-centrosymmetric environments. Thus, the

intensity of pre-edge features in transition metal XANES spectra is characteristic of the deviation of local symmetry away from ideal octahedral coordination.[226,227]

Samples studied by XANES in this work were intimately mixed with cellulose and pressed into 8 mm pellets for transmission experiments at room temperature on beamline B18 at the Diamond Light Source; data were collected by Dr Michael Gaultois (University of Cambridge).

## 2.6 Aims and outline of this thesis

The primary aim of this thesis is to develop and apply an $^{17}O$ NMR spectroscopic approach to study the local structure and oxide-ion dynamics of SOFC electrodes and electrolytes. In particular, its goals are to:

- Develop new experimental methodologies for acquiring and interpreting highly broadened, so-called wideline NMR spectra predominantly influenced by large hyperfine and/or quadrupolar interactions.
- Extend the previous theoretical methodology of Kim *et al.*[89] (*J. Am. Chem. Soc.* **2010**, *132*, 16825) for calculating Fermi contact shifts in paramagnetic materials to $^{17}O$ solid-state NMR spectroscopy of paramagnetic oxides, where the hyperfine interactions are expected to be even more pronounced due to direct bonding of oxygen to the transition metal sites.
- Investigate oxide-ion dynamics using $^{17}O$ solid-state NMR at variable temperatures relevant for SOFC operation (as well as coupled dynamics arising from other NMR-active nuclei, where applicable) and relate these to detailed mechanistic descriptions of local motion and exchange in oxide-ion conductors.
- Explore the extent to which the sensitivity of the hyperfine interaction in $^{17}O$ solid-state NMR spectra of functional paramagnetic oxides is sufficient to elucidate subtle structural distortions, as well as changes in the transition metal electronic structure.

Where appropriate, the $^{17}O$ NMR data are also interpreted with reference to results from complementary methods such as powder XRD, TGA, and XANES to obtain a more complete picture of the structure and composition of the oxide-ion conducting phases of interest.

In Chapter 3, an initial $^{17}O$ solid-state NMR study of the MIEC and SOFC cathode material $La_2NiO_{4+\delta}$ is performed. This work constitutes the first application of $^{17}O$ MAS NMR spectroscopy to a *paramagnetic* oxide-ion conductor, which requires specific $^{17}O$-enrichment and spectral acquisition procedures that are described therein. Assignment of the NMR spectra is aided by first-principles DFT calculations, which in turn suggest the potential of more advanced (*e.g.*, MATPASS) NMR experiments. The MATPASS spectra provide insight into local structural distortions surrounding the axial oxygen sites in this material. Variable-temperature NMR experiments (up to 140 °C) are also performed with the goal of developing a model describing the oxide-ion dynamics that accounts for the motion and exchange of all distinct oxygen sites.

This work in Chapter 3 is extended in Chapter 4 to a thorough investigation of the related $La_{2-x}Sr_xNiO_{4+\delta}$ phases ($0 < x \leq 1$) which are also MIEC SOFC cathode materials with improved electronic conductivity. Using the spectral assignment rationalized in Chapter 3, the evolution of the $^{17}O$ NMR spectra with increasing Sr incorporation is used to probe changes in the defect chemistry, *i.e.*, removal of interstitial defects and oxidation of Ni, and these results are linked to known changes in the ionic and electronic conductivity. The findings are further corroborated by Ni K-edge XANES spectroscopy as well as changes in the powder XRD patterns.

In Chapter 6, the focus of the thesis shifts from SOFC electrode materials to electrolytes, wherein a multinuclear variable-temperature MAS NMR study of the pseudo-cubic, fluorite-type phases $Bi_{1-x}V_xO_{1.5+x}$ and $Bi_{1-x}P_xO_{1.5+x}$ ($x$ = 0.087 or 0.148) is performed. By following ionic motion on the spectral timescale, a comparative analysis of the oxide-ion conduction mechanism(s) of these phases at temperatures up to 600 °C reveals differences in the oxide-ion exchange between the host and dopant sublattices, explaining the previously reported experimental variation in conductivity values. Additionally, $^{17}O$ $T_1$ (spin-lattice) relaxation data are recorded and analyzed so as to probe much faster oxide-ion motion, and activation energies for various types of oxide-ion motion are extracted. The study concludes by

suggesting principles for choosing optimal dopants to stabilize the $\delta$-$Bi_2O_3$ structure while minimizing the adverse impact on the oxide-ion conductivity.

# Chapter 3 Probing Oxide-ion Mobility in the Mixed Ionic–Electronic Conductor $La_2NiO_{4+\delta}$ by Solid-State $^{17}O$ MAS NMR Spectroscopy

## 3.1 Abstract

While solid-state NMR spectroscopic techniques have helped clarify the local structure and dynamics of ionic conductors, similar studies of mixed ionic–electronic conductors (MIECs) have been hampered by the paramagnetic behavior of these systems. Here we report high-resolution $^{17}O$ ($I$ = 5/2) solid-state NMR spectra of the mixed-conducting solid oxide fuel cell (SOFC) cathode material $La_2NiO_{4+\delta}$, a paramagnetic transition-metal oxide. Three distinct oxygen environments (equatorial, axial, and interstitial) can be assigned on the basis of hyperfine (Fermi contact) shifts and quadrupolar nutation behavior, aided by results from periodic DFT calculations. Distinct structural distortions amongst the axial sites, arising from the non-stoichiometric incorporation of interstitial oxygen, can be resolved by advanced magic-angle turning and phase-adjusted sideband separation (MATPASS) NMR experiments. Finally, variable-temperature spectra reveal the onset of rapid interstitial oxide motion and exchange with axial sites at ~130°C, associated with the reported orthorhombic-to-tetragonal phase transition of $La_2NiO_{4+\delta}$. From the variable-temperature spectra, we develop a model of oxide-ion dynamics on the spectral timescale that accounts for motional differences of all distinct oxygen sites. Though we treat $La_2NiO_{4+\delta}$ as a model system for a combined paramagnetic $^{17}O$ NMR and DFT methodology, the approach presented herein should prove applicable to MIECs and other functionally important paramagnetic oxides.

## 3.2 Introduction

Mixed ionic and electronic conducting (MIEC) ceramics have shown promise in recent years as oxygen-transport membranes in solid oxide fuel cells (SOFCs) and for chemical looping applications.[228–234] The use of mixed conductors, primarily perovskite-type oxides, as SOFC cathodes has been shown to improve oxygen reduction kinetics and thus enable device operation at lower temperatures.[26,235] Typically, the advanced functionality of these mixed-conducting systems derives from the mutual influence of metal cation mixed valency and oxygen non-stoichiometry.[236] While the latter property, manifesting as oxygen vacancies or interstitials, has been directly implicated in the bulk performance of MIECs, the mechanistic origins of oxide-ion conductivity often remain unclear at the atomic level. Atomistic simulations have provided insight into underlying interstitial– and vacancy–mediated contributions to ionic conductivity,[237] but direct experimental confirmation of these details of ionic motion remains a challenge.

Unlike conventional diffraction-based methods sensitive to long-range order, solid-state NMR spectroscopy can provide insight into local, atomic-scale distortions in solids, with direct relevance to ionic conduction.[238–241] Moreover, exchange rates and activation energies for thermally-activated transport processes can be derived from NMR spectra acquired at variable temperature (VT-NMR). Grey and coworkers[242–247] and others[134,168,248–254] have shown that solid-state $^{17}$O VT-NMR in particular can enable detailed mechanistic studies of fast oxide-ion conductors, subject to successful enrichment[213,255] of samples with $^{17}$O (natural abundance 0.037%). Moreover, as a spin-5/2 nucleus with moderate electric quadrupole moment, $^{17}$O is sensitive to electric field gradients (EFGs) generated by local charge and bonding asymmetry, as quantified through site-specific quadrupole coupling constants ($C_Q$). This quadrupolar interaction can further discriminate amongst different coordination environments in diamagnetic oxides.[130]

Similar $^{17}$O NMR studies of *paramagnetic* oxides such as MIECs, however, have met with comparatively limited success.[256] In paramagnetic materials, electron–nuclear spin interactions lead to large Fermi contact (hyperfine) shifts and anisotropic dipolar broadening that complicate spectral detection, resolution and assignment. Previous reports have generally

been confined to single crystal samples, with spectra often recorded at cryogenic temperatures.[257–259] In a significant advance by Kong *et al*., the first $^{17}O$ magic-angle spinning (MAS) NMR spectra of paramagnetic transition metal complexes have been recorded and assigned.[203] In this chapter, we extend paramagnetic $^{17}O$ MAS NMR to perform advanced pulse sequence techniques and variable-temperature measurements on a model MIEC, $La_2NiO_{4+\delta}$, to explore the structural and mechanistic details of the oxide-ion transport in this material.

As described in Section 1.2, $La_2NiO_{4+\delta}$, a perovskite-derived $K_2NiF_4$-type mixed ionic–electronic conductor, shows high oxygen transport across a large temperature range and is an important candidate SOFC cathode material.[260] With both paramagnetic (axial $O_{ax}$, equatorial $O_{eq}$) and diamagnetic (interstitial $O_i$) oxygen sites, the system is an elegant model for initial $^{17}O$ MAS NMR studies of MIECs. (By a "paramagnetic" or "diamagnetic" site, we here refer to the presence or absence, respectively, of electron spin-bearing cations such as $Ni^{2+}$ in the local (first shell) oxygen coordination environment.)

Structurally, $La_2NiO_{4+\delta}$ is a member of the Ruddlesden-Popper family and consists of alternating $LaNiO_3$ perovskite-like layers and "$La_2O_2$" rocksalt-like layers in an offset *ABA′B′* arrangement (Figure 1.3 and Figure 3.1a). Equatorial oxygen sites lie within the perovskite plane; axial sites bridge the layers. Incorporation of interstitial oxygen within the rocksalt layers is remarkably facile, and affords a considerable range of oxygen hyperstoichiometry ($\delta$), reported from $\delta = 0$ to ~0.3, with $\delta > 0.15$ for SOFC applications.[54,261] Structural and magnetic properties are very sensitive to oxygen excess.[40,41] In this work, therefore, we consider only the highly hyperstoichiometric phases most relevant for fast oxide-ion conduction in SOFC cathodes. We first show that incorporation of interstitial oxygen leads to distinct and well-resolved displacement of axial oxygen sites, and paramagnetic $^{17}O$ NMR is uniquely sensitive to these local structural distortions. Results from periodic density-functional theory (DFT) calculations are integral in the interpretation of the $^{17}O$ NMR spectra; the axial distortion leads to a splitting of calculated hyperfine shifts, as observed experimentally, and calculated $C_Q$ values corroborate assignment of the $O_{eq}$ and $O_{ax}$ sites.

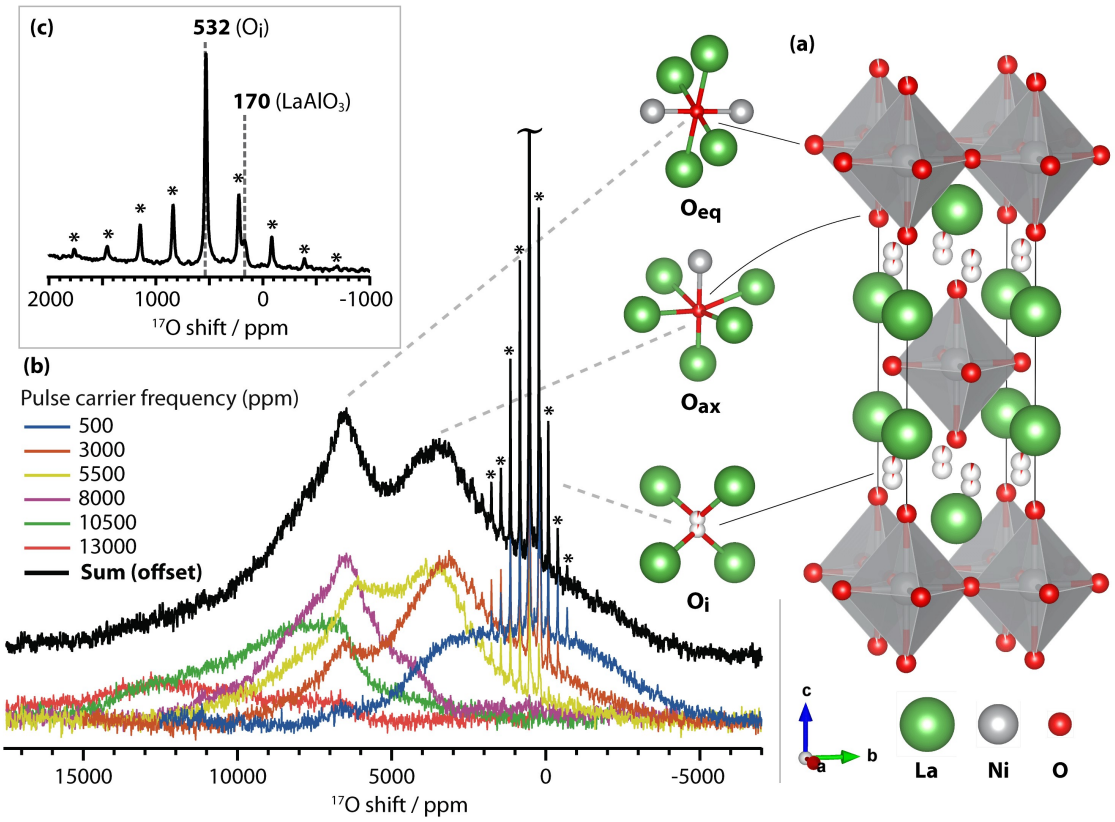


Figure 3.1: Room-temperature $^{17}$O MAS NMR spectrum of $La_2NiO_{4+\delta}$ with proposed assignments. (a) Crystal structure of the high-temperature tetragonal (space group *I4/mmm*) phase of $La_2NiO_{4.17}$ as reported by Skinner *et al.*[54] Partially occupied sites ($O_{ax}$, $O_i$) are depicted as partially filled spheres. The structure of the high-temperature tetragonal phase, rather than the low-temperature orthorhombic phase, is depicted to more clearly illustrate the three distinct types of local O environments (given that some O positions are split in the orthorhombic structure). (b) Individual sub-spectra collected at different offset frequencies (colored) summed to give the broadband spin-echo mapping spectrum (black). Proposed assignments depict the local geometry about each oxygen environment (equatorial $O_{eq}$, axial $O_{ax}$, and interstitial $O_i$). A rotor-synchronized Hahn echo pulse sequence ($\pi/6$ - $\tau$ - $\pi/3$ - $\tau$ - acquire) was used for each sub-spectrum. Spectra were collected at 7.05 T at a MAS rate of 12.5 kHz, with 120,000 scans per sub-spectrum and a recycle delay of 0.5 s. Asterisks denote spinning sidebands. (c) Inset showing the "diamagnetic region" of the summed spin-echo mapping spectrum in (b). Features at 532 ppm and 170 ppm are assigned to interstitial oxygen ($O_i$) in $La_2NiO_{4+\delta}$, and a $LaAlO_3$ impurity phase, respectively. (The $LaAlO_3$ phase arises from reaction with Al-containing media.) Asterisks denote spinning sidebands.

We next perform variable-temperature NMR to probe oxide-ion dynamics associated with the orthorhombic-to-tetragonal phase transition of $La_2NiO_{4+\delta}$ reported near 150 °C. At the composition $\delta$ = 0.3, Aguadero *et al.* have reported the phase transition temperature

$T_p$ = 132°C.[65] We argue that this transition is directly correlated with the onset of rapid interstitial motion between 110 °C and 130 °C, a process for which we extract an activation energy $E_a$ = 0.59 ± 0.07 eV. In particular, fast exchange between interstitial and axial oxygen sites, as in the hypothesized interstitialcy mechanism of Chroneos *et al.*,[71] occurs simultaneously with the abrupt disappearance of the aforementioned local distortion. This in turn induces the disruption of the cooperative tilting of perovskite layers responsible for the long-range orthorhombic (*Fmmm*) distortion, incoherently averaging the structure to the tetragonal (*I*4/*mmm*) phase. The proposed model of oxide-ion dynamics at these temperatures involves two coupled motional processes, 1) exchange between interstitial and axial sites, and 2) "rocking" of $NiO_6$ octahedra dynamically altering the displacement of axial and equatorial sites that together determine the observed $^{17}O$ VT-NMR lineshapes. In summary, we report the first $^{17}O$ MAS solid-state VT-NMR spectra of a paramagnetic oxide-ion conductor, with DFT-aided assignment of the local structure and oxide-ion dynamics, which should ultimately enable future studies of functionally relevant paramagnetic oxides by similar methods.

## 3.3 Experimental and theoretical methods

### 3.3.1 Synthesis, $^{17}O$-enrichment and characterization

Samples of $La_2NiO_{4+\delta}$ were prepared by a solid-state reaction route as described previously.[262–264] Stoichiometric amounts of $La_2O_3$ (Alfa Aesar, REacton, 99.999%; pre-dried) and NiO (Aldrich, 99.999%) were mixed in a mortar and pestle, pressed isostatically, sintered in air at 1300 °C for 6–12 h, and ground into powder. Multiple intermediate sintering and grinding steps were repeated until phase purity was achieved, as determined by laboratory powder X-ray diffraction (Figure 3.2).

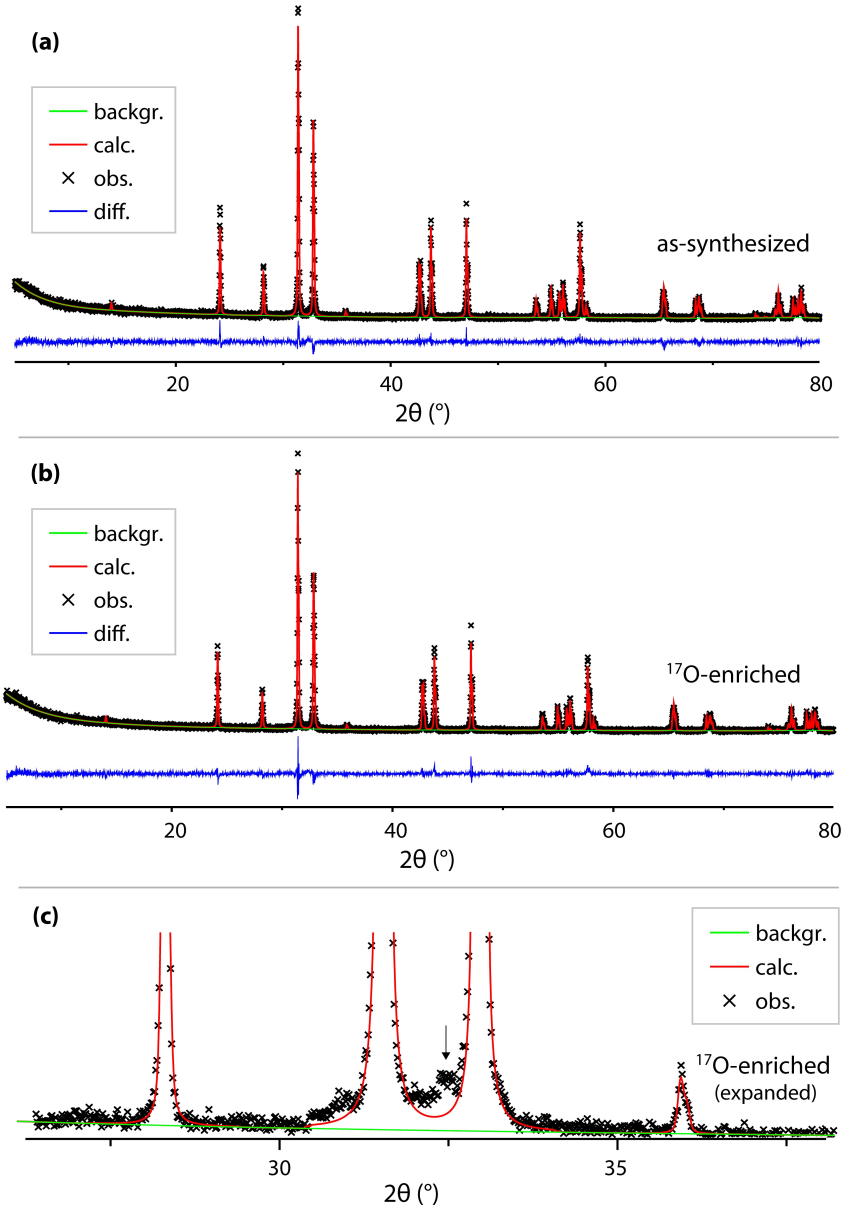


Figure 3.2: Powder XRD characterization of $La_2NiO_{4+\delta}$ samples. XRD patterns and Rietveld refinements of (a) as-synthesized and (b) $^{17}O$-enriched $La_2NiO_{4+\delta}$. All patterns were refined to the low-temperature orthorhombic (*Fmmm*) structure of $La_2NiO_{4.17}$ in the ICSD (no. 98557). For this sample, refined lattice parameters were $a$ = 5.460(8) Å, $b$ = 5.464(6) Å, and c = 12.684(1) Å after synthesis and $a$ = 5.458(8) Å, $b$ = 5.465(0) Å, and c = 12.686(9) Å following $^{17}O$-enrichment. (c) Expanded view of the XRD pattern of the $^{17}O$-enriched sample highlighting the presence of an impurity phase. The feature at 2θ = 32.4° (arrow) is consistent with the (117) reflection of $La_4Ni_3O_{10}$ (ICSD no. 80279). The fraction of $La_4Ni_3O_{10}$ was estimated to be ~3 wt. %. (The proportion of the $LaAlO_3$ impurity phase was estimated at <1 mol % by NMR, below the XRD detection limit.)

Samples were also prepared *via* a modified sol-gel (Pechini) method similar to that previously reported.[265] Stoichiometric amounts of $La(NO_3)_3 \cdot 6H_2O$ (Alfa Aesar, REacton, 99.999%) and $Ni(NO_3)_2 \cdot 6H_2O$ (Aldrich, 99.999%) were dissolved in an aqueous solution of polyvinyl alcohol (15% w/v; Merck, $M_W$ = 60,000), with a mole ratio of metal cations to hydroxyl groups in polyvinyl alcohol of approximately 1:3. Continuous heating at 100 °C produced a viscous green xerogel which was subsequently heated to autoignition at 400 °C. The resulting off-black powder was pressed isostatically and sintered in air at 1300 °C for 12 h. Sol-gel–synthesized samples did not differ appreciably in phase purity or excess oxygen content from samples obtained *via* the solid-state reaction route.

Samples of $^{17}O$-enriched $La_2NiO_{4+\delta}$ were obtained by heating the as-synthesized powder (0.1–0.3 g) to 1000 °C under an atmosphere of 70% $^{17}O_2$ (Cambridge Isotope Labs, used as received) in a sealed quartz tube for 24 h. Samples were slowly cooled (1 °C $min^{-1}$) from the enrichment temperature to maximize uptake of $^{17}O$. Given the relative quantities of sample and $^{17}O_2$ gas, the maximum $^{17}O$ enrichment level in the sample was estimated to be ~30%.

Phase purity of all samples was determined with powder X-ray diffraction (XRD) using a Panalytical Empyrean X-ray diffractometer equipped with a Cu Kα source (λ = 1.5406 Å and 1.5418 Å) and X'celerator CCD detector. Scans were performed on a spinning sample stage in reflection mode over the range 2θ = 5° to 80° (step size 2θ = 0.0167°). Diffraction patterns were analyzed with the X'Pert HighScore Plus software package and PDF pattern database, and Rietveld refinements were performed with the GSAS and EXPGUI software packages.[266,267]

Oxygen excess ($\delta$) in $La_2NiO_{4+\delta}$ was determined *via* thermogravimetric analysis (TGA) performed with a Mettler Toledo TGA/SDTA 851 thermobalance. Powder samples of 20–40 mg were placed in a 100 μL $Al_2O_3$ crucible and heated to 900 °C (at 3 °C $min^{-1}$) under a reducing atmosphere of 5% $H_2$ in $N_2$ (50 mL $min^{-1}$). Raw mass data collected during the heating profile were corrected from blank experiments and smoothed subject to a local regression (LOESS) algorithm. Sample non-stoichiometry was calculated as the ratio of mass losses during the two discrete reduction steps (Figure 3.3), where we assumed these mass losses correspond to the reactions

$$La_2NiO_{4+\delta} + \delta\ H_2 \rightarrow La_2NiO_4 + \delta\ H_2O \quad (3.1)$$

$$La_2NiO_4 + H_2 \rightarrow La_2O_3 + Ni + H_2O \quad (3.2)$$

which were driven to completion given the gas flow conditions.[268]

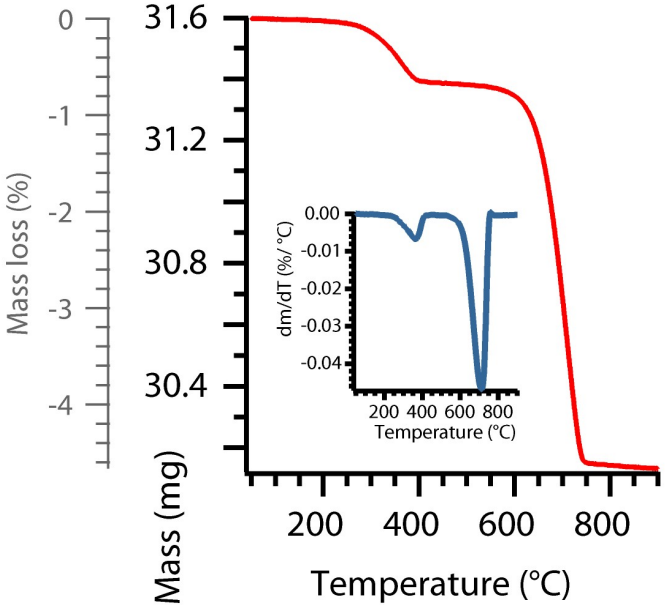


Figure 3.3: Representative TGA and DTG curves (under 5% $H_2$ in $N_2$) of $La_2NiO_{4+\delta}$. Thermogravimetric analysis (TGA) data for as-synthesized $La_2NiO_{4+\delta}$ reveal two reduction steps corresponding to the reactions given in Equations (3.1) and (3.2). The differential thermogravimetry (DTG) trace (inset), the numerical first derivative of the TGA data, was used to determine the flattest region of each plateau from which each mass loss was determined. Here the mass losses for the two reduction steps were 0.67% and 4.59%, yielding a calculated oxygen excess of $\delta = 0.15$.

### 3.3.2 Solid-state NMR spectroscopy

Solid-state $^{17}O$ MAS NMR experiments were carried out on 7.05 T Bruker Avance II and Avance III 300 MHz spectrometers using a Bruker 4 mm HX probe; a 4.7 T Bruker Avance III 200 MHz using a Bruker 1.9 mm HX probe; and a 16.4 T Bruker Avance III 700 MHz spectrometer using a Bruker 4 mm X probe. Experimental parameters for all NMR data are summarized below.

Spin-echo mapping experiments (as described in Section 2.1.2.1) were performed at 7.05 T under a MAS frequency of 12.5 kHz using a rotor-synchronized Hahn echo pulse sequence of

the form $(\pi/6)_x$–τ–$(\pi/3)_y$–τ–acquire with a pulse length of 1.67 μs (π/6 for liquid $H_2O$) at an inherent rf field strength of ~50 kHz and a quantitative recycle delay of 0.5 s. Similar experiments at 4.7 T were carried out at a MAS frequency of 40 kHz using a pulse length of 0.75 μs (π/6 for liquid $H_2O$) at an inherent rf field strength of ~111 kHz, and a recycle delay of 20 ms. The pulse carrier frequency step size was 2500 ppm (~102 kHz at 7.05 T, ~68 kHz at 4.7 T), *i.e.* smaller than the rf field strength, and a total of six sub-spectra were acquired at 500, 3000, 5500, 8000, 10500, and 13000 ppm. Further spin-echo mapping experiments at 4.7 T employed longer pulse lengths of 2.2 μs (π/2 for liquid $H_2O$) at an inherent rf field strength of ~114 kHz, with identical pulse carrier frequency offsets. Finally, all other experiments not employing spin-echo mapping for broadband excitation (i.e. MATPASS or variable temperature measurements) fixed the pulse carrier frequency offset at 3000 ppm (at 7.05 T and 4.7 T) or 500 ppm (at 16.4 T). Standard saturation-recovery experiments (at 7.05 T) were used to obtain $T_1$ values.

Projection magic-angle turning and phase adjusted sideband separation (MATPASS) NMR experiments[153] (as described in Section 2.1.2.2) were performed at 4.7 T and were rotor-synchronized at a MAS rate of 40 kHz. A series of five $\pi/6$ (or $\pi/2$) pulses with pulse lengths of 0.73 μs (or 2.2 μs) were employed. A total of eight $t_1$ increments were recorded in each experiment. The recycle delay was 50 ms.

Temperature calibration of the probes was performed in separate one-pulse MAS experiments at 7.05 T and 16.4 T using the $^{207}Pb$ resonance of $Pb(NO_3)_2$, with an accuracy of ±5 °C.[269,270] All $^{17}O$ NMR spectra were collected on recently $^{17}O$-enriched samples packed in $ZrO_2$ rotors with Kel-F or $ZrO_2$ caps (for room temperature and variable temperature experiments, respectively). $^{17}O$ chemical shifts were externally referenced to $H_2O$ at 0.0 ppm at room temperature. NMR spectra were processed and deconvoluted with the Bruker Topspin 3.2[271] and dmfit[272] software packages.

### 3.3.3 First-principles calculations

Calculations were performed with the **CRYSTAL09** linear combinations of atomic orbitals (LCAO) code[200] using the B3LYP spin-polarized hybrid exchange-correlation functional. In a two-step approach as described in Section 2.2.2, initial experimental structures were first

geometry optimized with respect to lattice parameters and atomic positions using a more limited basis set (denoted BS-I). Next, single-point energy calculations were performed with an extended basis set (BS-II) to model the core region more accurately. Relevant NMR parameters (spin density at the nuclear positions, electron-nuclear dipolar tensors, and quadrupolar coupling constants) were computed after convergence of the wavefunction in the second step. The smaller basis set BS-I was derived from the **CRYSTAL** online basis set repository and used for structural optimizations, band structure calculations and density of states plots. Atomic species were represented in BS-I as (30s21p10d)/[1s6sp3d] for La, (20s12p5d)/[1s4sp2d] for Ni, and (14s6p1d)/[1s3sp1d] for O, with the number of Gaussian primitives given in parentheses and the contraction scheme in square brackets. Hyperfine properties and quadrupolar coupling constants were computed from single-point energy calculations with the larger basis set BS-II, wherein (13s9p5d)/[7s5p3d] and (10s6p2d)/[6s5p2d] sets were adopted for Ni and O, respectively; the La basis set was the same as for BS-I. Initial exponents and coefficients were derived from IGLO-III (O) and DZP (Ni) basis sets as used previously.[89] Prior to use of BS-II, the most diffuse exponents in the basis set for each atomic species were first energy-optimized in the simpler NOI system (see below) using a numerical conjugate method implemented through the LoptCG script included with the **CRYSTAL** code. For all calculations, truncation thresholds of $10^{-7}$, $10^{-7}$, $10^{-7}$, $10^{-7}$, and $10^{-14}$ were applied to the integral series for Coulomb overlap, Coulomb penetration, exchange overlap, g- and n-exchange penetration, respectively.

Two classes of supercells, denoted NOI and LNO, were constructed and optimized. NOI ("no interstitials") was derived from the experimental high-temperature tetragonal (*I4/mmm*) structure of stoichiometric $La_2NiO_4$ and converted to a primitive triclinic 7-atom cell with isotropic lattice parameters of ~6.96 Å. For LNO, the experimental room-temperature orthorhombic (*Fmmm*) structure of $La_2NiO_{4+\delta}$ ($\delta = 0.17$)[54] was used to construct a 2×2×2 57-atom supercell ($La_{16}Ni_8O_{33}$) corresponding to $\delta = 0.125$. The supercell was tetragonal due to expansion of the orthorhombic structure by $\sqrt{2}$ along new axes equivalent to $[110]_{Fmmm}$ and $[1\bar{1}0]_{Fmmm}$. The supercells are depicted in Figure 3.4. Different initial $Ni^{3+}/Ni^{2+}$ configurations were explored with only minimal changes in the final optimized geometry, electronic structure, and computed properties. $Ni^{3+}$ ions ($d^7$) were initialized in the low-spin

configuration ($t_{2g}^6 e_g^1$, $S = ½$), as suggested by experimental evidence;[273] calculations failed to converge in the high-spin configuration. Full structural optimizations of atomic positions and lattice parameters were performed without symmetry constraints, with convergence tolerances on the SCF cycle total energy, root-mean-square (rms) gradient, and rms displacement of $10^{-7}$ au, 0.0003 au $Å^{-1}$, and 0.0012 Å, respectively. As a consequence of lattice anisotropy, reciprocal space sampling employed a compressed 3×3×2 Monkhorst-Pack k-point mesh.

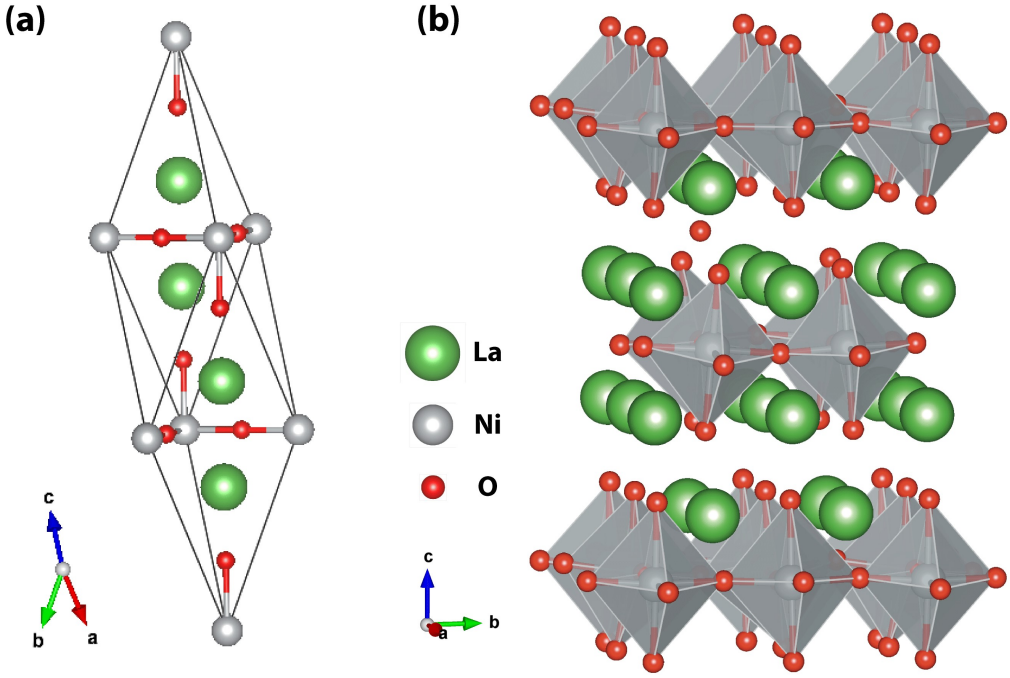


Figure 3.4: Depictions of DFT-optimized supercells (a) "NOI" ($La_2NiO_4$) and (b) "LNO" ($La_{16}Ni_8O_{33}$). In (b), atoms outside the supercell boundaries have been shown in order to clearly depict the rocksalt and perovskite layers. The interstitial oxygen in the LNO supercell is visible in the upper rocksalt layer, with induced displacements of nearby $NiO_6$ octahedra.

Two types of NMR parameters were extracted from the calculations: 1) quadrupolar coupling constants (and associated asymmetry parameters) and 2) hyperfine shifts for all oxygen sites. Quadrupolar coupling constants $C_Q = eQV_{ZZ} / h$ and asymmetry parameters $\eta_Q = \frac{V_{YY} - V_{XX}}{V_{ZZ}}$ were determined from the principal components of the calculated electric field gradient (EFG) tensor, ordered such that $|V_{ZZ}| \geq |V_{XX}| \geq |V_{YY}|$, where $Q$ is the nuclear quadrupole moment (-25.58 mbarn for $^{17}O$, as experimentally determined[274]). Values of the electron spin

density at the oxygen nuclear positions were converted to hyperfine (Fermi contact) $^{17}O$ NMR shifts using the theoretical methodology detailed in Section 2.2.3.1.[89,202] In brief, calculations were first performed in the ferromagnetic state by "locking" the alignment of the Ni spins, and then the system was allowed to relax in the absence of spin constraints to a ferromagnetic local minimum. Spin density values obtained from the relaxed system were then scaled to the paramagnetic regime at the temperature of the NMR experiment assuming ideal Curie–Weiss behavior. Experimental values of $\mu_{eff}$ = 2.56 $\mu_B$ and $\Theta \approx -400$ K were used, as previously reported for $La_2NiO_{4+\delta}$.[78,88]

## 3.4 Results

### 3.4.1 Characterization of $La_2NiO_{4+\delta}$ by XRD and TGA

Owing to the wide range of oxygen nonstoichiometry reported for this system, samples have been carefully characterized by XRD and TGA. Calculated values of $\delta$ from TGA measurements were found to range from $\delta$ = 0.12 to 0.17 (Figure 3.3). The oxygen content is slightly affected by the $^{17}O$-enrichment procedure, increasing from $\delta$ = 0.13 ± 0.01 for as-synthesized batches to $\delta$ = 0.16 ± 0.01 following $^{17}O$-enrichment. This work concurs with previous findings: treatment of $La_2NiO_{4+\delta}$ under high oxygen pressure leads to even more highly nonstoichiometric samples with $\delta$ as large as 0.3.[63]

As-synthesized samples are found to be phase-pure by XRD (Figure 3.2). Laboratory XRD data are not sufficiently sensitive to the lighter O atoms to permit refinement of low-occupancy interstitial sites. Nonetheless, changes in the lattice parameters (as refined to the room-temperature *Fmmm* structure) mirror differences in oxygen content, as previously shown.[76,261,263,275] Here, incorporation of additional interstitial oxygen in the $^{17}O$-enriched samples leads to expansion of the lattice along *c*, with concomitant decrease of the *a* and *b* lattice parameters (Figure 3.5). The refined lattice parameters for the $^{17}O$-enriched samples are in good agreement with Skinner[54] and also Aguadero *et al.*[63,65] at similar levels of oxygen excess (that is, similar values of $\delta$) determined by TGA.

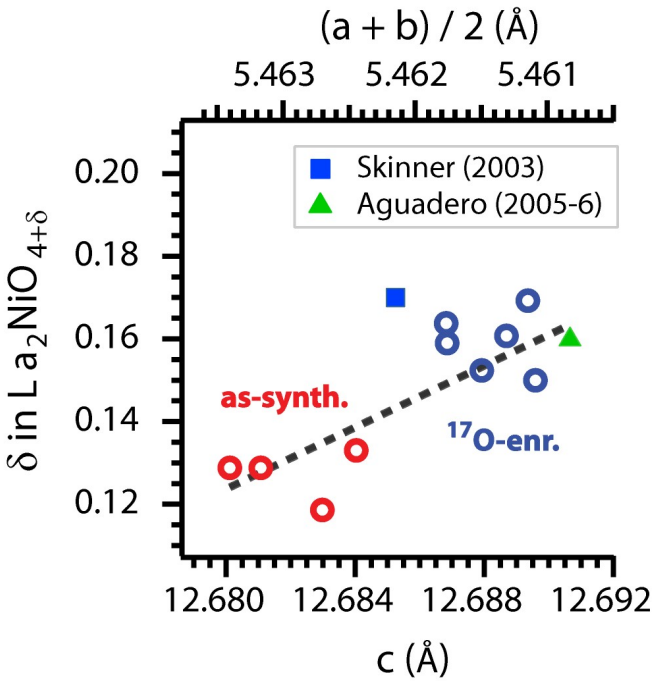


Figure 3.5: Correlation between oxygen excess ($\delta$) and refined lattice parameters. As-synthesized samples (red) show smaller *c* lattice parameters and larger *a* and *b* lattice parameters as determined from refinements of XRD patterns, correlating with a smaller oxygen excess ($\delta$ = 0.13 ± 0.01) as determined by TGA. After $^{17}$O-enrichment of several batches of samples (blue), the lattice expands along *c*, with concomitant decrease of the *a* and *b* lattice parameters and an increase in the oxygen hyperstoichiometry ($\delta$ = 0.16 ± 0.01). The grey best-fit line traces the correlation. (Excellent correlation between the *c* lattice parameter and the average of the *a* and *b* lattice parameters allows for plotting both values along the same dimension.) The refined lattice parameters and oxygen excess values are in reasonable agreement with the literature.[54,63,65]

Following $^{17}$O-enrichment, a weak, broad feature is observed in the XRD pattern, which is consistent with the (117) reflection of $La_4Ni_3O_{10}$ (Figure 3.2), suggesting that the $La_4Ni_3O_{10}$ impurity phase (estimated at ~3 wt. %) forms during the enrichment step. Aguadero *et al*. and Sayers *et al*. also note the decomposition of $La_2NiO_{4+\delta}$ into the higher-order Ruddlesden-Popper phases $La_3Ni_2O_7$ and $La_4Ni_3O_{10}$ at high temperature and under highly oxidizing conditions.[63,276] In this case, these phases are difficult to distinguish from $La_2NiO_{4+\delta}$ (and from each other) due to the small phase fractions and considerable overlap of XRD reflections (Figure 3.2c). We turn to NMR as a more sensitive probe of the minor impurity phases as well as the local structure of the low-occupancy interstitial sites of $La_2NiO_{4+\delta}$.

### 3.4.2 Room temperature NMR

#### 3.4.2.1 Acquisition of broadband spectra

Initial $^{17}O$ MAS NMR spectra of the enriched samples (Figure 3.1b) reveal an extremely broad set of features spanning more than 0.5 MHz at 7.05 T, exceeding the excitation bandwidth of a single rf pulse, a direct consequence of the paramagnetism of $La_2NiO_{4+\delta}$. As described in Section 2.1.2.1, acquiring the complete broadband spectrum necessitates the use of "spin-echo mapping" or "variable offset cumulative spectroscopy" (VOCS)[142] here performed by collecting and summing six sub-spectra (colored traces, Figure 3.2b) with progressively larger rf carrier frequency offsets (step size equal to 2500 ppm or ~102 kHz). Pell *et al*. have shown that, for non-quadrupolar nuclei, spin-echo mapping under MAS achieves nearly uniform broadband excitation,[145] but no work to date has demonstrated the validity of the technique for quadrupolar nuclei such as $^{17}O$. Given the significant width of the major features in these spectra, however, any lineshape distortions are likely insignificant, and the use of a short, non-selective rf pulse ensures quantitative excitation that is independent of $C_Q$. As seen in Figure 3.1b, the spin-echo mapped spectrum (black) comprises two very broad components centered at ~6500 ppm and ~3500 ppm, and a narrow peak at 532 ppm with associated spinning sideband (ssb) manifold. A minor component appears at 170 ppm (Figure 3.1c), but its intensity is sample-dependent (Figure 3.6).

#### 3.4.2.2 Peak assignments

The resonances at 532 and 170 ppm fall within the 0–1000 ppm region occupied by shifts of diamagnetic oxides. Yang *et al*.[277] have reported a $^{17}O$ shift of the tetrahedral oxygen site in hexagonal $La_2O_3$ of 584 ppm. Given the known[47] pseudo-tetrahedral coordination of interstitial oxygen ($O_i$) in $La_2NiO_{4+\delta}$ (Figure 3.1a, bottom right), we, therefore, assign the 532 ppm feature to the interstitial oxygen environment in $La_2NiO_{4+\delta}$. We also assign the sample-dependent 170 ppm resonance to a very minor $LaAlO_3$ impurity phase (as previously reported by Bastow *et al.*[278]) formed during synthesis (in an alumina crucible) but not immediately apparent in the XRD data. (Conversely, the $La_4Ni_3O_{10}$ impurity seen by XRD is not observed

in the initial NMR experiments, but is later resolved in later high-temperature spectra as a minor feature at ~2400 ppm (see below).)

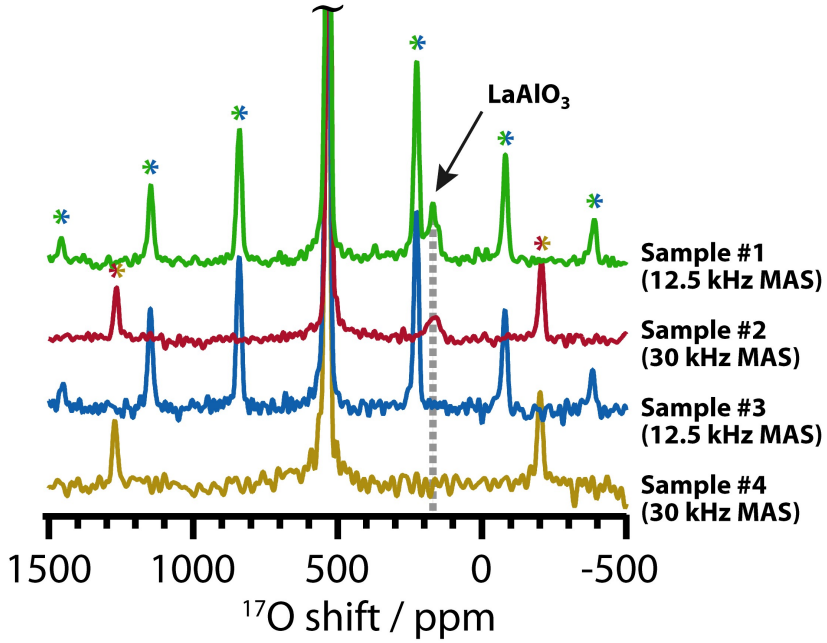


Figure 3.6: Comparison of $LaAlO_3$ impurity for various $^{17}O$-enriched samples of $La_2NiO_{4+\delta}$. Four different samples show varying signal from the feature at 170 ppm relative to the $O_i$ feature (at 532 ppm), confirming that the former oxygen environment is not associated with $La_2NiO_{4+\delta}$ but instead depends on variable synthesis conditions. The assignment agrees with the formation of $LaAlO_3$ during sintering and/or enrichment in the presence of alumina-containing media, and moreover matches the $^{17}O$ shift of this phase as reported by Bastow *et al.*[278] From the uppermost (quantitative) spectrum, we calculate the proportion of $LaAlO_3$ to be at most 0.7–0.8 mol% (assuming that $\delta = 0.15$–$0.17$). Here, only the centerband intensity of the two features is compared, as no spinning sidebands are visible for $LaAlO_3$. Sample #1 was used to acquire the room-temperature spectrum in Figure 3.1; sample #3 was used in the room-temperature MATPASS experiments (Figure 3.9); and sample #4 was used in the broadband VT-NMR measurements (Figure 3.13). Spectra were acquired at 4.7 T with a MAS rate of either 12.5 kHz or 30 kHz. Asterisks denote spinning sidebands. All spectra are normalized to the $O_i$ feature at 532 ppm.

The highly shifted and broadened features at ~6500 ppm and ~3500 ppm are assigned to equatorial $O_{eq}$ and axial $O_{ax}$ sites, respectively (Figure 3.1a, top and middle right). These large hyperfine shifts are attributable to delocalization of unpaired electron spin density from the 3*d* orbitals of the $Ni^{2/3+}$ cations to the *s* orbitals of proximate $^{17}O$ nuclei: equatorial $O_{eq}$ sites lying in the perovskite layer, with two nearby $Ni^{2/3+}$ cations at a short distance (~1.9 Å),

are expected to experience a stronger hyperfine coupling than $O_{ax}$ sites with only one directly bonded $Ni^{2/3+}$ further away (~2.2 Å). Additional support for this assignment comes from $T_1$ relaxation measurements, being sensitive to proximity to paramagnetic centers.[279] As expected, the $T_1$ value for the assigned $O_{eq}$ site (<500 μs) is noticeably shorter than that for $O_{ax}$ (~1 ms). Finally, experimental evidence presented in Section 3.4.4 of a much larger quadrupolar coupling constant ($C_Q$) for $O_{eq}$ is in good agreement with DFT-calculated values (Section 3.4.3), confirming the assignment.

#### 3.4.2.3 Quantification

All sub-spectra in Figure 3.1b have been recorded using a quantitative recycle delay (500 ms, at least 5 times $T_1$ for the $O_i$ site) so as to compare intensity across different environments. To this end, we have fitted the broadband spectrum to a sum of two Lorentzian functions (justified simply because it provided the best fit) with associated satellite transition intensity for $O_{eq}$ and $O_{ax}$ and a CSA-only spinning sideband manifold for $O_i$ (Figure 3.7). The integrated intensity ratio of the model, $O_{eq} : O_{ax} : O_i = 48 : 47 : 5 \approx 2 : 2 : 0.2$, agrees with the sample stoichiometry and is suggestive of a fully stochastic (*i.e.*, not selective) $^{17}O$-enrichment. A stochastic enrichment indirectly confirms fast ionic conduction involving all distinct oxygen sites in $La_2NiO_{4+\delta}$ at the enrichment temperature (1000 °C), as expected of a fast oxide-ion conductor. We also note that the relative integrated intensity of the $O_i$ site (~0.2) concurs reasonably well with the oxygen excess calculated by TGA (0.15–0.17) given that we have not accounted for the signal lost from the paramagnetically-relaxed $O_{eq}$ and $O_{ax}$ sites during the refocusing period prior to acquisition, *i.e.*, we have not performed a spin-spin ($T_2$) relaxation correction. (We note that the short rf pulse length of $\pi/6$ is quantitative[166,280] given the size of the $C_Q$ values as determined later.) Finally, in comparing the weak $LaAlO_3$ signal to the $O_i$ centerband intensity, we calculate the proportion of this minor impurity for this sample to be 0.7–0.8 mol%.

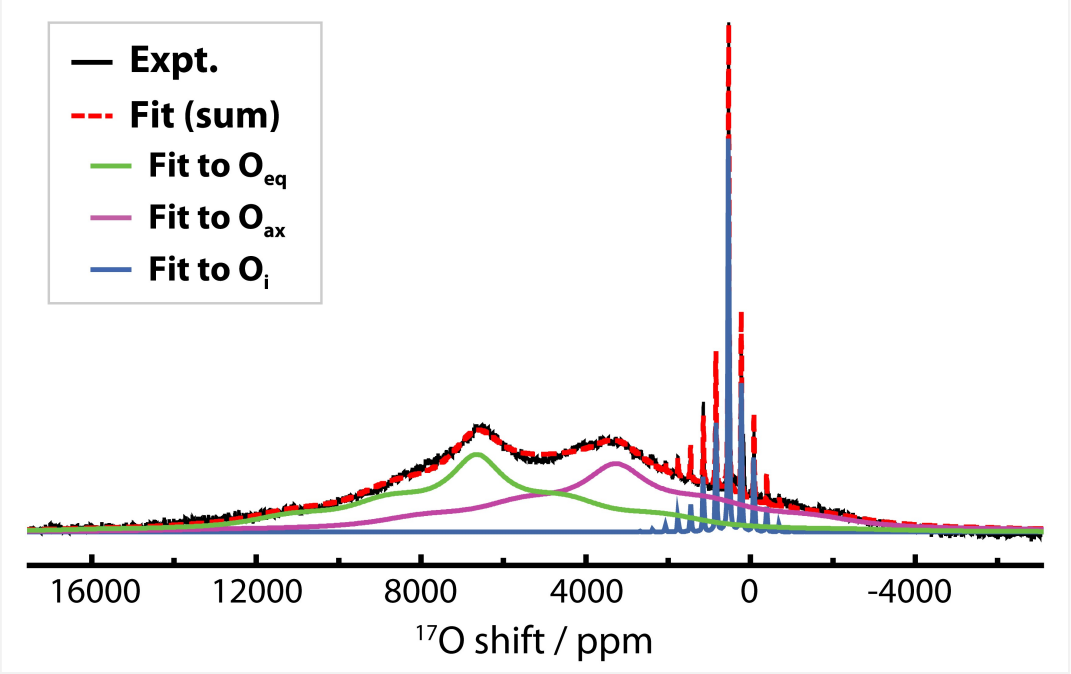


Figure 3.7: Empirical fit to broadband room-temperature spectrum of $La_2NiO_{4+\delta}$ for quantitation. Lorentzian functions centered at ~6650 ppm and ~3272 ppm, with additional intensity arising from satellite transitions, are fit to the $O_{eq}$ and $O_{ax}$ sites, while a simple spinning sideband manifold (CSA only) is fit to $O_i$ at 532 ppm. The model has been computed and optimized using the dmfit software.[272] Though the fit does not capture the $O_{eq}$ and $O_{ax}$ lineshapes perfectly, and moreover does not resolve accurate $C_Q$ values for these sites, we nonetheless obtain a relative integrated intensity ratio of $O_{eq}$ : $O_{ax}$ : $O_i$ = 47.7 : 47.5 : 4.8 that is in very good agreement with that expected from stochastic $^{17}$O-enrichment of all sites.

### 3.4.3 DFT calculations

First-principles periodic DFT calculations were performed to corroborate the argument for the given peak assignment, as well as to gain additional structural insights. The $La_{16}Ni_8O_{33}$ supercell, corresponding to $La_2NiO_{4.125}$, contains a single interstitial oxygen defect ($O_i$) within one of the two rocksalt layers (Figure 3.4b). Following geometry optimization, we observe the rotation of the $NiO_6$ octahedra away from the neighboring interstitial defect. Frayret *et al*. have also reported interstitial-induced octahedral tilting in a compositionally identical supercell, corresponding to rotation along the $[100]_{I4/mmm}$ or, equivalently, $[010]_{I4/mmm}$ axes.[55] The tilt axes in this work could be described as being intermediate between the $[100]_{I4/mmm}$ and $[110]_{I4/mmm}$ directions, with the former dominant. Unlike the previous work, we observe minor tilting among octahedra not directly adjacent to the

interstitial defect, possibly due to cooperative contraction of the unit cell along the stacking direction (*c*-axis).

Importantly, as also shown by Frayret *et al.*, $O_{ax}$ sites directly adjacent to $O_i$ are displaced away from the interstitial defect and slightly towards their respective Ni centers.[55] This differential displacement, correlated with proximity to the interstitial site, amounts to a splitting of the $O_{ax}$ sites into different types. On the basis of Ni–O bond lengths, four $O_{ax}$ types are identified, as depicted in Figure 3.8: (1) $O_{ax,1}$, which are immediately adjacent to $O_i$; (2) $O_{ax,2}$, which are located within the same rocksalt layer as $O_i$ but not adjacent to $O_i$; (3) $O_{ax,3}$, which are the oppositely positioned $O_{ax}$ sites in the $NiO_6$ octahedra containing $O_{ax,1}$; and (4) $O_{ax,4}$, which are the oppositely positioned $O_{ax}$ sites in $NiO_6$ octahedra containing $O_{ax,2}$. The $O_{ax,3}$ and $O_{ax,4}$ sites are located within the "empty" (*i.e.*, interstitial-free) rocksalt layer and hence not directly displaced by the interstitial defect. Average Ni–$O_{ax}$ bond lengths for the split sites ($O_{ax,1}$ through $O_{ax,4}$) are 2.13, 2.16, 2.24, and 2.26 Å, respectively, as compared to the experimental value of 2.25–2.26 Å for the stoichiometric ($\delta = 0$) compound.[47,58]

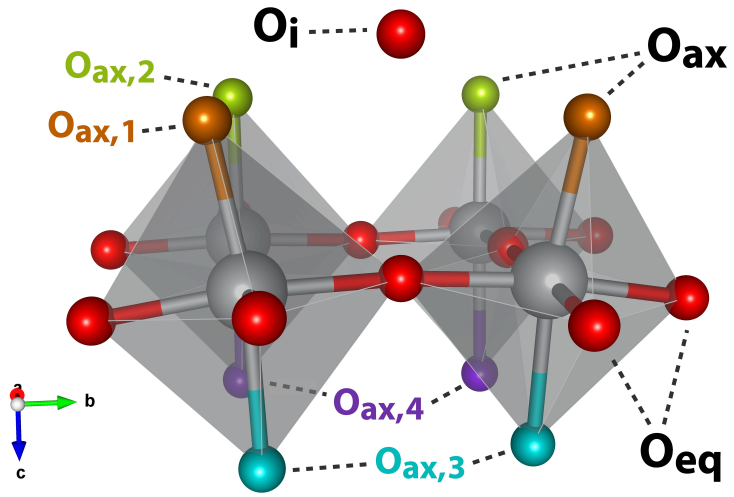


Figure 3.8: Local structural distortion induced by nearby interstitial defect ($O_i$), from part of the DFT-optimized $La_{16}Ni_8O_{33}$ supercell. Axial sites (in orange) closest to the interstitial undergo the largest displacement towards the Ni center, with concomitant tilting of the $NiO_6$ octahedra. The four types of axial oxygen sites, ordered by increasing Ni–$O_{ax}$ bond length, are depicted in orange ($O_{ax,1}$), green ($O_{ax,2}$), cyan ($O_{ax,3}$) and purple ($O_{ax,4}$). Nickel atoms are depicted in grey and non-axial (equatorial) oxygen atoms in red. (For clarity only part of the structure is shown, omitting La.)

Although this axial distortion depends on subtle, long-range interstitial and charge ordering effects (see Section 3.5.1), it strongly affects the calculated NMR parameters. Table 3.1 provides the average hyperfine shifts for equatorial, axial and interstitial sites. For each of the four $O_{ax}$ types (labeled $O_{ax,1}$ through $O_{ax,4}$ in Table 3.1 and depicted in Figure 3.8) we calculate a distinct hyperfine shift, ranging from ~3200 to ~3900 ppm. Shifts are inversely correlated with the Ni–$O_{ax}$ distance. Although distinct resonances cannot be resolved in the initial spin-echo mapped room temperature spectrum, where all $O_{ax}$ sites appear within a single broad feature, the calculated hyperfine shift averaged amongst all axial sites (3539 ppm) is in good agreement with the experimental $O_{ax}$ shift of ~3500 ppm.

Table 3.1: Calculated and experimental structural and $^{17}O$ NMR parameters (computed Ni–O bond lengths, experimental isotropic chemical shifts $\delta_{iso,exp}$, calculated Fermi contact shifts $\delta_{FC,calc}$, and quadrupolar coupling constants $C_Q$) for $La_2NiO_{4+\delta}$ at room temperature.[a]

| **O site** | **Ni–O distance (Å)** | **$\delta_{iso,exp}$ (ppm)** | **$\delta_{FC,calc}$ (ppm)** | **$C_Q$ (MHz)** | |
|---|---|---|---|---|---|
| | | | | Exp | Calc |
| $O_{eq}$ | ~1.9 (avg) | ~6500; 6860(6) (MATPASS) | 10322 | ≥ 4.6 | 4.73 |
| $O_{ax}$ | ~2.2 (avg) | ~3500 | 3539 (avg) | < 4.6 | 1.14 (avg) |
| $O_{ax,0}$ | —* | 5590(5) | —* | < 4.6 | —* |
| $O_{ax,1}$ | 2.13 | 4775(4) | 3914 | < 4.6 | 2.35 |
| $O_{ax,2}$ | 2.16 | 4315(3) | 3821 | < 4.6 | 1.09 |
| $O_{ax,3}$ | 2.24 | 3960(3) | 3234 | < 4.6 | 0.67 |
| $O_{ax,4}$ | 2.26 | 3640(2) | 3189 | < 4.6 | 0.46 |
| $O_i$ | —† | 532(1) | 19 | < 4.6 | 0.38 |

[a] Standard errors in the fitted experimental shifts are given in parentheses. *Not observed in DFT-optimized supercell. †Not bonded to Ni.

The calculated shifts of the more distant equatorial oxygen sites are less influenced by the interstitial defect. In this case competing effects are at work: 1) a distribution of Ni–$O_{eq}$ bond lengths due to lattice distortion of the -Ni–$O_{eq}$–Ni- chains, and 2) differences in spin density

transfer to $O_{eq}$ *via* the Ni $d_{x^2-y^2}$ orbital due to $Ni^{2/3+}$ charge ordering. Moreover, the range of calculated hyperfine shifts across all $O_{eq}$ sites is small relative to the average shift of ~10,000 ppm. In short, $O_{eq}$ shifts do not cluster in distinct groups and, unlike the axial environments, cannot be easily classified by structural type. Nonetheless, the calculated hyperfine shift is much larger for $O_{eq}$ than $O_{ax}$, as expected, confirming the spectral assignment. The theoretical and experimental shifts for $O_{eq}$, however, differ by nearly 4000 ppm. This large discrepancy is not entirely unreasonable; theoretical calculations of $^{17}O$ hyperfine shifts in the solid state remain rudimentary, particularly at the level of hybrid DFT. Only Kong *et al*. have reported attempts for various paramagnetic coordination complexes, with results highly functional-dependent and with errors as large as 2500 ppm.[203] We believe the error is partly attributable to a non-optimal choice of functional (Kong *et al.* describe errors of nearly 6000 ppm before selection of an appropriate functional), but ultimately derives from the self-interaction error in DFT described in Section 2.2.1 that enables excessive spin density delocalization onto the nearby $O_{eq}$ sites.[281] We also note that the higher concentration of $Ni^{2+}$ in the theoretical supercell relative to experiment would increase the calculated $O_{eq}$ (but not $O_{ax}$) shift. Additionally, residual antiferromagnetic couplings within the perovskite layers could lead to smaller experimental $O_{eq}$ shifts than predicted.

The interstitial site has a very small calculated hyperfine shift (of only 19 ppm), as expected, and hence the experimentally observed shift (of 532 ppm) is dominated by the chemical shift, not considered in these calculations.

Calculated quadrupolar coupling constants (Table 3.1) reflect the diversity of local charge and bonding asymmetry amongst oxygen environments. Typical values of $C_Q$ for $^{17}O$ nuclei in inorganic oxides vary from hundreds of kHz in highly symmetric alkaline earth oxides to 5-10 MHz in phosphates and chlorates;[282] here, calculated $C_Q$'s for $La_{16}Ni_8O_{33}$ span the known experimental range. The single interstitial oxygen site has a very nearly tetrahedral coordination to $La^{3+}$, and a correspondingly small $C_Q$ (0.38 MHz). By contrast, $O_{ax}$ sites possess an octahedrally-coordinated geometry with five $La^{3+}$ and one $Ni^{2/3+}$. In this case the charge asymmetry (tri- vs. bivalent neighboring cations), distorted bond angles, and the short Ni–$O_{ax}$ distance yield larger $C_Q$ values. Furthermore, the axial displacement generating a distribution of Ni–$O_{ax}$ bond lengths also yields distinct $C_Q$'s for each split $O_{ax}$ site, ranging

from ~0.5 MHz to 2.4 MHz. Lastly, equatorial sites ($O_{eq}$) experience a locally octahedral environment as well, but with different neighbors: four $La^{3+}$ and two $Ni^{2/3+}$ in an axially compressed arrangement. Much shorter Ni–$O_{eq}$ distances (1.9 Å) relative to La–$O_{eq}$ (2.5–2.7 Å), combined with the effect of $NiO_6$ tilting distortions, give rise to a much larger $C_Q$ (4.73 MHz).

As an aside, the quality of the calculations can also be evaluated as a function of the choice of basis set (BS-I vs. BS-II). Although there is essentially no dependence on the basis set for the calculated NMR parameters of the $O_{ax}$ site, a significant difference is observed for $O_{eq}$; for this site the calculated Fermi contact shift is 8739 ppm for BS-I (compared to 10322 ppm for BS-II), and the calculated quadrupolar coupling constant is 4.00 MHz for BS-I (compared to 4.73 MHz for BS-II). That is, the hyperfine shift calculated using BS-I is in better agreement with experiment, but not the calculated $C_Q$ value. Counterintuitively, this would suggest that the spin delocalization onto the $O_{eq}$ sites is perhaps better modeled by the minimal basis set (BS-I), although at the expense of an accurate depiction of the charge asymmetry. However, looking closely at the Mulliken charge analysis, the Ni cations appear significantly more $Ni^{3+}$-like in the case of BS-I compared to BS-II. This higher valence state for Ni would indeed lead to a smaller Fermi contact shift solely on $O_{eq}$, and a smaller $C_Q$ for this site as well (due to the greater similarity of the charges of the neighboring La and Ni cations). One can conclude the extended basis set BS-II does indeed provide a more accurate picture of the overall electronic structure of the chosen supercell, and, as discussed, the discrepancy between calculated and experimental Fermi contact shifts of the $O_{eq}$ resonance instead arises from the slightly inaccurate composition of the supercell relative to experiment. (More exactly, a greater concentration of $Ni^{2+}$ exists in the theoretical structure as compared to the experimental material.)

### 3.4.4 Room-temperature MATPASS NMR with spectral editing

Suspecting from DFT calculations that additional spectral features could appear at higher resolution, we have performed further NMR experiments at faster magic-angle spinning (40 kHz). Spin-echo mapped spectra acquired at this spinning frequency now show evidence for overlapping spinning sidebands from additional sites (Figure 3.9, upper black trace).

However, even with fast spinning, it is difficult to clarify details of the underlying fine structure due to spinning sideband overlap. The use of higher spinning speeds (*e.g.*, 60 kHz) is unfortunately not feasible here, as the reduced sample volume would prohibitively increase acquisition time. Alternatively, experiments at lower magnetic field would increase the effective spectral distance between sidebands, improving resolution at a given spinning speed, but second-order quadrupolar effects would likely worsen resolution.

We therefore turn to a method of spinning sideband separation, (projection) magic-angle turning and phase-adjusted sideband separation, or MATPASS, as described in greater detail in Section 2.1.2.2. This two-dimensional pulse sequence has been used by Hu *et al.* to obtain broadband "infinite"–MAS spectra in the case of large (>1 MHz) shift anisotropy.[283] The MATPASS experiment also succeeds in the familiar case of moderately quadrupolar nuclei ($^{6}$Li, $^{7}$Li) in paramagnetic environments.[153] Applying the technique to $^{17}$O-enriched $La_2NiO_{4+\delta}$ and extracting the isotropic slice (Figure 3.9, bottom black trace and Figure 3.10, inset) reveals six distinct paramagnetic features from ~3500–7000 ppm, in addition to the usual peak at 532 ppm previously assigned to $O_i$.

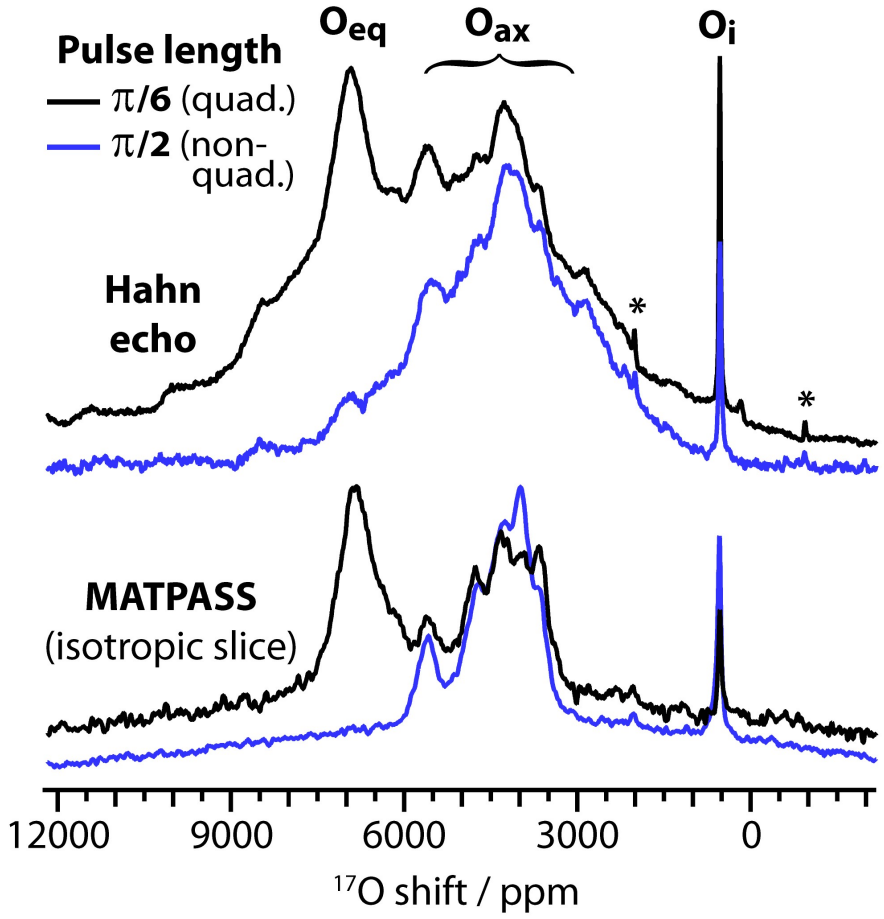


Figure 3.9: Comparison of Hahn echo and MATPASS NMR spectra of $La_2NiO_{4+\delta}$, with quadrupolar filtering. Spectra were acquired at 4.7 T with a MAS rate of 40 kHz. Splitting of $O_{ax}$ is partially resolved in the Hahn echo and fully resolved in the MATPASS data. Both experiments show pulse length dependence ($\pi/6$ vs. $\pi/2$) consistent with a single highly quadrupolar environment ($O_{eq}$). Asterisks denote spinning sidebands where apparent.

Since the calculated hyperfine shifts from DFT (Section 3.4.3) are not necessarily sufficiently accurate to discriminate amongst the different sites, we employ a form of spectral editing, quadrupolar filtering, exploiting the quadrupolar interaction to selectively suppress environments with large $C_Q$ to aid in the assignments. As described in Section 2.1.4.1, this approach hinges on $C_Q$-dependent differences in quadrupolar nutation behavior, wherein sites with quadrupolar frequencies $\omega_Q$ much larger than the rf field strength $\omega_1$ experience more efficient excitation by short rf pulses, on account of selective excitation of the central transition.[284] (For spin-5/2 nuclei, the quadrupolar frequency $\omega_Q$ is equal to $3C_Q/20$.) In practice, rf pulses with short flip angles will resolve all sites regardless of $C_Q$, whereas

application of longer rf pulses (*e.g.* $\pi/2$ for a liquid reference) will preferentially select small-$C_Q$ environments. Kentgens has shown (see Figure 2.5) that for spin-5/2 nuclei, a value of $\omega_Q \geq 6\omega_1$is a reasonable threshold for full attenuation of signal using a longer, $\pi/2$ pulse (calibrated on a liquid reference).[166] In the present case, where $\omega_1$ = 114 kHz, this corresponds to a threshold $C_Q$ of 4.6 MHz.

Repeating the MATPASS experiment using a longer $\pi/2$ pulse (bottom blue trace, Figure 3.9), we observe the loss of the paramagnetic feature centered at 6860 ppm; we conclude that the $C_Q$ of this site must equal or exceed 4.6 MHz. Amongst all DFT-calculated $C_Q$'s, only that of $O_{eq}$ (4.73 MHz) does so. On this basis, the furthest shifted feature is again assigned to $O_{eq}$. None of the other environments are fully attenuated by the longer rf pulse. Thus, the remaining five paramagnetic sites are all assigned to (distorted) $O_{ax}$ sites, for which $C_Q < 4.6$ MHz (Table 3.1).

The five distinct $O_{ax}$ features resolved by MATPASS experiments are extremely suggestive of the split $O_{ax}$ sites obtained from DFT. Here, we do not necessarily imply that the experimental axial environments correspond to the geometries depicted in Figure 3.8, but rather that the presence of some form of axial displacement is consistent with the splitting of $O_{ax}$ features in the spectra. For completeness we "assign" four of the five experimental $O_{ax}$ features to the $O_{ax,1}$–$O_{ax,4}$ sites. The range of experimental and calculated hyperfine shifts is in reasonable agreement, though results from DFT underestimate the experimental values. The otherwise unassigned, highly shifted $O_{ax}$ feature at 5590 ppm (labelled $O_{ax,0}$ in Table 3.1) could correspond to a structural motif not considered in the DFT calculations, such as an axial oxygen with two nearby interstitials, which would experience a substantial displacement and much larger hyperfine shift. This assertion seems plausible given the higher experimental concentration of interstitials ($\delta$ = 0.15–0.17) compared to the DFT-optimized supercell ($\delta$ = 0.125). It is interesting that the $O_{ax}$ features cluster in well-defined peaks rather than display a broad continuum, suggesting a discrete set of Ni–$O_{ax}$ bond lengths, which may imply a degree of two-dimensional ordering of the interstitial defects. We can compare these results to the neutron diffraction study of Demourgues *et al.* of "$La_8Ni_4O_{17}$" ($\delta$ = 0.25), wherein eight $O_{ax}$ sites are identified, with five distinct Ni–$O_{ax}$ distances.[61]

Relative intensities of split $O_{ax}$ sites in the MATPASS spectra cannot be considered quantitative, as the apparent intensities are inversely weighted by dipolar broadening. That is, sites with large values of electron–nuclear dipolar anisotropy have significant intensity distributed across the spinning sideband manifold and so appear smaller in the isotropic slice. The presence of residual spinning sidebands in the isotropic slice, as well as $T_2$ relaxation effects and the use of a very short recycle delay (50 ms) further complicate quantification. However, the presence of several split features in the spectra implies that most axial oxygens reside in slightly displaced environments.

As a conclusive check, the isotropic shifts obtained from MATPASS were used to model spinning sideband patterns that approximately reproduce the Hahn echo spectra recorded at 40 kHz, with both short ($\pi/6$) and long ($\pi/2$) rf pulse lengths (upper traces, Figure 3.9) as shown in Figure 3.10.

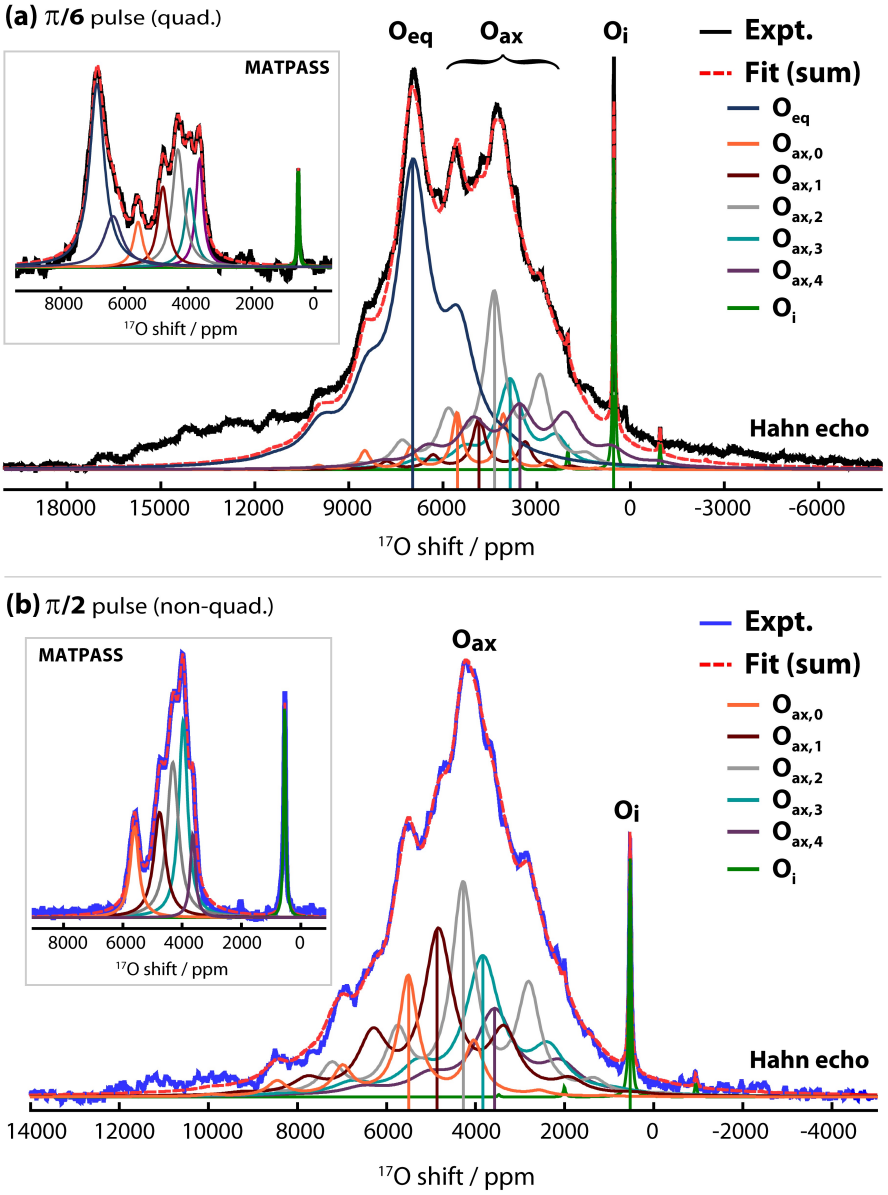


Figure 3.10: Deconvolution of broadband Hahn echo spectra (40 kHz MAS) using MATPASS-resolved shifts. For both (a) short ($\pi/6$) and (b) long ($\pi/2$) rf pulse lengths, the MATPASS spectra (insets) are fit to Lorentzians for each of the distinct oxygen sites, including the five distorted axial environments, $O_{ax,0}$–$O_{ax,4}$. (For $O_{eq}$, a sum of two Lorentzian functions is used only to capture the asymmetric lineshape, not to indicate a separate resonance.) Spinning sideband manifolds arising from chemical shift anisotropy (CSA), centered at the positions determined from the MATPASS data, are then optimized (using the dmfit software[272]) to fit to the Hahn echo spectra from Figure 3.9. As seen, the fits are highly satisfactory except in the high-frequency region of the upper spectrum ($\pi/6$ pulse length), with excess experimental signal attributed to $O_{eq}$ satellite transition intensity. (For simplicity in fitting, we have not included contributions from satellite transition intensity in the model, relevant mainly for the high-$C_Q$ $O_{eq}$ site.)

### 3.4.5 Variable-temperature NMR (≤ 150 °C)

We hypothesize that the orthorhombic-to-tetragonal phase transition near 150 °C may be associated with changes in the local distortion of the $O_{ax}$ environments induced by motion of nearby $O_i$. To test this conjecture, we employ $^{17}O$ VT-NMR as a probe of thermally-activated oxygen motion in $La_2NiO_{4+\delta}$. As technical restrictions limit the concurrent use of fast MAS and sample heating, the following spectra have been acquired under slower spinning (12.5 kHz).

#### 3.4.5.1 Focus on interstitial site

We first study the variable-temperature behavior of the interstitial oxide site at ~535 ppm, choosing a field strength of 16.4 T. (This feature moves by ~+3 ppm at high field, which is possibly a small second-order quadrupolar shift effect, as described in Section 2.1.4.2.) At such a large field, though the paramagnetic features ($O_{ax}$, $O_{eq}$) broaden and become difficult to separate, more spinning sidebands arise for the $O_i$ feature, potentially providing detailed information about the local geometry of this site.

Figure 3.11 shows the $^{17}O$ MAS NMR spectra of the interstitial oxide site in $La_2NiO_{4+\delta}$ from room temperature to 134 °C. The most salient change in the spectra is a slight broadening and a loss of signal at and above 80 °C, especially between 94 °C and 107 °C (Figure 3.11a). At the highest temperature measured (134 °C), at most, 3% of the initial intensity remains. Concurrent with the loss of $O_i$ signal at 107 °C and 134 °C, a broad, asymmetric shoulder appears at a higher frequency of approximately 30 ppm, at 565 ppm (Figure 3.11b). The resonance falls between the pseudo-tetrahedral interstitial environment of $La_2NiO_{4+\delta}$ at 535 ppm and the tetrahedrally-coordinated oxygen environment of $La_2O_3$ previously reported at 584 ppm.[277] Among $OLa_4$ sites with known $^{17}O$ shifts (only $La_2NiO_{4+\delta}$ in this work, LaO(OH), and $La_2O_3$), the shift moves to higher frequency with reduction of the average O–La bond length and an increase in local tetrahedral symmetry.[285] A shift of 565 ppm is therefore suggestive of $OLa_4$ in a less stretched and distorted environment as compared to $O_i$ in $La_2NiO_{4+\delta}$, although not as symmetric as in $La_2O_3$. On this basis, we tentatively suggest that the feature at 565 ppm arises from $OLa_4$ sites in a slightly distorted $La_2O_3$ phase at the

surface of the $La_2NiO_{4+\delta}$ particles. (This feature is not due to a separate bulk $La_2O_3$ phase, as the 584 ppm shift of $OLa_4$ in bulk $La_2O_3$ remains at this shift with increase in temperature; see Figure 3.12.) Assuming the immobile $La_2O_3$–like site at 565 ppm possesses a similar $T_2$ to the interstitial feature at room temperature, the relative intensity ratio gives one such $OLa_4$ site in surface $La_2O_3$ to ~10 interstitial oxides in the bulk sample. Given a sample composition of $\delta = [O_i'']$ = 0.17, and assuming that two-thirds of the oxygen sites in the $La_2O_3$ phase are tetrahedrally-coordinated (as in the bulk compound), the molar phase fraction of surface $La_2O_3$ is calculated to be 2–3%. (For comparison, assuming roughly 1 μm spherical particles, this corresponds to a surface depth of 7–10 nm.) The existence of a La-enriched surface layer is consistent with reports on the unexpectedly strong preference for AO termination in $ABO_3$ perovskites, and has moreover been observed experimentally in $La_2NiO_{4+\delta}$ *via* SIMS-LEIS.[286,37]

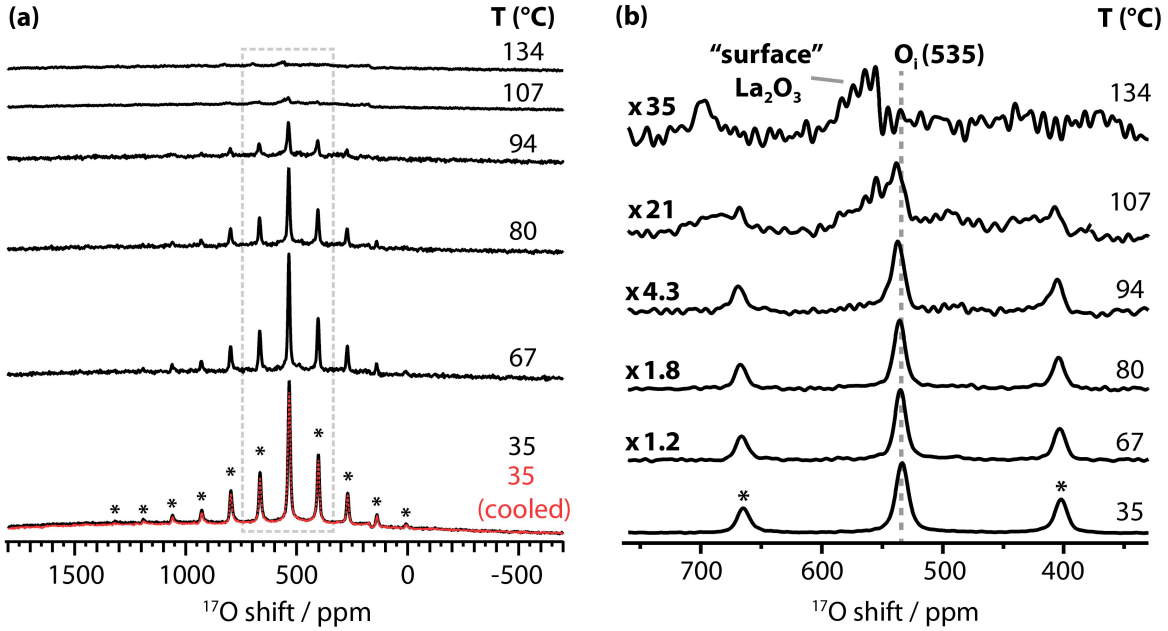


Figure 3.11: Variable-temperature NMR spectra of $La_2NiO_{4+\delta}$, focusing on the interstitial oxygen site. (a) $^{17}O$ MAS-NMR spectra of $La_2NiO_{4+\delta}$ acquired at the indicated temperatures, and at 35 °C after cooling from high temperature (red). The difference between normal room temperature and the lowest sample temperature (35 °C) is due to frictional heating by MAS. Spectra were acquired at 16.4 T under a MAS rate of 12.5 kHz. Spectra shown are normalized to the number of scans. (b) Detail of (a) with spectra scaled to highlight broadening and shift of interstitial site. Asterisks denote spinning sidebands (for clarity shown only at 35 °C).

Lastly, on cooling to room temperature (red trace, Figure 3.11a), the $O_i$ signal returns at 535 ppm with, remarkably, nearly quantitative (98%) recovery of the original integrated intensity. We argue in Section 3.5.2 that the intensity changes are consistent with a motional process involving the interstitial defects.

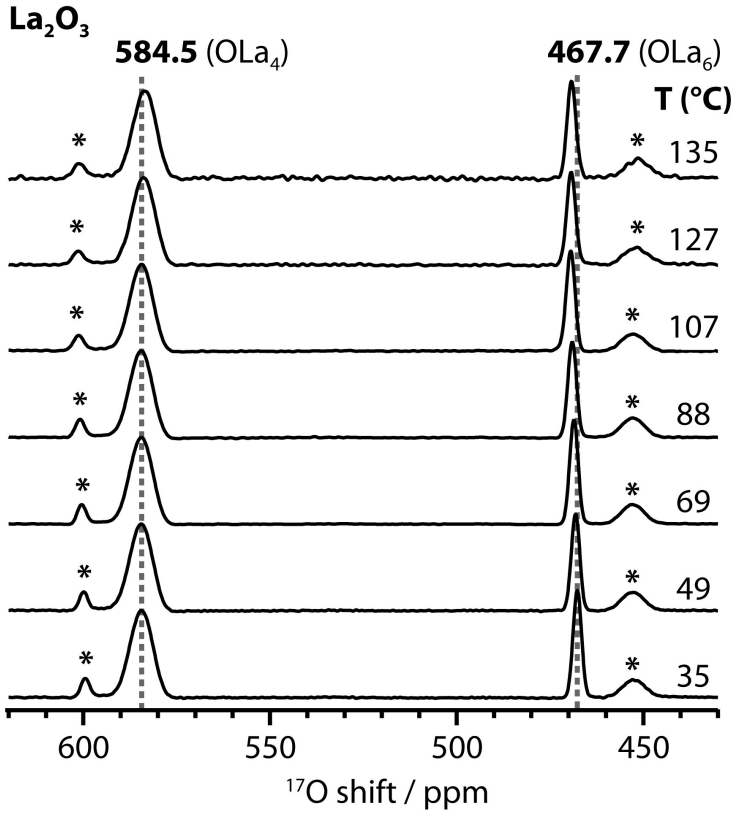


Figure 3.12: Temperature dependence of $^{17}O$ NMR shifts of $La_2O_3$. The $^{17}O$ NMR spectra of $La_2O_3$ (35–135 °C) consist of two features corresponding to the distinct crystallographic O sites in hexagonal $La_2O_3$: a tetrahedral $OLa_4$ site (584.5 ppm) and an octahedral $OLa_6$ site (467.7 ppm). The shifts change only slightly (<2 ppm) across the studied temperature range; at 135 °C, the $OLa_4$ and $OLa_6$ sites are located at approximately 583.6 ppm and 469.2 ppm, respectively. In particular, the $OLa_4$ feature does not change significantly with increase in temperature to 140 °C, supporting the claim that the 565 ppm feature observed in high temperature (130–140 °C) spectra of $La_2NiO_{4+\delta}$ does not arise from a bulk $La_2O_3$ impurity, but rather a distorted $La_2O_3$-like layer at the surface of $La_2NiO_{4+\delta}$. Spectra were acquired at 16.4 T with a recycle delay of 5 s at a spinning speed of 12.5 kHz, on a sample of $La_2O_3$ previously $^{17}O$-enriched by exposure to 1 atm of 70% $^{17}O_2$ at 1000 °C for 24 h. All spectra have been normalized to the number of scans. Asterisks denote spinning sidebands.

### 3.4.5.2 Broadband spectra

To correlate the onset of interstitial motion with mechanistic details by probing temperature-dependent changes in the paramagnetic sites, broadband spectra have been recorded at similar temperatures. Here, a lower field strength (7.05 T), and thus narrower spectral width, ensures that some signal is recorded from all sites ($O_{eq}$, $O_{ax}$, and $O_i$) when acquiring from a single rf carrier frequency. This central-carrier approach obviates a time-consuming spin-echo mapping experiment, though also preventing quantitative comparison of intensities between different sites.

The broadband VT spectra (Figure 3.13) display a complex temperature-dependent behavior that, for convenience, is described sequentially in terms of the diamagnetic region (near $O_i$), the near paramagnetic region (near $O_{ax}$), and the far paramagnetic region (near $O_{eq}$). A significant loss of intensity occurs across all sites with increasing temperature, such that the spectra in Figure 3.13 are scaled arbitrarily to present similar overall signal strength.

In the diamagnetic region, signal from $O_i$ at 532 ppm decreases with increasing temperature. The absolute integrated intensity of $O_i$ shows a qualitatively similar loss as a function of temperature as seen at high field. As before, the $O_i$ feature vanishes in the high-temperature spectra (130 °C and 140 °C), revealing the 565 ppm shoulder near $O_i$. Weak features at 380 ppm ($ZrO_2$ sample holder[287]) and 170 ppm ($LaAlO_3$ impurity) are also rendered more obvious at these temperatures in the absence of overlap by spinning sidebands of $O_i$ (see Figure 3.14).

The near paramagnetic region at modest temperatures (to 110 °C) shows a moderate loss of signal at $O_{ax}$, which is slightly more pronounced than that for $O_i$, concurrent with the appearance of spinning sidebands on top of the broad underlying paramagnetic feature. The positions of these spinning sidebands are highly temperature-dependent, and they are not associated with the fixed-position $O_i$ feature. Above 110 °C, a major narrowing of the $O_{ax}$ site occurs, centering the shift at 3650 ppm, and revealing a minor feature at 2400 ppm. Moreover, small spinning sidebands associated with this latter feature appear at lower frequencies (between 2200 ppm and 800 ppm).

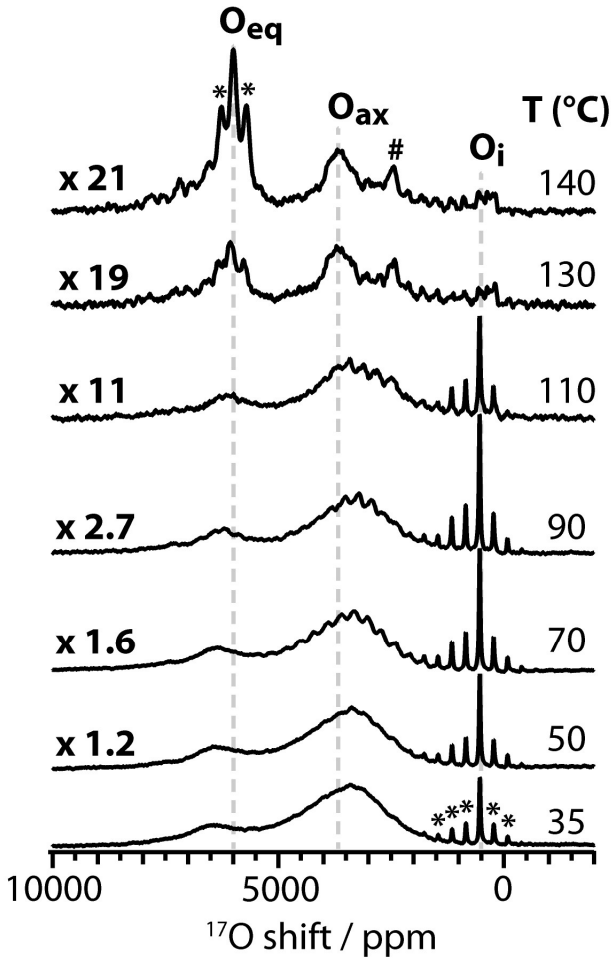


Figure 3.13: Broadband variable-temperature NMR spectra of $La_2NiO_{4+\delta}$. Spectra were acquired at 7.05 T at a MAS rate of 12.5 kHz. Spectra were normalized to number of scans (between ~300,000 and ~6,700,000 per spectrum) and then scaled as shown to obtain similar intensity for the $O_{ax}$ feature (~3500 ppm) present in all spectra. # indicates the feature at 2400 ppm assigned to the $La_3Ni_2O_7/La_4Ni_3O_{10}$ impurity phase (see Section 3.4.6). Asterisks denote visible spinning sidebands, for clarity only indicated for $O_i$ at 35 °C and for $O_{eq}$ at 140 °C. (A close-up view of the spectrum at 140 °C depicting the weakly resolved peaks in the diamagnetic region is shown in Figure 3.14.)

Finally, the far paramagnetic region is characterized by a decrease in intensity but very little change in the lineshape until above 110 °C, where the $O_{eq}$ site suddenly sharpens and grows in intensity relative to $O_{ax}$. This narrowing is so profound that, at 140 °C, spinning sidebands flank either side of the isotropic shift, and the apparent isotropic shift also moves to lower frequency (6000 ppm). Higher-frequency features are observed out to 8000 ppm and are approximately spaced at the MAS rate relative to the $O_{eq}$ isotropic shift indicating that they correspond to the satellite transitions of $O_{eq}$.

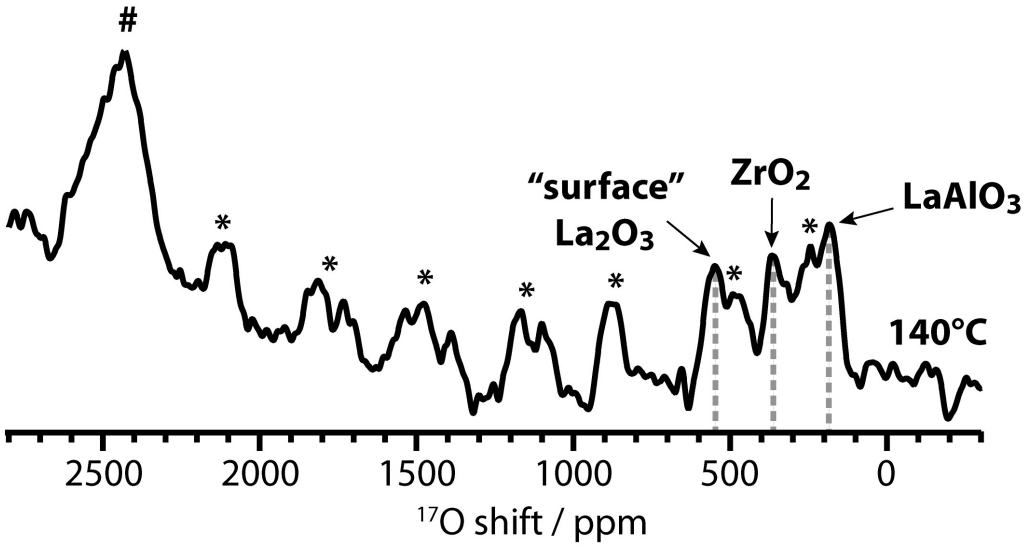


Figure 3.14: Close-up view of the broadband $^{17}O$ NMR spectrum of $La_2NiO_{4+\delta}$ at 140 °C (taken from Figure 3.13). The feature at 2400 ppm assigned to the $La_3Ni_2O_7/La_4Ni_3O_{10}$ impurity phase is indicated by #, with asterisks denoting spinning sidebands of this feature. The weakly resolved peaks in the diamagnetic region are assigned to "surface" $La_2O_3$ (~565 ppm), the $ZrO_2$ sample container (~380 ppm), and the $LaAlO_3$ impurity phase (~170 ppm). The spectrum was acquired at 7.05 T at a MAS rate of 12.5 kHz.

### 3.4.6 Assigning spectral features due to higher-order phases

We have established that the feature at 2400 ppm seen above 110 °C (Figure 3.13 and Figure 3.14) arises from the $La_4Ni_3O_{10}$ impurity phase (previously resolved by XRD), as well as other higher-order Ruddlesden-Popper phases such as $La_3Ni_2O_7$ that form during high-temperature $^{17}O$-enrichment. Although synthesis and $^{17}O$-enrichment of the pure higher-order phases did not prove possible due to interconversion between these phases induced by the high-temperature treatment with $^{17}O_2$ gas, $^{17}O$-enrichment of a mixture of $La_2NiO_{4+\delta}$ and NiO at 1000°C yielded a $^{17}O$-enriched sample of 55 wt. % $La_2NiO_{4+\delta}$, ~25 wt. % $La_4Ni_3O_{10}$ and ~20 wt. % $La_3Ni_2O_7$ as determined by XRD, with the latter two phases difficult to distinguish due to significant overlap of reflections (Figure 3.15).

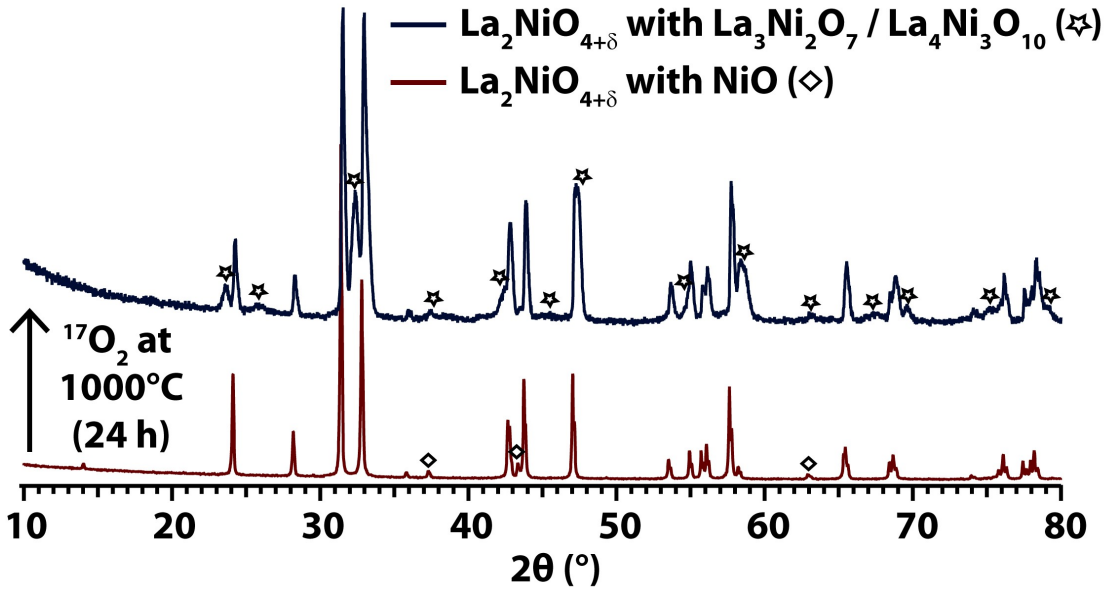


Figure 3.15: Powder XRD characterization of mixed samples of $La_2NiO_{4+\delta}$, NiO, $La_3Ni_2O_7$ and $La_4Ni_3O_{10}$ before and after $^{17}O$-enrichment. After exposure to $^{17}O_2$ at 1000 °C for 24 h, a prepared mixture of as-synthesized $La_2NiO_{4+\delta}$ (93 wt. %) and NiO (7 wt. %) [bottom trace, red] converts to a mixture of $La_2NiO_{4+\delta}$ (55 wt. %), $La_3Ni_2O_7$ (~25 wt. %) and $La_4Ni_3O_{10}$ (~20 wt. %) [upper trace, blue]. Reflections assigned to NiO are marked by diamonds; those assigned exclusively to $La_3Ni_2O_7$ and/or $La_4Ni_3O_{10}$ (*i.e.*, not $La_2NiO_{4+\delta}$) are marked by stars. Almost all reflections of the $La_3Ni_2O_7$ and $La_4Ni_3O_{10}$ phases overlap, rendering difficult the refinement and calculation of phase fractions. All weight percentages have been estimated using Rietveld refinements to the known structures of $La_2NiO_{4.17}$ (ICSD no. 98557), NiO (ICSD no. 9866), $La_3Ni_2O_7$ (ICSD no. 91142), and $La_4Ni_3O_{10}$ (ICSD no. 80279). The change in the intensity ratio of reflections of the primary phase upon $^{17}O$-enrichment, *e.g.* the relative increase in intensity of the reflection at 47.5°, is attributable to overlapping intensity from the higher-order phases.

The room-temperature $^{17}O$ NMR spectrum of this mixed sample contains the typical features of $La_2NiO_{4+\delta}$ but with the familiar additional peak at 2400 ppm (Figure 3.16). This resonance, clearly associated with the impurity phase(s), is tentatively assigned to an axial oxygen site with two nearby Ni cations, *i.e.* the oxygen environment present in $La_3Ni_2O_7$ and $La_4Ni_3O_{10}$ but not in $La_2NiO_{4+\delta}$. Its smaller hyperfine shift compared to $O_{ax}$ in $La_2NiO_{4+\delta}$, despite the proximity of the site to an additional paramagnetic center, is attributed to the higher concentration of $Ni^{3+}$ (S = ½), as well as to the onset of metallic behavior and Pauli paramagnetism in the higher-order phases.[288] The latter property in particular gives rise to a smaller Knight shift rather than a pure Fermi (Curie-Weiss) contact shift, as previously shown for $^{17}O$ NMR spectra of metallic oxides.[289] As with the shoulder assigned to the

distorted $La_2O_3$ phase, the higher-order impurity feature is apparent for the $La_2NiO_{4+\delta}$ sample only in high temperature spectra, such that signal from the main phase is greatly diminished. Based on the above assignment and the integrated NMR signal, we estimate a molar phase fraction of $La_3Ni_2O_7$ / $La_4Ni_3O_{10}$ equal to 2–4%, in good agreement with earlier refined XRD results (~3 wt. % of $La_4Ni_3O_{10}$). (The uncertainty in the molar phase fraction arises from the lack of knowledge of the exact contribution of each of the very similar higher-order phases to the signal at 2400 ppm.) The extensive spinning sideband manifold associated with this feature suggests a highly anisotropic environment with significant local structural disorder, possibly caused by oxygen vacancies, or otherwise ascribed to the situation of the higher-order phases in the disordered subsurface region of $La_2NiO_{4+\delta}$, as predicted by Wu *et al.*[37] These results indicate that the oxidation mechanism of $La_2NiO_{4+\delta}$ to $La_3Ni_2O_7$ and $La_4Ni_3O_{10}$, which is of relevance to SOFC cathode operation and degradation, involves the preferential incorporation of $O_2$ (here as $^{17}O_2$) into the axial sites bridging the perovskite layers (as seen at 2400 ppm).

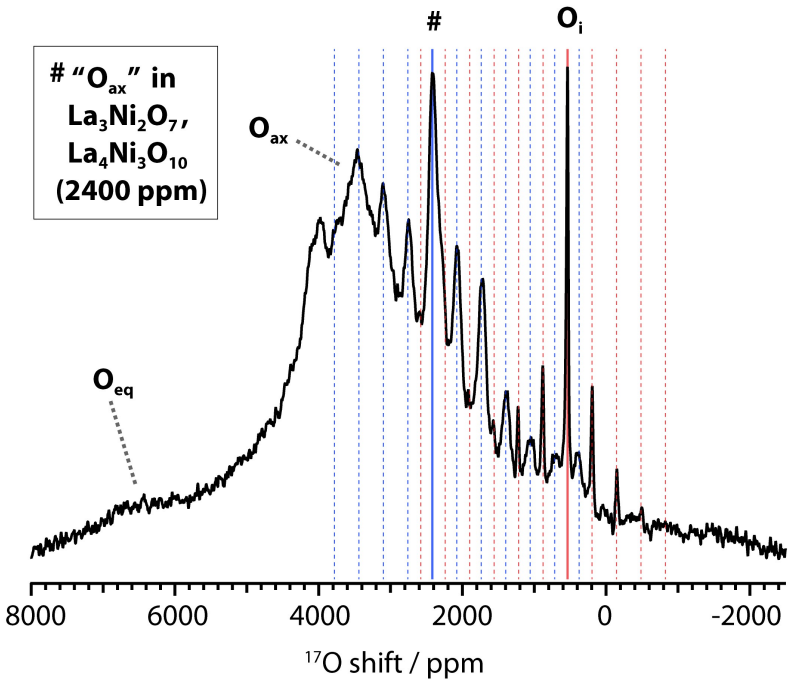


Figure 3.16: $^{17}O$ NMR spectrum of $^{17}O$-enriched mixture of $La_2NiO_{4+\delta}$, $La_3Ni_2O_7$ and $La_4Ni_3O_{10}$. The appearance of an additional feature in the spectrum at 2400 ppm (indicated by #), with associated spinning sideband manifold, is assigned to the higher-order Ruddlesden-Popper phases $La_3Ni_2O_7$ and $La_4Ni_3O_{10}$, and specifically to the unique $O_{ax}$-like sites bridging adjacent perovskite layers in these phases. Intensity of the sites is not

quantitative; the pulse carrier frequency is centered at 3000 ppm and so the $O_{eq}$ resonance is not efficiently excited. Dashed blue lines indicate positions of spinning sidebands of the 2400 ppm feature; dashed red lines indicate positions of spinning sidebands of the feature assigned to interstitial oxygen ($O_i$) in $La_2NiO_{4+\delta}$. The room-temperature Hahn echo spectrum was acquired at 7.05 T with a MAS rate of 14 kHz, using a $\pi/6$ rf pulse centered at 3000 ppm.

## 3.5 Discussion

### 3.5.1 Causes of local distortion of axial oxygen sites

The displacement of axial oxygen into split sites has implications for the calculation and assignment of the NMR spectra; we briefly discuss its origin. The phenomenon is associated with, but distinct from, rotation of the $NiO_6$ octahedra. As Perrichon *et al*. note in the case of $Nd_2NiO_{4+\delta}$, octahedral rotation may occur with minor changes in the Ni–$O_{ax}$ distance, and conversely a large contraction may not necessarily accompany a large tilt.[290] Disregarding octahedral rotation, therefore, one can rationalize the displacement of axial sites *via* steric or electronic arguments. According to the former, axial oxygen initially positioned "between" $O_i$ and Ni sites, if repelled along a path directly away from a nearby interstitial, will move to an environment with a shorter Ni–$O_{ax}$ distance. Alternatively, in the latter argument, charge compensation of $O^{2-}$ interstitials occurs *via* oxidation of some $Ni^{2+}$ sites to $Ni^{3+}$, with a more nuanced and longer-range effect on axial sites. The smaller ionic radius of $Ni^{3+}$ favors shorter overall Ni–O bonds; this effect competes with the axial elongation arising from the Jahn-Teller distortion of $Ni^{3+}$. Regardless of the net change in bond length, charge ordering on Ni may contribute to a range of Ni–$O_{ax}$ distances. We note that in the calculations in this thesis the Ni sites not adjacent to $O_i$ have marginally more $Ni^{3+}$ character, with slightly shorter equatorial bonds and longer axial bonds, and this represents the source of the variation in Ni–$O_{ax}$ distances we observe within a rocksalt layer.

The exact nature of the $O_{ax}$ distortion is expected to be highly dependent on the specific superstructural arrangement of interstitials. In these calculations, this three-dimensional superstructure is artificially constrained by the periodicity of the relatively small supercell. Nonetheless, experimental evidence for a more complex model of long-distance interstitial

ordering, as in the neutron diffraction study by Demourgues *et al*. of "$La_8Ni_4O_{17}$" ($\delta = 0.25$), is associated with a similar splitting of $O_{ax}$ sites into several types based on proximity to Ni.[61,62] However, diffraction-based approaches (with patterns indexed on unit cells of high symmetry) generally resolve one "normal" and one distorted $O_{ax}$ site with averaged, and thus comparable, Ni bond lengths. Only for materials with significant stacking-axis contraction (*e.g*. $Nd_2NiO_{4+\delta}$ [290]), or containing transition metal cations that undergo large changes in Jahn-Teller distortion upon oxidation (*e.g*. $La_{1.2}Sr_{0.8}MnO_{4+\delta}$ [291]), do diffraction data evidence a clear reduction of the average Ni–$O_{ax}$ bond length. The sensitivity of paramagnetic $^{17}O$ NMR to subtle forms of local disorder, even in the absence of any long-range superstructure (as required for diffraction), is a distinct advantage of this methodology, and ultimately derives from the exceptional strength of the hyperfine interaction and its dependence on small changes in distance to nearby paramagnetic centers.

### 3.5.2 Kinetics of interstitial motion

One can postulate several reasons for the dramatic loss of the interstitial feature on heating (Figure 3.11), such as changes in the Boltzmann distribution of spin states or the physical removal (outgassing) of $^{17}O$ as $O_2$. The first case proves unlikely, as a decrease in the population difference of the central transition spin states on heating from 35 to 134 °C (308 to 407 K) can only diminish the signal by at most about 25% (as the spin population difference varies essentially linearly with temperature). Notably, the previously assigned $LaAlO_3$ impurity feature at 170 ppm retains the majority of its intensity with increase in temperature (Figure 3.17), which is consistent with this. We also discount the gaseous elimination of $^{17}O$ at elevated temperature, because the recovery of the original spectrum on cooling suggests that the post-VT sample remains comparably $^{17}O$-enriched.

Instead, we propose that the spectral changes in Figure 3.11 are consistent with the onset of oxide-ion dynamics on the NMR timescale, namely, exchange between the interstitial site and a paramagnetic oxygen environment. As described in Sections 2.1.5.1 and 2.1.5.2.1, in an ideal, thermally-activated two-site exchange, as the exchange rate increases, the two spectral features broaden and eventually coalesce. Furthermore, rapid exchange enhances spin dephasing and leads to greatly reduced $T_2$ relaxation times. This in turn induces significant

loss of spectral intensity in multiple-pulse NMR sequences such as the Hahn echo experiments performed here.

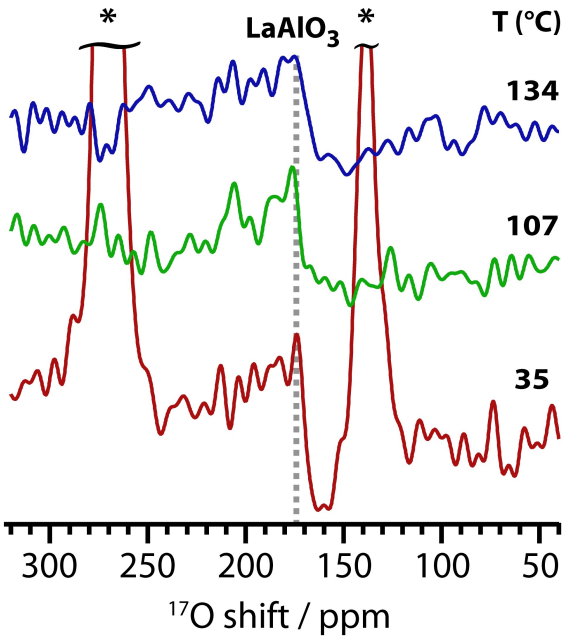


Figure 3.17: Variable-temperature comparison of intensity of $LaAlO_3$ impurity. Selected spectra from Figure 3.11 are shown centered about the 170 ppm feature assigned to $LaAlO_3$. The small reduction in signal (~20–30%) with increase in temperature is consistent with that expected from the temperature-dependent Boltzmann distribution of spin states. However, the signal does not vanish completely as does $O_i$ (with sidebands at ~138 and ~240 ppm), implying the loss of $O_i$ signal is due to other effects, *i.e.* a decrease in $T_2$ consistent with oxide-ion motion in $La_2NiO_{4+\delta}$. The $LaAlO_3$ feature is weak and difficult to phase due to a sloping baseline, accounting for the unusual lineshape seen at 35 °C. Spectra were acquired at 16.4 T under a MAS rate of 12.5 kHz. Spectra have been normalized to the number of scans acquired. Asterisks denote spinning sidebands of $O_i$ (centerband at 532 ppm, not shown).

Assuming thermally-activated (Arrhenius-type) exchange, in the so-called slow motion or "visit-limited" regime of the Meiboom chemical exchange model,[177,178]

$$\log I = \log I_0 - \frac{2\tau}{c} A_0 [\exp(-1/T)]^{E_a/R} \tag{3.3}$$

where $I$ is the integrated signal intensity as observed experimentally, $T$ is the sample temperature, $E_a$ is the activation energy, and the other variables are experimental constants or proportionality constants: $I_0$ is the integrated signal intensity from a one-pulse experiment,

$\tau$ is the (fixed) rotor period, $c = k_{ex} \cdot T_2$ (where $k_{ex}$ is the exchange rate), $A_0$ is the Arrhenius pre-exponential factor, and $R$ is the gas constant. (For derivation of Equation (3.3) and further details of the analysis, see Appendix A.) Analyzing the loss of integrated $O_i$ intensity in this way (after first subtracting the intensity belonging to the surface $OLa_4$ sites at 565 ppm), an $E_a$ for interstitial motion equal to 0.59 ± 0.07 eV is extracted (Figure A.1.2). This result agrees well with the MD–simulated value of 0.51 eV given by Chroneos *et al.* for exchange between axial and interstitial sites,[71] as well as a value of 0.54 eV for oxygen self-diffusion in polycrystalline $La_2NiO_{4+\delta}$ as determined by TOF-SIMS.[292] We thus assign this motional process to interstitial–axial exchange. We note, however, that the present activation energy is calculated over a much lower temperature range (<134°C) than in the previous literature (350–700 °C).

Using the MEXICO code[173] as described in Section 2.1.5.1, asymmetric two-site exchange simulations (Figure 3.18) were performed to explore the effect of exchange between the interstitial and axial anions on the observed lineshapes. From the simulations, we estimate a conservative upper bound $k_{ex}$ < 320 kHz for this process, with the correlation time for interstitial jumps no shorter than 3.2 μs, at 134 °C.

### 3.5.3 Analysis of broadband variable-temperature spectra

The complex lineshape changes in the paramagnetic features (Figure 3.13) allow us to explore the onset of oxygen motion in the context of the reported orthorhombic–tetragonal phase transition near 150 °C. The most prominent change in the spectra is the sudden narrowing of the $O_{eq}$ feature at 130 °C, which suggests a much smaller distribution of isotropic, time-averaged hyperfine shifts. The further increase in the $O_{eq}$ centerband intensity at 140 °C also indicates a significant lessening of sources of spectral anisotropy such as electron–nuclear dipolar broadening. We assign the $O_{eq}$ lineshape changes to the rocking motion of $NiO_6$ octahedra entering the fast motion regime at, or nearly at, the phase transition temperature. On the basis of the maximum frequency separation between $O_{eq}$ sites of ~2000 ppm ≈ ~82 kHz seen at room temperature, and using the coalescence condition for the exchange rate (Section 2.1.5.1), we calculate that the motional rate of rocking exceeds 180 kHz ($= \pi/\sqrt{2} \cdot 82$ kHz)[172] at 130 °C.

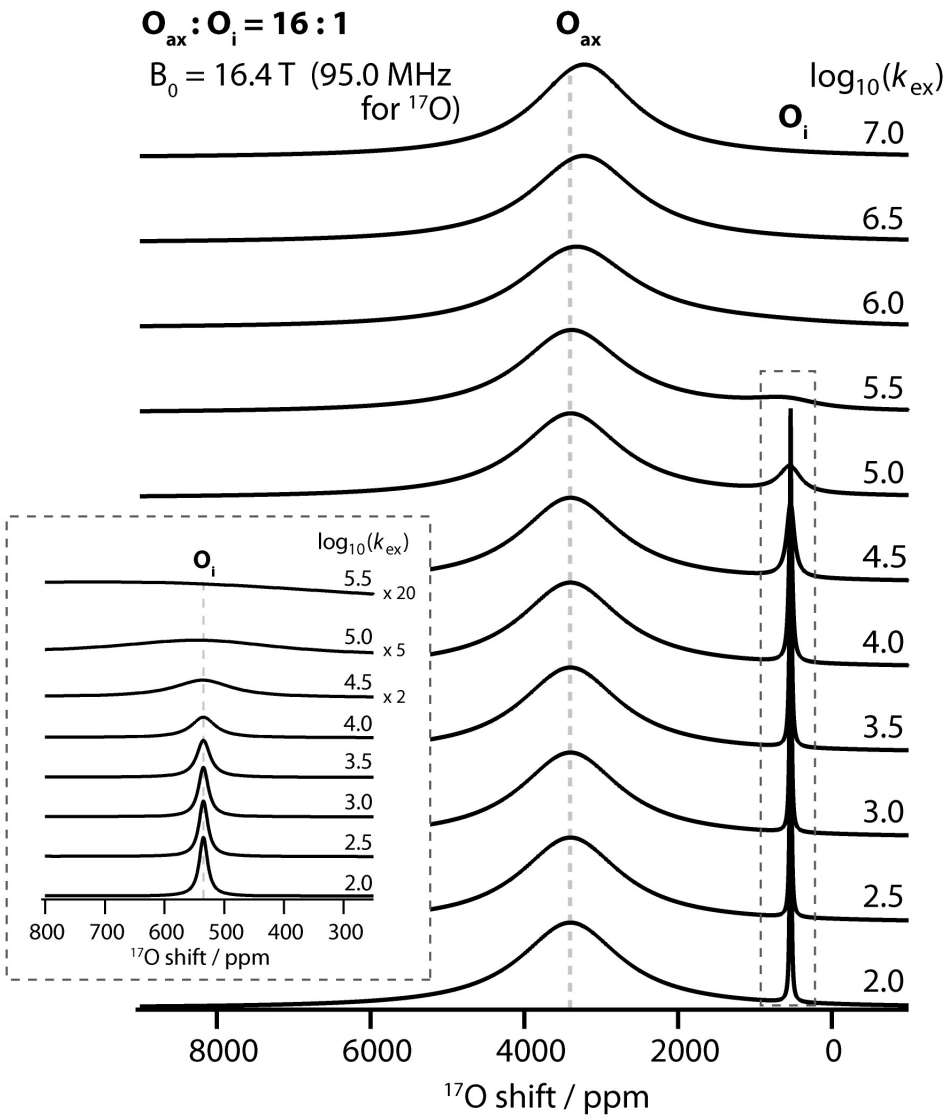


Figure 3.18: Asymmetric two-site simulations of axial–interstitial exchange. Simulated $^{17}O$ NMR spectra of the interstitial and axial oxygen environments (fixed at 532 ppm and 3400 ppm, respectively) are shown as a function of the axial–interstitial exchange rate $k_{ex}$). A shift of 3400 ppm for $O_{ax}$ is chosen in agreement with the apparent peak position of $O_{ax}$ at a MAS rate of 12.5 kHz (as in Figure 3.1) at 35 °C. The population ratio of axial to interstitial oxygen sites is fixed at 16:1. The Larmor frequency of $^{17}O$ has been set at ~95.0 MHz (corresponding to a magnetic field of 16.4 T), matching the experimental conditions of the VT-NMR spectra depicted in Figure 3.11. The inset shows the region around the $O_i$ feature; no distinguishable intensity from $O_i$ sites is observed above $\log_{10}(k_{ex}) \approx 5.5$, *i.e.* $k_{ex} \approx 320$ kHz. The shift of the $O_{ax}$ resonance reflects coalescence with the $O_i$ resonance: for simplicity the Curie-Weiss temperature-dependence of the $O_{ax}$ resonance has not been included. Simulations have been performed using the MEXICO code.[173]

The previous neutron diffraction study by Skinner has also resolved a significant loss of anisotropy of the equatorial oxygen site near the phase transition temperature.[54] In that work, the $O_{eq}$ thermal factors at 25 °C showed a significant *c*-axis displacement ($U_{33}/U_{11} \approx 2$, $U_{33}/U_{22} \approx 5$), similar to the out-of-plane equatorial distortion depicted in Figure 3.8. At and above 150 °C, however, the $O_{eq}$ thermal ellipsoid was found to be isotropic. Here, the VT-NMR spectra corroborate the collapse of the $O_{eq}$ environment to an isotropic (in-plane) environment at these temperatures, consistent with fast rocking of the $NiO_6$ octahedra.

The $O_{ax}$ resonance similarly narrows at and above 130 °C (Figure 3.13) to a feature approximately at the average of the distorted $O_{ax}$ environments resolved by MATPASS experiments (shown in Figure 3.9), which suggests a time-averaging of the mean $O_{ax}$ distortion. We attribute this change to a similar motional mechanism, *i.e.*, local rocking of $NiO_6$ octahedra, while noting that simultaneous exchange with interstitial sites competes by contributing to broadening of this site (relative to $O_{eq}$, which does not exchange at these temperatures). Furthermore, the $O_{ax}$ dynamics are likely subject to a distribution of motional correlation times. The presence of spinning sidebands at lower temperatures (~70 °C), for example, suggests a partial averaging of a subset of the distorted $O_{ax}$ environments by motion already in the fast exchange limit. In previous VT-NMR studies of anionic conductors, the coexistence of multiple correlation times has been attributed to vacancy–dopant ordering or to the presence of mobile and rigid domains with differing defect concentrations.[244,293] In this system, the apparent variation in $O_{ax}$ motional rates likely results from the much larger population of axial sites relative to that of the interstitial defects with which they exchange.[180]

The influence of interstitial motion on the dynamics of the $O_{ax}$ and $O_{eq}$ sites can be inferred in several ways. We note that the calculated motional rate of $NiO_6$ rocking (in excess of 180 kHz) is near the coalescence regime for interstitial–axial exchange (Figure 3.18), suggesting that near the phase transition temperature, the exchange motion is coupled to the octahedral rocking (or vice versa). Secondly, as clearly shown in the DFT calculations, and experimentally from the distribution of shifts, the $O_{ax}$ distortion arises from proximity to interstitial defects, and therefore the long-range motion of interstitials necessarily contributes to averaging of the $O_{ax}$ distortion. We conclude that the loss, or significant reduction of, the

local $O_i$–induced distortion occurs at or near the phase transition and is moreover correlated with exchange between interstitial and axial sites.

### 3.5.4 Extension to other systems and higher temperatures

The VT-NMR results clarify that the previously observed orthorhombic–tetragonal phase transition arises from the loss of a local structural distortion that is correlated with rapid oxide-ion dynamics. It remains unclear how this distortion leads to the cooperative tilting of perovskite layers in the bulk and thus the low-temperature orthorhombic structure, but we note that even for very subtle phase transitions, VT-NMR spectra should resolve the relevant motional changes that drive the transition. An example system is the related phase $La_2NiO_{4.11–4.13}$, which undergoes a subtle transition at ~300 K with both low- and high-temperature phases nominally tetragonal, but with long-range 3D interstitial ordering only apparent below 300 K.[66] The sensitivity of the NMR spectra could in this case provide a convenient check on the interplay of oxygen motion and interstitial ordering, even where the latter property is not readily apparent by diffraction or other techniques.

An extension to the present work would involve the acquisition and assignment of high-temperature (150 °C to 800 °C) $^{17}O$ NMR spectra of $La_2NiO_{4+\delta}$, to explore motion involving exchange between all of the oxygen sites and to examine the effect of temperature on oxygen interstitial content. This would in principle be achievable using a Bruker LASER-MAS NMR probe (which is employed to obtain the VT-NMR spectra in Chapter 5).

## 3.6 Conclusions and outlook

A combined experimental (NMR spectroscopy) and computational (DFT) methodology has been employed to clarify the local structure and dynamics of the mixed ionic–electronic conductor $La_2NiO_{4+\delta}$ by obtaining $^{17}O$ MAS NMR spectra of this paramagnetic oxide in the solid state. The main conclusions are as follows:

(1) Small compositional changes in $La_2NiO_{4+\delta}$ occur as a result of $^{17}O$-enrichment; we observe an increase in the oxygen excess (before: $\delta$ = 0.12–0.14; after: $\delta$ = 0.15–0.17 by

XRD, $\delta$ = ~0.2 by quantitative NMR) and the formation of small amounts (~3 wt. %) of an impurity assigned to the higher-order $La_4Ni_3O_{10}$ phase.

(2) Room-temperature $^{17}O$ MAS NMR spectra of $^{17}O$-enriched $La_2NiO_{4+\delta}$ acquired by spin-echo mapping reveal three distinct oxygen environments assigned to interstitial ($O_i$), axial ($O_{ax}$) and equatorial ($O_{eq}$) sites, with quantitative measurements suggesting fully stochastic $^{17}O$-enrichment.

(3) DFT calculations of $La_2NiO_{4+\delta}$ provide local structural insight and are used to obtain Fermi contact (hyperfine) shifts and quadrupolar coupling constants that corroborate the assignment of the experimental spectra. In particular, paramagnetic $O_{eq}$ and $O_{ax}$ features can be distinguished on the basis of the much larger $C_Q$ of the former (4.7 MHz vs. ~1.1 MHz).

(4) High-resolution MATPASS NMR spectra, in combination with quadrupolar filtering techniques, reveal the splitting of the $O_{ax}$ site into five discrete axial environments (3640–5590 ppm). The DFT calculations also show a similar clustering of four distinct $O_{ax}$ shifts, which can be rationalized on the basis of Ni–$O_{ax}$ distances. We demonstrate that this axial splitting arises from a local structural distortion directly induced by the interstitial defect.

(5) Variable-temperature NMR spectra at high field resolve the (reversible) loss of the interstitial oxide feature due to a thermally-activated motional process with $E_a$ = 0.59 ± 0.07 eV; we assign this motion to exchange with axial sites.

(6) Analysis of the entire broadband spectrum as a function of temperature allows us to elucidate the types of motion and exchange affecting the interstitial, axial, and equatorial oxygen sites. In brief, exchange between interstitial and axial sites dominates the intensity loss of the $O_i$ resonance. Local rocking motion of $NiO_6$ octahedra, with associated averaging effects on axial and equatorial displacement, is dominant for the $O_{ax}$ and $O_{eq}$ lineshapes, with a motional rate larger than 180 kHz at 130 °C. Abrupt changes in the VT-NMR spectra are associated with approach to the previously reported orthorhombic-to-tetragonal phase transition of $La_2NiO_{4+\delta}$, these changes occurring here between 110 °C and 130 °C. We observe a significant reduction in the magnitude of local structural distortions due to $NiO_6$ octahedral motion, correlated with interstitial–axial exchange, at the phase transition

temperature; this illustrates how oxide-ion motion at the atomic level directly influences the phase transition in the bulk.

The design of next-generation MIECs with improved oxide-ion conductivity relies on a fundamental understanding of the underlying anion dynamics across a wide temperature range, which $^{17}O$ VT-NMR spectroscopy is uniquely poised to resolve. An interesting extension to the present work would entail the acquisition of high-temperature spectra (>150 °C) of $La_2NiO_{4+\delta}$ to provide insight into oxygen conduction mechanisms in the conditions most relevant for IT-SOFC and sensor operation. Cation doping of perovskite MIECs, a common strategy in tuning material properties such as the electronic and ionic conductivity, should have significant effects on the paramagnetic $^{17}O$ spectra, and is explored in detail for the case of $La_{2-x}Sr_xNiO_{4+\delta}$ in Chapter 4 of this thesis. The present methodology will allow for comprehensive depictions of the local structure and dynamics, as well as the fundamental defect chemistry, of these functionally relevant oxides.

# Chapter 4 Study of Defect Chemistry in the System $La_{2-x}Sr_xNiO_{4+\delta}$ by $^{17}O$ Solid-State NMR Spectroscopy and Ni K-edge XANES

## 4.1 Abstract

The properties of mixed ionic–electronic conductors (MIECs) are most conveniently controlled through site-specific aliovalent doping, yet few techniques can report directly on the local structure and defect chemistry underpinning changes in ionic and electronic conductivity. In this work, we perform high-resolution $^{17}O$ ($I$ = 5/2) solid-state NMR spectroscopy of $La_{2-x}Sr_xNiO_{4+\delta}$, a MIEC and prospective solid oxide fuel cell (SOFC) cathode material, showing the sensitivity of $^{17}O$ hyperfine (Fermi contact) shifts and quadrupolar nutation due to local structural changes arising from Sr-doping ($x$). Previously in Chapter 3, we resolved resonances from three distinct oxygen sites (interstitial, axial, and equatorial) in the undoped $x$ = 0 material. Here, doping-induced changes in these three spectral features indirectly report on the ionic conductivity, local octahedral tilting, and electronic conductivity, respectively, of the doped materials. In particular, the intensity of the resonance arising from mobile interstitial defects decreases, and then disappears, at $x$ = 0.5, consistent with reports of lower bulk ionic conductivity in Sr-doped phases. Secondly, local distortions among the split axial sites diminish, even on modest incorporation of Sr ($x$ < 0.1), which is also accompanied by faster spin-lattice ($T_1$) relaxation of the interstitial resonances, indicating increased mobility of these sites. Finally, the hyperfine shift of the equatorial oxygen resonance decreases due to conversion of $Ni^{2+}$ ($d^8$) to $Ni^{3+}$ ($d^7$) by charge compensation, a mechanism associated with improved electronic conductivity in the Sr-doped phases. Valence

and coordination changes of the Ni cations are further supported by Ni K-edge X-ray absorption near edge structure (XANES) measurements, which show a decrease in the Jahn-Teller distortion of the $Ni^{3+}$ sites and a Ni coordination change consistent with the formation of oxygen vacancies. Ultimately, these insights into local atomic and electronic structure that rely on $^{17}O$ solid-state NMR spectroscopy should prove accessible for a broad range of aliovalently-doped functional paramagnetic oxides.

## 4.2 Introduction

In the past three decades, the development of mixed ionic–electronic conductors (MIECs) has brought about significant advances in the design and operation of solid oxide fuel cell (SOFC) cathodes and oxygen separation membranes, as well as in chemical looping and catalytic combustion applications.[228,229,232,294–296] As these functional materials permit simultaneous conduction of ions (typically oxide ions, $O^{2-}$) and electrons, their use in *e.g.* SOFC cathodes catalytically extends the available zone of reactivity for the oxygen reduction reaction from the triple phase boundary where cathode, electrolyte, and air meet to a larger two phase boundary; this in turn enables more efficient device operation at much lower temperatures.[30,229,297]

However, because the relative ionic and electronic conductivity of a given mixed-conducting phase may not be electrochemically optimal, structural modifications and/or the introduction of alternative ions by doping are commonly used to tune the functionality. Often, this is achieved indirectly by modifying the metal cation mixed valency. As discussed in Section 1.2 as well as Chapter 3, such is the case for mixed-conducting $La_2NiO_{4+\delta}$, a notable $K_2NiF_4$-type oxide with good oxide-ion conductivity ($D^* \approx 3 \cdot 10^{-8}$ cm$^2$ s$^{-1}$ at 700 °C); its modest electronic conductivity ($\sigma$ = 50–100 S cm$^{-1}$ above room temperature) is, however, insufficient for typical SOFC applications.[51,298] One possible alternative is the use of higher-order phases belonging to the Ruddlesden-Popper family, such as $La_3Ni_2O_7$ or $La_4Ni_3O_{10}$, which exhibit significantly improved electronic conductivity.[52] Alkaline earth (*i.e.,* A site) doping of $La_2NiO_{4+\delta}$ has also been used to alter conductivity via control of the $Ni^{2/3+}$ valence state,[299] and of these doped materials, $La_{2-x}Sr_xNiO_{4+\delta}$ has shown significant promise ($\sigma \approx 250$ S cm$^{-1}$ at

$x$ = 0.75).[298,300] Previous work on this system has revealed the influence of Sr-doping on structural and transport effects, whilst noting the lack of systematic bulk variations with doping as well as a strong deviation from Vegard's rule.[301] Therefore, local structure effects are expected to play a significant role in understanding changes in the mixed conductivity of $La_{2-x}Sr_xNiO_{4+\delta}$. In particular, uncertainty persists regarding the relative contribution to the electronic conductivity of (1) variations in the lattice parameters, and (2) the electronic configuration of the B-site $Ni^{2/3+}$ cations. Moreover, the origin of apparent biphasic behavior in the highly-substituted regime ($x$ > 0.5), where the electronic conductivity is maximal, is not fully understood.[298]

In Chapter 3, the utility of solid-state $^{17}O$ NMR spectroscopy was shown in the characterization of the local structure and oxide-ion dynamics of the undoped material $La_2NiO_{4+\delta}$, in one of the first reports of solid-state $^{17}O$ magic-angle spinning (MAS) NMR of a *paramagnetic* oxide. Despite the presence of electron–nuclear spin interactions in these systems that induce large hyperfine (Fermi contact) shifts and thus complicate spectral acquisition and assignment, we nonetheless showed that the sensitivity of the paramagnetic interaction can reveal subtle, defect-induced distortions amongst local oxygen environments that prove directly relevant to the oxide-ionic conductivity mechanism. Another local structural problem tractable by a similar paramagnetic $^{17}O$ NMR approach relates to changes in the transition metal electronic structure, as previously explored by Trokiner *et al.* in doped manganites (*e.g.,* $Pr_{0.5}Ca_{0.5}MnO_3$).[302] Because unpaired spin polarization is transferred by orbital overlap from transition metal *d* orbitals to oxygen *s* orbitals, $^{17}O$ hyperfine shifts can report on details of transition metal charge and orbital ordering, and indirectly on electronic conductivity. Moreover, the arrangement of oxygen sites surrounding the metal center (equatorial vs. axial) allows in principle for the accurate determination of the electronic occupation of specific metal *d* orbitals.[303]

As with the previously studied undoped material, $La_{2-x}Sr_xNiO_{4+\delta}$ is a paramagnetic MIEC, and amenable to the solid-state $^{17}O$ MAS NMR methodology we have developed. The structure of $La_{2-x}Sr_xNiO_{4+\delta}$ consists of alternating $La_{1-x}Sr_xNiO_3$ perovskite-like layers and "$La_{2-x}Sr_xO_2$" rock salt-like layers (Figure 4.1a) that form a tetragonal (*F*4/*mmm*) or subtly orthorhombic (*Fmmm*) phase with significant unit cell anisotropy (*c*/*a* ratio ≈ 3.3).[301,304] This

layered arrangement gives rise to two distinct oxygen sites: equatorial oxygen sites ($O_{eq}$) that sit within the perovskite-like layers, and axial oxygen sites ($O_{ax}$) that bridge the layers. For small $x$, interstitial oxide ions ($O_i$) are also easily incorporated in the rock salt-like layers and comprise a third type of oxygen environment (Figure 4.1b). Since equatorial and axial sites contain spin-bearing $Ni^{2/3+}$ cations in their first shell coordination environment, their resonances experience $^{17}O$ hyperfine shifts (so-called "paramagnetic" sites), whereas the resonance arising from the $O_i$ site does not and is "diamagnetic." These interstitial defects are moreover the source of the variable oxygen hyperstoichiometry (positive value of $\delta$), commonly reported at $\delta$ = 0.1–0.2 for the undoped material under standard synthetic conditions.[54,65,261]

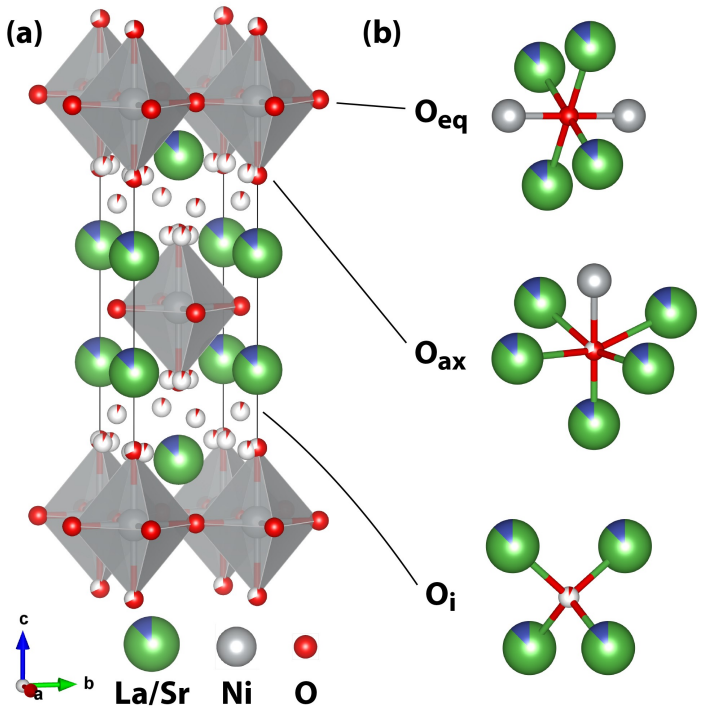


Figure 4.1: (a) Crystal structure of the tetragonal $La_{2-x}Sr_xNiO_{4+\delta}$ structure (space group $F4/mmm$), with $x$ = 0.25, as reported by Aguadero *et al.*[298] Axial oxygen sites are split into two distinct crystallographic environments, one of which is displaced. (b) Representations of the local geometry around the three oxygen environments: equatorial $O_{eq}$, axial $O_{ax}$, and interstitial $O_i$. For clarity only the undisplaced axial environment has its local coordination shown. Partially occupied or mixed occupancy sites ($O_{ax}$, $O_i$, and La/Sr) are depicted as partially filled spheres. Structures have been generated with VESTA 3.4.[305]

The rich defect chemistry of the $La_{2-x}Sr_xNiO_{4+\delta}$ system arises from charge compensation of $Sr^{2+}$ on $La^{3+}$ sites occurring through two distinct mechanisms: (1) oxidation of $Ni^{2+}$ to $Ni^{3+}$ and (2) removal of excess interstitial oxygen (or, for large $x$, formation of oxygen vacancies), which can be expressed in Kröger–Vink notation as

$$[\mathrm{Sr}'_{\mathrm{La}}] + 2[\mathrm{O}''_i] = [\mathrm{Ni}^{\bullet}_{\mathrm{Ni}}] + 2[V^{\bullet\bullet}_{\mathrm{O}}] \tag{4.1}$$

with the additional stipulation that oxygen interstitials $\mathrm{O}''_i$ and oxygen vacancies $V^{\bullet\bullet}_{\mathrm{O}}$ tend not to coexist (*i.e.*, the Frenkel disorder is minimal).[60] Previous reports have shown that these charge compensation mechanisms appear to operate simultaneously across the known substitutional range ($0 < x < 1.4$).[298,306] However, a detailed understanding of the defect chemistry is complicated by the range of stable phases with variable oxygen non-stoichiometry that can form for a given Sr content ($x$),[60] and previous results are therefore sensitive to thermal and oxidative history of the samples.

In the moderately-doped regime ($x < 0.5$), Gopalakrishnan *et al.* have reported an overall decrease in the unit cell volume on substitution of $Sr^{2+}$, ascribed to formation of the smaller low-spin $Ni^{3+}$ cation (0.56 Å), relative to $Ni^{2+}$ (0.70 Å).[301,307] A simultaneous increase in the $c$ lattice parameter and a decrease in $a$ (= $b$) is also observed in this regime, which has been explained by a greater concentration of Jahn-Teller elongated low-spin $Ni^{3+}$ cations ($t_{2g}^6 e_g^1$). However, with further Sr-doping ($x \geq 0.5$) this trend reverses, and $c$ decreases sharply while $a$ increases gradually. Gopalakrishnan *et al.* and others have ascribed this behavior to a change in the Jahn-Teller distortion from elongation to contraction on electronic crossover from $t_{2g}^6 d_{z^2}^1$ to $t_{2g}^6 d_{x^2-y^2}^1$.[301,308] On the other hand, Takeda *et al.* argue that the Jahn-Teller distortion remains an elongation, and a constant linear decrease in the distortion occurs with Sr-doping, suggesting a much more gradual electronic crossover.[58] It should be noted, however, that these conclusions generally disregard the influence of oxygen non-stoichiometry in the system; in undoped and lightly Sr-doped $La_2NiO_{4+\delta}$, the removal of interstitial oxygen (decreasing $\delta$) also leads to a decrease in the $c$ and an increase in the $a$ lattice parameters, consistent with closer layer spacing and less intralayer disorder.[261,263,275,309] Thus, the lattice parameters of heavily Sr-doped samples, with a negligible concentration of

interstitials and/or the highest concentration of oxygen vacancies, may also be dominated by effects arising from oxygen non-stoichiometry.

The structural and electronic changes arising from the defect chemistry of $La_{2-x}Sr_xNiO_{4+\delta}$ directly impinge on the ionic and electronic conductivity; these vary in an opposite fashion with increasing Sr incorporation. With regards to oxide-ionic conductivity, Vashook *et al.* have noted the correlation between decreasing oxygen content ($\delta$) and lower oxygen permeability flux at high temperatures, although at intermediate temperatures (below 750 °C) the functional difference in conductivity appears small between moderately-doped samples ($0 < x < 0.4$).[306] Inprasit *et al.* have found decreases by one to two orders of magnitude in both oxygen tracer diffusion coefficients ($D^*$) and surface exchange coefficients ($k^*$) for $La_{1.9}Sr_{0.1}NiO_{4+\delta}$ and $La_{1.9}Sr_{0.2}NiO_{4+\delta}$ compared to $La_2NiO_{4+\delta}$ at elevated temperatures;[310] these somewhat reduced values nonetheless compare favorably to other promising MIECs such as $La_{1-x}Sr_xCo_{1-y}Fe_yO_{3-\delta}$.[51]

By contrast, many studies have shown an *increase* in electronic (*p*-type) conductivity of $La_{2-x}Sr_xNiO_{4+\delta}$ with increasing $x$, in agreement with doping of holes into the $\sigma^*$ band of Ni $d_{x^2-y^2}$ parentage due to conversion of $Ni^{2+}$ ($d^8$) to $Ni^{3+}$ ($d^7$).[58,77,298,299] Takeda *et al.* also report a discontinuous drop in the semiconductor-metal transition temperature at $x = 0.6$ that coincides with the maximum in the unit cell anisotropy ($c/a$ ratio), suggesting that samples with $x > 0.6$ exhibit metallic-like conductivity.[58]

Others have speculated that the increase in electronic conductivity observed on Sr-doping of $La_2NiO_{4+\delta}$ arises not only from changes in the electronic configuration but also from lattice parameter variations. Ishikawa *et al.* have previously observed that the semiconductor-metal ratio of $La_{2-x}Sr_xNiO_{4+\delta}$ tracks closely with the *c* lattice parameter.[311] Separately, Aguadero *et al.* have suggested that the electronic conductivity inversely correlates with the $Ni–O_{eq}$ bond length.[298] The latter observation in particular suggests that changes in the average ionic radius and changing Jahn-Teller distortion of the Ni sites indirectly influence the electronic conductivity. These connections between bulk conductivity and atomic-level details highlight the importance of local structure probes in studying $La_{2-x}Sr_xNiO_{4+\delta}$.

Finally, reports of the existence of a biphasic region with significant Sr incorporation ($x > 0.5$) are inconsistent in the literature, with both positive[298,310,312] as well as negative[58,301,308,313] findings. This compositional range is, however, of particular importance in understanding the origin of the maximal electronic conductivity. Heaney *et al.* have reported two monoclinic (*F*112/*m*) phases coexisting for nominal compositions of both $x = 0.7$ and $x = 1.0$, *viz.* an insulating, Sr-poor phase, and a more conductive Sr-rich phase.[312] Similarly, Aguadero *et al.* identify two tetragonal (*F*4/*mmm*) phases for $x = 0.75$ and $x = 1.0$. For the latter sample, they determine on the basis of lattice parameter changes that the true Sr content of both coexisting phases is less than the nominal value of $x$; however, in the absence of additional Sr-containing phases, it remains unclear how residual $Sr^{2+}$ would be accommodated in that case. Again, the application of local structural techniques to this system could indicate the extent of dopant segregation and moreover the true doping level, through measurements of the average Ni valence.

In this work, we report a systematic investigation of the $La_{2-x}Sr_xNiO_{4+\delta}$ materials ($0 < x \leq 1$) with $^{17}O$ solid-state NMR spectroscopy, and, for select phases, Ni K-edge X-ray absorption near-edge structure (XANES) spectroscopy. We first show that moderately-doped phases ($0.1 \leq x \leq 0.3$) evidence a clear reduction in the concentration of interstitial sites ($O_i$), as well as the local distortion surrounding the axial environments ($O_{ax}$). To probe this more closely, we study the low-doping region ($x < 0.1$) and find that even very modest doping ($x = 0.025$) leads to a loss of the cooperative axial splitting, consistent with the tetragonal (rather than orthorhombic) symmetry generally reported for these phases. However, these changes are also accompanied by concomitant decreases in the $^{17}O$ spin-lattice ($T_1$) relaxation times of the interstitial defect resonances, suggesting the $O_i$ sites may become more mobile even at room temperature upon Sr incorporation. Next, we explore the changing shift of the equatorial oxygen resonance ($O_{eq}$), which indicates the evolving electronic occupation and structure of the Ni cations. We also confirm an increase in the average Ni oxidation state approaching $Ni^{3+}$ using results from Ni K-edge XANES. In contrast to some previous conclusions, the $O_{ax}$ and $O_{eq}$ shift data suggest that only a partial electronic crossover of the $Ni^{3+}$ orbital occupation occurs, *i.e.*, the occupation remains mostly $t_{2g}^6 d_{z^2}^1$, rather than $t_{2g}^6 d_{x^2-y^2}^1$, up to $x = 1.0$. Finally, changes in the paramagnetic broadening as well as the quadrupolar coupling

constants of the $O_{ax}$ and $O_{eq}$ sites indicate significant substitutional heterogeneity in the highly-doped samples ($x > 0.5$), in agreement with previous reports, although we argue that $Sr^{2+}$ remains incorporated at the nominal doping content for these compositions. Throughout, we show that local structural details are key to understanding lattice parameter variations and changes in the ionic and electronic conductivity. In particular, the spectral features of the various oxygen environments act as indirect surrogates of bulk properties (*e.g.*, the $O_i$ resonance as a probe of ionic conductivity). The insights obtained herein also prove applicable to other isostructural phases that necessitate incorporation of aliovalent dopants for their structural stability, *e.g.*, the $Sm_{2-x}Sr_xNiO_{4+\delta}$ and $Nd_{2-x}Sr_xNiO_{4+\delta}$ materials (Section 4.6).[57]

## 4.3 Experimental and theoretical methods

### 4.3.1 Synthesis, $^{17}$O-enrichment and characterization

Polycrystalline samples of $La_{2-x}Sr_xNiO_{4+\delta}$ ($x$ = 0.01, 0.025, 0.05, 0.1, 0.2, 0.3, 0.5, 0.75, and 1.0) were prepared by solid-state reaction as described elsewhere.[273,314] Stoichiometric amounts of $La_2O_3$ (Alfa Aesar, REacton, 99.999%; pre-dried), $SrCO_3$ (Sigma-Aldrich, 99.995%; pre-dried) and NiO (Aldrich, 99.999%) were mixed together in a mortar and pestle, isostatically pressed, sintered in air at 1350 °C for 12 h, and ground into powder. Several intermediate sintering and grinding steps were performed until >95 wt. % phase purity was achieved, as determined by laboratory powder X-ray diffraction (Figure 4.2). $^{17}$O-enriched samples of $La_{2-x}Sr_xNiO_{4+\delta}$ were obtained by heating the as-synthesized powder (~0.2 g) to 1000 °C under an atmosphere of 70% $^{17}O_2$ (CortecNet, used as received) in a sealed quartz tube. Samples were slowly cooled from the enrichment temperature to maximize uptake of $^{17}$O.

Phase purity of samples before and after $^{17}$O-enrichment was determined with powder X-ray diffraction (XRD) using a Panalytical Empyrean X-ray diffractometer equipped with a Cu K$\alpha$ source ($\lambda$ = 1.5406 and 1.5418 Å) and X'celerator CCD detector. Scans were performed on a spinning sample stage in reflection mode over the range $2\theta$ = 5° to 80° (with step size $2\theta$ = 0.0167°). Diffraction patterns were analyzed with the X'Pert HighScore Plus software

package (Panalytical) and associated PDF pattern database. Rietveld refinements were performed with the GSAS and EXPGUI software packages.[266,267]

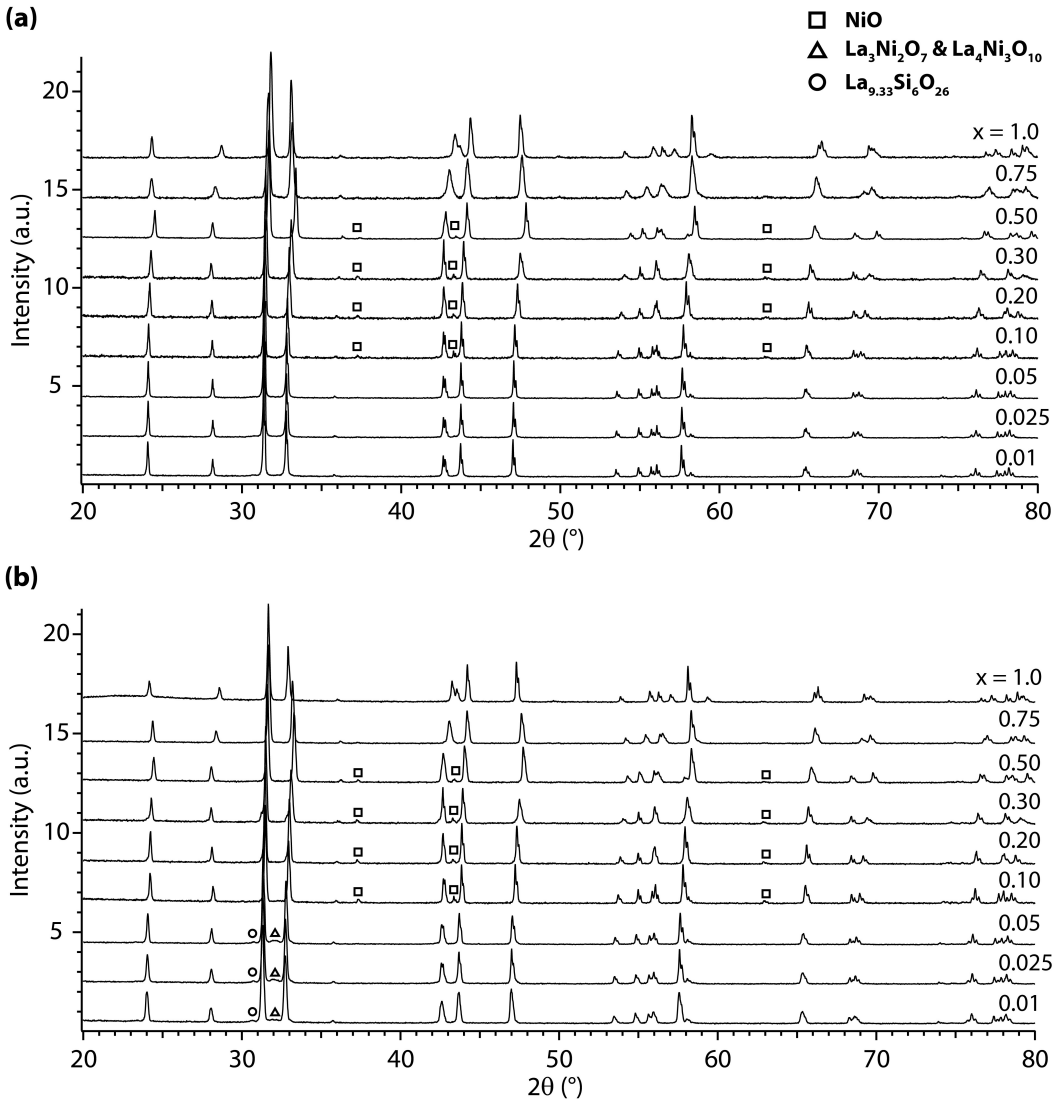


Figure 4.2: Powder XRD patterns of $La_{2-x}Sr_xNiO_{4+\delta}$ samples, both (a) as-synthesized and (b) following $^{17}O$-enrichment. Minor impurity phases (NiO, $La_3Ni_2O_7$/$La_4Ni_3O_{10}$, and $La_{9.33}Si_6O_{26}$) are indicated where apparent; all other reflections correspond to the primary orthorhombic (*Fmmm*) phase $La_{2-x}Sr_xNiO_{4+\delta}$. While the reflections between 30.6–30.9° are not by themselves diagnostic for $La_{9.33}Si_6O_{26}$, other $^{17}O$-enriched samples with much greater impurity content (not studied further) show both these and other reflections that corroborate the assignment. (The most intense reflections for the orthorhombic *Amam* $La_3Ni_2O_7$ and *Fmmm* $La_4Ni_3O_{10}$ phases, which are (115) and (117), respectively, typically overlap and are thus difficult to distinguish.)

### 4.3.2 Solid-state NMR spectroscopy

Solid-state $^{17}$O MAS NMR experiments were carried out on a 4.7 T Bruker Avance III 200 MHz spectrometer using a Bruker 1.9 mm HX probe. As described in Section 2.1.2.1, spin-echo mapping (variable offset cumulative spectroscopy, VOCS[142,144,146]) experiments were performed under a MAS frequency of 40 kHz using a rotor-synchronized Hahn echo pulse sequence of the form $(\pi/6)_x$–$\tau$–$(\pi/3)_y$–$\tau$–acquire [or $(\pi/2)_x$–$\tau$–$(\pi)_y$–$\tau$–acquire] with a pulse length of 0.8 $\mu$s ($\pi/6$ for liquid $H_2O$) [or 2.4 $\mu$s ($\pi/2$ for liquid $H_2O$)] at an inherent rf field strength of ~104 kHz and a recycle delay of 12 ms. The pulse carrier frequency step size was 2500 ppm (~68 kHz), *i.e.*, smaller than the rf field strength. Projection magic-angle turning and phase-adjusted sideband separation (MATPASS) NMR experiments[153] (see Section 2.1.2.2) were also performed with rotor synchronization at a MAS rate of 40 kHz, employing a series of five $\pi/6$ (or $\pi/2$) pulses. For some samples ($x$ = 0.75 and 1.0), additional MATPASS experiments were recorded using $\pi/4$ pulses with pulse lengths of 1.2 $\mu$s. For all MATPASS spectra, the pulse carrier frequency offset was fixed at 3000 ppm (or 1500 ppm, for the $x$ = 1.0 sample). A total of eight $t_1$ increments were recorded in each MATPASS experiment; the recycle delay was 60 ms. Values of the spin-lattice ($T_1$) relaxation were measured with standard saturation-recovery experiments with maximal delay of 0.6 s (for $O_i$ resonances) and 20 ms (for $O_{ax}$ and $O_{eq}$ resonances). All $^{17}$O chemical shifts were externally referenced to $^{17}$O-enriched $CeO_2$ at 877 ppm.[315,316] NMR spectra were processed and deconvoluted with the Bruker TopSpin 3.2[271] and dmfit[272] sofware packages.

### 4.3.3 Ni K-edge XANES measurements

Ni K-edge spectra were collected in transmission geometry at the Diamond Light Source (Didcot, UK) using beamline B-18 (courtesy of Dr Michael Gaultois, University of Cambridge). The materials studied were the $^{17}$O-enriched $x$ = 0, 0.1, 0.2, 0.3, 0.5, 0.75, and 1.0 phases. Samples were finely ground, intimately mixed with cellulose, and pressed to form pellets of appropriate optical density for transmission experiments. Transmission spectra were collected at room temperature with a step size of 0.2 eV through the absorption edge, and the incident photon energy was calibrated using a Ni metal foil ($E_0$ = 8333 eV) positioned behind the sample. No drift in energy was observed during the experiment.

## 4.4 Results

Three series of $La_{2-x}Sr_xNiO_{4+\delta}$ samples were synthesized: the lightly-doped ($x$ = 0.01, 0.025, 0.05), moderately-doped ($x$ = 0.1, 0.2, 0.3), and highly-doped ($x$ = 0.5, 0.75, 1.0) phases. All samples were obtained as black or very dark brown (for $x$ = 0.75, 1.0) powders; a similar color change for these compositions was also noted by Cava *et al.*[308] and Liu *et al.*[313] Following synthesis and characterization by XRD, all samples were $^{17}$O-enriched, again checked by XRD, and then studied by solid-state $^{17}$O MAS NMR spectroscopy. In the following, results have been compared to the previous data in Chapter 3 on samples of the undoped material $La_2NiO_{4+\delta}$, with $\delta = 0.15–0.17$ (as determined by TGA) following $^{17}$O-enrichment.

### 4.4.1 XRD

Laboratory XRD data show that the primary $La_{2-x}Sr_xNiO_{4+\delta}$ phase (space group $F4/mmm$) comprises the predominant majority (> 92 wt. %) of all as-synthesized and $^{17}$O-enriched samples (Figure 4.2 and Figure 4.3). Most samples with $x \geq 0.1$ have a variable amount of a secondary NiO impurity, estimated at 3–6 wt. % from Rietveld analysis. Aguadero *et al.* have also observed a significant NiO content in Sr-rich compositions, up to 18 wt. % for $x$ = 1, associated with difficulties in sintering the highly-doped phases to attain stoichiometric incorporation of Ni.[58,298] No impurities are observed in the as-synthesized samples with $x < 0.1$.

Following $^{17}$O-enrichment at 1000 °C, several samples show evidence of weak reflections due to the presence of higher-order Ruddlesden-Popper phases such as $La_3Ni_2O_7$ and $La_4Ni_3O_{10}$ (Figure 4.3b and Figure 4.4),[288,317] which is consistent with the known decomposition of $La_2NiO_{4+\delta}$ at high temperatures and under highly oxidizing conditions.[63,276] The maximum content of these higher-order phases is estimated at 5 wt. %, and they appear to a significant degree only in the $^{17}$O-enriched, lightly-doped samples ($x < 0.1$). Additionally, these samples contain 1–2 wt. % of a $La_{9.33}Si_6O_{26}$ impurity phase, as indicated by characteristic reflections between 30.6–30.9° (Figure 4.4).[318] From previous $^{17}$O MAS NMR results, the formation of lanthanum silicate is likely due to reaction with the quartz

($SiO_2$) tube during the $^{17}$O-enrichment procedure;[319] however, in the study of $La_2NiO_{4+\delta}$ in Chapter 3, this minimal amount of $La_{9.33}Si_6O_{26}$ was not detected by lab-based diffraction.

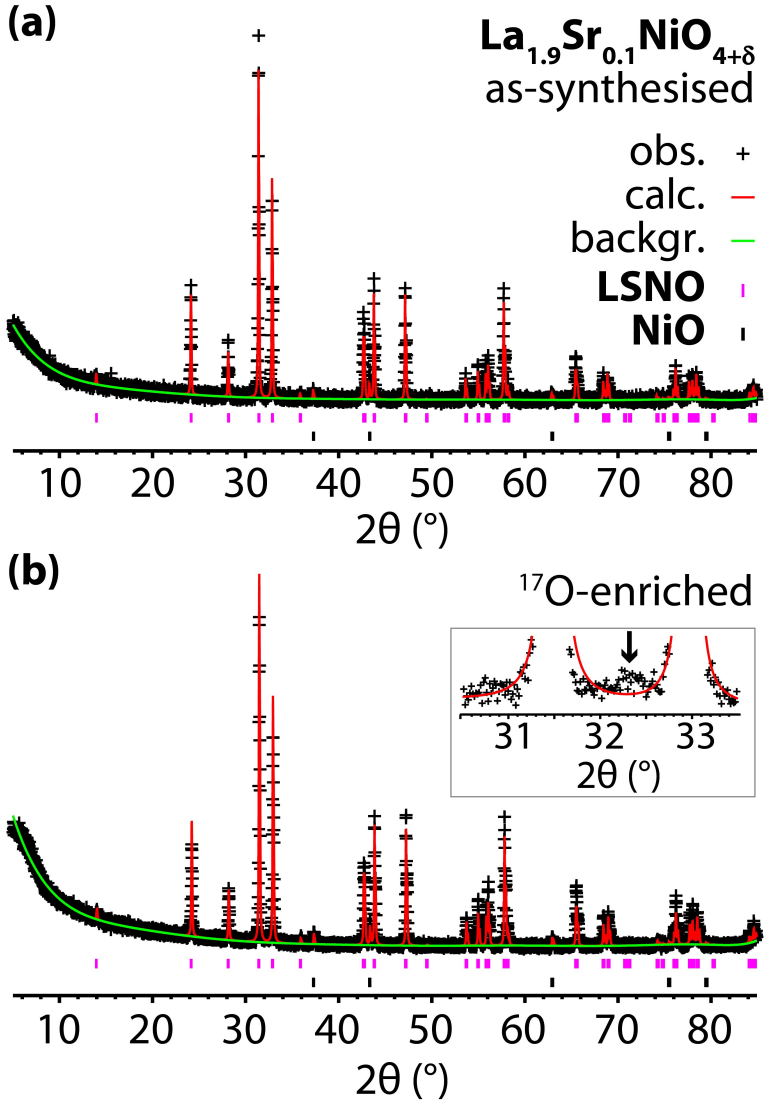


Figure 4.3: Raw XRD data (black crosses) and calculated patterns from Rietveld refinement (red traces) of the representative sample $La_{1.9}Sr_{0.1}NiO_{4+\delta}$, both (a) as-synthesized and (b) following $^{17}$O enrichment at 1000 °C; the first set of tick marks (in pink) indicates the reflections of the *F*4/*mmm* $La_{2-x}Sr_xNiO_{4+\delta}$ phase ("LSNO"), and the second set (in black) indicates the minor $Fm\bar{3}m$ NiO impurity phase, here ~6 wt. % for both samples. In an exploded view (inset), the arrow indicates the (117) reflection of the higher-order Ruddlesden-Popper phase $La_4Ni_3O_{10}$ (space group *Fmmm*), which is estimated at <1 wt. % of the $^{17}$O-enriched sample.

All XRD patterns of $La_{2-x}Sr_xNiO_{4+\delta}$ have been refined in the tetragonal *F*4/*mmm* model. Unlike the work of Aguadero *et al.* and Heaney *et al.*,[298,312] no significant improvement in the fit is obtained by adopting a two-phase model for samples in the highly-doped region, although broadening of the (00*l*) reflections suggests compositional heterogeneity (Section 4.5.5). The refined lattice parameters in the moderately-doped regime ($0.1 \leq x < 0.5$) are in good agreement with the previous study (Figure 4.5), as well as the general finding that with increased Sr incorporation, the *a* (= *b*) lattice parameters decrease whereas the *c* lattice parameter increases, with a modest overall decrease in the unit cell volume. Additionally, for any given composition in this regime, the change in the lattice parameters induced by $^{17}$O-enrichment (increase in *c* and decrease in *a*, *b*) is consistent with the incorporation of additional interstitial oxygen, as shown for $La_2NiO_{4+\delta}$ (Figure 3.5).

In the highly-doped region ($x > 0.5$), the refined *a* and *b* lattice parameters increase modestly while the *c* lattice parameter decreases dramatically (Figure 4.6), in good qualitative agreement with previous reports,[58,301,308] and consistent with a smaller Jahn-Teller elongation of the Ni cations. Although the refined lattice parameters for the $x = 1.0$ sample do not fall in the range of those of either phase of the comparable sample reported by Aguadero *et al.*, they are in excellent agreement with the sample prepared by Takeda *et al.*[58] This discrepancy is attributed in part to variations in the NiO impurity content (<2 wt. % in this work, and 18 wt. % in the study of Aguadero *et al.*), that lead to divergent sample compositions. (The lattice parameters of the phases obtained in the nominally $x = 1.0$ sample of Aguadero *et al.* are however consistent with actual Sr content values of $x = 0.5$ and $x = 0.6$, as they also previously suggested.) Finally, the effect of $^{17}$O-enrichment on the refined lattice parameters also reverses with respect to the moderately-doped samples. Enrichment increases the *a* and *b* parameters and decreases the *c* parameter, reflecting the negative value of $\delta$ in this regime. That is, a chemical contraction occurs with decrease in the vacancy concentration expected for samples prepared under higher oxygen partial pressures.[320]

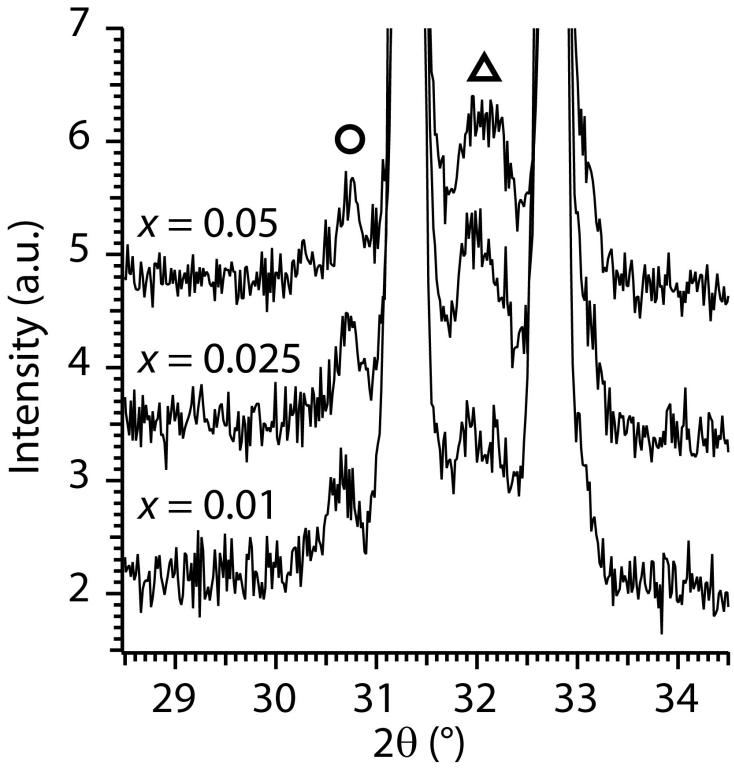


Figure 4.4: Powder XRD patterns of $^{17}$O-enriched $La_{2-x}Sr_xNiO_{4+\delta}$ ($x$ = 0.01, 0.025, 0.05), showing appearance of the (211), (311), and (112) reflections of the trigonal $P\bar{3}$ phase $La_{9.33}Si_6O_{26}$ at $2\theta$ = 30.7–30.9° (marked with open circle) and the (115) and (117) reflections of the orthorhombic *Amam* $La_3Ni_2O_7$ and *Fmmm* $La_4Ni_3O_{10}$ phases, respectively, at $2\theta$ = 31.7–32.4° (marked with open triangle). The small shift (~0.1°) to higher $2\theta$ with increasing $x$ occurs systematically for all reflections and is attributed to sample displacement. The shoulder at $2\theta$ = ~33° arises from the (200) reflections of both the $La_3Ni_2O_7$ and $La_4Ni_3O_{10}$ phases.

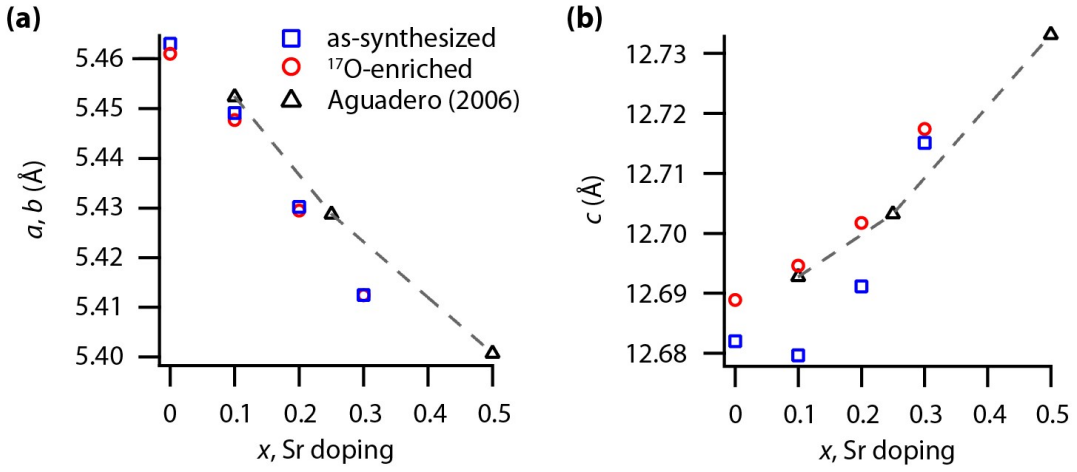


Figure 4.5: Changes in the (a) *a* and *b* lattice parameters, and (b) *c* lattice parameter, as a function of Sr-doping (*x*) in the moderately-doped samples ($0.1 \leq x \leq 0.5$), for as-synthesized samples (blue) and following $^{17}$O-enrichment (red). Lattice parameters have been obtained from Rietveld refinement by using the powder XRD data and the *F*4/*mmm* structure reported by Aguadero *et al.*,[298] and compared to the values in the previous study (black); the dotted line is a guide to the eye connecting the data points obtained previously. In the case of the undoped $x = 0$ phase, the lattice parameter values are taken from the work in Chapter 3; as this phase is orthorhombic, the average of the *a* and *b* lattice parameters is plotted in (a). Errors are within the symbols.

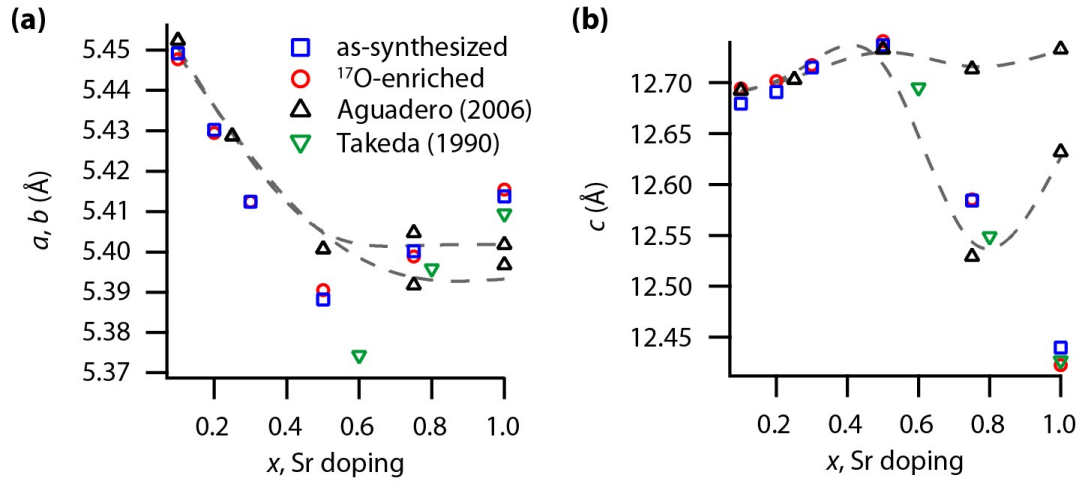


Figure 4.6: Changes in the (a) *a* and *b* lattice parameters, and (b) *c* lattice parameter, as a function of Sr-doping (*x*) in the moderately- and highly-doped samples ($0.1 \leq x \leq 1$), both as-synthesized (blue) and following $^{17}$O-enrichment (red). Lattice parameters have been obtained from Rietveld refinement using the powder XRD data and the *F*4/*mmm* structure reported by Aguadero *et al.*,[298] and compared to the values in the previous study (black), as well as the study of Takeda *et al.*[58] (green); the dotted lines (spline fits) are guides to the eye connecting the data points obtained previously. Where the earlier study reports two-phase behavior of highly-doped samples ($x = 0.75$ and 1.0), two sets of lattice parameters are depicted. Errors are within the symbols.

### 4.4.2 $^{17}$O solid-state NMR

$^{17}$O MAS NMR spectra of the moderately-doped samples ($0.1 \leq x \leq 0.3$) of $La_{2-x}Sr_xNiO_{4+\delta}$ (Figure 4.7) reveal the equatorial ($O_{eq}$), axial ($O_{ax}$), and interstitial ($O_i$) resonances also observed and assigned in the study of the undoped $La_2NiO_{4+\delta}$ sample (Figure 3.1). Because the presence of spinning sidebands would otherwise obscure the subtle splitting of the axial resonances into multiple features (Figure 4.8), we generally present sideband-suppressed spectra obtained from magic angle turning and phase adjusted sideband separation (MATPASS) experiments; this technique has previously been shown to produce "infinite"-MAS spectra, even in the case of quadrupolar nuclei affected by large hyperfine shifts.[153,283] In these spectra, the resonances from the equatorial environments ($O_{eq}$) in close proximity to two Ni cations exhibit the largest shifts of 6500–7000 ppm, whereas the resonances from axial sites ($O_{ax}$) with only one nearby Ni cation have a correspondingly weaker hyperfine interaction, and hence a smaller shift (centered at 4200 ppm; split into several features). The $O_{ax}$ splitting results from a local structural distortion induced by oxide interstitial defects. The resonance from the interstitial defect site ($O_i$) appears in the diamagnetic region at 532 ppm, in the known 530–590 ppm range of tetrahedral $OLa_4$ environments.[277,285]

The equatorial environment has a significantly larger quadrupole coupling constant ($C_Q$) (as shown for the undoped compound both experimentally and via DFT calculations) which is a measure of the local charge and bonding asymmetry. Quadrupolar filtering could therefore be used to separate contributions from the equatorial and axial oxygen resonances. In practice, this spectral editing technique entails acquiring spectra with both short ($\pi/6$) radiofrequency (rf) pulses, in which resonances from all sites appear, and long ($\pi/2$) rf pulses, which selectively suppress resonances from large-$C_Q$ sites, *i.e.*, only $O_{eq}$.

With increasing Sr content, the major change observed in the $O_{eq}$ feature is a gradual shift towards lower frequency, from 7000 ppm in the undoped sample to 6500 ppm at $x = 0.3$. By contrast, the center of mass of the $O_{ax}$ feature does not change, but the splitting of axial sites seen in the undoped sample entirely disappears, even at $x = 0.1$, and this resonance narrows significantly with greater Sr incorporation. Finally, the intensity of the resonance from the $O_i$

site decreases dramatically, and this resonance is not clearly observed in either of the MATPASS spectra of the $x = 0.3$ sample.

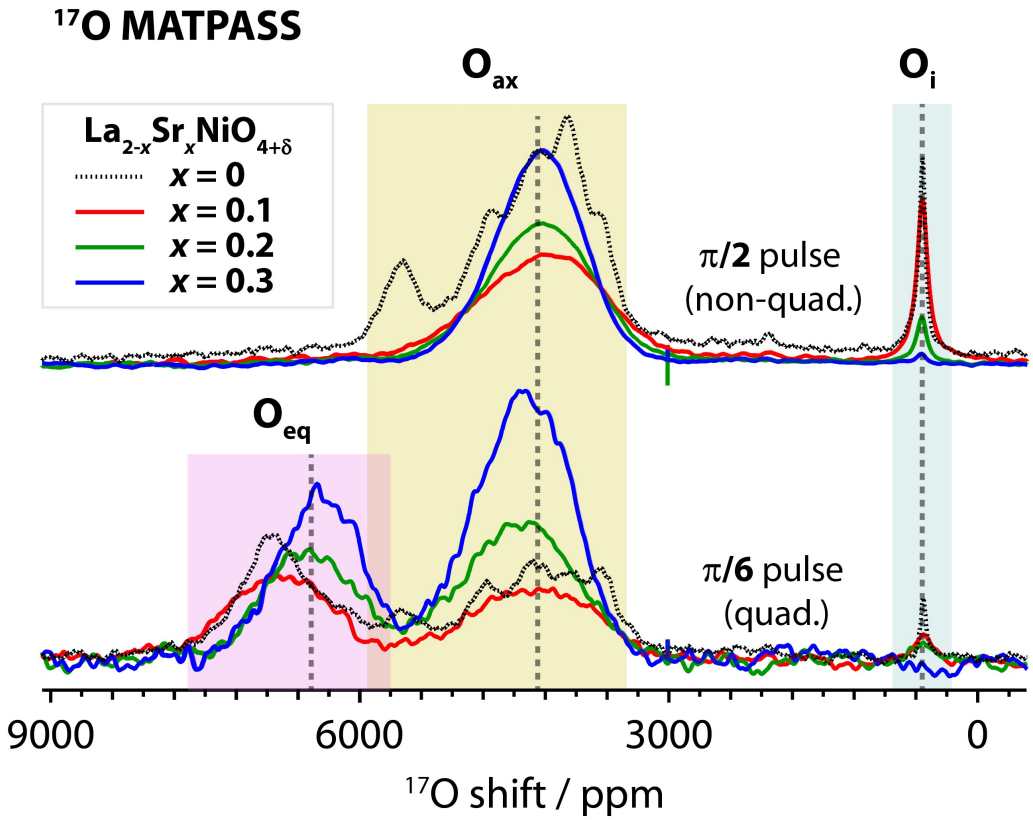


Figure 4.7: $^{17}$O MATPASS NMR spectra of the moderately-doped samples ($0.1 \leq x \leq 0.3$) of $La_{2-x}Sr_xNiO_{4+\delta}$, with the corresponding spectrum of the undoped sample ($La_2NiO_{4+\delta}$) for reference. The range of shifts for the $O_{eq}$, $O_{ax}$, and $O_i$ features are highlighted in magenta, yellow, and cyan boxes, respectively. The resonance from the highly quadrupolar environment $O_{eq}$ is only observed in spectra acquired with a shorter pulse length ($\pi/6$), as expected from quadrupolar nutation effects. Splitting of the $O_{ax}$ feature into multiple resonances is only resolved in the undoped $x = 0$ sample. Spectra have been collected at 4.7 T with a MAS rate of 40 kHz.

In order to probe more closely the sudden changes in the $O_{ax}$ and $O_i$ features between $x = 0$ and $x = 0.1$, a series of lightly-doped samples ($x = 0.01$, 0.025, 0.05) have been studied. Figure 4.9 shows the $^{17}$O MATPASS spectra of these phases acquired with a longer $\pi/2$ rf pulse in order to enhance the relative intensity of the $O_{ax}$ resonance(s), with the equivalent spectrum of the undoped sample for comparison. Only for the undoped and $x = 0.01$ samples does a characteristic $O_{ax}$ lineshape appear that is indicative of splitting of the axial sites into several locally distorted environments. In particular, the highest frequency shift at 5600 ppm

that is associated with the most displaced $O_{ax}$ sites has largely vanished by $x$ = 0.025, suggesting the $O_{ax}$ distortion is lost upon very modest doping. (These spectra also contain minor resonances at 2000 and 2400 ppm previously associated in Figure 3.16 with the higher-order Ruddlesden-Popper impurity phases, namely $La_3Ni_2O_7$ and $La_4Ni_3O_{10}$, in good agreement with the XRD results.)

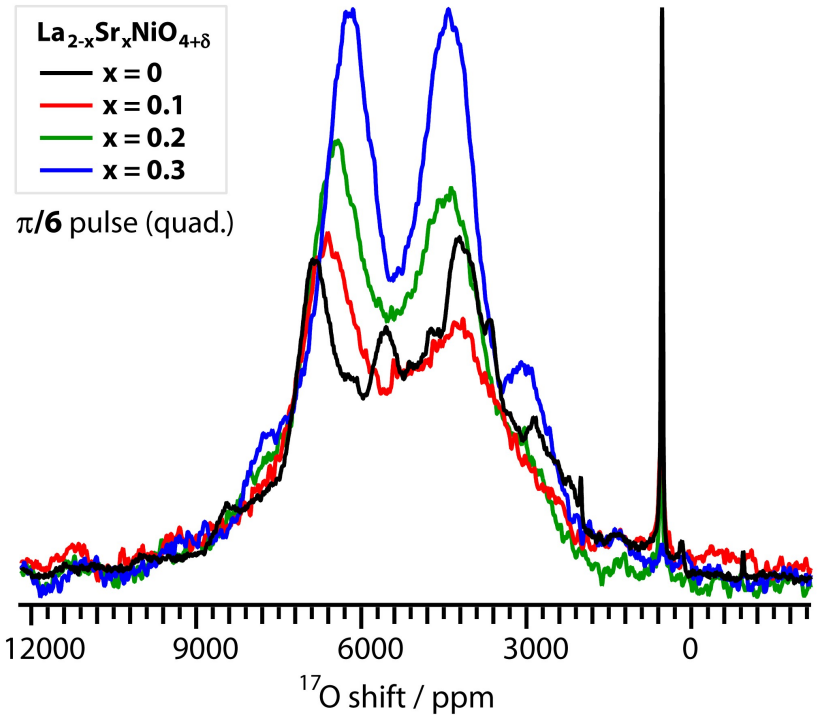


Figure 4.8: Spin-echo $^{17}O$ NMR spectra of $La_{2-x}Sr_xNiO_{4+\delta}$ ($x$ = 0, 0.1, 0.2, and 0.3) acquired as variable-offset cumulative spectra (VOCS) with a shorter pulse length ($\pi/6$). Resonances from the paramagnetic $O_{eq}$ and $O_{ax}$ sites cannot be individually deconvoluted due to spinning sideband overlap. Spectra have been collected at 4.7 T with a MAS rate of 40 kHz.

For these samples, the decrease in the intensity of the $O_i$ feature with Sr doping appears more clearly in Hahn echo spectra (Figure 4.10), which have been recorded under quantitative conditions. In the lightly-doped samples, a moderate decrease in the $O_i$ intensity occurs between $x$ = 0.01 and $x$ = 0.025 (Figure 4.10a), and this is also correlated with the loss of axial splitting in these samples (Figure 4.9; Section 4.5.3). Figure 4.10b shows that the resonance from the $O_i$ site at 532 ppm has mostly disappeared by $x$ = 0.3, and is roughly the same intensity as additional weak features at 585 and 468 ppm assigned to $OLa_4$ and $OLa_6$ in $La_2O_3$,[277] which comprises a very minor impurity phase in these samples. These results imply

the loss of nearly all the interstitial defects in $La_{2-x}Sr_xNiO_{4+\delta}$ at $x = 0.3$ (Section 4.5.2). In all spectra, the interstitial defect sites resonate at 532 ppm, indicating no discernible change in the chemical environment of these sites.

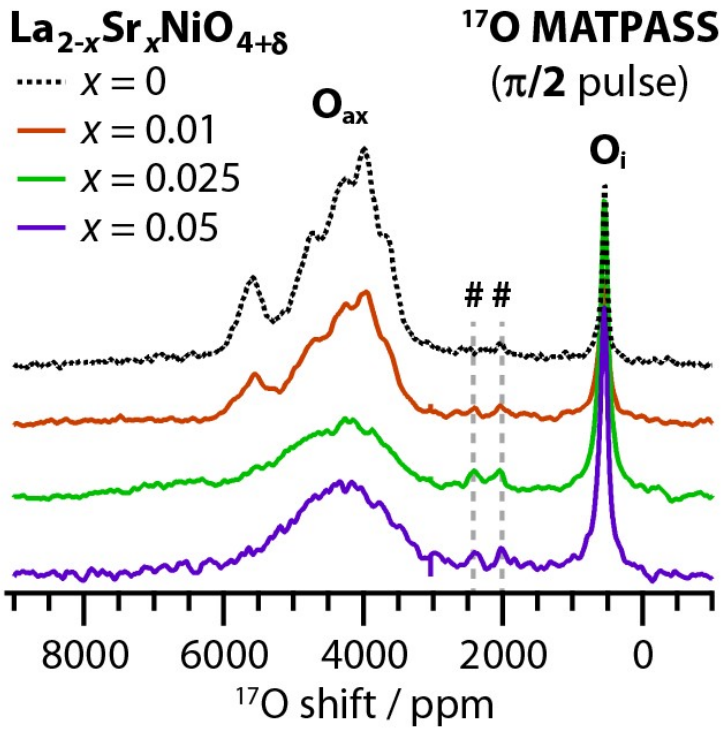


Figure 4.9: $^{17}O$ MATPASS NMR spectra of the lightly-doped samples ($0.01 \leq x \leq 0.05$), with the corresponding spectrum of the undoped sample $La_2NiO_{4+\delta}$ (black) for reference. A longer rf pulse length ($\pi/2$) has been used, suppressing the $O_{eq}$ feature but providing additional signal intensity from the $O_{ax}$ feature(s). Splitting of $O_{ax}$ into multiple resonances is resolved in the undoped and $x = 0.01$ samples. Minor resonances at 2400 and 2000 ppm (denoted with #) are consistent with the $^{17}O$ shifts expected from higher-order phases, *e.g.*, $La_3Ni_2O_7$ and $La_4Ni_3O_{10}$ (cf. Figure 3.16). Spectra have been acquired at 4.7 T with a MAS rate of 40 kHz.

Finally, by recording spectra of the highly-doped ($x = 0.5$, 0.75, 1.0) phases (Figure 4.11), we have followed the doping-induced changes in the $O_{eq}$ feature, moving towards smaller shifts. At $x = 0.5$, the $O_{eq}$ resonance undergoes a jump towards lower frequency but also broadens significantly (Figure 4.11a); this trend continues for $x = 0.75$ and $x = 1.0$ (Figure 4.11b, c), such that the $O_{eq}$ and $O_{ax}$ resonances begin to overlap and can no longer be resolved on the basis of their shifts alone. Instead, quadrupolar filtering reveals that at $x = 0.75$, the resonance from the equatorial environment actually possesses on average a *smaller* shift than the resonance from the axial site, although both features are also significantly broadened. The

overlapping feature shifts to even lower frequency (~2000 ppm) at $x$ = 1.0; thus, the $O_{eq}$ resonance undergoes a massive, maximal displacement of 5000 ppm across the entire compositional range (Figure 4.12).

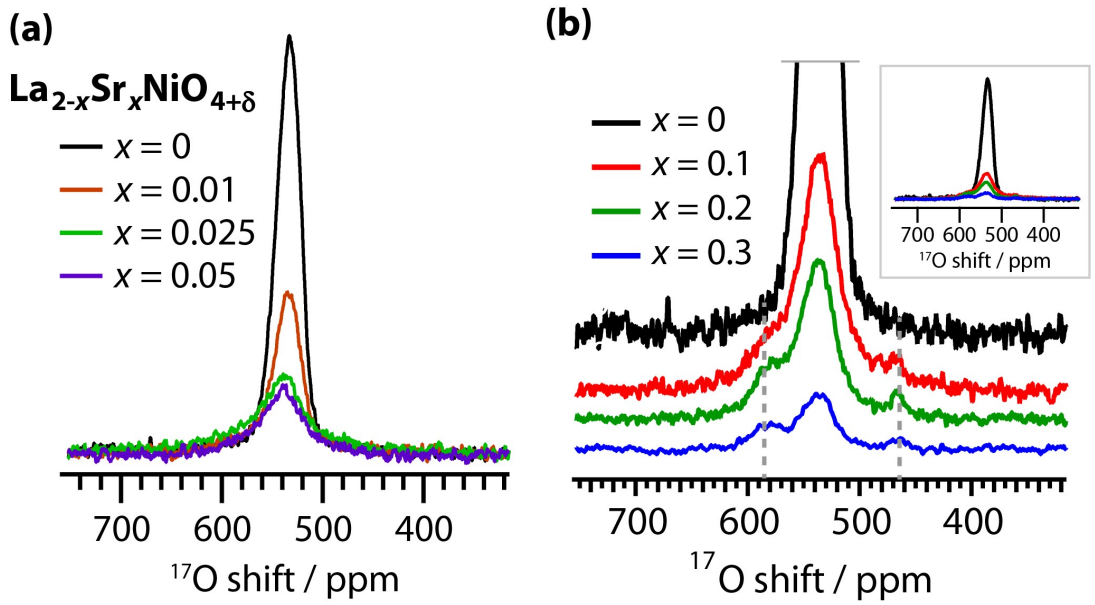


Figure 4.10: $^{17}$O Hahn echo spectra of the (a) lightly-doped ($0.01 \leq x \leq 0.05$) and (b) moderately-doped ($0.1 \leq x \leq 0.3$) $La_{2-x}Sr_xNiO_{4+\delta}$ samples, with the equivalent spectrum of the undoped material ($x$ = 0), focusing on the diamagnetic region and the interstitial $O_i$ resonance (532 ppm). Spectra in (b) are presented as a stack plot for clarity; the inset shows the full intensity of the $x$ = 0 sample for comparison. Spectra have been collected with a quantitative recycle delay and the signal intensity of the $O_i$ feature is therefore proportional to the concentration of these sites ($\delta$) in each sample. Weak features at 585 and 468 ppm (grey dotted lines) corresponding to $OLa_4$ and $OLa_6$ in a minor $La_2O_3$ impurity phase are also observed in (b). Very weak features observed at 160–170 ppm in the $x$ = 0.025 and $x$ = 0.05 samples (not depicted) are tentatively assigned to $La_{9.33}Si_6O_{26}$, which also appears as a minor impurity phase (1–2 wt. %) in the corresponding XRD data (Figure 4.2). Spectra have been acquired at 4.7 T with a MAS rate of 40 kHz, using a $\pi/2$ rf pulse length.

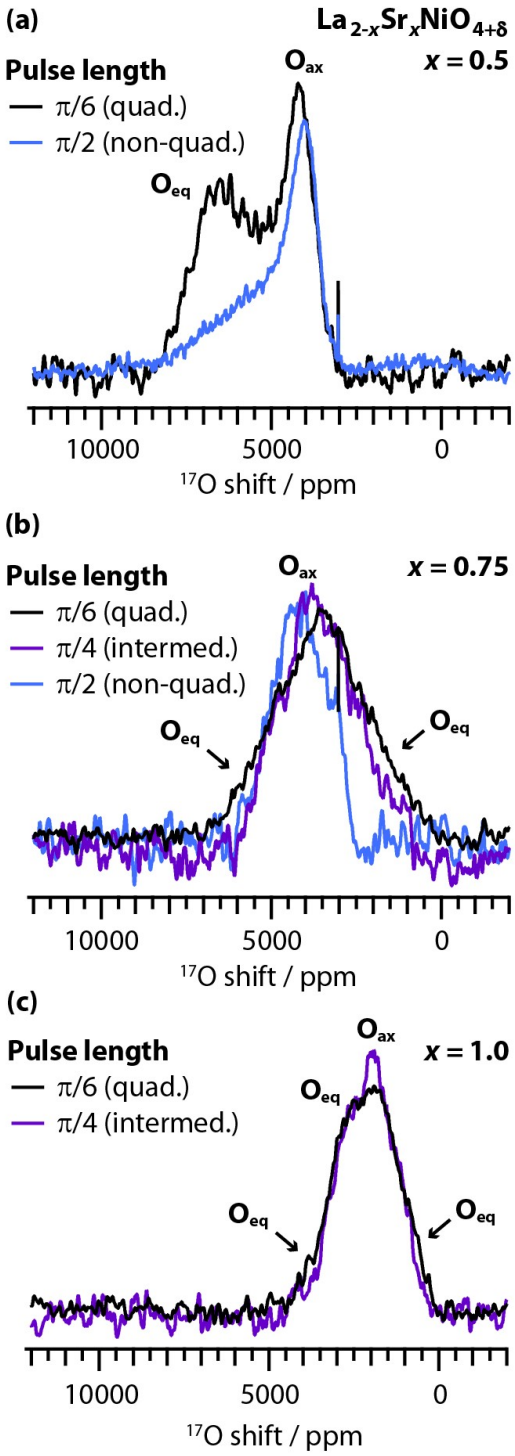


Figure 4.11: $^{17}$O MATPASS NMR spectra of the highly-doped samples ($0.5 \leq x \leq 1.0$) as a function of the rf pulse length ($\pi/6$, $\pi/4$ and $\pi/2$). No signal is observed using a $\pi/2$ pulse length for the $x = 1.0$ sample, which is consistent with a large quadrupolar coupling constant (> 4.2 MHz) for all sites, including the $O_{ax}$ environment. Spectra have been acquired at 4.7 T with a MAS rate of 40 kHz.

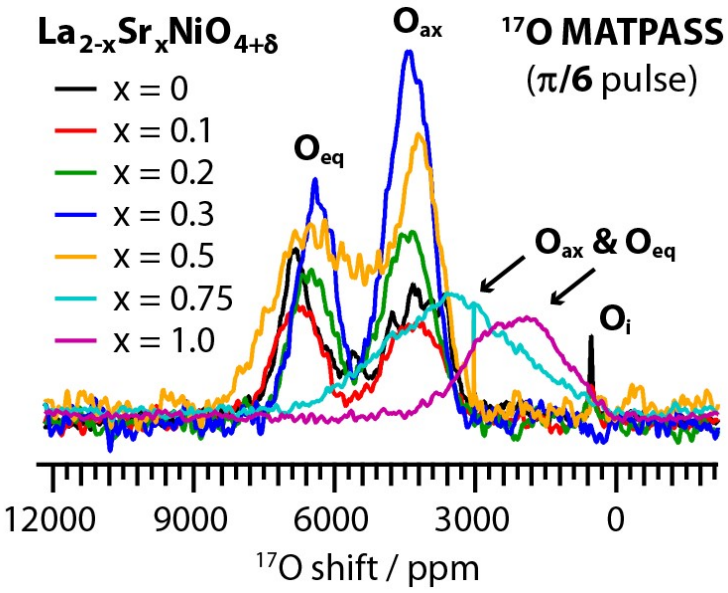


Figure 4.12: Comparison of the $^{17}$O MATPASS NMR spectra acquired with short ($\pi/6$) rf pulse length of all $La_{2-x}Sr_xNiO_{4+\delta}$ samples ($0 \leq x \leq 1.0$), including the undoped phase. Spectra have been acquired at 4.7 T with a MAS rate of 40 kHz.

These shift changes are also accompanied by the subtle evolution of the quadrupole coupling constants of both sites. At $x$ = 0.5, the incomplete suppression of the $O_{eq}$ feature with application of the longer $\pi/2$ rf pulse implies a somewhat smaller $C_Q$ than in the moderately-doped regime ($x$ < 0.5). On the other hand, the $C_Q$ of the axial environment increases significantly with additional Sr doping, such that at $x$ = 1.0, no NMR signal whatsoever is observed using a $\pi/2$ rf pulse. Thus, given a rf field strength $\omega_1 \approx 104$ kHz in these experiments, both the $O_{eq}$ and $O_{ax}$ sites possess $C_Q$ values larger than 4.2 MHz for the $x$ = 1.0 sample.[166] Variations in the $C_Q$ values can be rationalized on the basis of changes in the Ni–O and La(Sr)–O bond lengths, as well as increasing similarity of neighboring cationic charges (Section 4.5.6).

### 4.4.3 Ni K-edge XANES

As described in Section 2.5, the X-ray absorption near-edge structure (XANES) at the K-edge of first-row transition metals is an important local structure technique complementary to solid-state NMR, as transition metal sites are typically inaccessible by the latter approach. In particular, the position of the K-edge is diagnostic of the average transition metal oxidation

state, as the absorption energy is strongly dependent on the ground-state electron density. In this work, Ni K-edge XANES spectra have been recorded of the $^{17}$O-enriched phases of composition $x$ = 0, 0.1, 0.2, 0.3, 0.5, 0.75, and 1.0. The Ni K-edge XANES spectra of moderately- and highly-doped $La_{2-x}Sr_xNiO_{4+\delta}$ show clear changes in the edge absorption energy, associated with the conversion of $Ni^{2+}$ to $Ni^{3+}$ with increasing Sr incorporation (Figure 4.13a). The Ni K-edge energy for each sample is most easily determined as the zero-crossing of the second derivative of the absorption (Figure 4.13b), and values extracted by this method are given in Table 4.1. Only a minor shift ($\leq$ 0.1 eV) occurs for the moderately-doped samples ($x \leq 0.3$), but the highly-doped phases undergo a significant increase in absorption energy, with the Ni K-edge of the $x$ = 1.0 phase nearly 2 eV higher than that of undoped $La_2NiO_{4+\delta}$. These absorption energies have been converted to average values of the Ni valence state using the calibration curve previously reported by Woolley *et al.* in their study of the $La_2NiO_{4+\delta}$ and $La_4Ni_3O_{10-\delta}$ phases.[75] The undoped and more lightly Sr-doped phases retain (within error) a constant average Ni valence of 2.20(5)+, while the Sr-rich materials consistently increase in $Ni^{3+}$ concentration, up to an average valence of 2.86(9)+. Under the strict assumption that the charge compensation mechanism occurs exclusively through incorporation of $O^{2-}$ interstitials (or equivalently by formation of oxygen vacancies with effective charge of +2), values of the oxygen non-stoichiometry ($\delta$) have also been calculated (Table 4.1). These demonstrate the loss of interstitial defects for the moderately-doped samples, consistent with the $^{17}$O NMR data (Sections 4.4.2 and 4.5.2). For $x \geq 0.3$, the calculated oxygen content becomes hypostoichiometric ($\delta < 0$), indicating formation of oxygen vacancies, and remains roughly constant within error. A slightly sub-stoichiometric oxygen content in highly-doped samples prepared under ambient conditions has also been previously reported, with Aguadero *et al.* and Millburn *et al.* finding by means of iodometric titration similar values of $\delta$ = -0.03 for $x = 0.5$ and $\delta \approx$ -0.05 for $0.8 \leq x \leq 1.0$, respectively.[59,298]

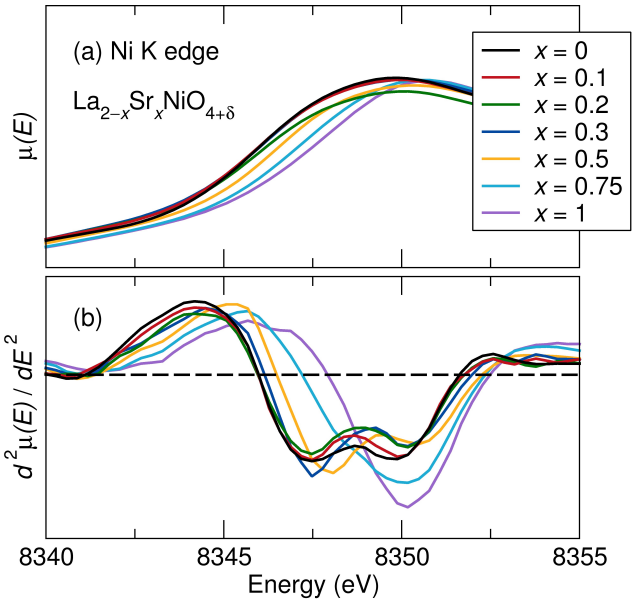


Figure 4.13: (a) Ni K-edge XANES spectra of undoped ($x$ = 0), moderately- and highly-doped ($0.1 \leq x \leq 1$) $^{17}$O-enriched phases of $La_{2-x}Sr_xNiO_{4+\delta}$, showing the increase in the K-edge energy on Sr-doping, consistent with conversion from $Ni^{2+}$ to $Ni^{3+}$. (b) The second derivative of the absorption $\mu$ with respect to the incident energy $E$, where the change in the Ni K-edge position is seen as a shift of the zero-crossing to higher $E$ (cf. Table 4.1).

Table 4.1: Ni K-edge energy from XANES data, and corresponding Ni oxidation state and oxygen non-stoichiometry.

| Sample[a] | Ni K-edge energy (eV)[b] | Ni valence[c] | Oxygen non-stoichiometry ($\delta$)[d] |
|---|---|---|---|
| $La_2NiO_{4+\delta}$ | 8346.0 | 2.20(5) | 0.10(3) |
| $La_{1.9}Sr_{0.1}NiO_{4+\delta}$ | 8346.0 | 2.20(5) | 0.05(3) |
| $La_{1.8}Sr_{0.2}NiO_{4+\delta}$ | 8346.0 | 2.20(5) | 0.00(3) |
| $La_{1.7}Sr_{0.3}NiO_{4+\delta}$ | 8346.1 | 2.25(6) | -0.03(3) |
| $La_{1.5}Sr_{0.5}NiO_{4+\delta}$ | 8346.5 | 2.35(6) | -0.08(3) |
| $La_{1.25}Sr_{0.75}NiO_{4+\delta}$ | 8347.2 | 2.58(7) | -0.09(4) |
| $LaSrNiO_{4+\delta}$ | 8347.9 | 2.86(9) | -0.07(5) |

[a] Note all samples have been $^{17}$O-enriched (exposed to $^{17}O_2$ at 1000 °C for 24 h). By convention, positive (negative) values of $\delta$ indicate oxygen excess (deficiency). [b] Edge energy obtained from second derivative (Figure 4.13b), to within ± 0.1 eV. [c] Calculated from calibration curve as reported by Woolley *et al.*[75] [d] The values have been calculated assuming that $\delta$ strictly corresponds to oxygen interstitials with an effective charge of 2- (for $\delta > 0$) and oxygen vacancies with an effective charge of 2+ (for $\delta < 0$).

First row transition metal K-edge XANES spectra are also of use in characterizing the local structure and coordination geometry of the metal center. Deviations from octahedral symmetry give rise to pre-edge features, *i.e.*, additional transitions at lower energy than the primary absorption edge. As described in Section 2.5, these features are due to 1*s* to 3*d* transitions that are formally forbidden according to angular momentum selection rules ($\Delta l \pm 1$), but are nonetheless experimentally observed with deviations of the coordination geometry from ideal (octahedral) symmetry due to mixing with 4*p* states. For undoped $La_2NiO_{4+\delta}$, a weak pre-edge feature is observed at 8334 eV, which is slightly suppressed with increasing Sr incorporation, but this then increases significantly for $x \geq 0.3$ (Figure 4.14). We ascribe this behavior to (1) an increase in local octahedral symmetry due to the initial decrease in distortions induced by the removal of interstitial defects, followed by (2) a decrease in the average Ni coordination in the highly-doped samples due to the increasing concentration of oxygen vacancies at (predominately) axial sites. That is, while the local geometry initially approaches ideal octahedral symmetry, suppressing the probability of the 1*s* to 3*d* transition, the subsequent decrease in coordination number caused by oxygen vacancies ($\delta < 0$) leads to a more substantial increase in the pre-edge intensity with increased Sr substitution for $x \geq 0.3$.

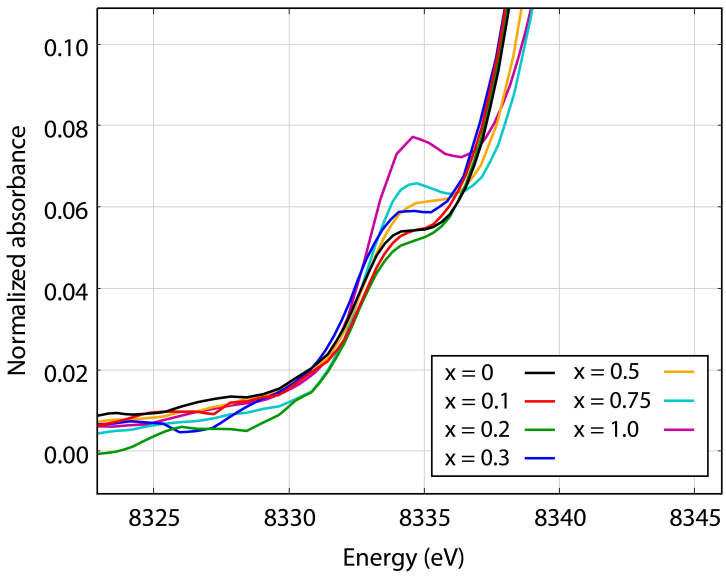


Figure 4.14: Pre-edge features of Ni K-edge XANES spectra of undoped ($x = 0$), moderately- and highly-doped ($0.1 \leq x \leq 1$) $^{17}O$-enriched phases of $La_{2-x}Sr_xNiO_{4+\delta}$.

## 4.5 Discussion

### 4.5.1 Structural considerations and changes in lattice parameters

While highly hyperstoichiometric phases ($\delta \geq 0.15$) of the undoped material $La_2NiO_{4+\delta}$ adopt an orthorhombic structure (space group *Fmmm*) at room temperature,[54,64] previous findings concur that $La_{2-x}Sr_xNiO_{4+\delta}$ (for $x \geq 0.1$) is instead best described by a tetragonal crystal structure (space group *F*4/*mmm*).[309,321] (The existence of a very small orthorhombic splitting for $0 < x < 0.1$ cannot be ruled out from the present data; Sreedhar *et al.* have, however, reported a tetragonal structure for their $x = 0.05$ sample.[322]) The appearance of this higher symmetry structure upon Sr incorporation can be ascribed to several concerted structural factors: (1) increased structural stability, (2) suppression of formation of interstitial oxide defects, and (3) steric effects between $Sr^{2+}$ and $NiO_6$ octahedra.

(1) As quantified by a small Goldschmidt tolerance factor $t < 1$, stoichiometric $La_2NiO_4$ is near the structural stability limit for the $K_2NiF_4$ geometry, where the short La–O distance stretches the rock salt layers and compresses the perovskite layers.[323] This structural strain is relieved by cooperative tilting of the $NiO_6$ octahedra that gives rise to an asymmetric distortion converting the tetragonal $K_2NiF_4$ structure to an orthorhombic one. As the ionic radius of nine-fold coordinated $Sr^{2+}$ is larger than that of $La^{3+}$ (1.31 Å *vs.* 1.22 Å),[57,307] the tolerance factor for $La_{2-x}Sr_xNiO_{4+\delta}$ increases with $x$, minimizing the tendency of $NiO_6$ octahedra to tilt and thus leading to a smaller (or negligible) orthorhombic distortion of the structure. (The oxidation of $Ni^{2+}$ to $Ni^{3+}$, the latter with a smaller ionic radius, also leads to a larger tolerance factor and improves structural stability/reduces the octahedral tilts.)

(2) Incorporation of $Sr^{2+}$ for $La^{3+}$ leads to removal of excess interstitial oxygen, which for modest Sr-doping is the major charge compensation mechanism in these samples; for $x < 0.5$, the XANES data show only minimal change in the Ni valence (Table 4.1), whereas the concentration of interstitial oxide defects as quantified by $^{17}O$ NMR decreases dramatically (Figure 4.10). This decrease in $\delta$ thus results in a less significant interstitial-

induced distortion of the $NiO_6$ octahedra and/or the axial oxygen sites, also consistent with tetragonal symmetry.

(3) The larger $Sr^{2+}$ cation minimizes the extent to which the axial and equatorial oxygens can displace away from ideal octahedral coordination to Ni, given the position of the Sr site with respect to these oxygen sites (Figure 4.1), thus inducing greater structural rigidity and leading to an arrangement approaching the idealized tetragonal $K_2NiF_4$-type structure.

As noted earlier, the lattice parameter changes in the $La_{2-x}Sr_xNiO_{4+\delta}$ system strongly deviate from Vegard's rule. The structural changes that occur for $0 < x \leq 0.5$, in particular, remain counterintuitive. For this region of phase space, both in the present study and in previous findings, a small but continuous decrease in the unit cell volume of $La_{2-x}Sr_xNiO_{4+\delta}$ has been observed with increasing $x$. Previous studies have attributed this decrease to a greater concentration of smaller $Ni^{3+}$ cations relative to $Ni^{2+}$ (ionic radii of 0.56 Å and 0.70 Å, respectively). However, this mechanism cannot be operative in these samples, as the average Ni valence does not appreciably change below $x = 0.3$ (Table 4.1). (Indeed, the only relevant cationic substitution effect, *i.e.*, $Sr^{2+}$ at $La^{3+}$ sites, would induce an increase in the unit cell volume.) Instead, we assign the observed volume decrease to the removal of interstitial oxygen from the structure, as is known to occur in undoped $La_2NiO_{4+\delta}$ upon lowering of the excess oxygen content.[63]

However, the changes in the lattice parameters for $0 < x \leq 0.5$, namely an increase in $c$ and decrease in $a$, $b$ (Figure 4.5) cannot result directly from a decrease in $\delta$; neither are they explained by a larger Jahn-Teller elongation of the Ni cations, as this distortion decreases across the entire substitutional range (see below). Instead, we ascribe the change in the $c$ parameter to a larger spacing between the perovskite layers induced by substitution of $Sr^{2+}$, which significantly increases the length of the La(Sr)–$O_{ax}$ bond along the $c$ axis, due to both the larger size and smaller charge of the doped cation. Analysis of the powder XRD data, including Rietveld refinement of the atomic coordinates, also suggests lengthening of this bond (by ~0.4 Å, or ~2%) for $x < 0.5$, despite the somewhat significant errors in the bond length data (Figure 4.15). As for the $a$ parameter, we propose the decrease is a consequence of the overall contraction of the unit cell due to loss of excess oxygen.

In this modest doping region, a small decrease is apparent in the Jahn-Teller elongation (*i.e.*, ratio of Ni–$O_{ax}$ to Ni–$O_{eq}$ bond lengths), partially from Rietveld refinement of the atomic positions and bond lengths (Figure 4.16), but also from changes in the XANES spectra (Section 4.4.3 and Figure 4.14); this change is in agreement with the findings of Takeda *et al.*[58] Refined positions of the light oxygen atoms are not determined with sufficient accuracy to follow a definitive decrease in the Jahn-Teller elongation in this region, but the decreasing intensity of the XANES pre-edge feature ($x \leq 0.2$) indicates a smaller deviation away from ideal octahedral symmetry. The modestly changing Jahn-Teller distortion and in particular the decreasing Ni–$O_{ax}$ bond length also prove consistent with the expected increase in the La(Sr)–$O_{ax}$ bond along the *c* axis.

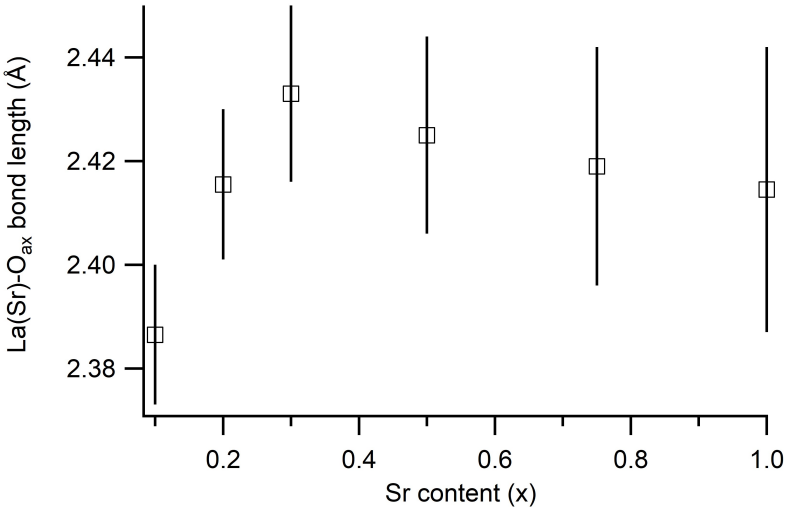


Figure 4.15: The La(Sr)–$O_{ax}$ bond length along the *c* axis, as a function of the Sr incorporation (*x*), in $^{17}$O-enriched samples of $La_{2-x}Sr_xNiO_{4+\delta}$; values have been determined from Rietveld refinement of both lattice parameters and atomic positions. Error bars are indicated by vertical lines.

In the highly-doped region ($x \geq 0.5$), the unit cell volume consistently decreases, in accordance with the larger concentration of smaller $Ni^{3+}$ cations. However, the relative behavior of the *c* and *a* lattice parameters is reversed (decrease in *c*, increase in *a*), resulting from a very significant reduction in the Jahn-Teller elongation at $Ni^{3+}$ sites for the $x = 0.75$ and 1.0 samples (Figure 4.16), even as the Ni oxidation state continues to increase. The lessening of this distortion is expected to arise from the changing occupation of the $e_g(Ni^{3+})$ states that start to include greater $d_{x^2-y^2}$ (or less $d_{z^2}$) character for $x > 0.5$, coincident with

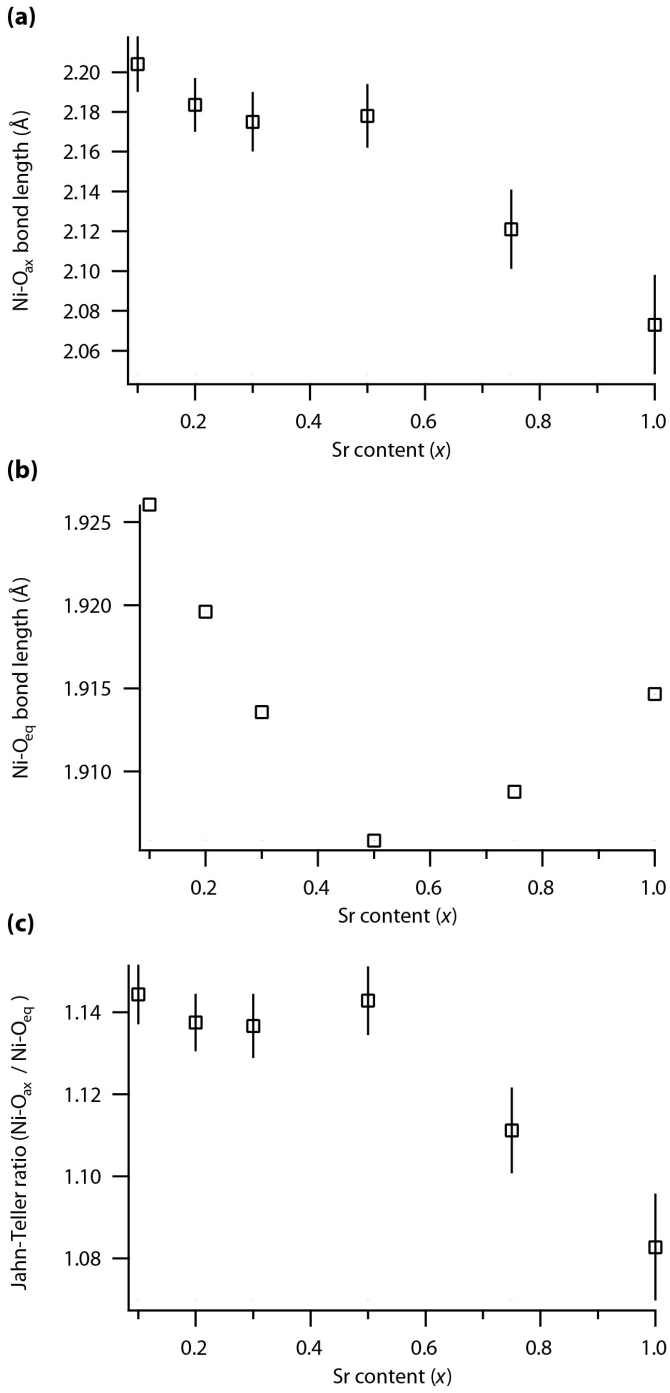


Figure 4.16: (a) The Ni–$O_{ax}$ bond length, (b) the Ni–$O_{eq}$ bond length, and (c) the Jahn-Teller distortion at the Ni site, as quantified by the ratio of the Ni–$O_{ax}$ and Ni–$O_{eq}$ bond lengths, as a function of the Sr incorporation ($x$) in $^{17}$O-enriched samples of $La_{2-x}Sr_xNiO_{4+\delta}$. Values have been determined using Rietveld refinement of both lattice parameters and atomic positions. Error bars are indicated by vertical lines. The error in the Ni–$O_{eq}$ bond length in (b) is within the symbols; this error is small as the Ni-$O_{eq}$ distance is exactly half the $a$ (= $b$) lattice parameter.

the onset of increased electronic (*i.e.*, quasi-metallic) conductivity.[59] The variation of the $O_{eq}$ and $O_{ax}$ hyperfine $^{17}O$ NMR shifts, and in particular the much lower frequency of the $O_{ax}$ resonance (Figure 4.11), is also in agreement with a gradual $e_g$ electronic crossover that promotes a smaller Jahn-Teller distortion, as described later (Section 4.5.4). Finally, the observed lattice parameter changes may also arise from an increase in the oxygen vacancy concentration for these samples (reflected in more negative values of $\delta$ in Table 4.1). A changing oxygen stoichiometry is corroborated by increased errors in refined bond lengths (Figure 4.15 and Figure 4.16), which is inferred to arise from decreased occupancy of mainly axial oxygen sites.

### 4.5.2 Interstitial defect concentration and oxide-ion conductivity

As $^{17}O$ NMR spectra focusing on the interstitial oxygen ($O_i$) resonance have been acquired under quantitative conditions for $x \leq 0.3$ (Figure 4.10), we have calculated the interstitial concentration in this region of phase space to provide insight into the underlying defect chemistry. The calculated hyperstoichiometry values (Figure 4.17), which also make use of the prior TGA data in Chapter 3, reveal a continuous decrease in the oxygen excess that approaches $\delta \approx 0.01$ for x = 0.3, as expected. However, the change is distinctly non-linear with $x$. In particular, the substantial decrease from $\delta \approx 0.16$ ($x = 0$) to $\delta \approx 0.08$ ($x = 0.01$) suggests that very minimal Sr incorporation initially has an outsize effect on the interstitial defect concentration. The net charge increase due to loss of $O_i$ (nominally +0.16 per formula unit, assuming $O^{2-}$) is clearly not balanced by Sr incorporation (−0.01 per formula unit). Moreover, the charge compensation mechanism does not appear to involve a change in the Ni oxidation state, as the XANES spectra reveal negligible differences in the Ni valence at this doping level (Table 4.1). Possible explanations include (1) a decrease in the effective charge of the interstitial defects on doping, or (2) the presence of higher-order impurity phases ($La_3Ni_2O_7$ and $La_4Ni_3O_{10}$) in the lightly-doped samples.

In the first case, one can consider $O_i$ in the undoped $x = 0$ material to possess a slightly less negative charge than the maximal value of 2-, but this then approaches 2- upon Sr incorporation, balancing the charge increase due to loss of $O_i$. In support of this, precedent exists in the literature for unusually charged oxygen species in these systems. Lee and

Hoffmann have discussed the possibility of interstitials with peroxide- or subperoxide-like character in the isostructural cuprates $La_2CuO_4$,[324] and Demourgues *et al.* have suggested for highly hyperstoichiometric samples of $La_2NiO_{4+\delta}$ ($\delta \approx 0.25$) the association of interstitial defects with axial oxygen sites, forming $O_3^{5-}$ polyoxide clusters.[62] Assuming such clusters in the undoped material, the more ionic behavior of $O_i$ upon Sr doping would then result from reduced crowding of interstitial defects in the rock salt layers. On the other hand, the $^{17}O$ NMR shift of the $O_i$ resonance does not appreciably change between $x = 0$ and any of the Sr-doped samples, whereas any change in the peroxide-like character of $O_i$ would be expected to alter the nuclear shielding and thus the observed NMR shift.[325,326] Therefore, covalency changes involving the interstitial sites would seem unlikely.

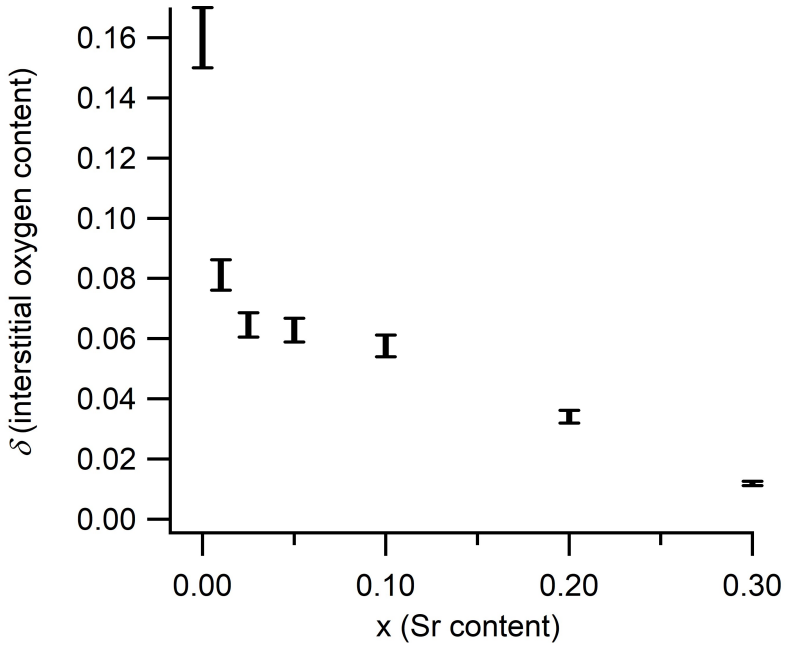


Figure 4.17: Values of the oxygen excess ($\delta$) in $^{17}O$-enriched $La_{2-x}Sr_xNiO_{4+\delta}$, quantified by $^{17}O$ NMR spectra of the interstitial oxygen defect ($O_i$). Here, the value of $\delta = 0.15–0.17$ for the undoped sample $La_2NiO_{4+\delta}$ has been derived from previous TGA measurements in Figure 3.3 and Figure 3.5 and used for all other samples to extract a value of $\delta$ from the relative integrated spectral intensity of the $O_i$ feature, as acquired under quantitative conditions (Figure 4.10). Contributions from the minor $La_2O_3$ impurity phase have been excluded in the integrated intensity. Error bars reflect the relative signal-to-noise ratio of the $O_i$ feature in the quantitative $^{17}O$ NMR spectra, or the (scaled) error in the TGA measurement for the undoped material, whichever is larger.

The second and more probable explanation is that, for the $x = 0.01$, 0.025, and 0.05 phases, the actual average Ni valence of the primary $La_{2-x}Sr_xNiO_{4+\delta}$ phase is somewhat less than that

of the undoped material due to the presence of impurity phases formed on $^{17}$O-enrichment. From both powder XRD and $^{17}$O NMR data, these samples possess small quantities of $La_3Ni_2O_7$ and $La_4Ni_3O_{10}$ phases with considerably higher $Ni^{3+}$ content (average Ni valence of 2.5+ and 2.67+, respectively). In that case, the calculated average Ni oxidation state from XANES would overestimate the actual Ni valence in the primary phase. The less positive charge on Ni sites would then balance the charge increase due to loss of $O_i$. Additionally, this hypothesis suggests that the lightly-doped phases could in principle accommodate significantly more interstitial defects, provided that higher-order Ruddlesden-Popper phases are not formed during or after synthesis.

The quantitative interstitial concentrations obtained from $^{17}$O NMR intensities (scaled by the TGA-derived value) generally agree with the oxygen excess values derived from the Ni K-edge XANES data (Table 4.1) that are calculated from the Ni average oxidation state. However, the $\delta$ values obtained from XANES are consistently smaller (or more negative). In particular, the oxygen excess of the undoped material $La_2NiO_{4+\delta}$ is significantly underestimated by XANES ($\delta \approx 0.10(3)$), compared to the value previously obtained from TGA measurements in Section 3.4.1 ($\delta \approx 0.16(2)$). The most likely explanation is that the XANES experiments were performed over ~1 year after the synthesis, $^{17}$O-enrichment and NMR study of the original $La_2NiO_{4+\delta}$ phase, with the discrepancy being attributed to the gradual decrease of interstitial defects from the structure even at room temperature; this assertion is consistent with partial loss of $^{17}$O-enrichment of the same sample over this period.

As for the lower oxide-ion conductivity of some of these phases observed in previous studies, this appears to directly correlate with the decreasing concentration of interstitial oxide defects. Between $x = 0.2$ and $x = 0.4$, a compositional space that corresponds in this work to complete removal of interstitials, Inprasit *et al.* have recorded a decrease of roughly three orders of magnitude in the oxygen tracer diffusion coefficient $D^*$.[310] As a caveat, the oxygen excess will tend to decrease at the high temperatures (*e.g.*, 823–1123 K) at which the ionic conductivity is measured; thus the interstitial defect concentrations extracted from the room temperature $^{17}$O NMR spectra are not perfectly comparable. Moreover, at large $x$, mechanisms involving oxygen vacancy (rather than interstitial) motion begin to dominate the

ionic conductivity, and the acquired (room temperature) spectra are not directly sensitive to vacancy formation, a process that is more obvious from XANES and also from changes in the quadrupolar coupling constants (Section 4.5.6). Nonetheless, the $^{17}O$ NMR data, and in particular the quantified interstitial intensity, provide a qualitative measure of the ionic conductivity of the $x \leq 0.3$ phases.

Finally, the (diamagnetic) shift of the $O_i$ feature does not deviate from 532 ppm for any composition $x \leq 0.3$. Only minor differences are expected for the $^{17}O$ NMR shifts corresponding to, *e.g.*, $OLa_4$ vs. $OSr_4$,[327] but the absence of any change in the shift indicates that the local coordination environment of $O_i$ remains dominated by $La^{3+}$ rather than $Sr^{2+}$ in the $O_i$ first cation coordination shell. We further suggest that $O_i$ ions will preferentially occupy environments that do not have $Sr^{2+}$ in their local coordination shell. Even for $x = 0.3$, a random distribution of Sr on La sites would imply that 52% of all (occupied and unoccupied) interstitial sites are surrounded by $La^{3+}$ only, and hence the availability of potential $OLa_4$ environments does not limit the $O_i$ concentrations.

### 4.5.3 Loss of local structural distortions

While changes in the interstitial oxide feature mainly provide insight into the defect chemistry and oxide-ion conductivity of $La_{2-x}Sr_xNiO_{4+\delta}$, the axial ($O_{ax}$) environments are instead highly sensitive to an indirect effect of the interstitials, that is, the local structural distortions of the $NiO_6$ octahedra. We showed in Chapter 3 through a combination of $^{17}O$ NMR and hybrid DFT calculations on the $La_2NiO_{4+\delta}$ system that the high concentration of interstitial defects in the rock salt layers leads to a systematic displacement of some of the axial oxygen sites by nearby interstitials, and the emergence of four distinct $O_{ax}$ sites (Figure 3.8) with characteristic Ni–$O_{ax}$ distances, leading to resonances with differing $^{17}O$ hyperfine shifts. (We also assigned an additional resonance at even higher frequency, observed in the experimental $^{17}O$ NMR spectra (black traces, Figure 4.7 and Figure 4.9), to a fifth and even more distorted $O_{ax}$ environment not captured by the calculations due to the slightly smaller value of the oxygen excess, *i.e.*, $\delta = 0.125$ in the DFT-optimized structure and $\delta = 0.15$–$0.17$ experimentally. Such a distorted environment might correspond to an axial site with two nearby interstitial defects.)

In the $La_{2-x}Sr_xNiO_{4+\delta}$ phases, as the concentration of interstitial defects decreases due to Sr incorporation, the interstitial-induced axial distortion also disappears. This is shown by both XANES and $^{17}O$ NMR results, with an increase in $NiO_6$ octahedral symmetry revealed by the former technique, and more homogeneous $O_{ax}$ environments indicated by the latter. In particular, looking at the $^{17}O$ MATPASS NMR spectra of the lightly-doped samples (Figure 4.9), the sharp, distinct $O_{ax}$ resonances disappear between $x = 0.01$ and $x = 0.025$, although the overall distribution of shifts mostly remains. We ascribe this to a change in the nature of the axial distortion. The system progresses from a longer-range, cooperative axial distortion in the undoped phase, to local distortions at lower levels of $O_i$, with a distribution of octahedral tilts in different directions leading to broadening of the discrete $O_{ax}$ signals. From the quantitative $O_i$ data, this doping level corresponds to a decrease in the oxygen excess from $\delta \approx 0.08$ to $\delta \approx 0.06$, suggesting that a critical concentration of interstitials ($\delta > 0.06$) is required to induce a cooperative axial distortion.

Interestingly, Tranquada *et al.* have previously shown, through single-crystal neutron diffraction experiments on $La_2NiO_{4+\delta}$ samples of varying $\delta$, that a transition involving the long-range staging of oxygen interstitials also occurs between $\delta = 0.085$ and $\delta = 0.074$.[66] In particular, they have proposed a single-phase "stage-2" intercalated structure for larger oxygen excess samples such as $\delta = 0.085$, in which consecutive rocksalt layers are alternately occupied by and empty of interstitials; this interstitial ordering is similar to that in the DFT-optimized supercell studied in the work in Chapter 3. However, the $\delta = 0.074$ phase comprises both stage-2 and stage-3 (*i.e.*, interstitial filling of every third rocksalt layer) phases, with considerable stacking disorder of both phases at room temperature. It is therefore likely that the relatively sharp $O_{ax}$ resonances for the $x = 0$ ($\delta = 0.16$) and $x = 0.01$ ($\delta \approx 0.08$) samples, and the corresponding axial distortion visualized in Figure 3.8, reflects at least a degree of ordering of the type represented by the stage-2 intercalated phase of Tranquada *et al.* A uniform alternation of interstitial-occupied and -empty rocksalt layers would give rise to relatively few Ni–$O_{ax}$ distances, consistent with the relatively sharp $O_{ax}$ resonances. On the other hand, the increased variety of different environments in the stage-3 structure, combined with partial ordering, could lead to distinct $O_{ax}$ resonances no longer distinguishable in the $^{17}O$ NMR spectra. In the current investigation, the specific staging structures of Tranquada *et al.* cannot be directly confirmed in these samples. The main point

here is that ordering schemes have been proposed that explain the appearance of well-resolved resonances, despite the distribution of local environments that might be expected. Small differences in the $O_i$ concentration could frustrate these ordering schemes, which might explain why small changes in the Sr level have such significant effects; essentially, any Sr helps to prevent these longer-range ordering mechanisms. (While incorporation of Sr also increases structural rigidity and lessens the axial distortion, we would expect these effects to be negligible in the lightly-doped regime.)

The narrowing of the $O_{ax}$ resonance continues for the $x \leq 0.3$ samples (Figure 4.7), indicative of a smaller distribution of Ni–$O_{ax}$ bond lengths, in good agreement with an even smaller concentration of interstitials, a more tetragonal crystal structure, and thus a greater homogeneity in the axial environments. However, no increase in the $O_{ax}$ shift is observed, despite the small decrease in the average Ni–$O_{ax}$ distance (from 2.20(1) Å to 2.17(2) Å at $x$ = 0.1 and 0.3, respectively) as determined by refinement using the XRD patterns and the decrease in the Jahn-Teller distortion (Figure 4.16). This suggests that the small expected increase in the paramagnetic shift of the resonances from the $O_{ax}$ sites is negated by a decrease due to electronic effects, *i.e.*, a small decrease in the electronic occupation of the $d_{z^2}$ orbital, which is coordinated to $O_{ax}$, due to increased Ni average oxidation state. However, the removal of spin density from this orbital is negligible compared to that occurring for the $d_{x^2-y^2}$ orbital, as is apparent by the large decrease in the shift of the $O_{eq}$ resonance (Section 4.5.4). As discussed later, the changing paramagnetic shift of $O_{eq}$ is a more sensitive probe of the average Ni valence than the XANES Ni K-edge results, which show no change within the relatively larger errors associated with the calculation of oxidation state from the data.

Lastly, the loss of the axial distortion is accompanied by decreasing $^{17}O$ spin-lattice ($T_1$) relaxation times of the interstitial resonances by an order of magnitude, in particular between the undoped and $x$ = 0.1 phase; above this doping level, the $T_1$ time for the $O_i$ resonance is roughly constant (Table 4.2). We previously observed similarly short $T_1$ values for interstitial resonances in $La_2NiO_{4+\delta}$ upon modest heating of the material (up to 150 °C) and ascribed this phenomenon to the onset of oxide-ion motion involving the interstitial defects (Section 3.5.2). Thus, we suggest that Sr doping in fact initially leads to an increase in the $O_i$ mobility, which is consistent with reduced crowding of the rocksalt layers by interstitial oxygen as just

described. However, as the population of charge carriers is significantly smaller for these moderately Sr-doped samples, the net effect of Sr incorporation on the oxide-ion conductivity is detrimental, as previously shown.

Table 4.2: Spin-lattice ($T_1$) relaxation times for the axial ($O_{ax}$) and interstitial ($O_i$) sites in $^{17}$O-enriched $La_{2-x}Sr_xNiO_{4+\delta}$.[a]

| Sample | $T_1$, $O_{ax}$ (ms) | $T_1$, $O_i$ (ms) |
|---|---|---|
| $La_2NiO_{4+\delta}$ | 1.1(5) | 52(5) |
| $La_{1.9}Sr_{0.1}NiO_{4+\delta}$ | 1.1(5) | 4(1) |
| $La_{1.8}Sr_{0.2}NiO_{4+\delta}$ | 1.3(5) | 5(1) |
| $La_{1.7}Sr_{0.3}NiO_{4+\delta}$ | 1.0(5) | 3(1) |

[a] The $T_1$ values for the $O_{eq}$ site are consistently < 1 ms for all studied samples, within error.

### 4.5.4 Changes in Ni valence and electronic structure

The dramatic change in the hyperfine shift of the $O_{eq}$ feature across the full doping range closely tracks with the evolution of the electronic structure of $La_{2-x}Sr_xNiO_{4+\delta}$. In particular, the small initial decrease in the shift, followed by its large (~5000 ppm) movement towards lower frequency at $x$ = 1.0 (Figure 4.12) cannot be ascribed merely to changes in the Ni–$O_{eq}$ bond length, which based on structure refinement does not appreciably change (variation of Ni–$O_{eq}$ distances is within 0.02 Å or ~1%; see Figure 4.16). Instead, we ascribe the significantly reduced hyperfine shift to electronic structure changes consistent with the gradual conversion of $Ni^{2+}$ ($t_{2g}^6 e_g^2$) to $Ni^{3+}$ ($t_{2g}^6 e_g^1$), and specifically, a preferential decrease in the electronic occupation of the Ni $d_{x^2-y^2}$ orbital that is directly coordinated to the $O_{eq}$ environments. This result is in good agreement with previous work that suggests the doping of holes into the $\sigma^*$ band derived from the $d_{x^2-y^2}$ orbital leads to the experimentally observed increase in *p*-type electronic conductivity in the Sr-doped phases;[58] moreover, this finding demonstrates the unique sensitivity of paramagnetic $^{17}$O NMR to details of metal orbital occupation.

While according to the XANES results (Figure 4.13 and Table 4.1), the average Ni valence remains at 2.20(5)+ for the $x \leq 0.2$ samples, the modest decrease in the $O_{eq}$ shift from 6900 ppm ($x$ = 0) to 6500 ppm ($x$ = 0.2) shows that the $^{17}O$ hyperfine shift is potentially more sensitive to small changes in the Ni oxidation state. In particular, assuming for convenience that the $Ni^{2+}$ to $Ni^{3+}$ conversion exclusively induces hole doping on the $d_{x^2-y^2}$ orbital and thus affects the magnitude of the $O_{eq}$ shift only, this change from $x$ = 0 to 0.2 represents an increase of +0.06 in the Ni valence, which is well within the error bars of the calculated values obtained from XANES experiments. Thus, although the charge compensation mechanism is clearly dominated by the loss of interstitial oxygen at low and intermediate Sr doping, the $^{17}O$ NMR spectra reveal that, to a limited extent, oxidation to $Ni^{3+}$ does occur even within this regime.

The large changes in the $O_{eq}$ shift that occur at high doping levels (~6000 ppm at $x$ = 0.5, ~3500 ppm at $x$ = 0.75, and ~2000 ppm at $x$ = 1.0) are consistent with the formation of increasing predominately $Ni^{3+}$-like paramagnetic centers, in good agreement with XANES. Again assuming depopulation of electron density solely from the Ni $d_{x^2-y^2}$ orbital, we calculate increases in the Ni valence of +0.15, +0.50, and +0.70 for these three samples, which all agree with the XANES data within error (Table 4.1). However, the decrease of the $O_{ax}$ shift at the highest doping level suggests the onset of depopulation of the Ni $d_{z^2}$ orbital; this is consistent with the slight overestimate, relative to XANES, of the Ni valence change in the above calculations, which assume only the $d_{x^2-y^2}$ orbital is affected. The hyperfine shift changes of both resonances also allow us to comment on the relative occupation of the Ni $d_{x^2-y^2}$ and $d_{z^2}$ orbitals. Although Gopalakrishnan *et al.* and Cava *et al.* earlier suggested, based on both changes in lattice parameters and electrical resistivity, *complete* crossover of the $Ni^{3+}$ orbital occupation from $t_{2g}^6 d_{z^2}^1$ to $t_{2g}^6 d_{x^2-y^2}^1$ in highly-doped $La_{2-x}Sr_xNiO_{4+\delta}$, as we observe a monotonic decrease of the $O_{eq}$ shift, we do not believe this to be the case. Were the electronic occupation of the $d_{x^2-y^2}$ orbital to again increase at high doping, the $O_{eq}$ hyperfine shift would also increase. Rather, we see evidence for removal of electrons from first the $d_{x^2-y^2}$ orbital exclusively, followed by removal from both Ni $e_g$ orbitals simultaneously, suggesting that the valence band predominately derived from the $d_{x^2-y^2}$ orbital lies mainly, but not entirely, above that of the $d_{z^2}$ orbital. This conclusion also indicates a specific

mechanism for the partial (but not total) loss of the Jahn-Teller elongation at the highest levels of Sr incorporation (Figure 4.16), tying the evolution of the electronic structure to the changes in the lattice parameters for $x > 0.5$, *i.e.*, the *c*-axis contraction.

Finally, we note that the hyperfine shift is proportional not only to the spin density transfer to the NMR observed center (in this case, $O_{eq}$), but also to the magnetic susceptibility of the material.[89] Therefore, it is important to qualify the analysis of the hyperfine shifts which focuses exclusively on the orbital occupation, by also checking the variation in the magnetic susceptibility. Sreedhar and Rao have shown that the magnetic susceptibility of these phases also decreases with *x* at room temperature, especially in the highly-doped regime ($x \geq 0.5$).[322] Thus, the observed decreases in the $O_{eq}$ shift are not exclusively attributable to the removal of electrons from the Ni $d_{x^2-y^2}$ orbital with concomitant reduction of the delocalized spin density. Nonetheless, the decrease in the magnetic susceptibility of these phases arises from the smaller value of the Curie constant, which is another manifestation of the conversion from $Ni^{2+}$ ($S = 1$) to $Ni^{3+}$ ($S = ½$), and ultimately arises from the same change in the transition metal electronic structure.

### 4.5.5 Multiphasic behavior in highly-doped $La_{2-x}Sr_xNiO_{4+\delta}$

Although unlike some previous reports[298,312] we observe no significant improvement in applying a two-phase model to Rietveld refinement using the powder XRD patterns for $x \geq 0.5$, we do however find that for these samples the (00*l*) reflections exhibit asymmetry and/or broadening consistent with bi- or multi-phasic intergrowths, in agreement with Heaney *et al*.[312] In particular, the increased broadening of the (004) reflection suggests the presence of a distribution of phases with divergent lattice parameters (Figure 4.18) and thus differing levels of Sr incorporation. The compositional heterogeneity of the highly-doped samples is more readily shown through the broadening of the $O_{eq}$ feature in the $^{17}O$ NMR spectra (Figure 4.11 and Figure 4.12); the wide distribution of paramagnetic shifts indicates a locally variable Ni valence (and thus variable Sr content), but does not necessarily confirm the existence of explicitly two-phase mixtures. (It is important to note the $^{17}O$-enrichment may not be uniform across the various phases, which would actually lead to an underestimate of the range of Ni valences.) Interestingly, the $x = 0.75$ sample shows the largest broadening for

both the (004) reflection and the $O_{eq}$ feature, suggesting that the variation in the Sr doping level is maximal for this phase.

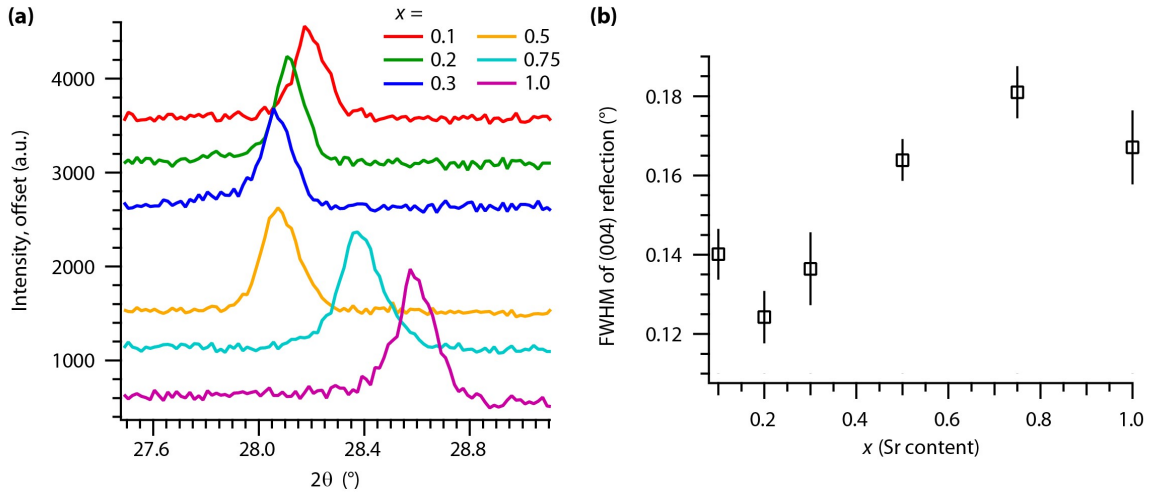


Figure 4.18: (a) Enlarged powder XRD patterns of $^{17}$O-enriched $La_{2-x}Sr_xNiO_{4+\delta}$ ($x$ = 0.1, 0.2, 0.3, 0.5, 0.75, and 1.0), showing only the (004) reflection, which undergoes asymmetric broadening for $x \geq 0.5$. (b) Values of the full width at half maximum (FWHM) of the (004) reflection for the studied samples, showing the increase in broadening of this reflection due to greater heterogeneity of Sr substitution in the $x \geq 0.5$ samples.

Note that we ascribe the significant broadening of the $O_{eq}$ (and $O_{ax}$) features to chemical shift dispersion arising from compositional heterogeneity, rather than from the presence of local structural distortions, as refinement analysis suggests that the highly-doped phases retain more highly symmetrical crystal structures than either the undoped or lightly-doped materials. On this basis, we can use the prior assumptions in Section 4.5.4 to approximate the Ni oxidation state from the paramagnetic $O_{eq}$ shift. We find that the variance in the Ni valence is ±0.18, ±0.24, and ±0.17, for $x$ = 0.5, 0.75, and 1.0, respectively. These values provide only a qualitative estimate of the degree of Sr inhomogeneity, as the extent of vacancy formation may differ across the distribution of phases; nonetheless, the results are in reasonable agreement with Aguadero *et al.* showing, for example, a biphasic mixture of $x$ = 0.6 and 0.8 for a nominal $x$ = 0.75 sample.[298] However, unlike the prior work, we find that the actual Sr content reflects the nominal value of $x$, whereas Aguadero *et al.* claim an overall lower Sr content for both phases in their nominal $x$ = 1.0 sample on the basis of unit-cell parameter changes in the undoped material. By contrast, the present $^{17}$O NMR and XANES data support a continuous increase in the Ni oxidation state even at $x$ = 1.0, suggesting an

overall increase in Sr incorporation. We propose that the lattice parameter changes in $La_2NiO_{4+\delta}$ as a function of the oxygen excess are not reliable indicators of the doping level in highly-doped $La_{2-x}Sr_xNiO_{4+\delta}$, because as discussed previously (Section 4.5.1) the predominant mechanism in the former case is the removal of interstitials from the rock salt-like layer, whereas in the latter case it is the decrease in the Jahn-Teller elongation that drives the evolution of the crystal structure. It is also possible that the discrepancies between the present work and that of Aguadero *et al.* could arise from small variations in the content of higher-order Ruddlesden-Popper phases; a reflection tentatively corresponding to these phases does appear in the powder XRD pattern for the $x = 0.75$ sample of Aguadero *et al.*[298] In any case, the $^{17}O$ NMR spectra allow us to infer both the degree of Sr incorporation in $La_{2-x}Sr_xNiO_{4+\delta}$, as well as its variation within a given phase, conclusions difficult to derive from powder XRD data alone due to the nonlinear changes in the lattice parameters.

### 4.5.6 Changes in quadrupolar coupling constants ($C_Q$): evolution of charge and bonding asymmetry

Finally, the changes in the quadrupolar coupling constants of the paramagnetic environments, and primarily the $O_{ax}$ environment, support (1) the replacement of $La^{3+}$ with $Sr^{2+}$ and $Ni^{3+}$ with $Ni^{2+}$, in good agreement with the defect chemistry, and (2) the proposed evolution of the Jahn-Teller distortion that is the origin of the distinctive change in the lattice parameters of $La_{2-x}Sr_xNiO_{4+\delta}$.

In the undoped material, despite possessing a nominally more symmetrical octahedral coordination to two $Ni^{2/3+}$ and four $La^{3+}$ neighbors (Figure 4.1b), the $O_{eq}$ site experiences a larger $C_Q$ (~4.7 MHz) than the $O_{ax}$ sites do (~0.5 to ~2.4 MHz), even though the latter sites have more distorted bond angles and a dihedrally asymmetric local bonding environment (*i.e.*, they are bonded to $Ni^{2/3+}$ cations in one direction and $La^{3+}$ in the other direction). This result suggests that in the case of $O_{eq}$ additional factors may be in play. It is possible that the charge asymmetry, which is larger for $O_{eq}$ due to the more diverse arrangement of neighboring charges, may predominate over the local bonding asymmetry in controlling the magnitude of $C_Q$. Alternatively, the covalency of the bonding between Ni and $O_{eq}$ (as well as $O_{ax}$) will play a significant role, as the $^{17}O$ $C_Q$ tends to be much larger for more covalent

oxides.[282] The presence of more covalent Ni–$O_{eq}$ bonding could also explain the much larger value of $C_Q$ for $O_{eq}$.

Assuming the charge asymmetry has a significant effect, with the onset of significant levels of Sr doping, both the average charge on the A site will decrease ($Sr^{2+}$ for $La^{3+}$) and that on the B site will increase ($Ni^{3+}$ for $Ni^{2+}$). In this case, the charge asymmetry is minimized, and thus the $O_{eq}$ $C_Q$ value should decrease.

This explanation is indeed consistent with the incomplete suppression of the $O_{eq}$ feature in the spectra acquired with a longer, $\pi/2$ pulse length for the $x = 0.5$ and $x = 0.75$ samples (Figure 4.11), which indicates a reduction in the $C_Q$ of the site associated with this resonance. However, by $x = 1.0$, as the charge asymmetry should again increase with the average B site charge exceeding that of the A site. As expected, the corresponding spectrum shows no intensity for the longer rf pulse length, indicating an increase in the $O_{eq}$ $C_Q$. Gopalakrishnan *et al.* have suggested that the Ni–$O_{eq}$ bonding becomes more covalent at the highest Sr-doping levels,[301] which would also lead to larger values of $C_Q$.

Conversely, the magnitude of the $C_Q$ of the $O_{ax}$ site increases continually and substantially with increased doping, such that at $x = 1.0$ it exceeds 4.2 MHz (Section 4.4.2). This change is readily ascribed to an increasingly covalent environment, although an increase in the bonding asymmetry may also contribute. That is, the Ni–$O_{ax}$ bond length decreases, and presumably the covalency of the $O_{ax}$ site increases, with the reduction of the Jahn-Teller elongation. This process occurs simultaneously with an increase in the opposing La(Sr)–$O_{ax}$ (parallel to *c*) distance due to substitution by the larger $Sr^{2+}$ cation, thus also increasing the bonding asymmetry of the $O_{ax}$ environment.

The diversity of local configurations for the more highly-doped samples (*e.g.*, variable numbers and arrangements of neighboring $La^{3+}$ and $Sr^{2+}$), as well as the compositional heterogeneity of these samples, is also expected to lead to a broad distribution of $C_Q$ values for both sites. Lastly, although we have neglected any effects of oxygen non-stoichiometry, the formation of (predominantly) axial vacancies will lead to local changes in the coordination that may also be expected to increase the bond and charge asymmetry of $O_{eq}$ and $O_{ax}$, although this would be expected to be quite a local effect.

## 4.6 Extension to other Ruddlesden-Popper systems

To extend the insights gained in the present $^{17}O$ NMR study of $La_{2-x}Sr_xNiO_{4+\delta}$ to other Ruddlesden-Popper systems, a similar methodology was applied to the isostructural $Sm_{2-x}Sr_xNiO_{4+\delta}$ class of materials. Single-phase materials of this composition form only for $0.4 \leq x \leq 1.0$, so that incorporation of Sr is necessary for stabilization of the structure.[328,329] Samples were synthesized by Dr A. P. Khandale (present address, School of Chemistry, University of St Andrews), according to an acetate pyrolysis technique described previously,[330] who also characterized the samples by powder XRD (Appendix B) and iodometric titration. Values of the oxygen excess $\delta$ = 0.03, 0.01 and -0.15 were determined for the compositions $x$ = 0.4, 0.5, and 1.0, respectively. The present author then $^{17}O$-enriched the as-synthesized samples ($x$ = 0.4, 0.5, and 1.0) by heating the powders (0.1–0.2 g) to 1000 °C under an atmosphere of 70% $^{17}O_2$ (Cambridge Isotope Labs, used as received) in a sealed quartz tube for 24 h.

Room-temperature $^{17}O$ MAS NMR spectra (acquired using spin-echo mapping) of the $Sm_{2-x}Sr_xNiO_{4+\delta}$ ($x$ = 0.4, 0.5, and 1) powders are presented in Figure 4.19. All spectra show qualitatively similar intensity, indicating uptake of $^{17}O$ during the gas-phase enrichment at 1000°C, and indirectly confirming high oxide-ion conductivity at this temperature. As expected, the spectra generally comprise two broad features (at 6500 and 4500 ppm, for $x$ = 0.4) for which selective suppression or enhancement can be achieved by quadrupolar filtering. Based on this nutation behavior, as well as the magnitude of the shifts, the high- and low-frequency features are assigned to equatorial and axial O sites, respectively.

Focusing at first on the lowest Sr-doped phase ($x$ = 0.4), a feature is observed comprising two overlapped resonances at 69 and -18 ppm with associated spinning sideband manifolds. For the nominal $x$ = 0.3 material, the powder XRD pattern (Figure B.1.1) reveals an impurity phase consistent with the B-type monoclinic (*C2/m*) polymorph of $Sm_2O_3$.[331] While this polymorph has not been studied by $^{17}O$ solid-state NMR, a roughly similar $^{17}O$ shift (at 10 ppm) has been reported for the (singular) oxygen environment in the cubic (A-type) polymorph of $Sm_2O_3$.[277] The present NMR feature is therefore assigned to an impurity of $Sm_2O_3$, which seems to have formed due to phase segregation of the $x$ = 0.4 sample at the

high temperature and oxygen partial pressure of the $^{17}$O-enrichment procedure. The signal arising from the $Sm_2O_3$ impurity phase is absent in the other compositions, suggesting that the $x$ = 0.5 and $x$ = 1.0 phases possess a relatively improved structural stability under the enrichment conditions. Additionally, no signal arising from interstitial oxygen was clearly observed in the slightly hyperstoichiometric phases ($x$ = 0.4 and 0.5), although based on the $La_{2-x}Sr_xNiO_{4+\delta}$ system, any interstitial resonance would be expected to be very weak for these small values of $\delta$.

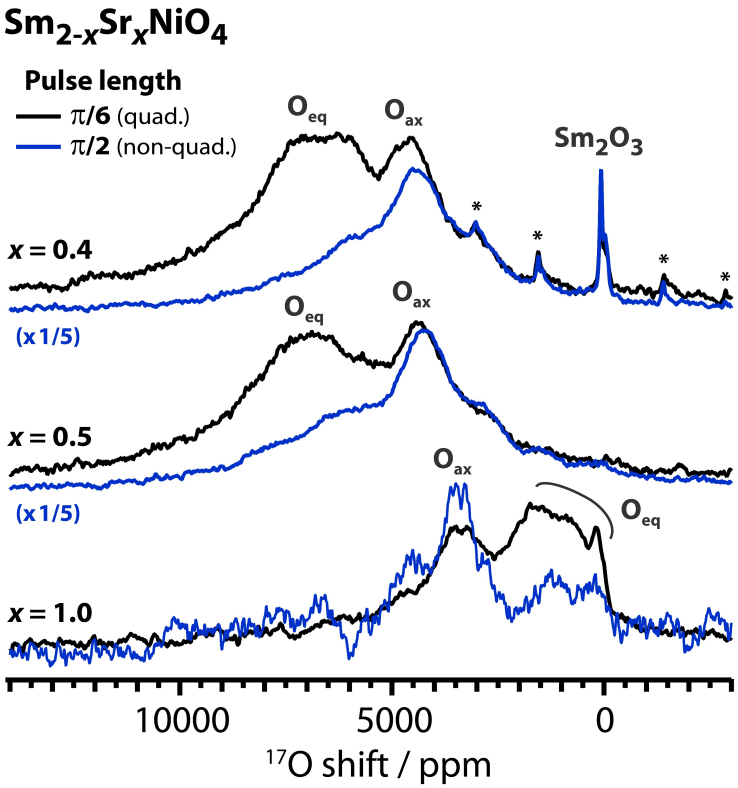


Figure 4.19: $^{17}$O MAS NMR spin-echo mapping spectra of $Sm_{2-x}Sr_xNiO_{4+\delta}$ at $x$ = 0.4, $x$ = 0.6, and $x$ = 1.0, recorded at 4.7 T under a MAS rate of 40 kHz. Assignments to oxygen environments in $Sm_{2-x}Sr_xNiO_{4+\delta}$ (and $Sm_2O_3$) are given above the respective peaks. Differing rf pulse lengths of π/6 (black traces) and π/2 (blue traces) have been used to suppress $O_{eq}$ and enhance $O_{ax}$; for the $x$ = 1.0 sample, this method is necessary to properly distinguish the intensity arising from the $O_{ax}$ and $O_{eq}$ sites. Spinning sidebands (where apparent) are denoted with asterisks. Spectra are scaled to the number of scans and further scaled where noted.

Comparing all the spectra in Figure 4.19, the most obvious change is the large decrease of the equatorial O shift (from 6500 ppm to 1000 ppm) with increase of the Sr content, which can be rationalized by direct analogy to changes in the spectra of the $La_{2-x}Sr_xNiO_{4+\delta}$ system

(Figure 4.12). That is, upon oxidation of $Ni^{2+}$ to $Ni^{3+}$ with increasing Sr content, the average $d_{x^2-y^2}$ orbital occupancy progresses from partially full (at $x$ = 0.4) to nearly empty (at $x$ = 1.0), with an almost complete disappearance of the spin delocalization onto the $O_{eq}$ site. Interestingly, the $O_{ax}$ shift is mostly unaffected by this process, whereas for $La_{2-x}Sr_xNiO_{4+\delta}$ the $O_{ax}$ and $O_{eq}$ features could not be readily distinguished at high levels of Sr due to spectral overlap. Because the analogous resonances in $Sm_{2-x}Sr_xNiO_{4+\delta}$ ($x$ = 1.0) are well-separated, this phase may present interesting possibilities for future work, including a study of the axial–equatorial oxygen exchange that would be anticipated at higher temperatures.

Other spectral details, such as apparent changes in the $C_Q$ values of the $O_{eq}$ and $O_{ax}$ sites, also bear close resemblance to the behavior observed for $La_{2-x}Sr_xNiO_{4+\delta}$ in the intermediate- and high-doping regime. The evolution of these parameters will be explored in future studies.

## 4.7 Conclusions and outlook

We have presented a local structure analysis primarily employing $^{17}O$ solid-state MAS NMR spectroscopy to explore the defect chemistry and electronic structure of the paramagnetic mixed ionic–electronic conductor $La_{2-x}Sr_xNiO_{4+\delta}$ ($x \leq 1$). The materials exhibit good phase stability, even following $^{17}O$-enrichment at elevated temperature, with the appearance of minor impurity phases $La_3Ni_2O_7$ and $La_4Ni_3O_{10}$ (for $x < 0.1$) and NiO (for $x \geq 0.1$). Room-temperature $^{17}O$ MAS NMR spectra of the $^{17}O$-enriched samples reveal resonances from three distinct oxygen environments: equatorial ($O_{eq}$), axial ($O_{ax}$), and interstitial ($O_i$). These spectral features act as proxies for electronic and ionic conductivity as well as subtle local structural distortions of the $NiO_6$ octahedra. Quantitative NMR experiments have been used to measure the interstitial concentration and thus the oxygen excess ($\delta$), which approaches 0 at $x$ = 0.3, a result consistent with the known lower oxide-ionic conductivity in the moderately Sr-doped phases. High-resolution MATPASS NMR spectra reveal that the axial distortion induced by nearby interstitial defects vanishes with very low levels of Sr doping, as expected from the defect chemistry, the higher symmetry (more tetragonal) crystal structure, and possible changes in interstitial ordering. Meanwhile, the hyperfine shift of the $O_{eq}$ resonance provides an accurate indication of the changing electronic structure of the

transition metal sites. Electron density is initially removed from the Ni $d_{x^2-y^2}$ orbital exclusively, but then also the $d_{z^2}$ orbital at high levels of Sr doping, providing a mechanistic understanding of the decrease in the Jahn-Teller distortion as well as the increased electronic conductivity upon Sr incorporation. These findings are supported by evidence from Rietveld refinement using XRD patterns for a diminishing Jahn-Teller elongation at the Ni sites, as well as analysis of Ni K-edge XANES spectra showing the average Ni valence approaching 3+ in the highly-doped regime. While the highly-doped phases do not show obvious biphasic behavior observed by some earlier studies, spectral broadening in the $^{17}$O NMR data is consistent with an inhomogeneous Sr distribution that is maximal for $x = 0.75$.

Understanding the diverse effects of A-site doping on the local structure of $La_{2-x}Sr_xNiO_{4+\delta}$ is relevant in tuning the mixed ionic–electronic conductivity of a wide range of perovskite and perovskite-derived structures for applications in intermediate-temperature SOFCs and oxygen sensors. Indeed, materials optimized for performance as SOFC cathodes, such as the isostructural $Sm_{2-x}Sr_xNiO_{4+\delta}$ phase, require some aliovalent A-site doping merely to retain the stability of the Ruddlesden-Popper structure, due to the small size of the lanthanide cation.[57,330] Local structural changes induced by doping, therefore, are of key importance in these phases and as we have shown can be readily ascertained by $^{17}$O NMR. Acquisition of $^{17}$O NMR spectra in operational temperature ranges (150 °C – 800 °C) is also a promising area of future study, as this could provide additional insights into the thermally-activated ion dynamics. For example, for the highly-doped phases, an exploration of the effects of the vacancy concentration on the exchange rate between axial and equatorial resonances would be possible at higher temperature. Additionally, understanding the effect of the interstitial ordering schemes described in Section 4.5.3 on the $O_{ax}$ lineshape should prove easier at slightly higher temperature due to sharpening of resonances. In general, we expect that paramagnetic $^{17}$O solid-state NMR spectroscopy, with its sensitivity to local atomic and electronic structure as well as oxide-ionic motion, will prove invaluable to the study of perovskite-derived phases and other functional paramagnetic oxides.

# Chapter 5 Variable-Temperature Multinuclear Solid-State NMR Study of Oxide-Ion Dynamics in Fluorite-Type Bismuth Vanadates and Phosphates

## 5.1 Abstract

Ionic conducting materials are crucial for the function of many advanced devices used in a variety of applications, especially in fuel cells and gas separation membranes. Many different chemical controls, such as aliovalent doping, have been used to try and stabilize $\delta$-$Bi_2O_3$, a material with exceptionally high oxide ion conductivity which is unfortunately only stable over a narrow temperature range. In this study, we employ a multinuclear, variable-temperature NMR spectroscopy approach to measure and characterize oxide ionic motion in the doped bismuth oxide materials $Bi_{0.913}V_{0.087}O_{1.587}$, $Bi_{0.852}V_{0.148}O_{1.648}$ and $Bi_{0.852}P_{0.148}O_{1.648}$, previously shown to have excellent conduction properties (Kuang *et al*., *Chem. Mater.* **2012**, *24*, 2162; Kuang *et al*., *Angew. Chem. Int. Ed.* **2012**, *51*, 690).[118,126] Using variable temperature (VT) measurements ranging from room temperature to 923 K, we are able to distinguish two main $^{17}O$ NMR resonances in each material, corresponding to O adjacent to Bi, and O in either $VO_4$ or $PO_4$ tetrahedra. The ionic motion experienced by these different sites has then been characterized, with coalescence of the two environments in the V-doped materials clearly indicating a conduction mechanism facilitated by exchange between the two sublattices. The lack of this coalescence in the P-doped materials indicates a different mechanism, confirmed by $^{17}O$ NMR to be driven purely by vacancy conduction in the Bi–O sublattice. Next, $^{51}V$ and $^{31}P$ VT-NMR experiments show high rates of tetrahedral rotation even at room temperature, increasing with heating. Activation energies for the different

motional processes have been determined using both relaxation and linewidth measurements, finding a lower activation barrier for $VO_4$ rotation compared to that for $PO_4$, and supporting inferences by Kuang *et al.* that variable coordination of V facilitates the more rapid ionic conduction in these materials (*Angew. Chem. Int. Ed.* **2012**, *51*, 690).[126] Finally, an additional V environment appears in $^{51}V$ and $^{17}O$ NMR spectra of $Bi_{0.852}V_{0.148}O_{1.648}$, corresponding to less distorted $VO_4$ tetrahedral units that disrupt the overall ionic motion, consistent with linewidth analysis of the $^{17}O$ VT-NMR spectra and experimental results of Kuang *et al.* showing a lower oxide ionic conductivity in this material compared to $Bi_{0.913}V_{0.087}O_{1.587}$ (*Chem. Mater.* **2012**, *24*, 2162).[118]

## 5.2 Introduction

Anionic conducting materials, especially oxide ion conductors, have been the focus of continued research efforts over the past decades due to their potential use in renewable energy applications, such as oxygen-permeable membranes and solid oxide fuel cells (SOFCs).[24,233,332] A crucial parameter holding back their widespread implementation is the undesirably high temperature at which they show sufficiently high ionic conduction, which even for the best materials (such as yttria-stabilized zirconia, YSZ) is >923 K.[333] There is still very much a need to discover and develop novel ionic conducting materials that operate at lower temperatures and to characterize the connection between structure and conductivity in order to move towards precise design of optimal materials.

Bismuth oxides and various doped derivatives have been plumbed as a rich compositional space within which to find new promising materials, sparked by the extremely high oxygen ionic conductivity values measured for the cubic $\delta$ phase of $Bi_2O_3$, which is not stable at lower temperatures due to transformation to a monoclinic polymorph below 1003 K.[92,334] Of the families of materials that have been explored, vanadium doped bismuth oxides have shown promising values of ionic conductivity at relatively lower temperatures.[118,126] These materials often exhibit complex superstructures, and understanding the role of the V dopant on the superionic behavior of the Bi–O lattice is correspondingly complex, but necessary in elucidating the best way to optimize these materials for device applications.

As detailed in Section 1.3, two novel bismuth-rich phases in the $Bi_{1-x}V_xO_{1.5+x}$ system ($x = 0.087$, 0.095) were found to have significantly high oxide ion conductivity between 573–773 K, competitive with the best-performing $Bi_2O_3$-based materials currently known.[126] Subsequent studies involving *ab initio* molecular dynamics simulations found for both these and a related phase with $x = 0.148$ (also called $\beta$-$Bi_{46}V_8O_{89}$) distinct structural features, such as variable-coordinated $VO_x$ polyhedra, played key roles in the ionic migration pathways through the material, facilitating oxygen exchange between the polyhedra and Bi–O sublattice.[118] The structure of the higher-doped material $Bi_{0.852}V_{0.148}O_{1.648}$ is shown in Figure 5.1, highlighting the layers containing Bi–O slabs interspersed with layers containing $VO_4$ polyhedra. This phase can be thought of as a defective pseudo-cubic long-range ordered fluorite structure where V replaces some of the Bi sites in $\delta$-$Bi_2O_3$, with concomitant reordering of oxygen vacancies to preserve fourfold coordination around the V atoms. A similar structure in the same monoclinic *C*2/*m* space group has been reported for the P-doped analogue $Bi_{0.852}P_{0.148}O_{1.648}$ (also reported as $Bi_{46}P_8O_{89}$), where $VO_4$ tetrahedra are replaced with $PO_4$.[114] At lower doping levels, $Bi_{0.913}V_{0.087}O_{1.587}$ adopts a long-range ordered pseudo-cubic 3 ×3 ×3 fluorite superstructure.

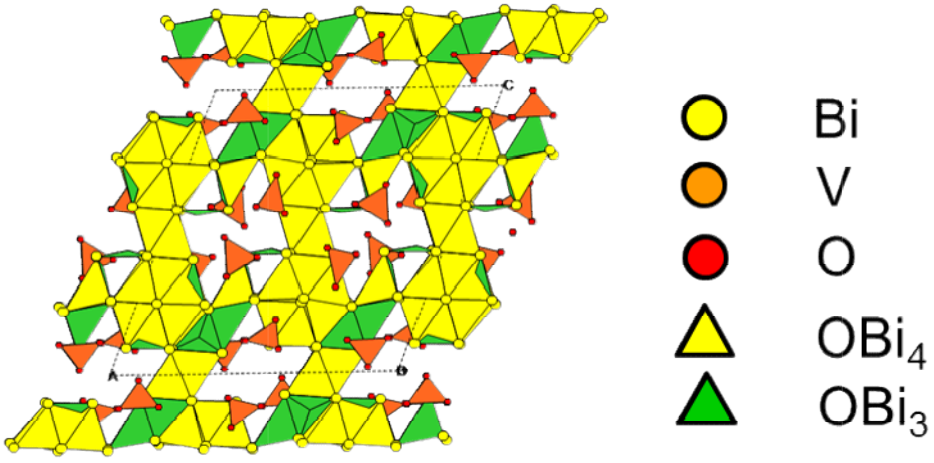


Figure 5.1: Crystallographic structure of $Bi_{0.852}V_{0.148}O_{1.648}$ (also known as $\beta$-$Bi_{46}V_8O_{89}$), shown in the (*ac*) projection. The monoclinic (space group *C*2/*m*) structure comprises a characteristic stacking of two layers containing $VO_4$ tetrahedra ($Bi_{14}V_4O_{31}$), with both $OBi_3$ and $OBi_4$ building blocks, and one bismuth oxide rock salt layer ($Bi_{18}O_{27}$) containing only $OBi_4$ units. All $VO_4$ groups are isolated, *i.e.*, the apparent corner sharing is due to perspective.

In this chapter, we report a comprehensive experimental study of the oxide ion dynamics of both $Bi_{0.913}V_{0.087}O_{1.587}$ and $Bi_{0.852}V_{0.148}O_{1.648}$ using multinuclear variable-temperature solid state nuclear magnetic resonance (VT-NMR), as well as comparing the conduction mechanisms of these phases to the P-doped analogue $Bi_{0.852}P_{0.148}O_{1.648}$. $^{17}O$ VT-NMR experiments have previously been shown to be particularly well-suited to the elucidation of the conduction mechanism in related materials such as $\alpha$-$Bi_4V_2O_{11}$, $\gamma$-$Bi_4V_{1.7}Ti_{0.3}O_{10.85}$, $Bi_{26}Mo_{10}O_{69}$, and $Bi_2WO_6$.[242,244,245] These experiments can distinguish amongst crystallographic oxygen environments present in these phases as well as their corresponding motional processes and rates. In this study, we have used $^{17}O$, $^{51}V$ and $^{31}P$ NMR to characterize the mechanisms of, and activation energy values for, ionic motion in these materials. We find that oxide-ionic exchange between the Bi and V sublattices occurs with increasing temperature for both $Bi_{0.913}V_{0.087}O_{1.587}$ and $Bi_{0.852}V_{0.148}O_{1.648}$, whereas no evidence of sublattice exchange is seen for $Bi_{0.852}P_{0.148}O_{1.648}$. We also find that the concentration of dopant is critical for maximizing the rate of conduction, with higher dopant concentrations leading to the formation of less distorted $VO_x$ polyhedra that do not participate in ionic pathways and instead hinder the overall movement of oxide ions through the structure. Furthermore, the use of dopant atoms that are unable to undergo variable O coordination (*e.g.*, P) blocks exchange between the two sublattices; this helps to explain previous reports of oxide ionic conductivity about half an order of magnitude lower for the P-doped phase over the same temperature range, relative to the $\beta$-$Bi_{46}V_8O_{89}$ material.[123]

## 5.3 Experimental methods

### 5.3.1 Synthesis and $^{17}O$-enrichment

Samples of $Bi_{0.913}V_{0.087}O_{1.587}$, $Bi_{0.852}V_{0.148}O_{1.648}$ and $Bi_{0.852}P_{0.148}O_{1.648}$ were synthesized according to the previous literature;[118,123,126] the syntheses were performed by Matthew L. Tate (Department of Chemistry, Durham University). The present author then performed $^{17}O$-enrichment of samples by heating as-synthesized powders to 900 °C under an atmosphere of 70% $^{17}O_2$ (Cambridge Isotope Labs, used as received) in a Pt crucible inside a sealed quartz tube for 24 h; samples were cooled slowly from the enrichment temperature to maximize $^{17}O$

uptake. Sample purity after $^{17}$O-enrichment was confirmed using room-temperature X-ray powder diffraction (XRD) data collected on a Panalytical X'Pert Pro diffractometer using Cu $K_\alpha$ radiation (data shown in Figure 5.2); the reflections can be indexed to a cubic space group for $Bi_{0.852}V_{0.148}O_{1.648}$ or a monoclinic space group for $Bi_{0.852}P_{0.148}O_{1.648}$ and $Bi_{0.852}V_{0.148}O_{1.648}$.

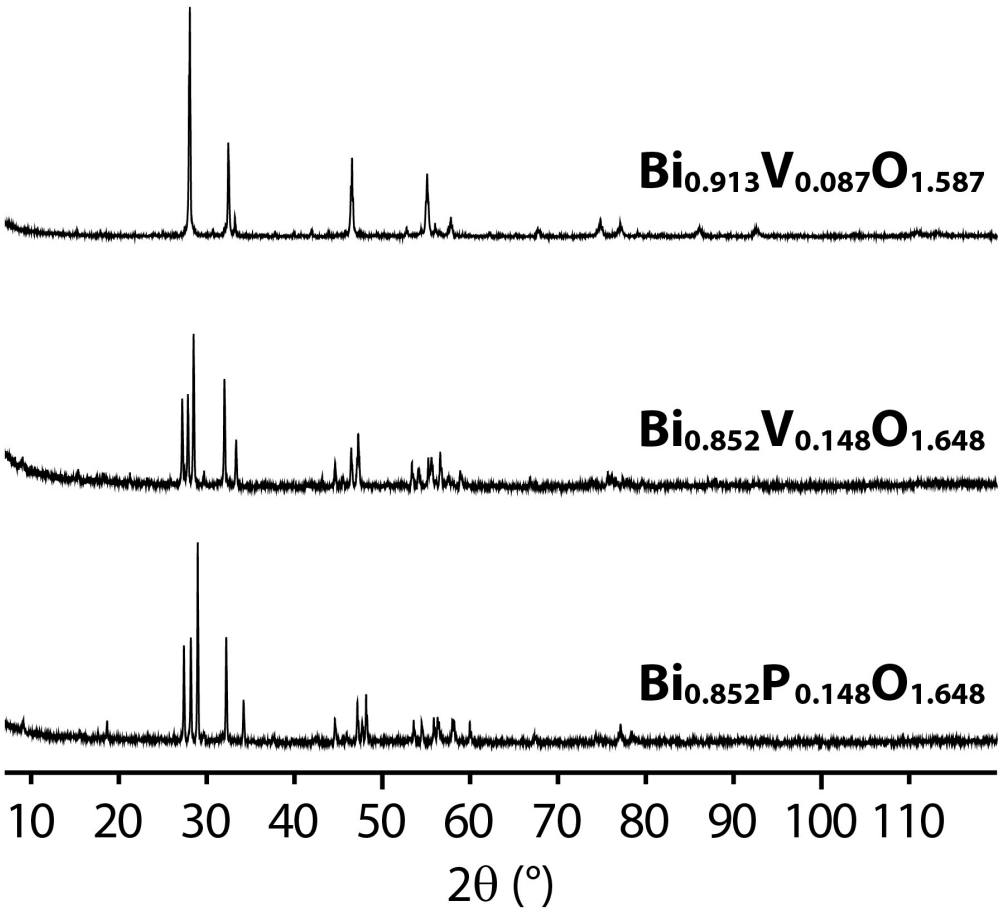


Figure 5.2: Ambient temperature powder XRD patterns of $^{17}$O-enriched samples of $Bi_{0.913}V_{0.087}O_{1.587}$, $Bi_{0.852}V_{0.148}O_{1.648}$, and $Bi_{0.852}P_{0.148}O_{1.648}$. The patterns are in good agreement with those previously reported in the literature,[118,126] confirming that the samples remain phase-pure following the $^{17}$O-enrichment procedure.

### 5.3.2 Solid-state NMR spectroscopy

Solid-state $^{17}$O, $^{51}$V and $^{31}$P magic-angle spinning (MAS) NMR spectra were obtained at 16.4 T on a Bruker Avance III 700 MHz spectrometer operating at a Larmor frequency of 94.95 MHz ($^{17}$O), 184.05 MHz ($^{51}$V) and 283.39 MHz ($^{31}$P); initial room temperature

measurements were performed using a double resonance 1.3 mm Bruker probe, at a MAS rate of 60 kHz, and using a rotor-synchronized spin-echo pulse sequence with a $\pi/2$ excitation pulse length of 1.4 $\mu$s (for $^{17}$O). Variable temperature measurements from room temperature to 973 K were performed at the same field using a triple resonance 7 mm Bruker laser probe.[335,336] Temperature calibration of the probe was carefully performed by measuring the $^{79}$Br resonance of KBr over the entire temperature range, with the KBr typically included in the same rotor as the sample as an internal temperature reference.[337] The temperatures given in the text correspond to actual sample temperatures with an estimated accuracy of ±10, 20 and 30 K in the 293–473 K, 473–673 K and 673–873 K temperature ranges, respectively. Samples were packed in 4 mm BN inserts within 7 mm zirconia rotors, which were subsequently spun at 4 kHz. One dimensional experiments were performed with a rotor-synchronized spin-echo pulse sequence, using a 9 $\mu$s, 4 $\mu$s, or 6.5 $\mu$s $\pi/2$ excitation pulse (for $^{17}$O, $^{51}$V, and $^{31}$P, respectively). Additional $^{17}$O measurements, including relaxation experiments, were obtained at 11.7 T on a Bruker Avance III 500 MHz spectrometer operating at a Larmor frequency of 67.83 MHz, using a double resonance 4 mm Bruker probe at a MAS rate of 12.5 kHz, with an excitation pulse of 2.2 $\mu$s (for Bi–O sites) or 5.0 $\mu$s (for V–O sites). Variable temperature spin-lattice ($T_1$) relaxation experiments at this field were performed using a standard saturation recovery pulse sequence, with a maximal delay of 2.4 s (for Bi–O sites) or 0.24 s (for V–O sites). Temperature calibration of this probe was also performed by measuring the $^{79}$Br resonance of KBr, with estimated accuracy of ±5 K. Finally, $^{17}$O measurements were performed at 4.7 T on a Bruker Avance III 200 MHz spectrometer operating at a Larmor frequency of 27.14 MHz, using a double resonance 1.3 mm Bruker probe at a MAS rate of 40 kHz, with an excitation pulse of 0.5 $\mu$s; these experiments were performed in order to extract quadrupolar parameters from the field-dependent second-order quadrupolar shift (see Section 2.1.4.2 for details of this method). $^{17}$O chemical shifts were externally referenced to $H_2O$ at 0 ppm, $^{51}$V chemical shifts were externally referenced to $NH_4VO_3$ at −570 ppm,[338,339] and $^{31}$P chemical shifts were externally referenced to $H_3PO_4$ (aq) at 0 ppm. NMR data were processed with TopSpin 3.2.[271]

## 5.4 Results

### 5.4.1 $^{17}$O NMR

Room temperature $^{17}$O NMR spectra of all three materials have been obtained at fast MAS rates (60 kHz) in order to achieve higher resolution, and are shown in Figure 5.3. For each spectrum, a number of different oxygen environments can be distinguished with resonances ranging from ~130–630 ppm. The common feature at 220 ppm observed in all three spectra is assigned to oxygen within the Bi–O sublattice, which is consistent with this chemical environment occurring in all three structures, as well as previous reports of similar $^{17}$O chemical shifts of oxygen environments coordinated to Bi, such as in $Bi_2O_3$ (195 ppm),[340] as well as the so-called BIMEVOX ($Bi_4V_{2(1-x)}M_{2x}O_{11-3x}$ with $M$ = Cu, Ni) systems[109,110,242] and $Bi_2WO_6$ (242 ppm).[244] The feature at 620 ppm present in both V-doped samples is attributed to O in $VO_4$ tetrahedra, in good agreement with the established shift range of V–O environments (600–1000 ppm).[242,341] Finally, the resonance at 130 ppm, only present in the P-doped sample, is assigned to $PO_4$ tetrahedra, with a shift that compares favorably to recent $^{17}$O NMR studies of solid inorganic acid phosphates.[247] A very minor peak is observed at 140 ppm in both V-doped samples as well, tentatively assigned to bismuth silicate that forms by reaction with the quartz vessel during the $^{17}$O-enrichment procedure. This feature is consistent with the $^{17}$O shifts reported for other silicates such as glasses and apatite oxide-ion conductors.[319,342] This impurity phase is below the detection limit of XRD, but is estimated at ~1 wt. % from the $^{17}$O NMR intensity.

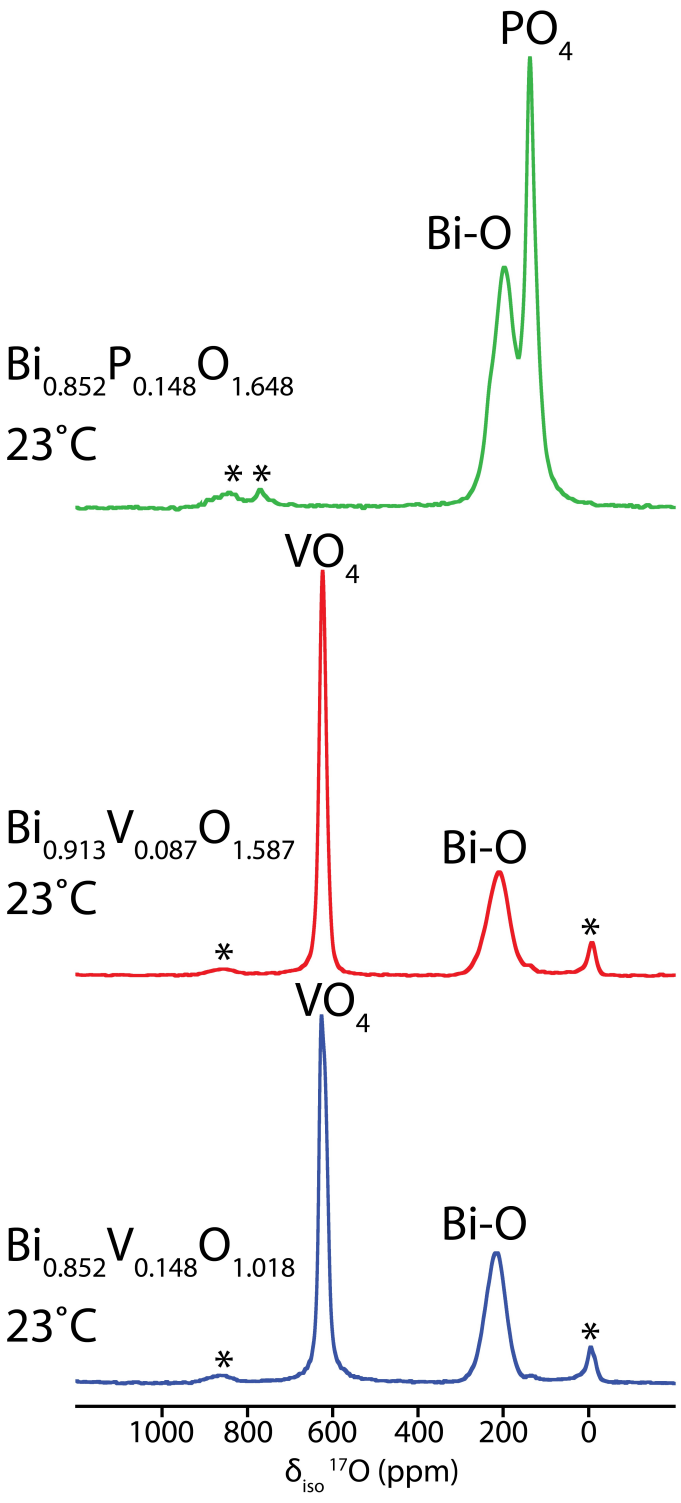


Figure 5.3: Room temperature $^{17}O$ NMR spectra of $Bi_{0.913}V_{0.087}O_{1.587}$, $Bi_{0.852}V_{0.148}O_{1.648}$ and $Bi_{0.852}P_{0.148}O_{1.648}$, obtained at 16.4 T at a spinning rate of 60 kHz. All three samples show a common feature at ~220 ppm, assigned to O in the $\delta$-$Bi_2O_3$ sublattice, with additional resonances arising from the $VO_4$ and $PO_4$ environments at ~620 ppm and ~130 ppm, respectively. Asterisks denote spinning sidebands.

The $^{17}O$ NMR spectra obtained upon heating all three materials to 823 K are summarized in Figure 5.4 (the full datasets are shown in Appendix C). The $^{17}O$ spectra for both V-doped samples show qualitatively similar behavior with increasing temperature, and in particular the resonances corresponding to the V–O environments narrow in linewidth up to 573 K. Above 573 K both resonances disappear in both samples, before reappearing as a single coalesced resonance at 823 K. This behavior is indicative of exchange between the two different sites occurring on the so-called NMR timescale, where the rate of motion approaches the frequency separation between the two spectral features (see Section 2.1.5.1). Interpolation of the spectra allows us to estimate the temperature at which the maximum broadening and initial coalescence is observed, where the rate of ionic motion is directly proportional to the frequency separation. On this basis we calculate sublattice exchange rates of 87 kHz at 723 K for pseudo-cubic $Bi_{0.913}V_{0.087}O_{1.587}$, and 86 kHz at 748 K for monoclinic $Bi_{0.852}V_{0.148}O_{1.648}$; thus, at comparable temperatures, the motional rate is slightly slower in the more highly V-doped, crystallographically lower symmetry material.

For each phase, the chemical shift of the fully coalesced peak also gives information as to the residence time of mobile $O^{2-}$ ions spent in Bi–O-like environments vs. V–O environments. The coalesced shift of 332 ppm for the $Bi_{0.913}V_{0.087}O_{1.587}$ phase corresponds to a ratio of 70:30 (Bi:V), compared to a shift of 391 ppm for $Bi_{0.852}V_{0.148}O_{1.648}$ that gives a ratio of 52:48 (Bi:V). This result is intuitively reasonable given the higher concentration of V in $Bi_{0.852}V_{0.148}O_{1.648}$. Furthermore, the ratio of O sites in the Bi:V sublattices expected from the nominal stoichiometry values, assuming isolated $VO_4$ tetrahedra, (*i.e.,* 79:21 for $Bi_{0.852}V_{0.148}O_{1.648}$ and 64:36 for $Bi_{0.913}V_{0.087}O_{1.587}$) are significantly larger than the ratios calculated from the coalescence data. This result suggests the VT-NMR data are sensitive to the presence of oxygen vacancies in the Bi–O sublattice and/or over-coordination of the $VO_4$ units. For $Bi_{0.852}V_{0.148}O_{1.648}$, the relative number and/or residence time of O sites in V–O environments is 33% larger than that expected solely from stoichiometry, whereas it is 43% larger than expected for $Bi_{0.913}V_{0.087}O_{1.587}$, implying that the latter phase has a higher average V coordination that also generates more vacancies in the Bi–O sublattice. Kuang *et al.* also found from *ab initio* molecular dynamics simulations that the coordination number of V sites varied between 4.0 and 4.3 for both V-doped phases, with the larger average coordination

number observed for the lower V-doped material, in good agreement with the present results.[118,126]

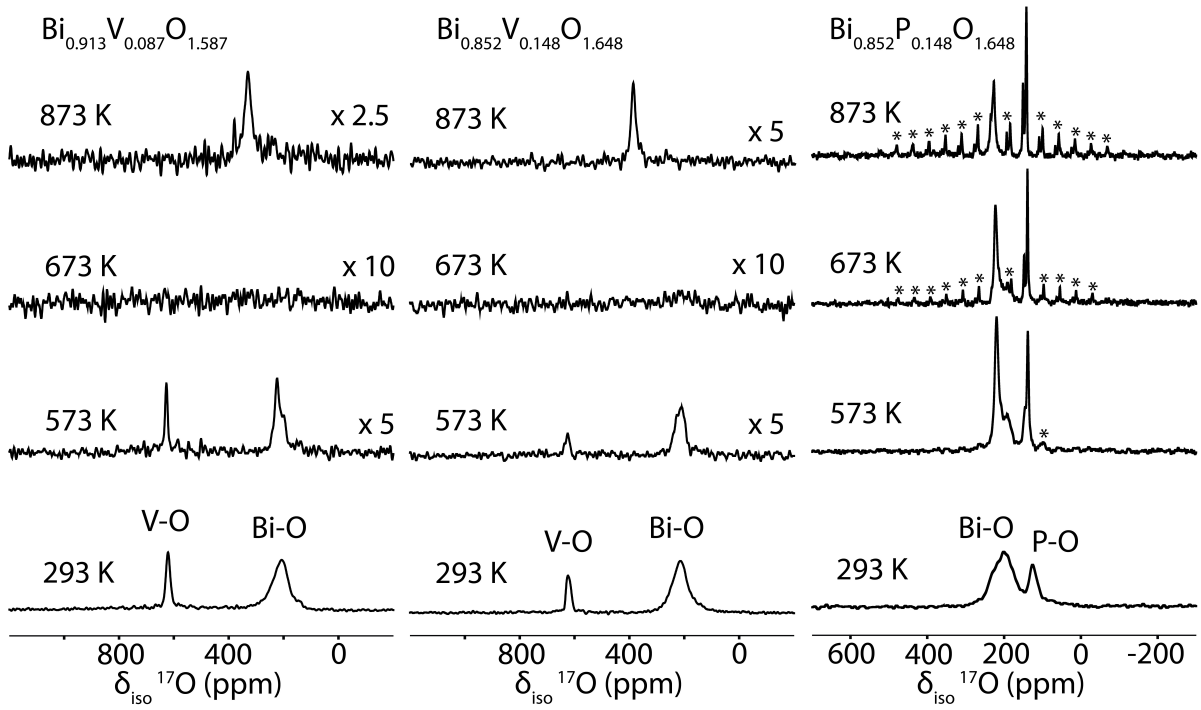


Figure 5.4: Variable-temperature $^{17}O$ NMR spectra of $Bi_{0.913}V_{0.087}O_{1.587}$, $Bi_{0.852}V_{0.148}O_{1.648}$ and $Bi_{0.852}P_{0.148}O_{1.648}$ obtained at 16.4 T at a spinning rate of 4 kHz. The high-temperature $^{17}O$ spectra for both V-doped samples show first the broadening and disappearance (at 673 K), and then the coalescence of the two distinct $^{17}O$ features at higher temperatures, indicative of increasingly fast motion between the V–O and Bi–O environments with increasing temperature. In comparison to the V-doped samples, for $Bi_{0.852}P_{0.148}O_{1.648}$ no coalescence of the two $^{17}O$ resonances is observed at increasing temperatures, indicating a minimal rate of O hopping between distinct environments over this temperature range. Spinning sidebands are denoted by asterisks.

For $Bi_{0.852}P_{0.148}O_{1.648}$, the temperature-dependent behavior of the $^{17}O$ spectra differ significantly from that of the V-doped samples. As shown in Figure 5.3, the narrow feature at ~130 ppm arises from O in the $PO_4$ environment, whereas the broader peak at ~210 ppm corresponds to O in a Bi–O-like environment. With increasing temperature, both resonances exhibit linewidth narrowing that is indicative of increased rates of local oxide-ionic motion, and this narrowing allows for observation of an additional resonance for each environment above ~473 K. However, even at 873 K, the two groups of resonances remain distinct, showing no sign of coalescence as is seen in $Bi_{0.913}V_{0.087}O_{1.587}$ and $Bi_{0.852}V_{0.148}O_{1.648}$. This

result is indicative of ionic motion that remains local (*e.g.*, $PO_4$ rotation) or is confined to distinct sublattices, with minimal long-range exchange between the P and Bi sublattices.

Closer examination of the isotropic peaks (*i.e.*, the centerband which arises principally from the central transition, or CT, intensity) corresponding to the $VO_4$ environments in the $^{17}O$ spectra of the V-doped samples shows that, for $Bi_{0.913}V_{0.087}O_{1.587}$, the CT centerband can be fit to a single Voigt function, corresponding to a single type of $VO_4$ environment. On the other hand, the $Bi_{0.852}V_{0.148}O_{1.648}$ CT centerband requires two Gaussian functions with relative intensity varying with temperature (Figure 5.5), indicating the presence of two distinct types of $VO_4$ environments in the more highly V-doped material. The simple fits to the spectra are justified, as second-order quadrupolar coupling effects are not expected to play a significant role. The quadrupole coupling constants ($C_Q$'s) of the $VO_4$ sites are below 0.9 MHz, and are therefore too small to account for the observed lineshapes (Figure 5.6).

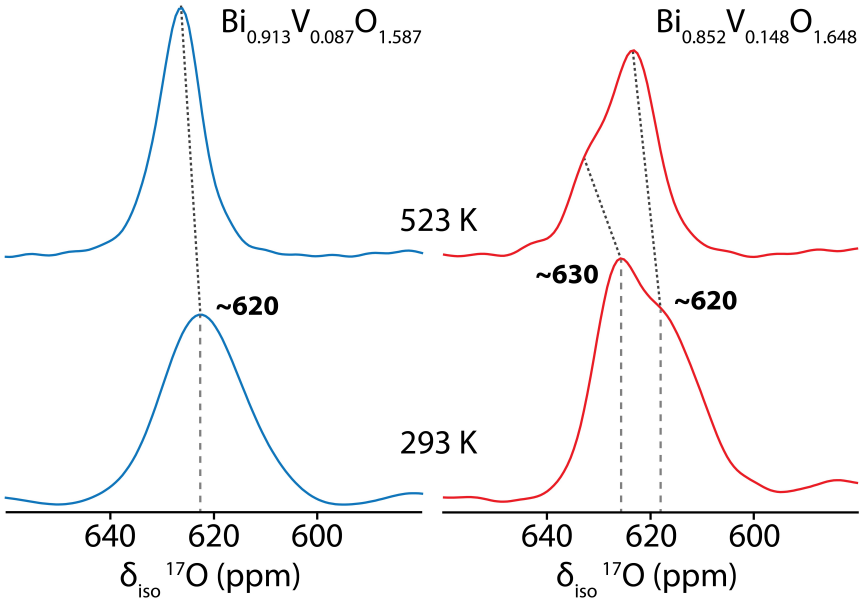


Figure 5.5: $^{17}O$ NMR spectra of $Bi_{0.913}V_{0.087}O_{1.587}$ and $Bi_{0.852}V_{0.148}O_{1.648}$, focusing on the isotropic peaks of the $VO_4$ environment(s), measured at 16.4 T at a spinning rate of 4 kHz at both room temperature and 523 K. Only one resonance is seen in the $Bi_{0.913}V_{0.087}O_{1.587}$ sample at both temperatures, which can be fitted to a single Voigt peak. However, the $VO_4$ resonance in the $Bi_{0.852}V_{0.148}O_{1.648}$ sample comprises two separate Gaussian functions with relative intensity changing with increasing temperature. The dotted lines between spectra track the temperature dependence of the shifts of the resonances.

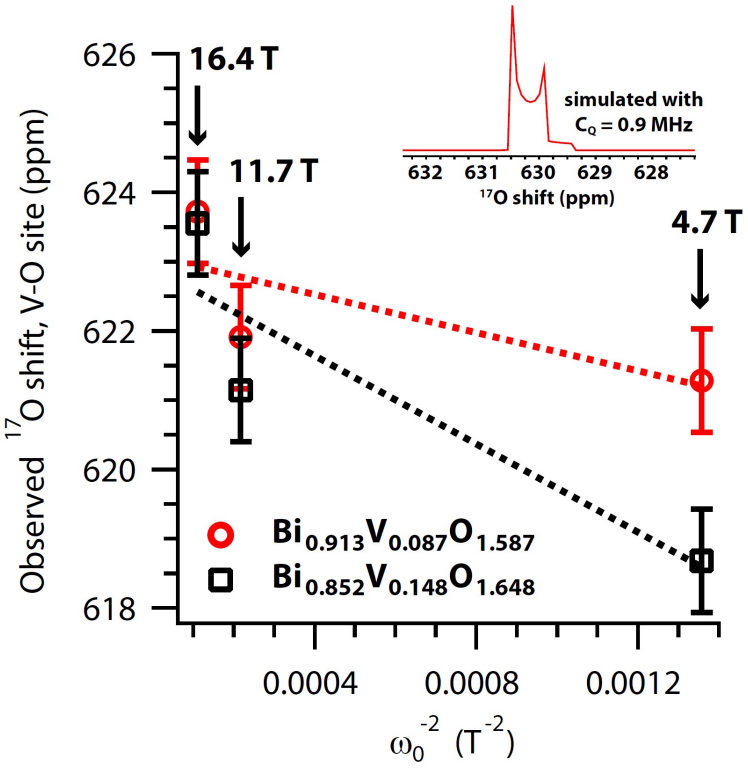


Figure 5.6: The observed $^{17}$O chemical shift of the V–O feature for the V-doped samples (at room temperature), as a function of the Larmor frequency $\omega_0$ for $^{17}$O; the experimental magnetic field is also indicated above each pair of points. (In the case of two features appearing in the spectra, as for $Bi_{0.852}V_{0.148}O_{1.648}$, the weighted average of the shifts of the two features is plotted.) The slope of the best-fit lines (depicted as dotted lines) has then been used to obtain upper bounds on the $C_Q$ values of 0.8 MHz and 0.9 MHz for $Bi_{0.913}V_{0.087}O_{1.587}$ and $Bi_{0.852}V_{0.148}O_{1.648}$, respectively, using Equation (2.18). The inset shows the expected lineshape due to second-order quadrupolar broadening (at 16.4 T) in the case of $C_Q$ = 0.9 MHz and $\eta_Q$ = 0, which spans approximately 0.5 ppm.

The two types of $VO_4$ environments display different temperature-dependent behavior and thus provide insights into the underlying oxide-ionic motional mechanisms that distinguish the V-doped samples. As seen in Figure 5.7a, both V-doped compounds share a common V–O environment centered at ~620 ppm at room temperature, which narrows as a function of increasing temperature until reaching a minimum CT linewidth between 473–523 K. This environment therefore undergoes thermally-activated ionic motion with a motional rate eventually exceeding the range of ionic motion to which the CT linewidth is sensitive, with no further narrowing above 523 K (Figures C.1.1 and C.1.2 in Appendix C). By contrast, the linewidth of the second peak (at ~630 ppm at room temperature), which is only seen in the

VT spectra of $Bi_{0.852}V_{0.148}O_{1.648}$, retains a relatively constant linewidth over the same temperature range. This indicates that the corresponding chemical environment either experiences no change in the rate of ionic motion, or that the rate of O motion at this site is already sufficiently fast at room temperature so as not to lead to changes in the CT linewidth. The small (constant) value of the linewidth of the ~630 ppm feature is nearly the same as that of the environment at ~620 ppm at high temperature, suggesting that the ~630 ppm feature does experience very fast ionic motion at lower temperatures.

For the $Bi_{0.852}P_{0.148}O_{1.648}$ sample, two $PO_4$ features can be resolved in the $^{17}O$ NMR spectra at and above 523 K, at 135 ppm and 145 ppm, respectively (Figure 5.8). Again, the quadrupolar coupling constant of this resonance is insufficiently large to cause the observed lineshape, as is apparent from a very weak dependence of the experimental shift on the magnetic field strength (Figure 5.9), so the two features are assigned to distinct chemical environments. Unlike the two $VO_4$ environments in $Bi_{0.852}V_{0.148}O_{1.648}$, both $PO_4$ features undergo linewidth narrowing with increasing temperature, reaching a minimum linewidth value above 650 K (Figure 5.7b). The higher temperatures required to achieve linewidth narrowing as compared to the $VO_4$ environments may indicate that $PO_4$ rotation is only activated at higher temperatures. Moreover, we conclude that all $PO_4$ environments show increasing rates of rotation within the NMR timescale over this intermediate temperature range, with no $PO_4$ tetrahedra already in the fast motional regime at lower temperatures (unlike the $VO_4$ resonance at ~630 ppm in the $^{17}O$ spectra of $Bi_{0.852}V_{0.148}O_{1.648}$).

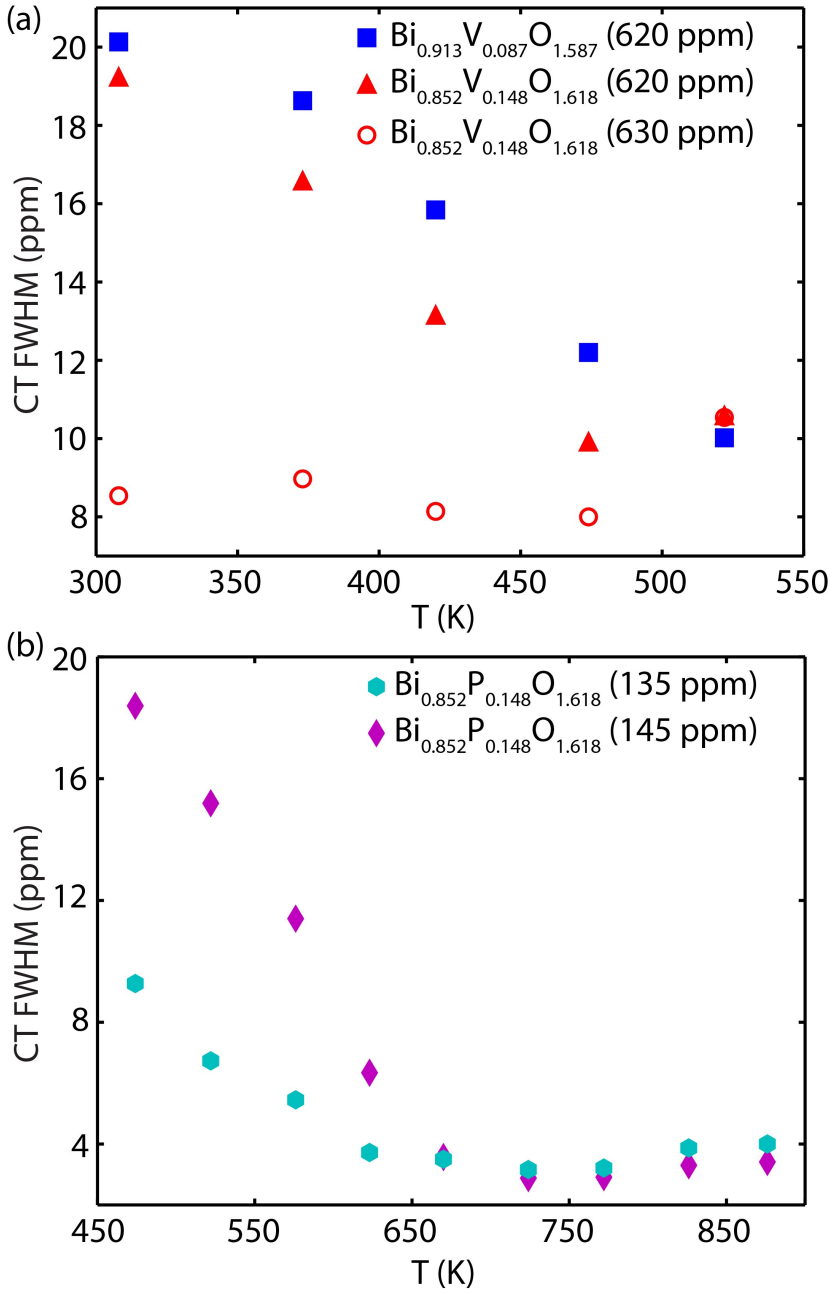


Figure 5.7: $^{17}$O NMR CT full width at half maximum (FWHM) linewidths of the $VO_4$ and $PO_4$ environments in the three phases, plotted against temperature. (a) In both vanadium-doped samples, one resonance at 620 ppm narrows with increasing temperature, indicative of increasing tetrahedral rotation, until a minimum linewidth is attained; further motional increases exceed the threshold above which CT linewidth is sensitive to motion. For the $Bi_{0.852}V_{0.148}O_{1.648}$ sample, a second resonance at 630 ppm is observed with temperature-invariant CT linewidth, indicating the presence of $VO_4$ tetrahedra that do not undergo motion on the spectral timescale. (b) Two distinct $PO_4$ resonances are resolved for $Bi_{0.852}P_{0.148}O_{1.648}$ at temperatures >473 K. The linewidth of both resonances narrows with increasing temperature, reaching a minimum value at 650 K.

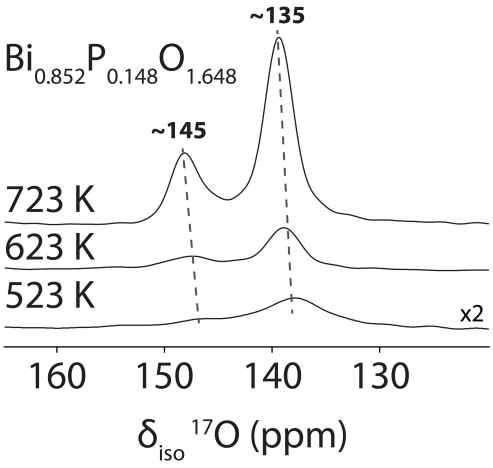


Figure 5.8: $^{17}O$ NMR spectra of $Bi_{0.852}P_{0.148}O_{1.648}$, focusing on the isotropic peaks of the $PO_4$ environments, measured at 16.4 T at a spinning rate of 4 kHz at 523–723 K. At temperatures ≤ 473 K, only one resonance is seen at ~135 ppm which can be fitted to a single Voigt peak. With higher temperatures a second resonance appears at ~145 ppm; its intensity increases with temperature. The dashed lines track the approximate temperature dependence of the shifts of the two resonances.

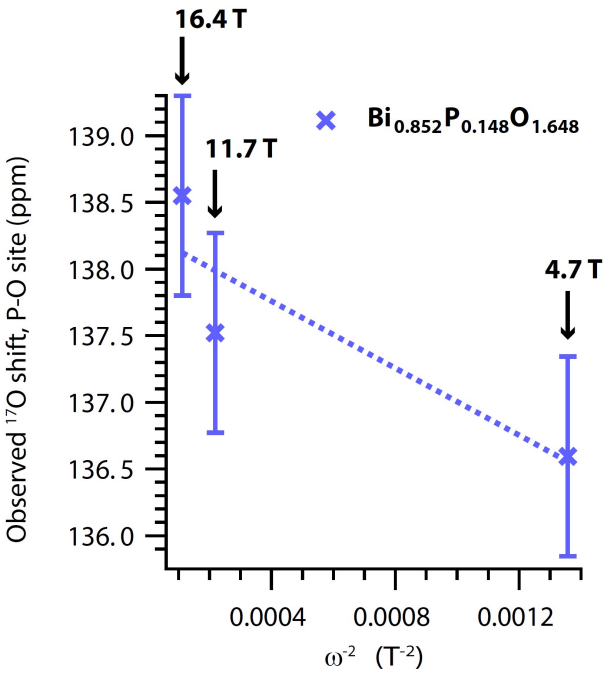


Figure 5.9: The observed $^{17}O$ chemical shift of the P–O feature for the P-doped sample (at room temperature), as a function of the Larmor frequency $\omega_0$ for $^{17}O$; the experimental magnetic field is also indicated above each point. The slope of the best-fit line (depicted as a dotted line) has then been used to obtain an upper bound on the $C_Q$ value of 0.6 MHz by applying Equation (2.18). Here, the poor fit to the data indicates a very small $C_Q$.

### 5.4.2 $^{51}$V NMR

The room temperature $^{51}$V NMR spectra for the more highly V-doped monoclinic sample, $Bi_{0.852}V_{0.148}O_{1.648}$, shown in Figure 5.10a, reveals two distinct sites with isotropic shifts at −486 and −493 ppm respectively, with sidebands arising from their corresponding satellite transitions (STs). The relatively small difference in chemical shift of these V environments is most likely due to small differences in the local structure surrounding the $VO_4$ tetrahedra, and the resonances lie within the known shift range for tetrahedrally-coordinated vanadium sites.[242] With increasing temperature, the linewidths of the two sets of ST sidebands behave differently. The site with the wider sideband manifold initially broadens to a point (at 473 K) where the sidebands can no longer be observed. This behavior then reverses, with the sidebands reappearing and narrowing up to 823 K. We assign these characteristic changes to increasing rates of ionic motion on the MAS rate, as seen in similar studies.[132,245] Conversely, the linewidths of the ST sidebands of the other V site with a much narrower manifold show virtually no change with increasing temperature, suggesting this site is not involved in motional processes upon heating.

The corresponding VT spectra of the lower V-doped pseudo-cubic phase $Bi_{0.913}V_{0.087}O_{1.587}$, however, show evidence for only one type of V environment, with a much broader CT linewidth at room temperature and no observed ST intensity, consistent with a distribution of similar $VO_4$ polyhedra. Upon heating, the CT linewidth narrows markedly, accompanied by the appearance and then linewidth narrowing of the ST sidebands; this behavior corresponds to the latter half of the behavior of the motionally active V site in the highly V-doped sample ($Bi_{0.852}V_{0.148}O_{1.648}$). Thus, the motion probed by the single V environment, even at room temperature, is already of a similar rate to the MAS spinning frequency (4 kHz) and therefore much faster than that experienced by the equivalent site in $Bi_{0.852}V_{0.148}O_{1.648}$. Additionally, there is no evidence of a second site with temperature-invariant ST linewidth in the lower V-doped $Bi_{0.913}V_{0.087}O_{1.587}$. These results from $^{51}$V NMR are in good agreement with the $^{17}$O NMR data in which only one feature in the V–O region is observed for $Bi_{0.913}V_{0.087}O_{1.587}$ (but two such peaks are present for $Bi_{0.852}V_{0.148}O_{1.648}$).

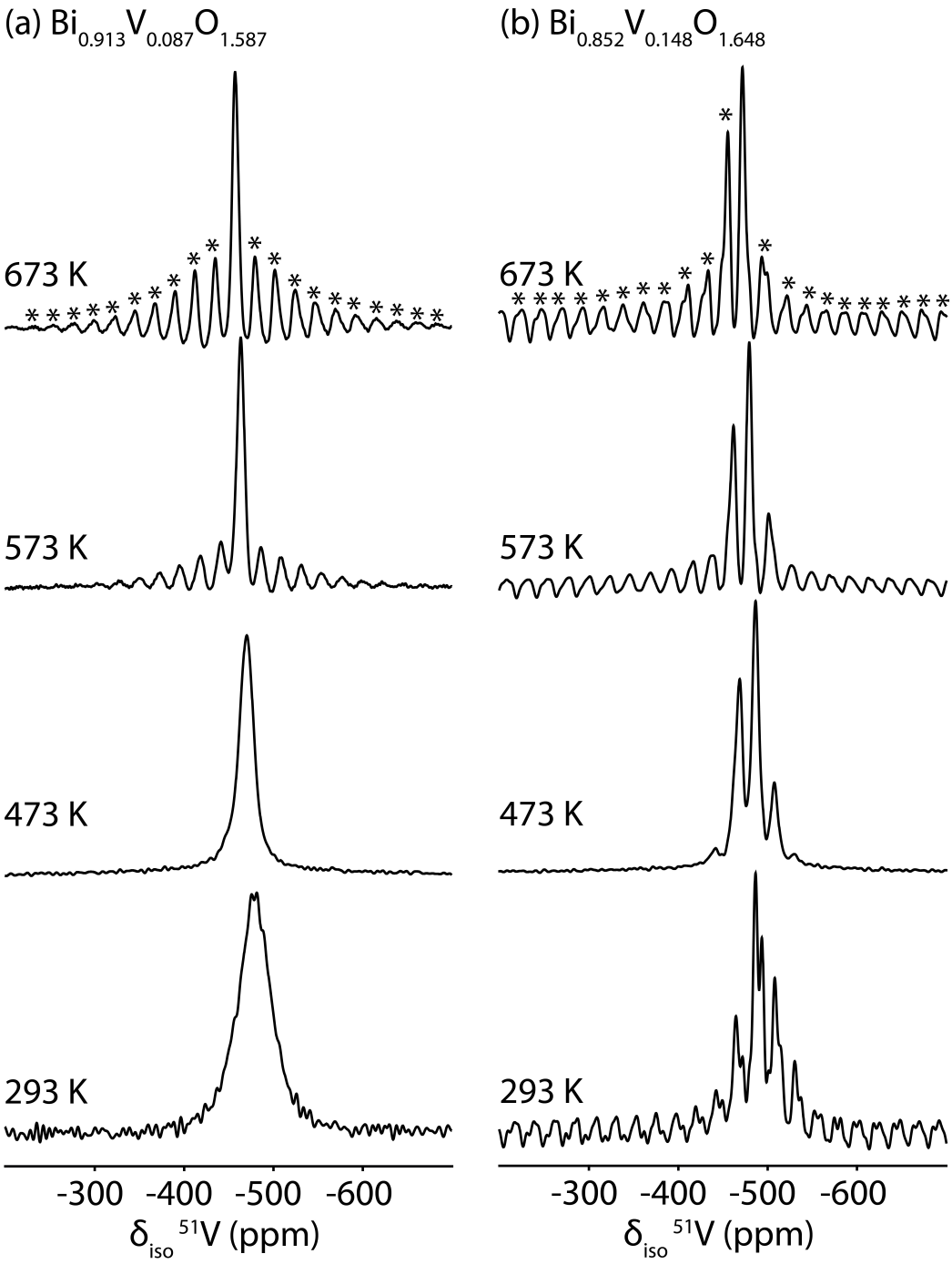


Figure 5.10: Variable-temperature $^{51}V$ NMR spectra of $Bi_{0.913}V_{0.087}O_{1.587}$ and $Bi_{0.852}V_{0.148}O_{1.648}$ obtained at 16.4 T at a spinning rate of 4 kHz. At room temperature, the isotropic resonance in the $^{51}V$ spectrum of $Bi_{0.913}V_{0.087}O_{1.587}$ is already broadened, indicating significantly fast motion involving the $VO_4$ environment with respect to the spinning frequency, whereas the corresponding spectrum of $Bi_{0.852}V_{0.148}O_{1.648}$ indicates a relatively slower motional rate. Asterisks denote spinning sidebands (only shown at highest temperature for clarity).

### 5.4.3 $^{31}$P NMR

The room temperature $^{31}$P NMR spectra of $Bi_{0.852}P_{0.148}O_{1.648}$ comprise a single broad resonance that narrows with increasing temperature (Figure 5.11), allowing us to distinguish four different local environments. We assign these linewidth changes to the influence of nearby oxygen motion that enters the fast motional regime at high temperature and thus no longer broadens the $^{31}$P resonances, a result that concurs with the narrowing linewidths seen in the corresponding $^{17}$O spectra. At high temperatures, the four distinct $^{31}$P resonances reflect small changes in the number and arrangement of nearby Bi and P atoms, in good agreement with the four different crystallographic P sites in the monoclinic $Bi_{0.852}P_{0.148}O_{1.648}$ structure. This same resolution is not achieved in the $^{51}$V spectra, which is ascribed to some second-order quadrupolar line broadening of $^{51}$V ($I$ = 7/2) that persists even at high temperatures.

### 5.4.4 $^{17}$O $T_1$ measurements

Measurement of the spin-lattice ($T_1$) relaxation times as a function of temperature can be used to gain insight into ionic motion correlation rates on the order of the Larmor frequency ($\sim 10^8$ Hz), a motional regime well above that accessible through CT linewidth measurements, which are only sensitive to motion on the order of the MAS rate ($\sim 10^4$–$10^5$ Hz). By measuring the $^{17}$O $T_1$ values for both the Bi–O and V–O sites, it is possible to separate their relative contributions to ionic motion in these materials. Results from $^{17}$O $T_1$ measurements for $Bi_{0.913}V_{0.087}O_{1.587}$, $Bi_{0.852}V_{0.148}O_{1.648}$ and $Bi_{0.852}P_{0.148}O_{1.648}$ are shown in Figure 5.12. For all three materials, the $T_1$ of the Bi–O environment decreases with increased temperature, suggestive of changes in ionic motion on the MHz timescale, whereas the $T_1$ values for the V–O environment in both V-doped materials remains relatively constant with temperature, indicating that the ionic motion involving these sites does not change significantly with increasing temperature (the P–O environment was not able to be resolved in the $Bi_{0.852}P_{0.148}O_{1.648}$ relaxation measurements due to overlap with the Bi–O resonance). While the earlier linewidth analysis of the V–O environment clearly probes increasing $VO_4$ rotational motion, the lack of any change to the $T_1$ relaxation rates indicates that this motion is not on the order of the Larmor frequency ($\sim 10^8$ Hz). The much faster motion involving the

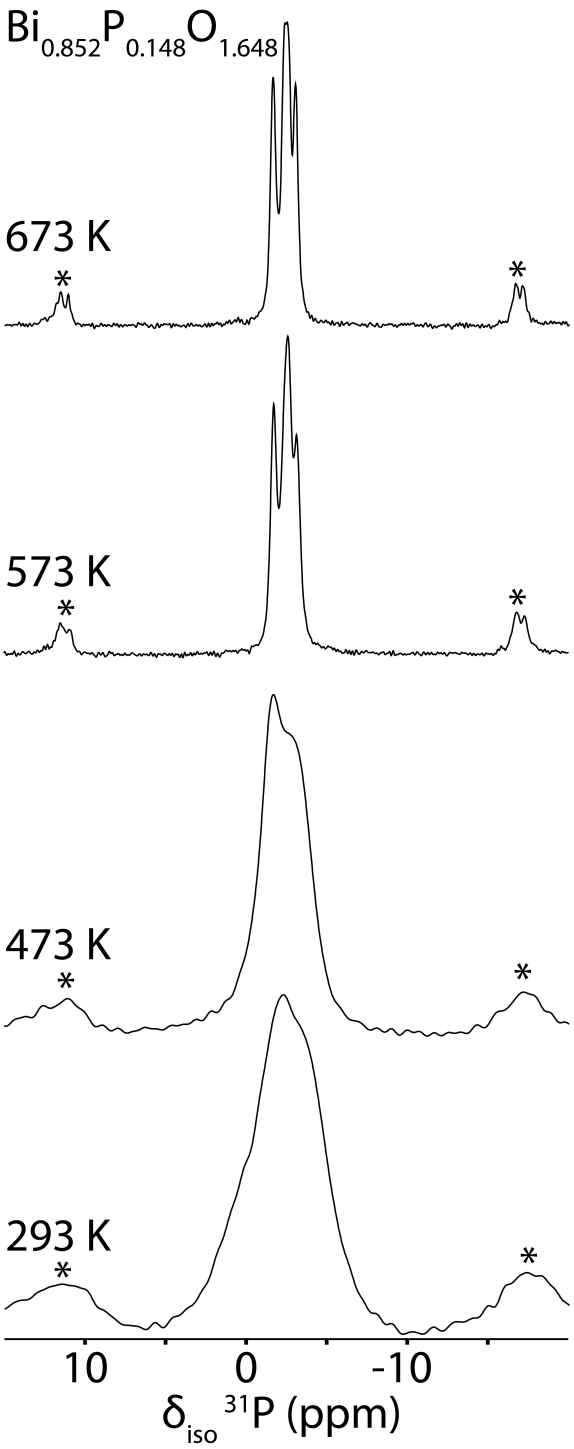


Figure 5.11: Variable-temperature $^{31}P$ NMR spectra of $Bi_{0.852}P_{0.148}O_{1.648}$ obtained at 16.4 T at a spinning rate of 4 kHz. At room temperature, the $^{31}P$ spectra show the same broad features as the $^{51}V$ spectra of $Bi_{0.913}V_{0.087}O_{1.587}$, as well as a narrowing isotropic linewidth with increasing temperature. Asterisks denote spinning sidebands.

Bi–O sublattice as probed by the $T_1$ relaxation measurements is ascribed to the movement and conduction of oxygen vacancies, which have previously been measured with $^{17}$O NMR relaxometry in other oxide-ion conductors, *e.g.*, Y-doped ceria[180] and $Bi_2WO_6$.[244]

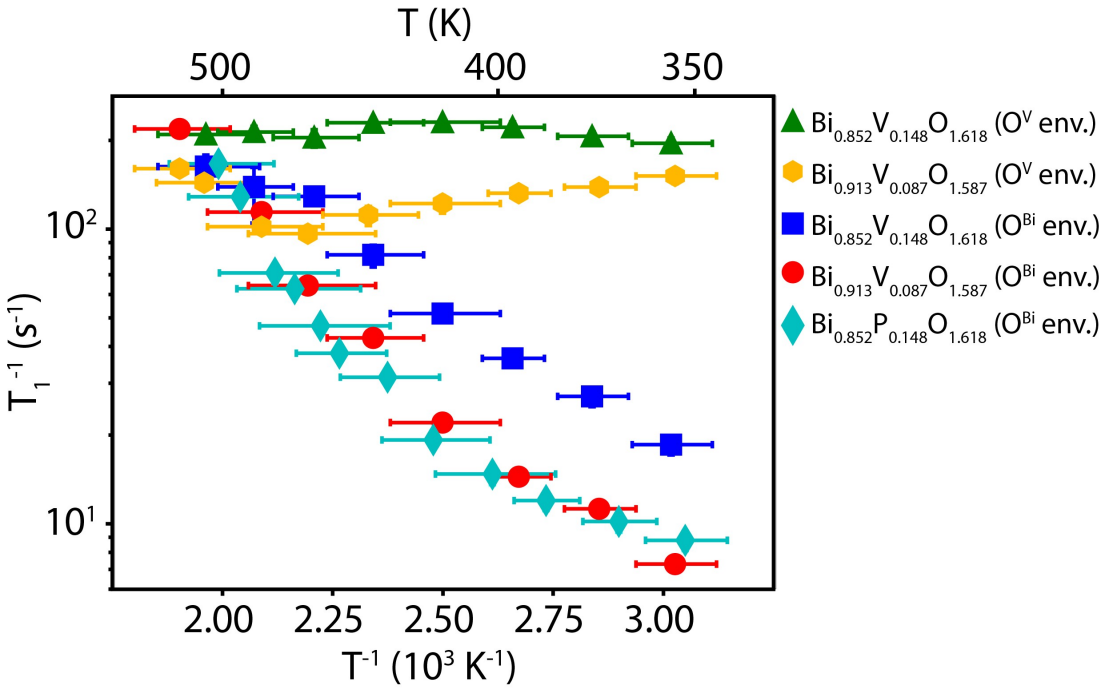


Figure 5.12: $^{17}$O relaxation rates $T_1^{-1}$ as a function of inverse temperature for $Bi_{0.913}V_{0.087}O_{1.587}$, $Bi_{0.852}V_{0.148}O_{1.648}$ and $Bi_{0.852}P_{0.148}O_{1.648}$, for both the Bi–O and V–O environments. In the case of $Bi_{0.852}V_{0.148}O_{1.648}$, the two V–O environments have similar $T_1^{-1}$ values and the features have been analyzed together, and similarly the P–O environments could not be resolved individually in the $Bi_{0.852}P_{0.148}O_{1.648}$ material.

## 5.5 Discussion: mechanisms of ionic motion

If it is assumed that spin-lattice relaxation is driven by transient changes in the apparent $^{17}$O quadrupolar coupling constant induced by motion, it is possible to extract activation energies for O ionic mobility from the $^{17}$O $T_1$ relaxation rates of the Bi–O environments.[174,175] Firstly inverse correlation times $\tau_c^{-1}$ are calculated, which can be derived from fits to the $T_1$ data using Equation (2.21) as described in Section 2.1.5.2.2:

$$\frac{1}{T_1} = \frac{2\pi^2}{25} \cdot C_Q^2 \left(1 + \frac{1}{3}\eta_Q^2\right) \cdot \left[\frac{\tau_c}{1+\omega_0^2\tau_c^2} + \frac{4\tau_c}{1+4\omega_0^2\tau_c^2}\right] \quad (5.1)$$

where $\omega_0$ is the $^{17}$O Larmor frequency ($\omega_0$ of $^{17}$O = 67.83 MHz at 11.7 T), and values of the proportionality constant $C_Q^2\left(1+\frac{1}{3}\eta_Q^2\right)$, which depend on the estimated quadrupole coupling constant $C_Q$ and quadrupolar asymmetry parameter $\eta_Q$ of the Bi–O environments, have been obtained by acquiring room-temperature spectra at multiple magnetic fields and determining the field-dependent second-order quadrupolar shift (details given in Figure 5.13).

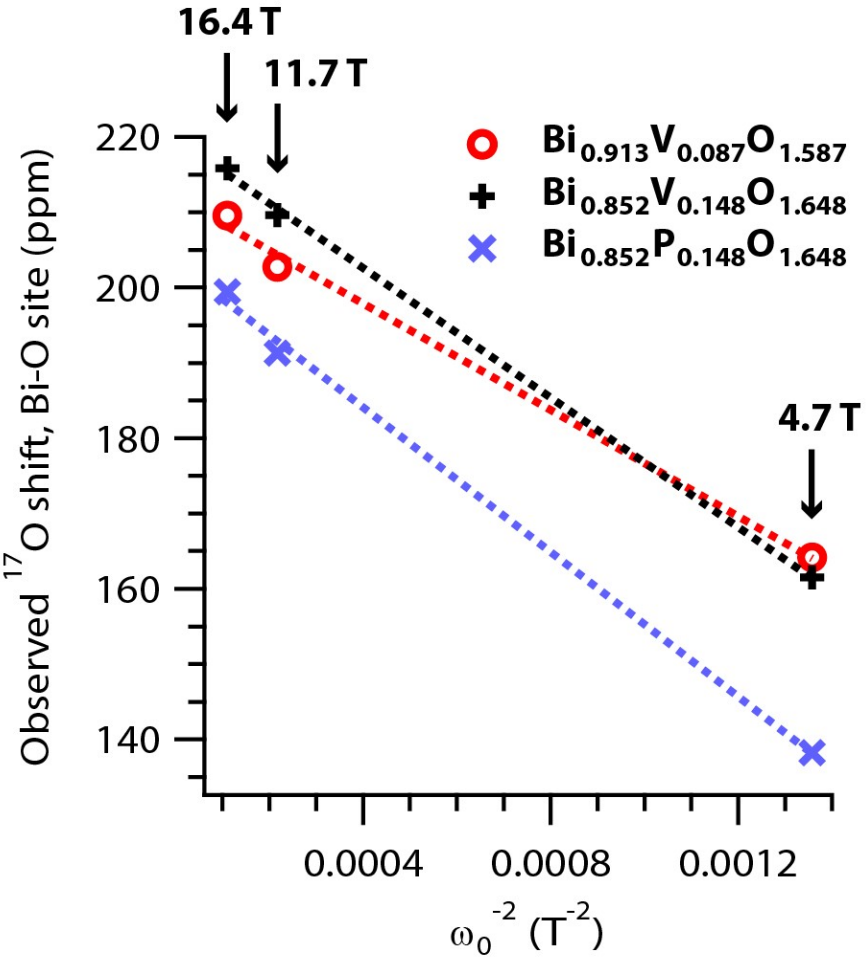


Figure 5.13: The observed $^{17}$O chemical shift of the Bi–O feature for all three V- and P-doped samples (at room temperature), as a function of the Larmor frequency $\omega_0$ for $^{17}$O; the experimental magnetic field is also indicated above each set of points. The slope of the best-fit lines (depicted as dotted lines) has then been used to extract the quadrupolar parameters using Equation (2.18). Depending on the value of $\eta_Q$ (between 0 and 1), the possible $C_Q$ values of the Bi–O site vary between 2.1 and 2.4 MHz for $Bi_{0.913}V_{0.087}O_{1.587}$, 2.3 and 2.7 MHz for $Bi_{0.852}V_{0.148}O_{1.648}$, and 2.5 and 2.8 MHz for $Bi_{0.852}P_{0.148}O_{1.648}$.

If we take the $\tau_c^{-1}$ values to be equal to the average jump rates of the relevant motional processes, $\tau^{-1}$, we can fit the linear parts of each curve to extract the activation energy $E_a$ and pre-exponential factor $\tau_i^{-1}$ for the ionic motion using the Arrhenius relationship:[174]

$$\tau^{-1} = \tau_i^{-1} \cdot \exp -\frac{E_a}{k_B T} \tag{5.2}$$

The results from this fitting are shown in Figure 5.14. The values of $\tau^{-1}$ for both V-doped materials derived in this way are 18 MHz at 527 K and 11 MHz at 511 K for $Bi_{0.913}V_{0.087}O_{1.587}$ and $Bi_{0.852}V_{0.148}O_{1.648}$ respectively, several orders of magnitude higher than the corresponding values measured for the interlattice exchange at even higher temperatures, indicating that the motional process probed by relaxometry occurs on a much faster timescale. Similar values for $Bi_{0.852}P_{0.148}O_{1.648}$ are derived, although two separate linear regions were able to be fitted within lower- and higher-temperature regimes, leading to two different values for $E_a$.

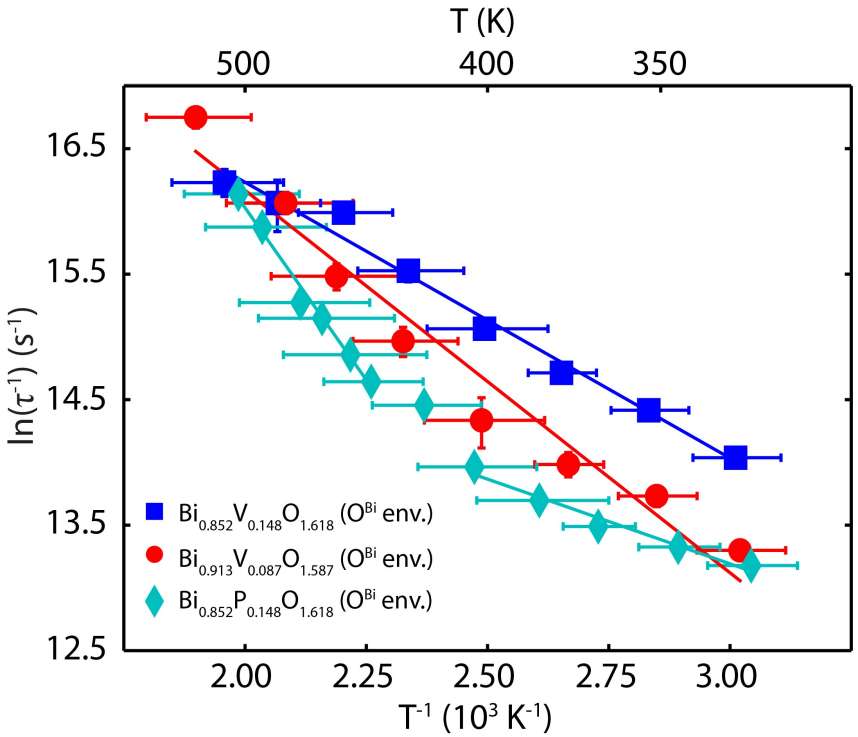


Figure 5.14: Arrhenius fitting of the inverse correlation times $\tau^{-1}$ extracted from the $^{17}O$ relaxation rates $T_1^{-1}$ of the Bi–O environments. The derived $E_a$ corresponds to O ionic motion through the Bi–O sublattice.

The same Arrhenius relationship can also be applied to the linear region of the temperature-dependent $^{17}O$ CT linewidth(s) for the $VO_4$ and $PO_4$ environments plotted in Figure 5.7, under the assumption that this variation is related to changes in the rate of O ionic motion (see Section 2.1.5.1). Other similar studies are able to utilize fitting of CT including the high- and low-temperature plateaus,[174] but we are only able to measure the intermediate linear region in this study. The results of this linewidth fitting are shown in Figure 5.15. The values of $E_a$ derived from both fitting methods are summarized in Table 5.1.

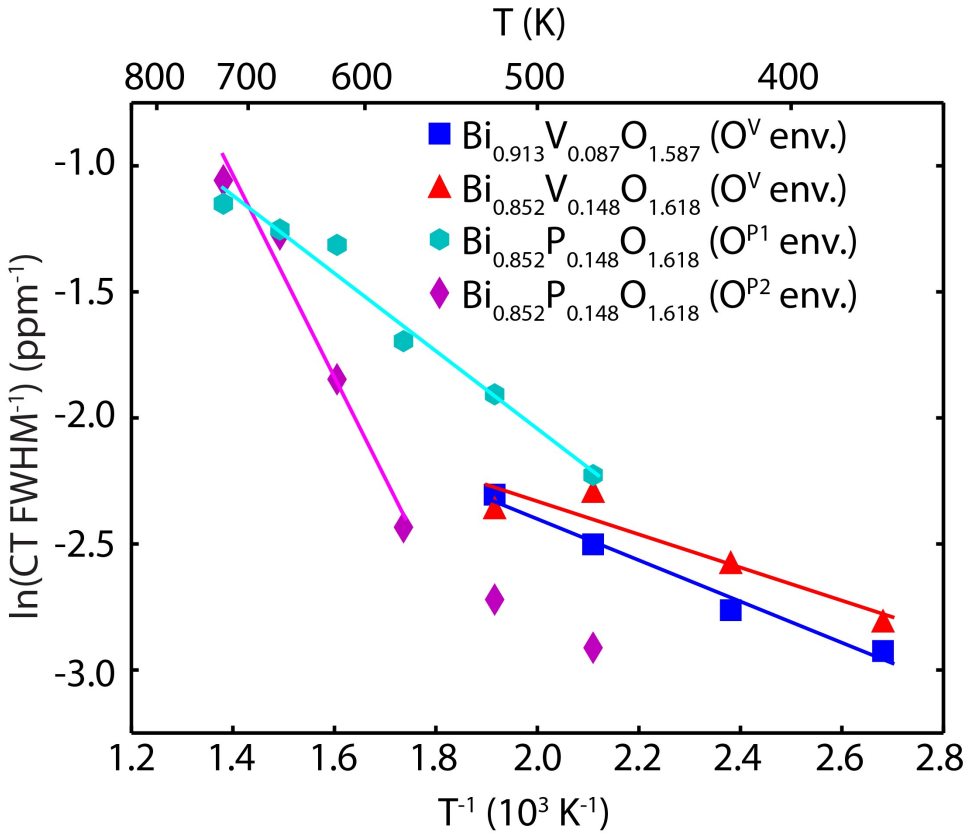


Figure 5.15: Arrhenius fitting of inverse $^{17}O$ CT linewidths of the $VO_4$ and $PO_4$ environments. The $O^{P1}$ and $O^{P2}$ environments correspond to the peaks at 135 ppm and 145 ppm, respectively, and the $O^{V}$ environment corresponds to the peak at ~620 ppm. Only the intermediate linear region of the data has been fitted (*e.g.* in the case of $O^{P2}$). The derived $E_a$ corresponds to O ionic motion within $VO_4$ and $PO_4$ tetrahedral units.

Table 5.1: Activation energies $E_a$ of oxide ion motion for the materials studied, determined from $^{17}O$ relaxation ($T_1$) measurements and analysis of the $^{17}O$ CT linewidths.

| Sample | Method | Environment | $E_a$ (eV) |
|---|---|---|---|
| $Bi_{0.913}V_{0.087}O_{1.587}$ | $T_1$ | Bi–O | 0.26 ± 0.05 |
| $Bi_{0.852}V_{0.148}O_{1.648}$ | $T_1$ | Bi–O | 0.19 ± 0.05 |
| $Bi_{0.852}P_{0.148}O_{1.648}$ | $T_1$ (low-T) | Bi–O | 0.12 ± 0.05 |
| $Bi_{0.852}P_{0.148}O_{1.648}$ | $T_1$ (high-T) | Bi–O | 0.47 ± 0.05 |
| $Bi_{0.913}V_{0.087}O_{1.587}$ | CT linewidth (620 ppm) | $VO_4$ | 0.07 ± 0.02 |
| $Bi_{0.852}V_{0.148}O_{1.648}$ | CT linewidth (620 ppm) | $VO_4$ | 0.06 ± 0.02 |
| $Bi_{0.852}P_{0.148}O_{1.648}$ | CT linewidth (145 ppm) | $PO_4$ | 0.35 ± 0.05 |
| $Bi_{0.852}P_{0.148}O_{1.648}$ | CT linewidth (135 ppm) | $PO_4$ | 0.13 ± 0.05 |

Considering the $E_a$ values derived from the various NMR parameters, several insights are apparent. In the first instance, for both V-doped samples the activation energies for exchange through the Bi–O sublattice and within the $VO_4$ tetrahedral units, respectively, are found to be the same within error; this suggests a common conduction mechanism operates in both phases. The previously published structural and molecular dynamics (MD) studies of these systems[118,126] suggested that oxide ionic motion in $Bi_{0.852}V_{0.148}O_{1.648}$ (referred to as $\beta$-$Bi_{46}V_8O_{89}$ in the earlier work[118]) and $Bi_{0.913}V_{0.087}O_{1.587}$ takes place through exchange between the Bi–O and V–O sublattices, facilitated by the variable coordination number of V. The $^{17}O$ VT-NMR spectra clearly support this mechanism, as the coalesced resonance observed at high temperatures is indicative of a motionally averaged O environment sampling both Bi and V neighbors, albeit occurring at a slower rate than the motional processes within the Bi–O sublattice. Additionally, the proposed variable V coordination agrees with the $^{51}V$ resonances measured between −450 and −510 ppm (Figure 5.10), which are consistent with both 4- and 5-coordinate vanadium environments observed previously,[343–345] although these shifts are difficult to fully resolve at the slow spinning speeds used in these VT experiments.

For $Bi_{0.852}P_{0.148}O_{1.648}$, the $E_a$ values found for $PO_4$ rotation agree well with activation barriers previously found using $^{17}O$ NMR in other phosphate materials (e.g. $CsH_2PO_4$),[247] indicating

that the relatively straightforward CT linewidth analysis nonetheless leads to reasonable activation energy values. However, these $E_a$ values for $PO_4$ motion are 2–5 times higher than those obtained for $VO_4$ motion, even in nominally isostructural materials, *i.e.*, $Bi_{0.852}V_{0.148}O_{1.648}$ and $Bi_{0.852}P_{0.148}O_{1.648}$. Furthermore, the $E_a$ obtained in the high-temperature regime from $T_1$ measurements of $Bi_{0.852}P_{0.148}O_{1.648}$ is also approximately twice that of the V-doped materials, with low-temperature data giving a lower $E_a$ than either V-doped sample, possibly corresponding to more localized O motion. These higher activation energies for both $PO_4$ rotation and O vacancy mobility may explain why no coalescence is observed in the $^{17}O$ VT spectra for $Bi_{0.852}P_{0.148}O_{1.648}$, in that even higher temperatures than those measured may be required to activate O exchange between the Bi–O sublattice and the $PO_4$ tetrahedral units. This difference may result from the inability of phosphorus to accommodate more O atoms in highly-coordinated environments (unlike vanadium). That is, the smaller jump distances between oxygen sites in a 5-coordinate irregular polyhedron, as compared to a more regular tetrahedron, promote a lower activation energy barrier for rotation within the dopant sublattice. Additionally, oxygen ionic motion arising from cooperative coupling between tetrahedral rotation and sublattice exchange likely leads to lower activation energy barriers for both sublattices, as compared to tetrahedral rotation within the dopant sublattice only.

This study also provides insight as to the different conduction mechanisms operating in the different phases. Firstly, the previously measured differences in anionic conduction seen for $Bi_{0.913}V_{0.087}O_{1.587}$ and $Bi_{0.852}V_{0.148}O_{1.648}$, $\sigma = 10^{-2}$ and $10^{-3}$ S cm$^{-1}$ at 673 K respectively, now become apparent in terms of variations in V environments present in these materials. For the more highly V-doped monoclinic $Bi_{0.852}V_{0.148}O_{1.648}$, two distinct types of $VO_4$ environments are observed, with different rates of associated O motion as revealed by the different trends in the temperature dependence of their $^{17}O$ CT linewidths. By comparison, only a single type of $VO_4$ environment is resolved for $Bi_{0.913}V_{0.087}O_{1.587}$. We can assign these environments on the basis of local structural arguments. While the original structural refinement of $Bi_{0.852}V_{0.148}O_{1.648}$ by combined neutron and X-ray powder diffraction fixed the $VO_4$ tetrahedra as rigid bodies[118] (due to the insensitivity of neutrons and X-rays to V and O positions, respectively), we can reasonably assume that the local distortions to the $VO_4$ geometries resemble those affecting $PO_4$ in the isostructural $Bi_{0.852}P_{0.148}O_{1.648}$.[114] In this latter material, one of the four crystallographically distinct P sites has a uniquely distorted

geometry in its local coordination environment, with a highly distorted O–P–O angle of 97° compared to 109° for an ideal tetrahedron, as well as the largest P–O bond length amongst the $PO_4$ tetrahedra. Therefore, we propose that for both $Bi_{0.852}V_{0.148}O_{1.648}$ and $Bi_{0.852}P_{0.148}O_{1.648}$, O environments within these distorted and undistorted tetrahedra correspond to the two distinct $PO_4/VO_4$ features in the $^{17}O$ spectra. For $Bi_{0.852}V_{0.148}O_{1.648}$, we assign the resonance at lower chemical shift (620 ppm) to O within distorted tetrahedra, as on average these sites are closer to Bi, and hence undergo a shift towards the Bi–O resonance. (For $Bi_{0.852}P_{0.148}O_{1.648}$, we assign the higher frequency resonance at ~147 ppm, which is again closer to the Bi–O shift, to O in distorted tetrahedra. This assignment is further supported by the ~1:3 intensity ratio of the distorted and undistorted sites as seen in Figure 5.8.) The distorted $VO_4$ environment at 620 ppm is also observed in $Bi_{0.913}V_{0.087}O_{1.587}$; this feature exhibits a similar chemical shift as well as narrowing linewidth with increasing temperature. Therefore we can conclude that the distorted tetrahedral units are more conducive to oxide ion motion than the undistorted type, and so the presence of the latter in $Bi_{0.852}V_{0.148}O_{1.648}$ hinders the ionic conduction pathways and leads to a lower overall level of isotropic oxide ionic motion in the material. This structural distortion of the $VO_4$ units, together with the ability of V to support coordination of additional O from the Bi–O sublattice, is crucial to the excellent oxide ion conductivity of $Bi_{0.913}V_{0.087}O_{1.587}$.

The $^{17}O$ NMR spectra of $Bi_{0.852}P_{0.148}O_{1.648}$ (Figure 5.4) indicate a conduction mechanism different to the sublattice exchange evident from the two-site coalescence observed for the V-doped samples. Focusing on the Bi–O region of the spectra, three distinct regimes are active at different temperatures. From room temperature to 473 K, only one broad resonance is resolved for the different Bi–O environments, consistent with slow ionic motion that is insufficient to resolve individual sites. From 523–673 K two distinct environments are resolved, ascribed to O near (and not near, respectively) to an oxide ion vacancy in the Bi–O sublattice, in agreement with the oxygen vacancies observed in this phase previously.[114] At these temperatures, the higher-frequency resonance at ~220 ppm displays a narrowing linewidth with increasing temperature; we assign this to the vacancy-adjacent oxygen atoms undergoing localized hopping into vacancy sites. By contrast, the isolated oxygens in fully occupied regions of the lattice cannot participate in this hopping motion, and therefore the corresponding spectral feature (at ~190 ppm) exhibits an invariant linewidth with increasing

temperature. These two resonances (at ~220 ppm and ~200 ppm) are also observed in the Bi–O region of the $^{17}O$ spectra of both V-doped samples, especially in the spectra collected at 573 K (Figure 5.4), showing that regions with and without O vacancies can be distinguished in all the studied phases through solid-state NMR.

Finally, at temperatures >723 K, the two Bi–O environments in the P-doped material coalesce to a single peak as O ionic motion is active through the entire Bi–O sublattice on the NMR timescale. Over the same temperature range, both the $^{17}O$ and the $^{31}P$ NMR spectra reveal an increasing number of different $PO_4$ environments that can be resolved due to motional narrowing as oxygen mobility increases; however, this motion must be restricted to localized tetrahedral rotations because no spectral coalescence between the sublattices is observed. This same behavior cannot be observed in the V-doped samples due to the coalescence of the Bi–O and $VO_4$ resonances due to rapid sublattice exchange.

The variable coordination of the dopant ion plays a crucial role in understanding the differing ionic conductivities of these fluorite-type materials; the P-doped sample exhibits the lowest conductivity, followed by $Bi_{0.852}V_{0.148}O_{1.648}$ and $Bi_{0.913}V_{0.087}O_{1.587}$.[118,123,126] Even as they aid in stabilizing the cubic $\delta$-$Bi_2O_3$ structure, dopants generally disrupt three-dimensional isotropic conduction within the Bi–O sublattice. However, cooperative exchange between dopant and Bi–O sublattices can offset this effect. The difference in conductivity values between the pseudo-cubic $Bi_{0.913}V_{0.087}O_{1.587}$ and monoclinic $Bi_{0.852}V_{0.148}O_{1.648}$ underlines this first point, with the maintenance of the 3D isotropic nature of the material in the former case leading to its exceptional conduction properties. In the case of $Bi_{0.852}P_{0.148}O_{1.648}$, although increasing rates of oxide-ion motion occur within the Bi–O sublattice (as discussed earlier), the inability of phosphorus to adopt variable O coordination hinders significant sublattice exchange and leads to overall lower bulk conductivity. Similar observations have been made in related work on $Bi_{28}Re_2O_{49}$ and $Bi_{1-x}Nb_xO_{1.5+x}$ phases,[346,347] materials which also utilize dopant atoms able to adopt variable O coordination, but in which doping leads to symmetry lowering of the crystal structure from cubic to tetragonal, leading to correspondingly lower oxide-ion conductivity than the vanadate materials. This work underscores these important design guidelines that must be followed in future synthetic efforts towards the development of more optimal oxygen ionic conducting materials.

## 5.6 Conclusions and outlook

In this study, a multinuclear VT-NMR approach has been applied to elucidate the role of different dopant atoms (V and P) and their concentrations on the oxide-ionic conductivity of promising stabilized bismuth oxide phases. It has been shown that solid state NMR is particularly well suited to understanding connections between local structural features and ionic mobility and can quantify the evolution of the ion dynamics with temperature.

Room temperature $^{17}$O NMR measurements have first characterized the local environments present in each material; we are able to distinguish between bismuth oxide-like environments and other sites corresponding to $VO_4$ and $PO_4$ units due to doping. Next, upon heating the V-doped samples, the $^{17}$O resonances arising from these chemically distinct regions broaden beyond detection and then reappear as a single coalesced peak at high temperature, definitively establishing oxide-ion exchange between the two sublattices. By contrast, spectra of the phosphate phase do not evidence two-site coalescence within the studied temperature range (up to 873 K), and therefore utilize a different mechanism for oxide ionic conduction, as supported by previously measured lower values of ionic conductivity.

Arrhenius fitting analyses of both the $^{17}$O $T_1$ relaxation rates and central transition (CT) linewidth data allow us to determine activation energies for motional processes within the two distinct sublattices (Bi–O and $VO_4$/$PO_4$), with the much lower activation energy for $VO_4$ rotations compared to those of $PO_4$ driving the different conduction properties of the materials. Furthermore, two different $VO_4$ environments were found for the higher V-doped phase $Bi_{0.852}V_{0.148}O_{1.648}$, suggesting that the symmetry lowering from pseudo-cubic to monoclinic with increased V doping leads to two different types of tetrahedral environments with differing rates of local ionic motion, in turn disrupting the three-dimensional conduction network in undoped $Bi_2O_3$. These findings underline the crucial interplay between dopant concentration and its effect on the long-range ionic conduction pathways, as well as highlighting the influence of the coordination flexibility of the dopant; these factors directly control the available oxide-ion mobility mechanisms in these $Bi_2O_3$-based materials, which in turn determines the overall level of ionic conductivity.

This work highlights the potential for multinuclear variable-temperature solid-state NMR, with its specificity for different nuclei as well as sensitivity to local dynamics, to provide unique insights into the underlying mechanisms driving bulk ionic conduction in superionic conductors. In turn, these mechanisms suggest design rules that can be utilized in future work to optimize the next generation of ionic conducting materials, with the ultimate goal of truly rational materials design.

# Chapter 6 Conclusions and Future Work

The primary objective of this thesis has been to study the local structure and ion dynamics in oxide-ion conducting materials using solid-state $^{17}$O NMR spectroscopy. Where possible, the NMR results have been assigned and interpreted with reference to first-principles calculations, with further corroboration from other experimental techniques including X-ray diffraction, thermogravimetric analysis and X-ray absorption spectroscopy.

While solid-state $^{17}$O variable-temperature NMR of diamagnetic oxide-ionic conductors is an established if somewhat uncommon technique to explore oxide-ion mobility,[240] analogous studies of paramagnetic systems are far rarer, having been considered mostly intractable due to the formidable technical challenges involved in acquiring and interpreting spectra affected by hyperfine interactions.[289] The work presented in Chapter 3 constitutes the first example of the use of solid-state $^{17}$O variable-temperature MAS NMR to study a *paramagnetic* oxide-ion conductor ($La_2NiO_{4+\delta}$), in combination with spectral assignment relying on shifts calculated from first-principles. This represents an important step forward in applying combined NMR- and DFT-based local structure techniques to a class of SOFC electrode materials previously regarded as inaccessible.

Importantly, the oxide-ion dynamics in $La_2NiO_{4+\delta}$ could be followed as a function of temperature (up to 150°C), leading to determination of an activation energy for the relevant interstitial–axial exchange process that was shown to be in good agreement with other experimental and computational studies. This work has also shown that while the hyperfine interactions in solid-state $^{17}$O NMR can lead to very large hyperfine shifts, this distance sensitivity to paramagnetic centers can be exploited to probe subtle structural changes, such as the local interstitial-induced distortions of axial oxygen sites in $La_2NiO_{4+\delta}$. The ability to resolve relatively small variations in bond distance and/or local coordination is also of

relevance to other systems such as battery electrode materials undergoing phase transformations by formation of stacking faults, for which paramagnetic solid-state $^{17}$O NMR has recently proved useful.[213] Of course, in any methodology employing solid-state NMR of paramagnetic systems, the importance of first-principles calculations, which allow for meaningful interpretation of the spectra by comparison to expected structural motifs, cannot be understated.

An obvious extension of the work presented in Chapter 3 would involve the acquisition of $^{17}$O NMR spectra of $La_2NiO_{4+\delta}$ at the higher temperatures (*i.e.*, 500–700 °C) most relevant to SOFC operation. One could hypothesize that these spectra would evidence exchange between axial and equatorial oxygen sites, which was not able to be detected at the lower temperatures examined in this work. However, such a study would not be without significant challenges, and would benefit from the development of new high-temperature NMR probes with improved MAS capabilities, as well as innovative pulse programs more powerful than MATPASS to handle extensive spinning sideband overlap in spectra broadened by electron–nuclear dipolar anisotropy. Moreover, temperature-dependent changes in the hyperfine shifts, as well as the possibility of Knight shifts arising from the metal–insulator transition in this system, would need to be taken into account.

In Chapter 4, the earlier work was extended to the system of Sr-substituted $La_{2-x}Sr_xNiO_{4+\delta}$; these phases are MIECs with improved electronic conductivity as compared to the parent compound. At the outset, our motivation was to indirectly control the concentration of interstitial oxide defects with doping in order to explore effects on the local structure. Thus the previous insights in Chapter 3, in particular the connection between specific spectral lineshapes and the presence of a distortion amongst the axial oxygen sites, were crucial to interpretation of the paramagnetic $^{17}$O NMR spectra. Both the interstitial oxygen content and the extent of the axial oxygen distortion resolved by $^{17}$O NMR were found to be surprisingly sensitive to the Sr content. From this it was concluded that the axial distortion was likely reflective of the interstitial ordering scheme previously proposed by Tranquada *et al.*[66] One interesting avenue for future work might therefore consist in confirming specific interstitial ordering motifs by using first-principles calculations, in an approach resembling NMR crystallography as traditionally applied to organic molecules.[348]

An additional aspect of the paramagnetic $^{17}$O NMR methodology revealed in Chapter 4 was its ability to probe the electronic structure, and in particular the *d* orbital occupation, of (first-row) transition metal centers. As the $^{17}$O resonances arising from axial and equatorial oxygen environments in $La_{2-x}Sr_xNiO_{4+\delta}$ were found to have orbital-dependent spin delocalization pathways, the hyperfine shifts could be used as a measure of the relative electronic occupation of the $d_{z^2}$ and $d_{x^2-y^2}$ orbitals of $Ni^{3+}$ sites. One could envisage applications of this approach to the characterization of orbital ordering in a variety of perovskite-derived structures, with relevance not only to mixed ionic–electronic conduction, but also to high-temperature superconduction and colossal magnetoresistance.[303]

In contrast to Chapter 3, variable-temperature NMR measurements were not performed on the $La_{2-x}Sr_xNiO_{4+\delta}$ materials in Chapter 4; oxide-ion dynamics were only inferred indirectly from faster $T_1$ relaxation rates of mobile interstitial defects with incorporation of Sr. By studying the Sr-substituted phases at elevated temperatures in future work, it might be possible to probe differences in the interstitial–axial (and potentially axial–equatorial) exchange rates due to changes in stoichiometry, *i.e.*, decreases in the interstitial content and/or an increase of oxygen vacancies.

In Chapter 5, the $^{17}$O NMR approach was applied to purely ionic-conducting materials of composition $Bi_{1-x}V_xO_{1.5+x}$ and $Bi_{1-x}P_xO_{1.5+x}$ ($x$ = 0.087 and 0.148). Although these diamagnetic phases proved relatively straightforward from the previous paramagnetic viewpoint, as the structural crystallography of the fluorite-type materials was known to be quite challenging, unraveling the oxide-ionic conduction mechanisms proved correspondingly complex. Unlike in Chapter 3, the temperatures reached in this study were much higher (up to 600 °C) due to the use of a laser-heated MAS NMR probe. The major disadvantage of this approach from a technical point of view was the much slower MAS rate (~4 kHz), which discouraged using this hardware in studying the systems with extensive paramagnetic broadening encountered in Chapters 3 and 4.

The major result in Chapter 5 was the direct observation of oxygen exchange on the NMR timescale between the Bi–O and $VO_4$ sublattices for the V-doped samples at ~550 °C, but the absence of an equivalent exchange process for the P-doped sample below 600 °C. Additionally, slightly faster sublattice exchange was found for the lower V-doped sample, in

agreement with the previously observed conductivity differences in the phases. Oxygen motion both within and between discrete sublattices could also be distinguished, with differing values of activation energy for various processes. Intrinsic rotations of the $VO_4$ and $PO_4$ polyanion units were found to have very low activation energies; however, their motion was highly localized except at higher temperatures. Finally, in considering the propensity of the vanadium cations to form transient and highly variable coordination to O sites, design principles were suggested for the next generation of oxide-ion conductors.

For the $Bi_{1-x}V_xO_{1.5+x}$ and $Bi_{1-x}P_xO_{1.5+x}$, other spectroscopic techniques could certainly be performed to provide further experimental probes of motion. Although not discussed in this thesis, double-resonance $^{51}V/^{17}O$ TRAPDOR NMR measurements can distinguish which sites are responsible for conductivity, and were previously used to show oxide-ion motion in Aurivillius-type layered phases $\alpha$-$Bi_4V_2O_{11}$ close to room temperature, also involving motion within the V–O sublattice.[242]

Finally, as discussed in the Introduction, long-term conductivity decay adversely impacts many of the oxide-ion conductors derived from $\delta$-$Bi_2O_3$, and this phenomenon has been attributed to slow ordering of the anionic sublattice.[104] In this case, the use of solid-state $^{17}O$ NMR techniques at elevated temperatures for extended periods would be expected to reveal changes in local structure and activation energies for oxide-ion motion, which to our knowledge has not been previously explored by this approach. The class of Nb-doped $\delta$-$Bi_2O_3$ materials, some of which possess a highly complex incommensurately moderated superstructure,[108] are also interesting targets for future study; while NMR would not be expected to clarify long-range structural aspects of these phases, well-resolved $^{17}O$ resonances might be anticipated, especially with the onset of oxygen ordering.

Regardless of the practical application of these phases, *i.e.*, as electrolytes or electrodes in SOFC, as oxygen-ion sensors or membranes, or for chemical looping applications, an understanding of local structure and oxide-ion dynamics at the atomic level is critical to the development of novel superionic conductors with improved functionality, and solid-state $^{17}O$ NMR spectroscopy is poised to play a key role in future discoveries.

# References


(1) BP Global. *Statistical Review of World Energy*; 2009.

(2) Song, C. *Catal. Today* **2002**, *77* (1–2), 17.

(3) Ormerod, R. M. *Chem. Soc. Rev.* **2003**, *32* (1), 17.

(4) Brett, D. J. L.; Atkinson, A.; Brandon, N. P.; Skinner, S. J. *Chem. Soc. Rev.* **2008**, *37* (8), 1568.

(5) Pomfret, M. B.; Demircan, O.; Sukeshini, A. M.; Walker, R. A. *Environ. Sci. Technol.* **2006**, *40* (17), 5574.

(6) Van der Hoeven, M. World Energy Outlook 2012. *International Energy Agency*, 2013.

(7) Costamagna, P.; Srinivasan, S. *J. Power Sources* **2001**, *102* (1), 242.

(8) Wee, J.-H. *Renew. Sustain. Energy Rev.* **2007**, *11* (8), 1720.

(9) Perry, M. L.; Fuller, T. F. *J. Electrochem. Soc.* **2002**, *149* (7), S59.

(10) Williams, M. C.; Maru, H. C. *J. Power Sources* **2006**, *160* (2), 863.

(11) Wee, J.-H. *Appl. Energy* **2011**, *88* (12), 4252.

(12) Wee, J.-H. *Renew. Sustain. Energy Rev.* **2014**, *32* (Supplement C), 178.

(13) Stambouli, A. B.; Traversa, E. *Renew. Sustain. Energy Rev.* **2002**, *6* (5), 433.

(14) Haile, S. M. *Acta Mater.* **2003**, *51* (19), 5981.

(15) Choudhury, A.; Chandra, H.; Arora, A. *Renew. Sustain. Energy Rev.* **2013**, *20* (Supplement C), 430.

(16) Kee, R. J.; Zhu, H.; Goodwin, D. G. *Proc. Combust. Inst.* **2005**, *30* (2), 2379.

(17) Park, S.; Vohs, J. M.; Gorte, R. J. *Nature* **2000**, *404* (6775), 265.

(18) McIntosh, S.; Gorte, R. J. *Chem. Rev.* **2004**, *104* (10), 4845.

(19) Huang, K.; Goodenough, J. B. *Solid Oxide Fuel Cell Technology: Principles, Performance and Operations*; Woodhead Publishing in energy; Woodhead Pub., 2009.

(20) Hayashi, K.; Yokoo, M.; Yoshida, Y.; Arai, H. *NTT Tech. Rev.* **2009**, *7* (10), 1.

(21) Singhal, S. C. *MRS Bull.* **2000**, *25* (3), 16.

(22) Lashtabeg, A.; Skinner, S. J. *J. Mater. Chem.* **2006**, *16* (31), 3161.

(23) Singhal, S. C.; Kendall, K. *High Temperature Solid Oxide Fuel Cells: Fundamentals, Design, and Applications*; Electronics & Electrical; Elsevier, 2003.

(24) Aguadero, A.; Fawcett, L.; Taub, S.; Woolley, R.; Wu, K.-T.; Xu, N.; Kilner, J. A.; Skinner, S. J. *J. Mater. Sci.* **2012**, *47* (9), 3925.

(25) Orera, A.; Slater, P. R. *Chem. Mater.* **2010**, *22* (3), 675.

(26) Huang, K.; Wan, J.; Goodenough, J. B. *J. Mater. Sci.* **2001**, *36* (5), 1093.

(27) Figueiredo, F. M. L.; Marques, F. M. B. *Wiley Interdiscip. Rev. Energy Environ.* **2013**, *2* (1), 52.

(28) Ishihara, T.; Matsuda, H.; Takita, Y. *J. Am. Chem. Soc.* **1994**, *116* (9), 3801.

(29) Feng, M.; Goodenough, J. B. *Eur. J. Solid State Inorg. Chem.* **1994**, *31* (8–9), 663.

(30) Adler, S. B.; Lane, J. A.; Steele, B. C. H. *J. Electrochem. Soc.* **1996**, *143* (11), 3554.

(31) Adler, S. B. *Solid State Ion.* **1998**, *111* (1–2), 125.

(32) Mogensen, M.; Skaarup, S. *Solid State Ion.* **1996**, *86–88*, *Part 2*, 1151.

(33) Smith, J. R.; Chen, A.; Gostovic, D.; Hickey, D.; Kundinger, D.; Duncan, K. L.; DeHoff, R. T.; Jones, K. S.; Wachsman, E. D. *Solid State Ion.* **2009**, *180* (1), 90.

(34) Pavone, M.; Ritzmann, A. M.; Carter, E. A. *Energy Environ. Sci.* **2011**, *4* (12), 4933.

(35) Tsipis, E. V.; Kharton, V. V. *J. Solid State Electrochem.* **2011**, *15* (5), 1007.

(36) Chen, Y.; Jung, W.; Cai, Z.; Kim, J. J.; Tuller, H. L.; Yildiz, B. *Energy Environ. Sci.* **2012**, *5* (7), 7979.

(37) Wu, J.; Pramana, S. S.; Skinner, S. J.; Kilner, J. A.; Horsfield, A. P. *J. Mater. Chem. A* **2015**, *3* (47), 23760.

(38) Han, J. W.; Yildiz, B. *Energy Environ. Sci.* **2012**, *5* (9), 8598.

(39) Rabenau, A.; Eckerlin, P. *Acta Crystallogr.* **1958**, *11* (4), 304.

(40) Tavares, C. P. *Mater. Res. Bull.* **1985**, *20* (8), 979.

(41) Ganguly, P.; Rao, C. N. R. *J. Solid State Chem.* **1984**, *53* (2), 193.

(42) Buttrey, D. J.; Harrison, H. R.; Honig, J. M.; Schartman, R. R. *J. Solid State Chem.* **1984**, *54* (3), 407.

(43) Buttrey, D. J.; Honig, J. M.; Rao, C. N. R. *J. Solid State Chem.* **1986**, *64* (3), 287.

(44) Buttrey, D. J.; Ganguly, P.; Honig, J. M.; Rao, C. N. R.; Schartman, R. R.; Subbanna, G. N. *J. Solid State Chem.* **1988**, *74* (2), 233.

(45) Aeppli, G.; Buttrey, D. J. *Phys. Rev. Lett.* **1988**, *61* (2), 203.

(46) Rao, C. N. R.; Buttrey, D. J.; Otsuka, N.; Ganguly, P.; Harrison, H. R.; Sandberg, C. J.; Honig, J. M. *J. Solid State Chem.* **1984**, *51* (2), 266.

(47) Jorgensen, J. D.; Dabrowski, B.; Pei, S.; Richards, D. R.; Hinks, D. G. *Phys. Rev. B* **1989**, *40* (4), 2187.

(48) Kharton, V. V.; Viskup, A. P.; Naumovich, E. N.; Marques, F. M. B. *J. Mater. Chem.* **1999**, *9* (10), 2623.

(49) Kharton, V. V.; Viskup, A. P.; Kovalevsky, A. V.; Naumovich, E. N.; Marques, F. M. B. *Solid State Ion.* **2001**, *143* (3–4), 337.

(50) Kharton, V. V.; Yaremchenko, A. A.; Shaula, A. L.; Patrakeev, M. V.; Naumovich, E. N.; Logvinovich, D. I.; Frade, J. R.; Marques, F. M. B. *J. Solid State Chem.* **2004**, *177* (1), 26.

(51) Skinner, S. J.; Kilner, J. A. *Solid State Ion.* **2000**, *135* (1–4), 709.

(52) Amow, G.; Davidson, I. J.; Skinner, S. J. *Solid State Ion.* **2006**, *177* (13–14), 1205.

(53) Bassat, J. M.; Boehm, E.; Grenier, J. C.; Mauvy, F.; Dordor, P.; Pouchard, M. In *Fifth European Solid Oxide Forum Proceedings*; J. Huijsmans: Lucerne, Switzerland, 2002; p 586.

(54) Skinner, S. J. *Solid State Sci.* **2003**, *5* (3), 419.

(55) Frayret, C.; Villesuzanne, A.; Pouchard, M. *Chem. Mater.* **2005**, *17* (26), 6538.

(56) Singh, K. K.; Ganguly, P.; Goodenough, J. B. *J. Solid State Chem.* **1984**, *52* (3), 254.

(57) James, M.; Attfield, J. P. *J. Mater. Chem.* **1996**, *6* (1), 57.

(58) Takeda, Y.; Kanno, R.; Sakano, M.; Yamamoto, O.; Takano, M.; Bando, Y.; Akinaga, H.; Takita, K.; Goodenough, J. B. *Mater. Res. Bull.* **1990**, *25* (3), 293.

(59) Millburn, J. E.; Green, M. A.; Neumann, D. A.; Rosseinsky, M. J. *J. Solid State Chem.* **1999**, *145* (2), 401.

(60) Nakamura, T.; Yashiro, K.; Sato, K.; Mizusaki, J. *Solid State Ion.* **2009**, *180* (4–5), 368.

(61) Demourgues, A.; Weill, F.; Darriet, B.; Wattiaux, A.; Grenier, J. C.; Gravereau, P.; Pouchard, M. *J. Solid State Chem.* **1993**, *106* (2), 317.

(62) Demourgues, A.; Weill, F.; Darriet, B.; Wattiaux, A.; Grenier, J. C.; Gravereau, P.; Pouchard, M. *J. Solid State Chem.* **1993**, *106* (2), 330.

(63) Aguadero, A.; Pérez, M.; Alonso, J. A.; Daza, L. *J. Power Sources* **2005**, *151*, 52.

(64) Poirot, N.; Simon, P.; Odier, P. *Solid State Sci.* **2008**, *10* (2), 186.

(65) Aguadero, A.; Alonso, J. A.; Martínez-Lope, M. J.; Fernández-Díaz, M. T.; Escudero, M. J.; Daza, L. *J. Mater. Chem.* **2006**, *16* (33), 3402.

(66) Tranquada, J. M.; Kong, Y.; Lorenzo, J. E.; Buttrey, D. J.; Rice, D. E.; Sachan, V. *Phys. Rev. B* **1994**, *50* (9), 6340.

(67) Bassat, J. M.; Odier, P.; Villesuzanne, A.; Marin, C.; Pouchard, M. *Solid State Ion.* **2004**, *167* (3–4), 341.

(68) Burriel, M.; Garcia, G.; Santiso, J.; Kilner, J. A.; Chater, R. J.; Skinner, S. J. *J. Mater. Chem.* **2008**, *18* (4), 416.

(69) Burriel, M.; Téllez, H.; Chater, R. J.; Castaing, R.; Veber, P.; Zaghrioui, M.; Ishihara, T.; Kilner, J. A.; Bassat, J.-M. *J. Phys. Chem. C* **2016**, *120* (32), 17927.

(70) Minervini, L.; Grimes, R. W.; Kilner, J. A.; Sickafus, K. E. *J. Mater. Chem.* **2000**, *10* (10), 2349.

(71) Chroneos, A.; Parfitt, D.; Kilner, J. A.; Grimes, R. W. *J. Mater. Chem.* **2010**, *20* (2), 266.

(72) Yashima, M.; Enoki, M.; Wakita, T.; Ali, R.; Matsushita, Y.; Izumi, F.; Ishihara, T. *J. Am. Chem. Soc.* **2008**, *130* (9), 2762.

(73) Yashima, M.; Yamada, H.; Nuansaeng, S.; Ishihara, T. *Chem. Mater.* **2012**, *24* (21), 4100.

(74) Park, J.-C.; Kim, D.-K.; Byeon, S.-H.; Kim, D. *J. Synchrotron Radiat.* **2001**, *8* (2), 704.

(75) Woolley, R. J.; Illy, B. N.; Ryan, M. P.; Skinner, S. J. *J. Mater. Chem.* **2011**, *21* (46), 18592.

(76) Tamura, H.; Hayashi, A.; Ueda, Y. *Phys. C Supercond.* **1996**, *258* (1–2), 61.

(77) Nakamura, T.; Yashiro, K.; Sato, K.; Mizusaki, J. *Phys. Chem. Chem. Phys.* **2009**, *11* (17), 3055.

(78) Goodenough, J. B.; Ramasesha, S. *Mater. Res. Bull.* **1982**, *17* (3), 383.

(79) Bassat, J. M.; Odier, P.; Loup, J. P. *J. Solid State Chem.* **1994**, *110* (1), 124.

(80) Rodriguez-Carvajal, J.; Fernandez-Diaz, M. T.; Martinez, J. L. *J. Phys. Condens. Matter* **1991**, *3* (19), 3215.

(81) Zinkevich, M.; Aldinger, F. *J. Alloys Compd.* **2004**, *375* (1–2), 147.

(82) Yamada, K.; Omata, T.; Nakajima, K.; Hosoya, S.; Sumida, T.; Endoh, Y. *Phys. C Supercond.* **1992**, *191* (1–2), 15.

(83) Gopalan, P.; McElfresh, M. W.; Kąkol, Z.; Spałek, J.; Honig, J. M. *Phys. Rev. B* **1992**, *45* (1), 249.

(84) Tranquada, J. M.; Buttrey, D. J.; Sachan, V.; Lorenzo, J. E. *Phys. Rev. Lett.* **1994**, *73* (7), 1003.

(85) Tranquada, J. M.; Lorenzo, J. E.; Buttrey, D. J.; Sachan, V. *Phys. Rev. B* **1995**, *52* (5), 3581.

(86) Tranquada, J. M.; Wochner, P.; Moodenbaugh, A. R.; Buttrey, D. J. *Phys. Rev. B* **1997**, *55* (10), R6113.

(87) Bernal, O. O.; Brom, H. B.; de Kok, M. L.; Witteveen, J.; Menovsky, A. A. *Phys. C Supercond.* **1997**, *282–287*, *Part 3*, 1393.

(88) Ganguly, P.; Kollai, S.; Rao, C. N. R. *Magn Lett* **1980**, *1*, 107.

(89) Kim, J.; Middlemiss, D. S.; Chernova, N. A.; Zhu, B. Y. X.; Masquelier, C.; Grey, C. P. *J. Am. Chem. Soc.* **2010**, *132* (47), 16825.

(90) Takahashi, T.; Iwahara, H. *Mater. Res. Bull.* **1978**, *13* (12), 1447.

(91) Takahashi, T.; Esaka, T.; Iwahara, H. *J. Appl. Electrochem.* **1975**, *5* (3), 197.

(92) Takahashi, T.; Iwahara, H.; Nagai, Y. *J. Appl. Electrochem.* **1972**, *2* (2), 97.

(93) Sammes, N. M.; Tompsett, G. A.; Näfe, H.; Aldinger, F. *J. Eur. Ceram. Soc.* **1999**, *19* (10), 1801.

(94) Boivin, J. C.; Mairesse, G. *Chem. Mater.* **1998**, *10* (10), 2870.

(95) Harwig, H. A. *Z. Für Anorg. Allg. Chem.* **1978**, *444* (1), 151.

(96) Shuk, P.; Wiemhöfer, H.-D.; Guth, U.; Göpel, W.; Greenblatt, M. *Solid State Ion.* **1996**, *89* (3), 179.

(97) Steele, B. C. H. *Solid State Ion.* **1995**, *75*, 157.

(98) Camaratta, M.; Wachsman, E. *Solid State Ion.* **2007**, *178* (23), 1411.

(99) Takahashi, T.; Esaka, T.; Iwahara, H. *J. Appl. Electrochem.* **1977**, *7* (4), 299.

(100) Azad, A. M.; Larose, S.; Akbar, S. A. *J. Mater. Sci.* **1994**, *29* (16), 4135.

(101) Drache, M.; Roussel, P.; Wignacourt, J.-P. *Chem. Rev.* **2007**, *107* (1), 80.

(102) Verkerk, M. J.; Burggraaf, A. J. *J. Electrochem. Soc.* **1981**, *128* (1), 75.

(103) Iwahara, H.; Esaka, T.; Sato, T.; Takahashi, T. *J. Solid State Chem.* **1981**, *39* (2), 173.

(104) Jiang, N.; Wachsman, E. D. *J. Am. Ceram. Soc.* **1999**, *82* (11), 3057.

(105) Wachsman, E. D. *J. Eur. Ceram. Soc.* **2004**, *24* (6), 1281.

(106) Punn, R.; Feteira, A. M.; Sinclair, D. C.; Greaves, C. *J. Am. Chem. Soc.* **2006**, *128* (48), 15386.

(107) Benkaddour, M.; Obbade, S.; Conflant, P.; Drache, M. *J. Solid State Chem.* **2002**, *163* (1), 300.

(108) Ling, C. D.; Schmid, S.; Blanchard, P. E. R.; Petříček, V.; McIntyre, G. J.; Sharma, N.; Maljuk, A.; Yaremchenko, A. A.; Kharton, V. V.; Gutmann, M.; Withers, R. L. *J. Am. Chem. Soc.* **2013**, *135* (17), 6477.

(109) Pernot, E.; Anne, M.; Bacmann, M.; Strobel, P.; Fouletier, J.; Vannier, R. N.; Mairesse, G.; Abraham, F.; Nowogrocki, G. *Solid State Ion.* **1994**, *70*, 259.

(110) Abraham, F.; Debreuille-Gresse, M. F.; Mairesse, G.; Nowogrocki, G. *Solid State Ion.* **1988**, *28*, 529.

(111) Takahashi, T.; Iwahara, H.; Esaka, T. *J. Electrochem. Soc.* **1977**, *124* (10), 1563.

(112) Zhou, W. *J. Solid State Chem.* **1988**, *76* (2), 290.

(113) Zhou, W. *J. Solid State Chem.* **1990**, *87* (1), 44.

(114) Darriet, J.; Launay, J. C.; Zúniga, F. J. *J. Solid State Chem.* **2005**, *178* (6), 1753.

(115) Mauvy, F.; Launay, J. C.; Darriet, J. *J. Solid State Chem.* **2005**, *178* (6), 2015.

(116) Kashida, S.; Hori, T.; Nakamura, K. *J. Phys. Soc. Jpn.* **1994**, *63* (12), 4422.

(117) Kashida, S.; Hori, T. *J. Solid State Chem.* **1996**, *122* (2), 358.

(118) Kuang, X.; Payne, J. L.; Farrell, J. D.; Johnson, M. R.; Evans, I. R. *Chem. Mater.* **2012**, *24* (11), 2162.

(119) Pang, G.; Feng, S.; Tang, Y.; Tan, C.; Xu, R. *Chem. Mater.* **1998**, *10* (9), 2446.

(120) Đorđević, T.; Karanović, L. *J. Solid State Chem.* **2014**, *220*, 259.

(121) Wignacourt, J. P.; Drache, M.; Confiant, P.; Boivin, J. C. *J. Chim. Phys.* **1991**, *88*, 1933.

(122) Wignacourt, J. P.; Drache, M.; Conflant, P. *J. Solid State Chem.* **1993**, *105* (1), 44.

(123) Watanabe, A. *Solid State Ion.* **1997**, *96* (1), 75.

(124) Watanabe, A.; Kitami, Y. *Solid State Ion.* **1998**, *113*, 601.

(125) Kharton, V. V.; Marques, F. M. B.; Atkinson, A. *Solid State Ion.* **2004**, *174* (1), 135.

(126) Kuang, X.; Payne, J. L.; Johnson, M. R.; Radosavljevic Evans, I. *Angew. Chem. Int. Ed.* **2012**, *51* (3), 690.

(127) Muktha, B.; Guru Row, T. N. *Inorg. Chem.* **2006**, *45* (12), 4706.

(128) Grey, C. P.; Dupré, N. *Chem. Rev.* **2004**, *104* (10), 4493.

(129) Blanc, F.; Leskes, M.; Grey, C. P. *Acc. Chem. Res.* **2013**, *46* (9), 1952.

(130) Blanc, F.; Middlemiss, D. S.; Gan, Z.; Grey, C. P. *J. Am. Chem. Soc.* **2011**, *133* (44), 17662.

(131) Forse, A. C.; Merlet, C.; Allan, P. K.; Humphreys, E. K.; Griffin, J. M.; Aslan, M.; Zeiger, M.; Presser, V.; Gogotsi, Y.; Grey, C. P. *Chem. Mater.* **2015**, *27* (19), 6848.

(132) Dunstan, M. T.; Griffin, J. M.; Blanc, F.; Leskes, M.; Grey, C. P. *J. Phys. Chem. C* **2015**, *119* (43), 24255.

(133) Buannic, L.; Blanc, F.; Hung, I.; Gan, Z.; Grey, C. P. *J. Mater. Chem.* **2010**, *20* (30), 6322.

(134) Hampson, M. R.; Evans, J. S. O.; Hodgkinson, P. *J. Am. Chem. Soc.* **2005**, *127* (43), 15175.

(135) Duer, M. J. *Introduction to Solid-State NMR Spectroscopy*; Wiley, 2004.

(136) Apperley, D. C.; Harris, R. K.; Hodgkinson, P. *Solid-State NMR: Basic Principles and Practice*; Momentum Press, 2012.

(137) Keeler, J. *Understanding NMR spectroscopy*; John Wiley & Sons, 2011.

(138) Ashbrook, S. E.; McKay, D. *Chem. Commun.* **2016**, *52* (45), 7186.

(139) Schurko, R. W. *Acc. Chem. Res.* **2013**, *46* (9), 1985.

(140) MacGregor, A. W.; O'Dell, L. A.; Schurko, R. W. *J. Magn. Reson.* **2011**, *208* (1), 103.

(141) Rhodes, H. E.; Wang, P.-K.; Stokes, H. T.; Slichter, C. P.; Sinfelt, J. H. *Phys. Rev. B* **1982**, *26* (7), 3559.

(142) Massiot, D.; Farnan, I.; Gautier, N.; Trumeau, D.; Trokiner, A.; Coutures, J. P. *Solid State Nucl. Magn. Reson.* **1995**, *4* (4), 241.

(143) Bräunling, D.; Pecher, O.; Trots, D. M.; Senyshyn, A.; Zherebtsov, D. A.; Haarmann, F.; Niewa, R. *Z. Für Anorg. Allg. Chem.* **2010**, *636* (6), 936.

(144) Tong, Y. Y. *J. Magn. Reson. A* **1996**, *119* (1), 22.

(145) Pell, A. J.; Clément, R. J.; Grey, C. P.; Emsley, L.; Pintacuda, G. *J. Chem. Phys.* **2013**, *138* (11), 114201.

(146) Pecher, O.; Halat, D. M.; Lee, J.; Liu, Z.; Griffith, K. J.; Braun, M.; Grey, C. P. *J. Magn. Reson.* **2017**, *275*, 127.

(147) Gan, Z. *J. Am. Chem. Soc.* **1992**, *114* (21), 8307.

(148) Antzutkin, O. N.; Shekar, S. C.; Levitt, M. H. *J. Magn. Reson. A* **1995**, *115* (1), 7.

(149) Hung, I.; Gan, Z. *J. Magn. Reson.* **2010**, *204* (1), 150.

(150) Dixon, W. T. *J. Chem. Phys.* **1982**, *77* (4), 1800.

(151) Antzutkin, O. N. *Prog. Nucl. Magn. Reson. Spectrosc.* **1999**, *35* (3), 203.

(152) Walder, B. J.; Dey, K. K.; Kaseman, D. C.; Baltisberger, J. H.; Grandinetti, P. J. *J. Chem. Phys.* **2013**, *138* (17), 174203.

(153) Hung, I.; Zhou, L.; Pourpoint, F.; Grey, C. P.; Gan, Z. *J. Am. Chem. Soc.* **2012**, *134* (4), 1898.

(154) Strobridge, F. C.; Middlemiss, D. S.; Pell, A. J.; Leskes, M.; Clément, R. J.; Pourpoint, F.; Lu, Z.; Hanna, J. V.; Pintacuda, G.; Emsley, L.; Samoson, A.; Grey, C. P. *J. Mater. Chem. A* **2014**, *2* (30), 11948.

(155) Massiot, D.; Montouillout, V.; Fayon, F.; Florian, P.; Bessada, C. *Chem. Phys. Lett.* **1997**, *272* (3), 295.

(156) Aurentz, D. J.; Vogt, F. G.; Mueller, K. T.; Benesi, A. J. *J. Magn. Reson.* **1999**, *138* (2), 320.

(157) Bertini, I.; Luchinat, C.; Parigi, G. *Prog. Nucl. Magn. Reson. Spectrosc.* **2002**, *40* (3), 249.

(158) Pintacuda, G.; Kervern, G. In *Modern NMR Methodology*; Topics in Current Chemistry; Springer, Berlin, Heidelberg, 2012; pp 157–200.

(159) Kaupp, M.; Köhler, F. H. *Coord. Chem. Rev.* **2009**, *253* (19–20), 2376.

(160) Kurland, R. J.; McGarvey, B. R. *J. Magn. Reson.* **1970**, *2* (3), 286.

(161) Bertini, I.; Luchinat, C. *Coord. Chem. Rev.* **1996**, No. 150, 77.

(162) Rubinstein, M.; Baram, A.; Luz, Z. *Mol. Phys.* **1971**, *20* (1), 67.

(163) Blundell, S. *Magnetism in condensed matter*; AAPT, 2003.

(164) Man, P. P. *eMagRes* **2007**.

(165) Ashbrook, S. E.; Duer, M. J. *Concepts Magn. Reson. Part A* **2006**, *28A* (3), 183.

(166) Kentgens, A. P. M. *Geoderma* **1997**, *80* (3–4), 271.

(167) Vega, A. J. *Encyclopedia of Magnetic Resonance: Quadrupolar Nuclei in Solids*; Harris, R. K., Ed.; John Wiley & Sons, Ltd: Chichester, UK, 2007.

(168) Spearing, D. R.; Farnan, I.; Stebbins, J. F. *Phys. Chem. Miner.* **1992**, *19* (5), 307.

(169) Levitt, M. H. *Spin dynamics: basics of nuclear magnetic resonance*; John Wiley & Sons, 2001.

(170) Forse, A. C.; Griffin, J. M.; Merlet, C.; Bayley, P. M.; Wang, H.; Simon, P.; Grey, C. P. *J. Am. Chem. Soc.* **2015**, *137* (22), 7231.

(171) Forse, A. C. Nuclear Magnetic Resonance Studies of Ion Adsorption in Supercapacitor Electrodes, University of Cambridge, 2016.

(172) Bain, A. D. *Prog. Nucl. Magn. Reson. Spectrosc.* **2003**, *43* (3–4), 63.

(173) Bain, A. D. *MEXICO: The McMaster Program for Exchange Lineshape Calculations*; McMaster University, Hamilton, Ont., Canada, 2002.

(174) Indris, S.; Heitjans, P.; Uecker, R.; Roling, B. *J. Phys. Chem. C* **2012**, *116* (27), 14243.

(175) Abragam, A. *Principles of nuclear magnetism (International series of monographs on physics)*; Clarendon Press, Oxford, 1961.

(176) Zhou, L.; Leskes, M.; Liu, T.; Grey, C. P. *Angew. Chem. Int. Ed.* **2015**, *54* (49), 14782.

(177) Meiboom, S. *J. Chem. Phys.* **1961**, *34* (2), 375.

(178) Brooks, R. A. *Magn. Reson. Med.* **2002**, *47* (2), 388.

(179) Spiess, H. W. In *Dynamic NMR spectroscopy*; Springer, 1978; pp 55–214.

(180) Adler, S. B.; Smith, J. W.; Reimer, J. A. *J. Chem. Phys.* **1993**, *98* (9), 7613.

(181) Read, M. S. D.; Islam, M. S.; King, F.; Hancock, F. E. *J. Phys. Chem. B* **1999**, *103* (9), 1558.

(182) Mastrikov, Y. A.; Merkle, R.; Heifets, E.; Kotomin, E. A.; Maier, J. *J. Phys. Chem. C* **2010**, *114* (7), 3017.

(183) Muñoz-García, A. B.; Ritzmann, A. M.; Pavone, M.; Keith, J. A.; Carter, E. A. *Acc. Chem. Res.* **2014**, *47* (11), 3340.

(184) Yildiz, B. *MRS Bull.* **2014**, *39* (2), 147.

(185) Pickard, C. J.; Mauri, F. *Phys. Rev. B* **2001**, *63* (24), 245101.

(186) Charpentier, T. *Solid State Nucl. Magn. Reson.* **2011**, *40* (1), 1.

(187) Bonhomme, C.; Gervais, C.; Babonneau, F.; Coelho, C.; Pourpoint, F.; Azaïs, T.; Ashbrook, S. E.; Griffin, J. M.; Yates, J. R.; Mauri, F.; Pickard, C. J. *Chem. Rev.* **2012**, *112* (11), 5733.

(188) Cuny, J.; Messaoudi, S.; Alonzo, V.; Furet, E.; Halet, J.-F.; Le Fur, E.; Ashbrook, S. E.; Pickard, C. J.; Gautier, R.; Le Polles, L. *J. Comput. Chem.* **2008**, *29* (13), 2279.

(189) Panchmatia, P. M.; Orera, A.; Rees, G. J.; Smith, M. E.; Hanna, J. V.; Slater, P. R.; Islam, M. S. *Angew. Chem. Int. Ed.* **2011**, *50* (40), 9328.

(190) Buannic, L.; Blanc, F.; Middlemiss, D. S.; Grey, C. P. *J. Am. Chem. Soc.* **2012**, *134* (35), 14483.

(191) Parr, R. G.; Yang, W. *Density-Functional Theory of Atoms and Molecules*; International Series of Monographs on Chemistry; Oxford University Press, 1994.

(192) Hohenberg, P.; Kohn, W. *Phys Rev* **1964**, *136* (3B), B864.

(193) Kohn, W.; Sham, L. J. *Phys Rev* **1965**, *140* (4A), A1133.

(194) Kümmel, S.; Kronik, L. *Rev. Mod. Phys.* **2008**, *80* (1), 3.

(195) Anisimov, V. I.; Zaanen, J.; Andersen, O. K. *Phys. Rev. B* **1991**, *44* (3), 943.

(196) Dudarev, S. L.; Botton, G. A.; Savrasov, S. Y.; Humphreys, C. J.; Sutton, A. P. *Phys. Rev. B* **1998**, *57* (3), 1505.

(197) Wang, L.; Maxisch, T.; Ceder, G. *Phys. Rev. B* **2006**, *73* (19), 195107.

(198) Becke, A. D. *J. Chem. Phys.* **1993**, *98* (2), 1372.

(199) Dovesi, R.; Orlando, R.; Roetti, C.; Pisani, C.; Saunders, V. R. *Phys. Status Solidi B* **2000**, *217* (1), 63.

(200) Dovesi, R.; Saunders, V. R.; Roetti, C.; Orlando, R.; Zicovich-Wilson, C. M.; Pascale, F.; Civalleri, B.; Doll, K.; Harrison, N. M.; Bush, I. J. *CRYSTAL09 User's Manual*; University of Torino: Torino, Italy, 2010.

(201) Carlier, D.; Ménétrier, M.; Grey, C. P.; Delmas, C.; Ceder, G. *Phys. Rev. B* **2003**, *67* (17), 174103.

(202) Zhang, Y.; Castets, A.; Carlier, D.; Ménétrier, M.; Boucher, F. *J. Phys. Chem. C* **2012**, *116* (33), 17393.

(203) Kong, X.; Terskikh, V. V.; Khade, R. L.; Yang, L.; Rorick, A.; Zhang, Y.; He, P.; Huang, Y.; Wu, G. *Angew. Chem. Int. Ed.* **2015**, *54* (16), 4753.

(204) Middlemiss, D. S.; Ilott, A. J.; Clément, R. J.; Strobridge, F. C.; Grey, C. P. *Chem. Mater.* **2013**, *25* (9), 1723.

(205) Clément, R. J.; Pell, A. J.; Middlemiss, D. S.; Strobridge, F. C.; Miller, J. K.; Whittingham, M. S.; Emsley, L.; Grey, C. P.; Pintacuda, G. *J. Am. Chem. Soc.* **2012**, *134* (41), 17178.

(206) Kim, J.; Ilott, A. J.; Middlemiss, D. S.; Chernova, N. A.; Pinney, N.; Morgan, D.; Grey, C. P. *Chem. Mater.* **2015**, *27* (11), 3966.

(207) Clément, R. J.; Xu, J.; Middlemiss, D. S.; Alvarado, J.; Ma, C.; Meng, Y. S.; Grey, C. P. *J. Mater. Chem. A* **2017**, *5* (8), 4129.

(208) Haeberlen, U. *Advances in magnetic resonance*; Academic Press, 1976; Vol. 1.

(209) Tompsett, D. A.; Middlemiss, D. S.; Islam, M. S. *Phys. Rev. B* **2012**, *86* (20), 205126.

(210) Seymour, I. D. A Combined Experimental and Theoretical Investigation of the Local Structure of Lithium Manganese Oxide Cathode Materials for Lithium Ion Batteries, University of Cambridge: Cambridge, UK, 2016.

(211) Pigliapochi, R.; Seymour, I. D.; Merlet, C.; Pell, A. J.; Murphy, D. T.; Schmid, S.; Grey, C. P. *Chem. Mater.* **2017**, accepted.

(212) Lejaeghere, K.; Bihlmayer, G.; Björkman, T.; Blaha, P.; Blügel, S.; Blum, V.; Caliste, D.; Castelli, I. E.; Clark, S. J.; Corso, A. D.; Gironcoli, S. de; Deutsch, T.; Dewhurst, J. K.; Marco, I. D.; Draxl, C.; Dułak, M.; Eriksson, O.; Flores-Livas, J. A.; Garrity, K. F.; Genovese, L.; Giannozzi, P.; Giantomassi, M.; Goedecker, S.; Gonze, X.; Grånäs, O.; Gross, E. K. U.; Gulans, A.; Gygi, F.; Hamann, D. R.; Hasnip, P. J.; Holzwarth, N. a. W.; Iuşan, D.; Jochym, D. B.; Jollet, F.; Jones, D.; Kresse, G.; Koepernik, K.; Küçükbenli, E.; Kvashnin, Y. O.; Locht, I. L. M.; Lubeck, S.; Marsman, M.; Marzari, N.; Nitzsche, U.; Nordström, L.; Ozaki, T.; Paulatto, L.; Pickard, C. J.; Poelmans, W.; Probert, M. I. J.; Refson, K.; Richter, M.; Rignanese, G.-M.; Saha, S.; Scheffler, M.; Schlipf, M.; Schwarz, K.; Sharma, S.; Tavazza, F.; Thunström, P.; Tkatchenko, A.; Torrent, M.; Vanderbilt, D.; Setten, M. J. van; Speybroeck, V. V.; Wills, J. M.; Yates, J. R.; Zhang, G.-X.; Cottenier, S. *Science* **2016**, *351* (6280), aad3000.

(213) Seymour, I. D.; Middlemiss, D. S.; Halat, D. M.; Trease, N. M.; Pell, A. J.; Grey, C. P. *J. Am. Chem. Soc.* **2016**, *138* (30), 9405.

(214) Sternheimer, R. M. *Phys. Rev.* **1954**, *95* (3), 736.

(215) van der Pers, N. M.; Hendrikx, R. W. A.; Delhez, R.; Böttger, A. J. *Rev. Sci. Instrum.* **2013**, *84* (4), 045102.

(216) Brentano, J. C. M. *Arch Sci Phys Nat* **1917**, *44*, 66.

(217) Coats, A. W.; Redfern, J. P. *Analyst* **1963**, *88* (1053), 906.

(218) Kim, S.; Park, J.; Chun, H. *J. Environ. Eng.* **1995**, *121* (7), 507.

(219) Janković, B.; Adnađević, B.; Mentus, S. *Chem. Eng. Sci.* **2008**, *63* (3), 567.

(220) Liu, W.; Ismail, M.; Dunstan, M. T.; Hu, W.; Zhang, Z.; Fennell, P. S.; Scott, S. A.; Dennis, J. S. *RSC Adv.* **2014**, *5* (3), 1759.

(221) Coats, A. W.; Redfern, J. P. *Nature* **1964**, *201* (4914), 68.

(222) Chen, H. X.; Liu, N. A.; Shu, L. F.; Zong, R. W. *J. Therm. Anal. Calorim.* **2004**, *78* (3), 1029.

(223) Kharton, V. V.; Tsipis, E. V.; Naumovich, E. N.; Thursfield, A.; Patrakeev, M. V.; Kolotygin, V. A.; Waerenborgh, J. C.; Metcalfe, I. S. *J. Solid State Chem.* **2008**, *181* (6), 1425.

(224) Henderson, G. S.; Groot, F. M. F. de; Moulton, B. J. A. *Rev. Mineral. Geochem.* **2014**, *78* (1), 75.

(225) Koningsberger, D. C.; Prins, R. (eds ). *X-ray absorption: principles, applications, techniques of EXAFS, SEXAFS, and XANES*; 1988.

(226) Mansour, A. N.; Melendres, C. A.; Pankuch, M.; Brizzolara, R. A. *J. Electrochem. Soc.* **1994**, *141* (6), L69.

(227) McBreen, J.; O'Grady, W. E.; Tourillon, G.; Dartyge, E.; Fontaine, A.; Pandya, K. I. *J. Phys. Chem.* **1989**, *93* (17), 6308.

(228) Skinner, S. J. *Int. J. Inorg. Mater.* **2001**, *3* (2), 113.

(229) Tarancón, A.; Burriel, M.; Santiso, J.; Skinner, S. J.; Kilner, J. A. *J. Mater. Chem.* **2010**, *20* (19), 3799.

(230) Haugsrud, R.; Norby, T. *Nat. Mater.* **2006**, *5* (3), 193.

(231) Yang, L.; Wang, S.; Blinn, K.; Liu, M.; Liu, Z.; Cheng, Z.; Liu, M. *Science* **2009**, *326* (5949), 126.

(232) Sengodan, S.; Choi, S.; Jun, A.; Shin, T. H.; Ju, Y.-W.; Jeong, H. Y.; Shin, J.; Irvine, J. T. S.; Kim, G. *Nat. Mater.* **2015**, *14* (2), 205.

(233) Sunarso, J.; Baumann, S.; Serra, J. M.; Meulenberg, W. A.; Liu, S.; Lin, Y. S.; Diniz da Costa, J. C. *J. Membr. Sci.* **2008**, *320* (1–2), 13.

(234) Luo, H.; Efimov, K.; Jiang, H.; Feldhoff, A.; Wang, H.; Caro, J. *Angew. Chem. Int. Ed.* **2011**, *50* (3), 759.

(235) Shao, Z.; Haile, S. M. *Nature* **2004**, *431* (7005), 170.

(236) Tuller, H. L. *Solid State Ion.* **1997**, *94* (1–4), 63.

(237) Chroneos, A.; Yildiz, B.; Tarancón, A.; Parfitt, D.; Kilner, J. A. *Energy Environ. Sci.* **2011**, *4* (8), 2774.

(238) Linford, R. G.; Hackwood, S. *Chem. Rev.* **1981**, *81* (4), 327.

(239) Reichert, D. *Annu. Rep. NMR Spectrosc.* **2005**, *55*, 159.

(240) Blanc, F.; Spencer, L.; Goward, G. R. *Encyclopedia of Magnetic Resonance: Quadrupolar NMR of Ionic Conductors, Batteries, and Other Energy-related Materials*; Harris, R. K., Ed.; John Wiley & Sons, Ltd: Chichester, UK, 2007.

(241) O'Dell, L. A.; Ratcliffe, C. I. *Encyclopedia of Magnetic Resonance: Quadrupolar NMR to Investigate Dynamics in Solid Materials*; Harris, R. K., Ed.; John Wiley & Sons, Ltd: Chichester, UK, 2007.

(242) Kim, N.; Grey, C. P. *Science* **2002**, *297* (5585), 1317.

(243) Kim, N.; Grey, C. P. *Dalton Trans.* **2004**, No. 19, 3048.

(244) Kim, N.; Vannier, R.-N.; Grey, C. P. *Chem. Mater.* **2005**, *17* (8), 1952.

(245) Holmes, L.; Peng, L.; Heinmaa, I.; O'Dell, L. A.; Smith, M. E.; Vannier, R.-N.; Grey, C. P. *Chem. Mater.* **2008**, *20* (11), 3638.

(246) Blanc, F.; Middlemiss, D. S.; Buannic, L.; Palumbo, J. L.; Farnan, I.; Grey, C. P. *Solid State Nucl. Magn. Reson.* **2012**, *42*, 87.

(247) Kim, G.; Griffin, J. M.; Blanc, F.; Haile, S. M.; Grey, C. P. *J. Am. Chem. Soc.* **2015**, *137* (11), 3867.

(248) Fuda, K.; Kishio, K.; Yamauchi, S.; Fueki, K.; Onoda, Y. *J. Phys. Chem. Solids* **1984**, *45* (11–12), 1253.

(249) Adler, S.; Russek, S.; Reimer, J.; Fendorf, M.; Stacy, A.; Huang, Q.; Santoro, A.; Lynn, J.; Baltisberger, J.; Werner, U. *Solid State Ion.* **1994**, *68* (3–4), 193.

(250) Witschas, M.; Eckert, H.; Freiheit, H.; Putnis, A.; Korus, G.; Jansen, M. *J. Phys. Chem. A* **2001**, *105* (28), 6808.

(251) Kim, N.; Hsieh, C.-H.; Huang, H.; Prinz, F. B.; Stebbins, J. F. *Solid State Ion.* **2007**, *178* (27–28), 1499.

(252) Buzlukov, A.; Trokiner, A.; Kozhevnikov, V.; Verkhovskii, S.; Yakubovsky, A.; Leonidov, I.; Gerashenko, A.; Stepanov, A.; Baklanova, I.; Tankeyev, A. *J. Solid State Chem.* **2011**, *184* (1), 36.

(253) Kiyono, H.; Matsuda, Y.; Shimada, T.; Ando, M.; Oikawa, I.; Maekawa, H.; Nakayama, S.; Ohki, S.; Tansho, M.; Shimizu, T.; Florian, P.; Massiot, D. *Solid State Ion.* **2012**, *228*, 64.

(254) Chien, P.-H.; Jee, Y.; Huang, C.; Dervişoğlu, R.; Hung, I.; Gan, Z.; Huang, K.; Hu, Y.-Y. *Chem. Sci.* **2016**, *7* (6), 3667.

(255) Dervişoğlu, R.; Middlemiss, D. S.; Blanc, F.; Lee, Y.-L.; Morgan, D.; Grey, C. P. *Chem. Mater.* **2015**, *27* (11), 3861.

(256) Martel, L.; Magnani, N.; Vigier, J.-F.; Boshoven, J.; Selfslag, C.; Farnan, I.; Griveau, J.-C.; Somers, J.; Fanghänel, T. *Inorg. Chem.* **2014**, *53* (13), 6928.

(257) Looyestijn, W. J.; Klaassen, T. O.; Poulis, N. J. *Phys. BC* **1978**, *93* (3), 349.

(258) Jurkutat, M.; Rybicki, D.; Sushkov, O. P.; Williams, G. V. M.; Erb, A.; Haase, J. *Phys. Rev. B* **2014**, *90* (14), 140504.

(259) Bert, F.; Olariu, A.; Zorko, A.; Mendels, P.; Trombe, J. C.; Duc, F.; Vries, M. A. de; Harrison, A.; Hillier, A. D.; Lord, J.; Amato, A.; Baines, C. *J. Phys. Conf. Ser.* **2009**, *145* (1), 012004.

(260) Woolley, R. J.; Skinner, S. J. *J. Power Sources* **2013**, *243*, 790.

(261) Demourgues, A.; Wattiaux, A.; Grenier, J. C.; Pouchard, M.; Soubeyroux, J. L.; Dance, J. M.; Hagenmuller, P. *J. Solid State Chem.* **1993**, *105* (2), 458.

(262) Sayer, M.; Odier, P. *J. Solid State Chem.* **1987**, *67* (1), 26.

(263) Tamura, H.; Hayashi, A.; Ueda, Y. *Phys. C Supercond.* **1993**, *216* (1–2), 83.

(264) Zhang, H. L.; Wu, X. S.; Chen, C. S.; Liu, W. *Phys. Rev. B* **2005**, *71* (6), 064422.

(265) Liu, T.; Xu, Y.; Li, Y.; Wang, Z.; Zhao, J. *Ceram. Int.* **2011**, *37* (8), 3361.

(266) Larson, A.C.; Von Dreele, R.B. *General Structure Analysis System (GSAS)*; Los Alamos National Laboratory Report LAUR 86-748; Los Alamos National Laboratory: Los Alamos, NM, 2000.

(267) Toby, B. H. *J. Appl. Crystallogr.* **2001**, *34* (2), 210.

(268) Boehm, E.; Bassat, J.-M.; Steil, M. C.; Dordor, P.; Mauvy, F.; Grenier, J.-C. *Solid State Sci.* **2003**, *5* (7), 973.

(269) Bielecki, A.; Burum, D. P. *J. Magn. Reson. A* **1995**, *116* (2), 215.

(270) Beckmann, P. A.; Dybowski, C. *J. Magn. Reson.* **2000**, *146* (2), 379.

(271) *TopSpin 3.2, software for NMR spectral analysis*; Bruker Biospin: Rheinstetten, Germany, 2012.

(272) Massiot, D.; Fayon, F.; Capron, M.; King, I.; Le Calvé, S.; Alonso, B.; Durand, J.-O.; Bujoli, B.; Gan, Z.; Hoatson, G. *Magn. Reson. Chem.* **2002**, *40* (1), 70.

(273) Winkler, E.; Rivadulla, F.; Zhou, J.-S.; Goodenough, J. B. *Phys. Rev. B* **2002**, *66* (9), 094418.

(274) Pyykkö, P. *Mol. Phys.* **2008**, *106* (16–18), 1965.

(275) Rice, D. E.; Buttrey, D. J. *J. Solid State Chem.* **1993**, *105* (1), 197.

(276) Sayers, R.; Skinner, S. J. *J. Mater. Chem.* **2011**, *21* (2), 414.

(277) Yang, S.; Shore, J.; Oldfield, E. *J. Magn. Reson.* **1992**, *99* (2), 408.

(278) Bastow, T. J.; Dirken, P. J.; Smith, M. E.; Whitfield, H. J. *J. Phys. Chem.* **1996**, *100* (47), 18539.

(279) Nordenskiold, L.; Laaksonen, A.; Kowalewski, J. *J. Am. Chem. Soc.* **1982**, *104* (2), 379.

(280) Massiot, D.; Bessada, C.; Coutures, J. P.; Taulelle, F. *J. Magn. Reson.* **1990**, *90* (2), 231.

(281) Seo, D.-H.; Lee, J.; Urban, A.; Malik, R.; Kang, S.; Ceder, G. *Nat. Chem.* **2016**, *8* (7), 692.

(282) Gerothanassis, I. P. *Prog. Nucl. Magn. Reson. Spectrosc.* **2010**, *57* (1), 1.

(283) Hu, Y.-Y.; Levin, E. M.; Schmidt-Rohr, K. *J. Am. Chem. Soc.* **2009**, *131* (24), 8390.

(284) Kentgens, A. P. M. *Encyclopedia of Magnetic Resonance: Quadrupolar Nutation Spectroscopy*; Harris, R. K., Ed.; John Wiley & Sons, Ltd: Chichester, UK, 2007.

(285) Ali, F.; Smith, M. E.; Steuernagel, S.; Whitfield, H. J. *J. Mater. Chem.* **1996**, *6* (2), 261.

(286) Druce, J.; Téllez, H.; Burriel, M.; Sharp, M. D.; Fawcett, L. J.; Cook, S. N.; McPhail, D. S.; Ishihara, T.; Brongersma, H. H.; Kilner, J. A. *Energy Environ. Sci.* **2014**, *7* (11), 3593.

(287) Bastow, T. J.; Stuart, S. N. *Chem. Phys.* **1990**, *143* (3), 459.

(288) Zhang, Z.; Greenblatt, M. *J. Solid State Chem.* **1995**, *117* (2), 236.

(289) Adler, S. B.; Reimer, J. A. *Solid State Ion.* **1996**, *91* (3–4), 175.

(290) Perrichon, A.; Piovano, A.; Boehm, M.; Zbiri, M.; Johnson, M.; Schober, H.; Ceretti, M.; Paulus, W. *J. Phys. Chem. C* **2015**, *119* (3), 1557.

(291) Broux, T.; Prestipino, C.; Bahout, M.; Hernandez, O.; Swain, D.; Paofai, S.; Hansen, T. C.; Greaves, C. *Chem. Mater.* **2013**, *25* (20), 4053.

(292) Sayers, R.; De Souza, R. A.; Kilner, J. A.; Skinner, S. J. *Solid State Ion.* **2010**, *181* (8–10), 386.

(293) Wang, F.; Grey, C. P. *J. Am. Chem. Soc.* **1998**, *120* (5), 970.

(294) Leo, A.; Liu, S.; Costa, J. C. D. da. *Int. J. Greenh. Gas Control* **2009**, *3* (4), 357.

(295) Tan, X.; Li, K.; Thursfield, A.; Metcalfe, I. S. *Catal. Today* **2008**, *131* (1–4), 292.

(296) Teraoka, Y.; Zhang, H. M.; Okamoto, K.; Yamazoe, N. *Mater. Res. Bull.* **1988**, *23* (1), 51.

(297) Zhu, X.; Yang, W. In *Mixed Conducting Ceramic Membranes*; Springer Berlin Heidelberg: Berlin, Heidelberg, 2017; pp 227–269.

(298) Aguadero, A.; Escudero, M. J.; Pérez, M.; Alonso, J. A.; Pomjakushin, V.; Daza, L. *Dalton Trans.* **2006**, No. 36, 4377.

(299) Tang, J. P.; Dass, R. I.; Manthiram, A. *Mater. Res. Bull.* **2000**, *35* (3), 411.

(300) Inprasit, T.; Limthongkul, P.; Wongkasemjit, S. *J. Electrochem. Soc.* **2010**, *157* (11), B1726.

(301) Gopalakrishnan, J.; Colsmann, G.; Reuter, B. *J. Solid State Chem.* **1977**, *22* (2), 145.

(302) Trokiner, A.; Yakubovskii, A.; Verkhovskii, S.; Gerashenko, A.; Khomskii, D. *Phys. Rev. B* **2006**, *74* (9), 092403.

(303) Trokiner, A.; Verkhovskii, S.; Gerashenko, A.; Volkova, Z.; Anikeenok, O.; Mikhalev, K.; Eremin, M.; Pinsard-Gaudart, L. *Phys. Rev. B* **2013**, *87* (12), 125142.

(304) Blasse, G. *J. Inorg. Nucl. Chem.* **1965**, *27* (12), 2683.

(305) Momma, K.; Izumi, F. *J. Appl. Crystallogr.* **2011**, *44* (6), 1272.

(306) Vashook, V. V.; Yushkevich, I. I.; Kokhanovsky, L. V.; Makhnach, L. V.; Tolochko, S. P.; Kononyuk, I. F.; Ullmann, H.; Altenburg, H. *Solid State Ion.* **1999**, *119* (1–4), 23.

(307) Shannon, R. D. *Acta Crystallogr. A* **1976**, *32* (5), 751.

(308) Cava, R. J.; Batlogg, B.; Palstra, T. T.; Krajewski, J. J.; Peck, W. F.; Ramirez, A. P.; Rupp, L. W. *Phys. Rev. B* **1991**, *43* (1), 1229.

(309) Nakamura, T.; Yashiro, K.; Sato, K.; Mizusaki, J. *Solid State Ion.* **2010**, *181* (5–7), 292.

(310) Inprasit, T.; Wongkasemjit, S.; Skinner, S. J.; Burriel, M.; Limthongkul, P. *RSC Adv.* **2014**, *5* (4), 2486.

(311) Ishikawa, K. *Bull. Chem. Soc. Jpn.* **1986**, *59* (3), 703.

(312) Heaney, P. J.; Mehta, A.; Sarosi, G.; Lamberti, V. E.; Navrotsky, A. *Phys. Rev. B* **1998**, *57* (17), 10370.

(313) Liu, C. J.; Mays, M. D.; Cowan, D. O.; Sanchez, M. G. *Chem. Mater.* **1991**, *3* (3), 495.

(314) DiCarlo, J.; Mehta, A.; Banschick, D.; Navrotsky, A. *J. Solid State Chem.* **1993**, *103* (1), 186.

(315) Wang, M.; Wu, X.-P.; Zheng, S.; Zhao, L.; Li, L.; Shen, L.; Gao, Y.; Xue, N.; Guo, X.; Huang, W.; Gan, Z.; Blanc, F.; Yu, Z.; Ke, X.; Ding, W.; Gong, X.-Q.; Grey, C. P.; Peng, L. *Sci. Adv.* **2015**, *1* (1), e1400133.

(316) Heinzmann, R.; Issac, I.; Eufinger, J.-P.; Ulbrich, G.; Lerch, M.; Janek, J.; Indris, S. *J. Phys. Chem. C* **2016**, *120* (16), 8568.

(317) Ling, C. D.; Argyriou, D. N.; Wu, G.; Neumeier, J. J. *J. Solid State Chem.* **2000**, *152* (2), 517.

(318) Sansom, J. E. H.; Richings, D.; Slater, P. R. *Solid State Ion.* **2001**, *139* (3–4), 205.

(319) Corrie, B. J.; Shin, J. F.; Hull, S.; Knight, K. S.; Vlachou, M. C.; Hanna, J. V.; Slater, P. R. *Dalton Trans.* **2015**, *45* (1), 121.

(320) Chen; Yu; Adler, S. B. *Chem. Mater.* **2005**, *17* (17), 4537.

(321) Aguadero, A.; Escudero, M. J.; Pérez, M.; Alonso, J. A.; Daza, L. *J. Fuel Cell Sci. Technol.* **2006**, *4* (3), 294.

(322) Sreedhar, K.; Rao, C. N. R. *Mater. Res. Bull.* **1990**, *25* (10), 1235.

(323) Goodenough, J. B. *J. Common Met.* **1986**, *116* (1), 83.

(324) Lee, K. H.; Hoffmann, R. *J. Phys. Chem. A* **2006**, *110* (2), 609.

(325) Bastow, T. J.; Stuart, S. N.; McDugle, W. G.; Eachus, R. S.; Spaeth, J. M. *J. Phys. Condens. Matter* **1994**, *6* (41), 8633.

(326) Plesničar, B. *Acta Chim Slov* **2005**, *52*, 1.

(327) Oldfield, E.; Coretsopoulos, C.; Yang, S.; Reven, L.; Lee, H. C.; Shore, J.; Han, O. H.; Ramli, E.; Hinks, D. *Phys. Rev. B* **1989**, *40* (10), 6832.

(328) Chaudhari, V. N.; Khandale, A. P.; Bhoga, S. S. *Solid State Ion.* **2014**, *268*, 140.

(329) Lou, H.; Ge, Y.; Chen, P.; Mei, M.; Ma, F.; Lü, G. *J. Mater. Chem.* **1997**, *7* (10), 2097.

(330) Chaudhari, V. N.; Khandale, A. P.; Bhoga, S. S. *J. Power Sources* **2014**, *248*, 647.

(331) Cromer, D. T. *J. Phys. Chem.* **1957**, *61* (6), 753.

(332) Mahato, N.; Banerjee, A.; Gupta, A.; Omar, S.; Balani, K. *Prog. Mater. Sci.* **2015**, *72*, 141.

(333) Steele, B. C. H.; Heinzel, A. *Nature* **2001**, *414* (6861), 345.

(334) Gattow, G.; Schröder, H. *Z. Für Anorg. Allg. Chem.* **1962**, *318* (3–4), 176.

(335) Taulelle, F.; Coutures, J.; Massiot, D.; Rifflet, J. In *Bulletin of Magnetic Resonance*; International Society of Magnetic Resonance, 1989; Vol. 11, pp 318–320.

(336) Ernst, H.; Freude, D.; Mildner, T.; Wolf, I. *Solid State Nucl. Magn. Reson.* **1996**, *6* (2), 147.

(337) Thurber, K. R.; Tycko, R. *J. Magn. Reson.* **2009**, *196* (1), 84.

(338) Eckert, H.; Wachs, I. E. *J. Phys. Chem.* **1989**, *93* (18), 6796.

(339) Hayashi, S.; Hayamizu, K. *Bull. Chem. Soc. Jpn.* **1990**, *63* (3), 961.

(340) Yang, S.; Park, K. D.; Oldfield, E. *J. Am. Chem. Soc.* **1989**, *111* (18), 7278.

(341) Wagner, G. W. *Inorg. Chem.* **1991**, *30* (8), 1960.

(342) Stebbins, J. F.; Oglesby, J. V.; Lee, S. K. *Chem. Geol.* **2001**, *174* (1), 63.

(343) Hardcastle, F. D.; Wachs, I. E.; Eckert, H.; Jefferson, D. A. *J. Solid State Chem.* **1991**, *90* (2), 194.

(344) Abrahams, I.; Bush, A. J.; Krok, F.; Hawkes, G. E.; Sales, K. D.; Thornton, P.; Bogusz, W. *J. Mater. Chem.* **1998**, *8* (5), 1213.

(345) Delmaire, F.; Rigole, M.; Zhilinskaya, E. A.; Aboukaïs, A.; Hubaut, R.; Mairesse, G. *Phys. Chem. Chem. Phys.* **2000**, *2* (19), 4477.

(346) Payne, J. L.; Farrell, J. D.; Linsell, A. M.; Johnson, M. R.; Evans, I. R. *Solid State Ion.* **2013**, *244* (Supplement C), 35.

(347) Tate, M. L.; Hack, J.; Kuang, X.; McIntyre, G. J.; Withers, R. L.; Johnson, M. R.; Radosavljevic Evans, I. *J. Solid State Chem.* **2015**, *225* (Supplement C), 383.

(348) Märker, K.; Pingret, M.; Mouesca, J.-M.; Gasparutto, D.; Hediger, S.; De Paëpe, G. *J. Am. Chem. Soc.* **2015**, *137* (43), 13796.

# Appendix A

## A.1 Full derivation of motion-induced changes in spectral intensity, and determination of $E_a$ of interstitial oxide ($O_i$) motion in $La_2NiO_{4+\delta}$

We first assume that the dominant source of $T_2$ relaxation arises from low-frequency motion, *i.e.* oxygen dynamics, and not high-frequency processes such as electron relaxation ($T_{1e}$) or electron hopping. (This assumption is justified by measurements at room temperature of a much longer $T_1$ (~60 ms) for $O_i$ compared to $T_2$ (~1.5 ms); high-frequency processes contribute to both $T_1$ and $T_2$, but low-frequency processes only influence $T_2$.) Then, in the slow motion regime, it is known[176–178] that the exchange rate $k_{ex}$ is inversely proportional to $T_2$:

$$\mathrm{k_{ex}} = \frac{c}{T_2} \tag{A.1.1}$$

for some positive proportionality constant $c$. Technically, the slow motion regime is influenced by the temperature dependence of the paramagnetic shifts, but this effect is expected to be small and at all temperatures we can assume we are at or below the coalescence temperature as argued in Section 3.5.2.

Secondly, we assume the integrated intensity of the interstitial feature, $I$, exhibits a mono-exponential $T_2$ decay, such that

$$I(\tau;\, T_2) = I_0 \exp\left(-\frac{2\tau}{T_2}\right) \tag{A.1.2}$$

where $\tau$ is the rotor period, experimentally fixed to a constant value of 80 μs for all Hahn echo experiments. We justify the exclusion of $T_1$ effects on the measured intensity as the recycle delay in these experiments is already quantitative (>5$T_1$), and we find that the $T_1$ of this site only decreases further with an increase in temperature. Thus, other than changes in the Boltzmann distribution of spin states considered later, we assume the signal loss is entirely due to $T_2$ relaxation prior to acquisition. Explicitly, a faster exchange rate at higher temperature leads to a shorter $T_2$ and thus a greater attenuation of signal. By contrast, in an ideal "one-pulse" experiment in which acquisition immediately follows application of the rf pulse, we would not expect any loss of signal, regardless of exchange rate; dynamics induce significant broadening, but no change in the overall integrated intensity. (As a conclusive test of the origin of the signal loss, one could measure $T_2$ at each temperature and compare the ideal $T_2$-induced and experimental decreases in intensity. In this study, however, we have not performed thorough $T_2$ measurements due to the prohibitive time cost of acquiring signal at high temperature in even a single Hahn echo experiment.)

Combining Equations (A.1.1) and (A.1.2), we obtain

$$I(\tau;\, T_2) = \mathrm{I}_0 \exp\left(-\frac{2\tau}{c}\mathrm{k}_{\mathrm{ex}}\right) = I_0 \exp\left(-\frac{2\tau}{c} A_0 \exp(-\mathrm{E}_\mathrm{a}/RT)\right) \tag{A.1.3}$$

where we have also assumed a simple Arrhenius relationship between $k_{\mathrm{ex}}$ and the sample temperature $T$, with corresponding pre-exponential factor $A_0$ and activation energy $E_a$. This gives:

$$\log I = \log I_0 - \frac{2\tau}{c} A_0 [\exp(-1/T)]^{\mathrm{E_a}/R} \tag{A.1.4}$$

which is a power-law dependence of log $I$ on the quantity exp(-1/$T$), with exponent $E_a/R$.

To obtain experimental values of $I$ at each temperature $T$, we integrate the centerband of the interstitial feature over a 12.5 kHz window (*i.e.* with boundaries equidistant from the centerband and nearest spinning sidebands). As the spinning sideband pattern is essentially temperature-independent, the centerband intensity accurately approximates a fixed fraction of the total intensity across the entire temperature range. We correct these values by the

expected loss in intensity due to a reduction in the population difference of the central transition spin states, *i.e.*,

$$I' = I \left[\exp\left(-\frac{\hbar\omega_0}{kT_0}\right) - 1\right] / \left[\exp\left(-\frac{\hbar\omega_0}{kT}\right) - 1\right] \approx \frac{T}{T_0} I, \tag{A.1.5}$$

such that the intensity is referenced to the lowest temperature ($T_0$ = 308 K) measurement. Here the Boltzmann-distributed population ratio of spin states is well-approximated linearly as a consequence of the small energy of the transition ($\omega_0 = 5.966 \cdot 10^8$ rad s$^{-1}$).

Finally, to extract $E_a$, we plot log $I'$ against exp(-$E_a$/$RT$) for a range of $E_a$ values, fit the data to a linear function, and compare $r^2$ values (coefficients of determination). From Figure A.1.1a, we see that a value of $E_a$ = 0.48 eV maximizes the goodness of fit to Equation (A.1.4) (with $r^2$ = 0.988).

Figure A.1.1b shows the reasonable linearity of the log $I'$ vs. exp(-$E_a$/$RT$) data when $E_a$ = 0.48 ± 0.06 eV, with the notable exception of the highest temperature data at 134°C (red cross). This point remains a persistent outlier regardless of the choice of $E_a$. The outsize intensity at this temperature arises from immobile oxide ions in similar but chemically distinct environments, possibly distorted $La_2O_3$–like environments near the surface. We have therefore excluded this data point when initially determining $E_a$. However, this additional intensity clearly contributes to the signal at all temperatures and leads to an underestimated value of $E_a$. Therefore, as a final correction, we repeat the analysis after subtracting the intensity measured at 134°C ($I'_{\text{high-T}}$) from the other data points. We then obtain a value of $E_a$ = 0.59 ± 0.07 eV (Figure A.1.2a) with an improved $r^2$ = 0.996, suggesting that removing the excess intensity does enhance the fit of Equation (A.1.4) to the data. Figure A.1.2b depicts the best-fit line with $E_a$ = 0.59 eV.

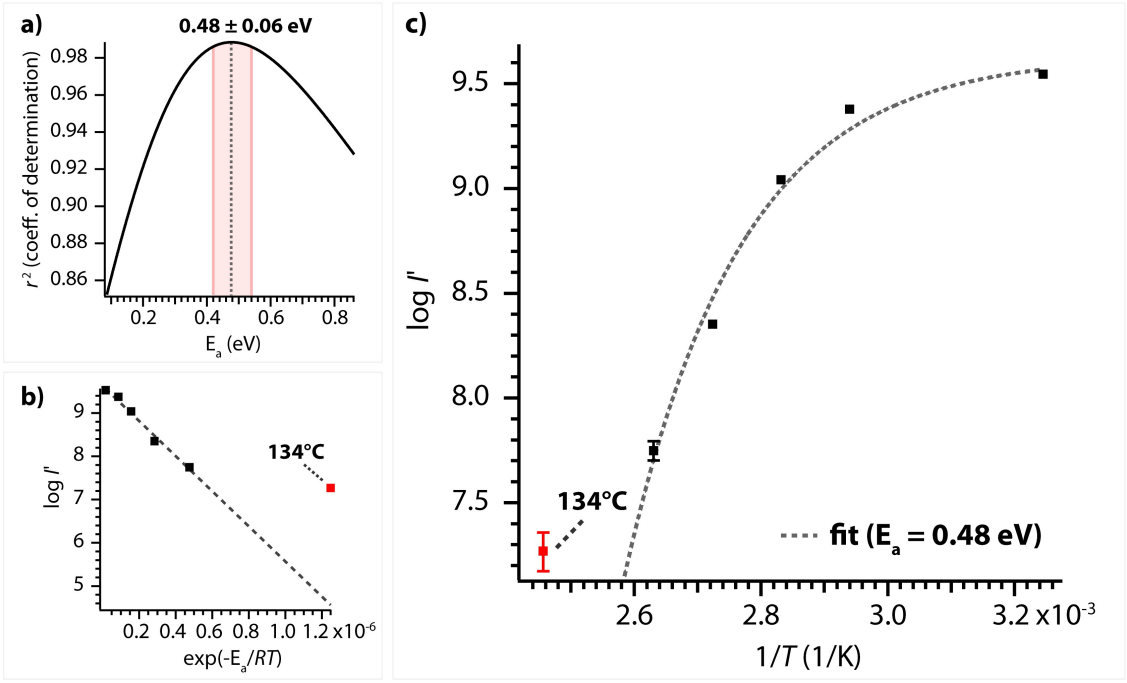


Figure A.1.1: **Initial determination of $E_a$ for interstitial motion. a)** For each $E_a$, the corrected intensity data (log $I'$) are plotted against the quantity exp(-$E_a$/$RT$), as depicted in b), and a linear fit to the data is performed, excluding the point corresponding to 134°C. The coefficient of determination $r^2$ is extracted for each linear fit as a measure of the goodness of fit. A value of $E_a$ = 0.48 ± 0.06 eV (grey dotted line with red error bars) is found to give the best fit to Equation (A.1.4) ($r^2$ = 0.988). The error in $E_a$ follows from considering the maximum variation in $r^2$ (≈ 0.0025) upon re-fitting the intensity data subject to their errors, which are inversely related to the signal-to-noise ratio of each spectrum. **b)** The corrected intensity data (log $I'$) are plotted against the quantity exp(-$E_a$/$RT$), where the optimized value of $E_a$ = 0.48 eV maximizes the collinearity of the data. The best fit line (grey dotted line) gives an $r^2$ coefficient of 0.988. The intensity at 134°C (red cross) is a persistent outlier and has been excluded from the fit. **c)** Plot of the corrected intensity data (log $I$ ') against 1/$T$, showing the best fit of Equation (A.1.4) assuming $E_a$ = 0.48 eV (again, excluding the outlier at 134°C). The observation that the signal at 134 °C is an outlier is consistent with its assignment to an environment that is not in the main phase.

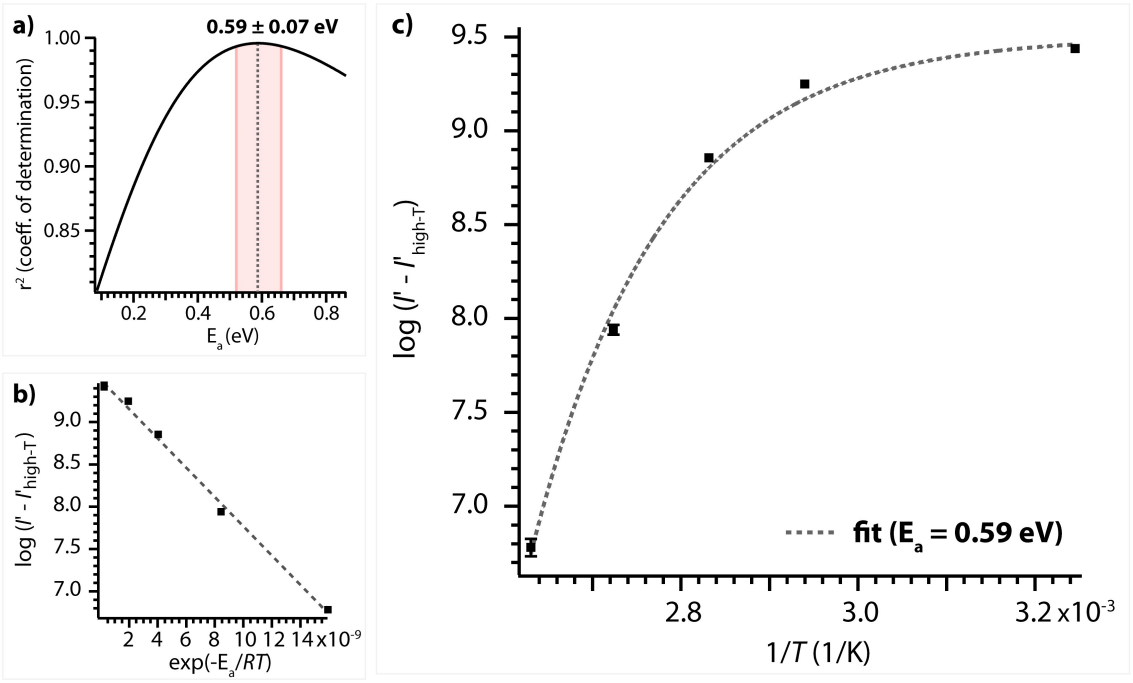


Figure A.1.2: **Revised determination of $E_a$ for interstitial motion. a)** For each $E_a$, the corrected intensity data, after subtracting the excess intensity of the feature at 134°C (log ($I$ ' - $I$ '$_{\text{high-T}}$)), are plotted against the quantity exp(-$E_a$/$RT$), as depicted in b). As before, a linear fit to the data is performed. The coefficient of determination $r^2$ is extracted for each linear fit as a measure of the goodness of fit. A value of $E_a$ = 0.59 ± 0.07 eV (grey dotted line with red error bars) is found to give the best fit with $r^2$ = 0.996, indicating a better agreement with Equation (A.1.4) than that obtained in the initial analysis (Figure A.1.1). The error in $E_a$ follows from considering the maximum variation in $r^2$ (≈ 0.0024) upon re-fitting the intensity data subject to their errors, which are inversely related to the signal-to-noise ratio of each spectrum. **b)** The corrected and subtracted intensity data (log ($I$ ' - $I'_{\text{high-T}}$)) are plotted against the quantity exp(-$E_a$/$RT$), where the optimized value of $E_a$ = 0.59 eV maximizes the collinearity of the data. The best fit line (grey dotted line) gives an $r^2$ coefficient of 0.996. The 134°C data point is not depicted; we cannot resolve any intensity at this temperature other than the overlapping feature at 565 ppm subtracted from the other data. **c)** Plot of the corrected and subtracted intensity data against 1/$T$, showing the best fit of Equation (A.1.4) assuming $E_a$ = 0.59 eV.

# Appendix B

## B.1 Powder XRD patterns of $Sm_{2-x}Sr_xNiO_{4+\delta}$

Samples were synthesized and characterized by Dr A. P. Khandale (present address, School of Chemistry, University of St Andrews, St Andrews) and were provided courtesy of Dr Yingjun Liu (Department of Materials Science and Metallurgy, University of Cambridge).

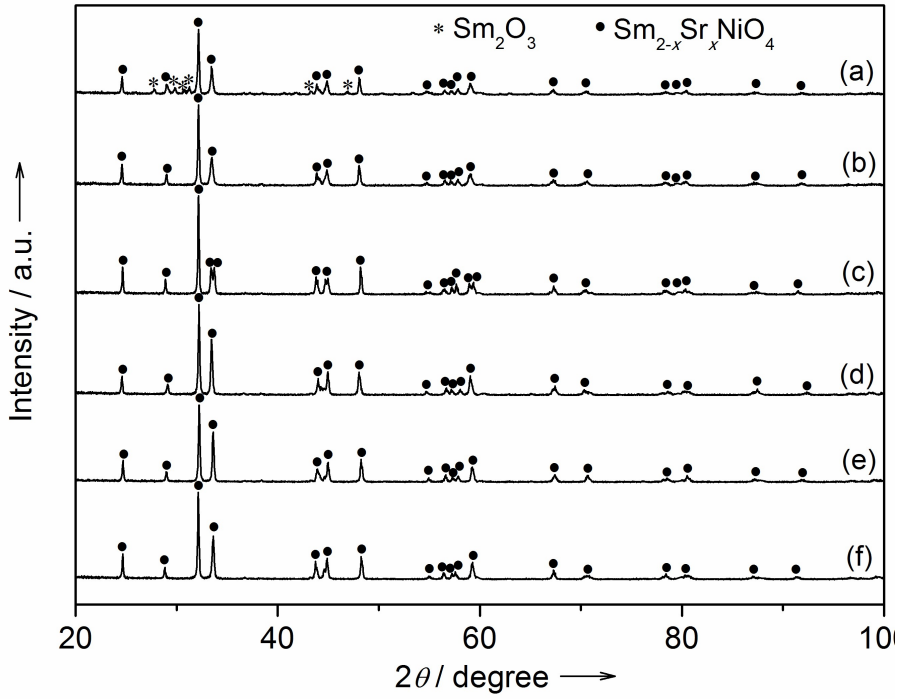


Figure B.1.1: X-ray powder diffraction patterns of $Sm_{2-x}Sr_xNiO_{4+\delta}$ for (a) $x$ = 0.3, (b) $x$ = 0.4, (c) $x$ = 0.5, (d) $x$ = 0.6, (e) $x$ = 0.8 and (f) $x$ = 1.0.

# Appendix C

## C.1 Full variable-temperature NMR datasets of $Bi_{1-x}V_xO_{1.5+x}$ and $Bi_{1-x}P_xO_{1.5+x}$ ($x$ = 0.087 and 0.148)

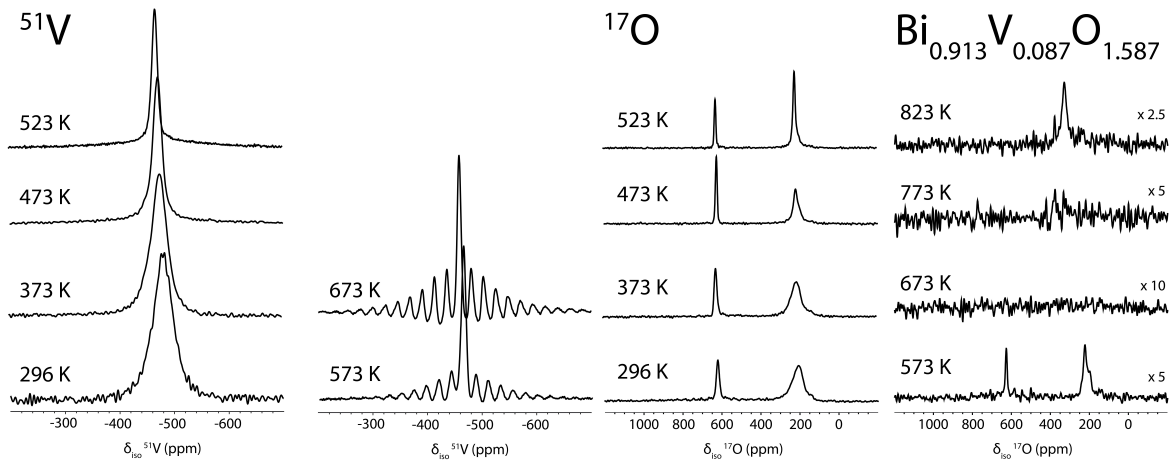


Figure C.1.1: Full set of variable temperature $^{17}O$ and $^{51}V$ NMR spectra of $Bi_{0.913}V_{0.087}O_{1.587}$ obtained at 16.4 T at a spinning rate of 4 kHz. At room temperature, the centerband in the $^{51}V$ NMR spectrum is already broadened, indicating significant motion on the spectral timescale involving the $VO_4$ environment. The $^{17}O$ NMR spectra show the coalescence of the two distinct $^{17}O$ features at higher temperatures, indicative of increasingly fast motion between these two different environments with increasing temperature.

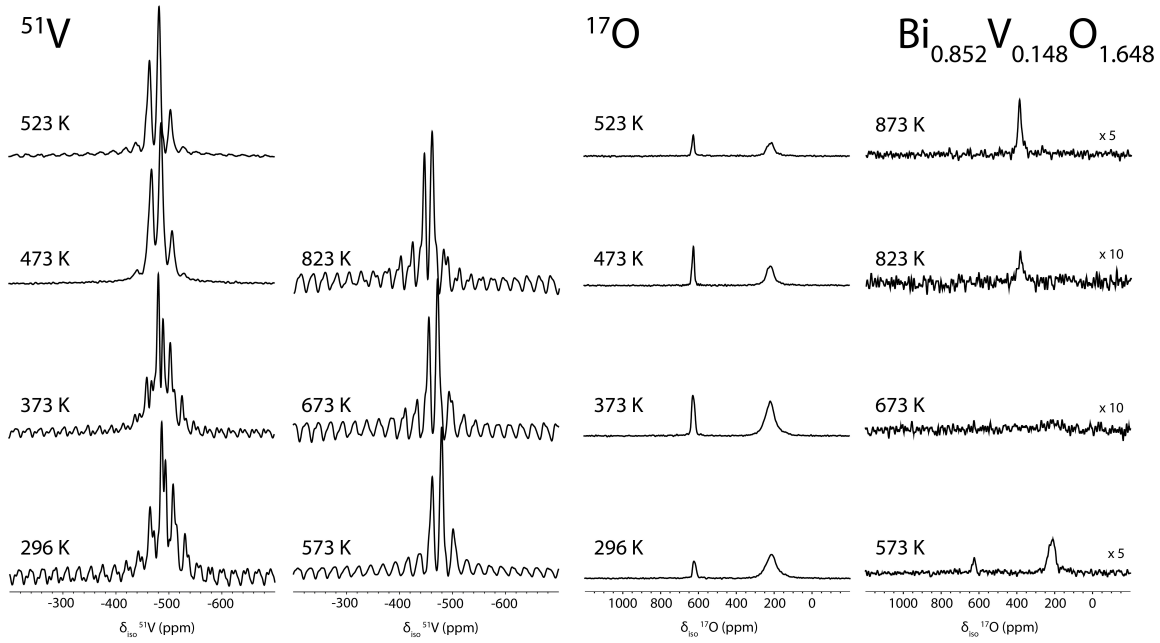


Figure C.1.2: Full set of variable temperature $^{17}O$ and $^{51}V$ NMR spectra of $Bi_{0.852}V_{0.148}O_{1.648}$ obtained at 16.4 T at a spinning rate of 4 kHz. At room temperature, the narrower centerband in the $^{51}V$ NMR spectrum indicates a slower motion relative to that observed for $Bi_{0.913}V_{0.087}O_{1.587}$. The $^{17}O$ NMR spectra show the coalescence of the two distinct $^{17}O$ features at higher temperatures, indicative of increasingly fast motion between these two different environments with increasing temperature.

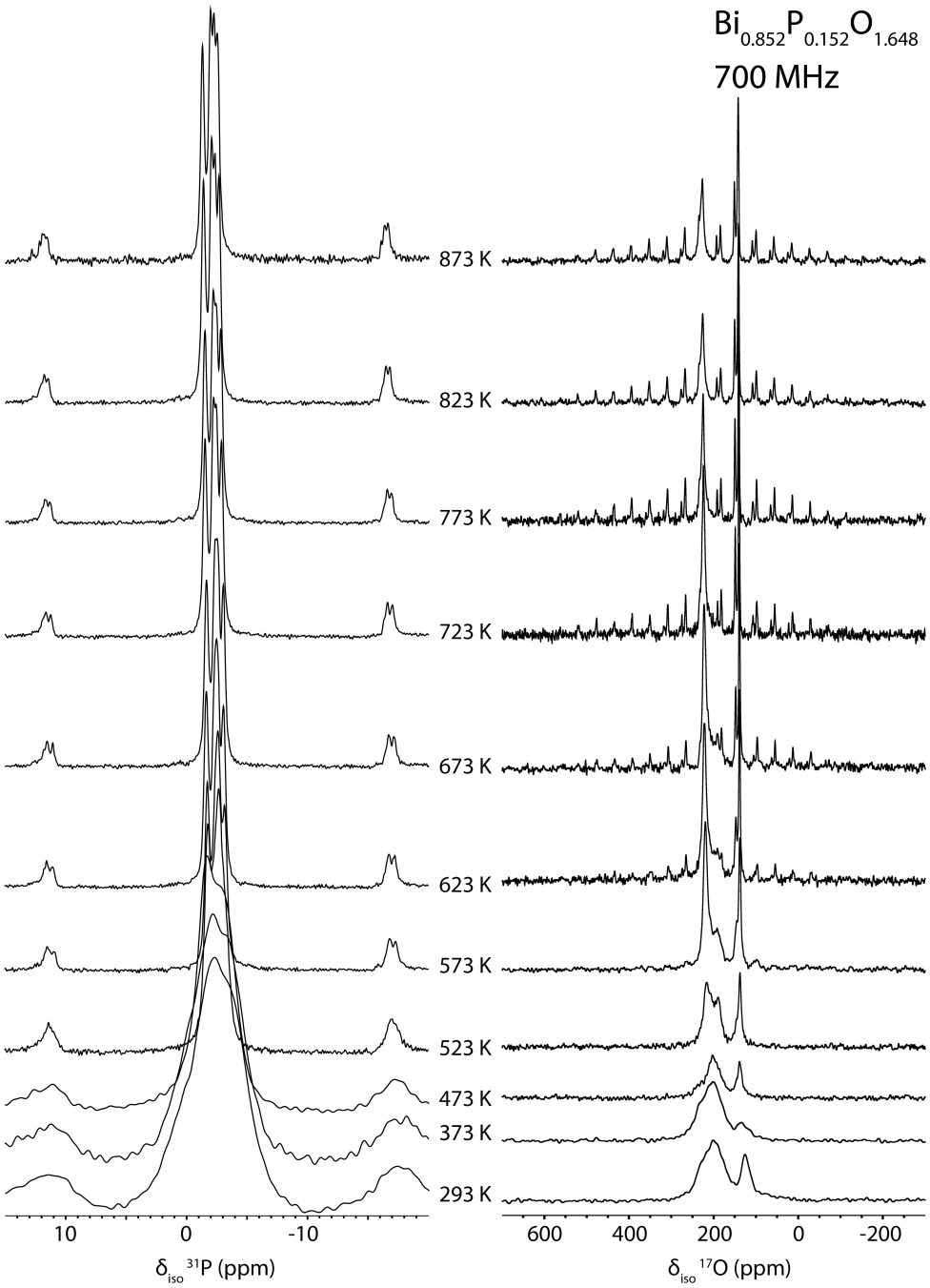


Figure C.1.3: Full set of variable temperature $^{31}$P and $^{17}$O NMR spectra of $Bi_{0.852}P_{0.148}O_{1.648}$ obtained at 16.4 T at a spinning rate of 4 kHz. The narrowing of the primary $^{31}$P resonance is ascribed to nearby oxygen motion that leads to motionally averaged local environments. At high temperature four $^{31}$P resonances are observed, in good agreement with the four crystallographically distinct environments known in this material. The $^{17}$O NMR spectra do not show any coalescence of the Bi–O and P–O features at higher temperatures, suggesting that motion remains confined to each sublattice, with sublattice exchange slower than the spectral timescale at these temperatures.